Cover Letter

Salah A Faroughi, PhD, PE
Email: salah.faroughi@txstate.edu, Phone: 404-917-9780

I am writing to express my strong interest in the tenure-track Assistant Professor position within the Lyles School of Civil Engineering at Purdue University focusing on environmental sustainability, data-driven approaches, and infrastructure resilience under extreme environments. With a proven track record in innovative research, impactful teaching, and successful mentoring, I firmly believe that my expertise aligns perfectly with the dynamic requirements of the advertised position, as well as the overarching vision of your institution. I am genuinely excited about the opportunity to contribute to the success of your esteemed institution.

Bio: I am a dynamic and accomplished scholar and educator in the field of Earth systems and geo-energy systems. I hold both a B.Sc. and an M.Sc. in Mechanical Engineering. I pursued a second M.Sc. in Earth & Atmospheric Sciences and later completed my Ph.D. in Civil and Environmental Engineering under the supervision of Dr. Christian Huber at the Georgia Institute of Technology (Georgia Tech). I engaged in postdoctoral research at the Massachusetts Institute of Technology (MIT), working with Prof. Gareth McKinley in the Department of Mechanical Engineering. Following my postdoc, I co-founded TubeIn Technology LLC in 2018, culminating in a successful exit with proven achievements in product development and project management. My time at MIT facilitated strong relationships with several oil and gas service firms, revealing their pain points related to hydraulic fracturing fluid design and sourcing complexities. I applied my extensive scientific knowledge of complex fluids, coupled with emerging computing technologies, to address this industry-wide challenge and successfully commercialized an accessible solution. I developed an AI-driven marketplace to reshape the fracturing fluid design and sourcing landscape. I bootstrapped the company from the ground up and expanded the team to bring the product to market. In early 2020, the technology was successfully licensed to a Houston-based company. In 2021, I made the decision to return to academia, joining the Civil Engineering Department in Ingram School of Engineering at Texas State University as a tenure-track Assistant Professor. Since then, I have established my research group, the Geo-Intelligence Lab, and sustained it through securing funding with a research focus driven by the "Energy-Environment" dual challenge.

Current Research: My interdisciplinary research has been marked by a relentless commitment to advancing the pursuit of affordable and reliable green/clean energy sources, all while ensuring environmental sustainability. My focus rests on investigating (i) the latent space in geo-climate data across different spatiotemporal scales in the context of exascale Earth systems (e.g., AI-augmented global and regional climate models, etc.), and (ii) the transport and biogeochemistry of complex fluids in heterogeneous porous media in the context of geo-energy systems (e.g., subsurface hydrogen and carbon storage, geothermal, etc.). At the core of my research lies the efforts to bridge knowledge gaps in order to address urgent challenges related to climate change and the adoption of green energy. Through the utilization of deep-learning and data-driven techniques firmly bounded by fundamental principles and physics developed using cutting-edge experimental setups and high-fidelity computational models, my research group dedicates itself to three fundamental research thrusts: (i) predicting the climate-change-induced stressors to assess infrastructure and community vulnerabilities and formulate adaptation strategies enhancing climate resiliency, (ii) understanding the pore-scale dynamics of multiphase flow in porous media under geologic, biotic, and flow uncertainty, and (iii) implementing deep learning-based algorithms for interpreting and visualizing big and multi-channel geo-climate datasets. My leadership and collaborations have culminated in the acquisition of approximately $5.0 million in funding from various private, state, and federal agencies such as DOE, NSF, USDA, TxDOT, ACS-PRF, and more. Our findings are disseminated across esteemed journals including Nature, GRL, PRE, POF, APS, JNNFM, and others. Among my ongoing projects, two endeavors particularly ignite my enthusiasm. The first encompasses the development of a surrogate model for subsurface gas storage, factoring in microbial-mediated biotic reactions. The second revolves around crafting a context-aware, neural-accelerated visualization platform tailored for multidimensional scientific geo-climate data. These projects showcase my interdisciplinary research portfolio and underline my dedication to advancing energy/climate solutions and addressing critical knowledge gaps.

Teaching and Mentoring: An integral part of my professional identity is formed by teaching and mentoring to stimulate critical thinking and collaborative problem-solving in students. My commitment lies in harnessing innovative teaching methods to ignite inspiration and equip students to navigate the intricate landscape of STEM fields. My dedication to fostering exceptional learning experiences stems from a profound grasp of the mechanisms underpinning student learning. My teaching philosophy, grounded in the recognition of the fragility of student learning, the promotion of practical application of foundational scientific concepts, and the practice of agile teaching and assessment, has been refined through my participation in the esteemed ExCEEd Teaching Workshop by ASCE, which has enriched my pedagogical approach. I have designed and successfully instructed a diverse array of graduate and undergraduate courses at Texas State University. For each course, I adeptly employed content-targeted teaching, interdisciplinary enrichment, and supervised peer-based assessments. In addition to my teaching efforts, I have provided mentorship to a diverse cohort of postdoctoral fellows, graduate, and undergraduate students, fostering their personal growth and professional accomplishments. My mentorship extends beyond Texas State University, as I had the privilege to guide graduate and undergraduate students at institutions like MIT and the University of Minho in Portugal. I also gained experience as a mentor, teaching assistant, and lab instructor at Georgia Tech. My dedication to student training and skill development finds manifestation in the establishment of the TxST-CCS program at Texas State University aiming to provide training in subsurface clean energy initiatives. Its overarching objectives encompass ensuring the institution possesses the requisite resources and capabilities for spearheading early-stage R&D endeavors focused on subsurface gas storage. Equally important, the program is designed to equip minority students from underrepresented and structurally marginalized communities with the knowledge and skills necessary to address pressing climate and energy challenges, positioning them as the future workforce in this crucial domain

Diversity: In my role as an educator and mentor, I also hold a strong commitment to diversity, equity, and inclusion. I believe in the transformative potential of cross-cultural exposure and highly value the insights gained from diverse backgrounds. Throughout my career, I have actively engaged with various cultures, languages, and religions, which has fostered within me a profound appreciation for the intrinsic value of diversity. My own experience as a minority has further solidified my dedication to amplifying the voices and perspectives of underrepresented groups. I've actively contributed to fostering inclusivity through roles such as a graduate resident advisor, organizing cultural events, and establishing initiatives for underrepresented students from structurally marginalized communities. At Texas State University, a cornerstone of my efforts is to amplify the presence of underrepresented students in STEM fields and to address the systemic underrepresentation of minority groups in STEM. My ultimate goal is to cultivate an environment where all individuals feel empowered to contribute their unique perspectives. Through this approach, we can drive innovation, foster progress, and diminish the influence of biases.

Final Remarks: My extensive research, teaching, and mentoring experience at institutions like MIT, Georgia Tech, and Texas State University underscore my dedication to fostering interdisciplinary research and my commitment to cutting-edge education. I am excited to bring my expertise to your institution and contribute to advancing student learning and intellectual growth. Enclosed herewith are my curriculum vitae, research portfolio, teaching philosophy, and diversity statements. I welcome the opportunity to engage in a comprehensive conversation about how my background seamlessly aligns with the objectives of this position. I extend my sincere gratitude for considering my application.

Salah A. Faroughi, Ph.D., P.E.

Website: Geo-Intelligence Lab
Profile: LinkedIn

Email: salah.faroughi@txstate.edu
Mobile : +1 404 917 9780
Last Updated: September 24, 2023

PROFESSIONAL PREPARATION

- **Massachusetts Institute of Technology** — Cambridge, MA
  Postdoctoral Fellow – Mechanical Engineering – Advisor: Prof. Gareth McKinley — *Oct 2016 - Jan 2018*
- **Georgia Institute of Technology** — Atlanta, GA
  Ph.D. – Civil & Environmental Engineering – Advisor: Prof. Christian Huber — *Aug 2012 - Aug 2016*
- **Georgia Institute of Technology** — Atlanta, GA
  M.Sc. – Earth & Atmospheric Sciences – Advisor: Prof. Christian Huber — *Aug 2012 - Dec 2014*
- **Sharif University of Technology** — Tehran, Iran
  M.Sc. – Mechanical Engineering – Advisor: Prof. Mehrdad T. Manzari — *Sep 2009 - Sep 2011*
- **Urmia University** — Urmia, Iran
  B.Sc. – Mechanical Engineering – Advisor: Prof. Mahdi Pestie — *Sep 2005 - Sep 2009*

PROFESSIONAL APPOINTMENTS

- **Assistant Professor — Tenure Track** — San Marcos, TX
  Texas State University — Ingram School of Engineering — *Aug 2021 - Present*
  - Established an interdisciplinary research team, Geo-Intelligence Lab, composed of a diverse group of talented postdoctoral fellows, graduate and undergraduate students focusing on the "energy-environment" dual challenge.
  - Secured around $5.0 million in funding from private, state, and federal agencies geared towards understating the latent space in geo-climate data across different spatiotemporal scales in the context of Exascale Earth systems and geo-energy systems.
  - Established TxST-CCS program to train students from underrepresented and structurally marginalized communities and prepare them, as the future workforce, to resolve the pressing climate change challenges and green energy adoption.
- **Co-founder** — San Marcos, TX
  TubeIn Technology LLC — *Nov 2017 - Present*
  - Bootstrapped the company, built and expanded the team, developed a cutting-edge SaaS platform to host a digital-twin marketplace, FluidMart™, providing a trusted platform for prescribing fracturing fluid design and selection, and successfully licensed the technology to a private company for a tangible return on investment.
  - Managed in-house and offshore engineers (8-12 people) with sectoral expertise in polymer physics, chemistry, computational fluid mechanics, machine learning and software engineering.
- **Senior R&D Scientist** — Houston, TX
  Petrolern LLC — *Mar 2020 - Aug 2021*
  - Managed a team of talented scientists (6-8 people) focused on projects and tenders related to the safety and monitoring of geothermal energy and CO2 subsurface storage, utilizing state-of-the-art computational technologies. This effort resulted in the successful development of GeoDeck™, a groundbreaking VR-based visualization pipeline designed to enable immersive exploration of complex and multidimensional subsurface data.
  - Led the design and development of a sophisticated down-hole tool to measure stress and strain in metal-casing and the surrounding rocks (we received NSF SBIR funding for this tool design).
  - Led the design and development of a vibration-to-stress statistical algorithm to guide drilling in real-time based on drilling dynamic data (we received DOE SBIR funding for this tool design).
- **Research Engineer II** — Houston, TX
  Flotek Industries — *Oct 2018 - Mar 2020*
  - Designed a road-map alongside senior executive team to move toward digital transformation by integrating disruptive digital innovations in all operations from procurement, product design, manufacturing, sales, and data collection. This practice shortened the sales cycle by a factor of 30 for frac fluids through detecting qualifying leads and extrapolating data to generate reports.
  - Led the development of patent-pending ultra-stable polymer-based slurries, introducing a highly cost-effective solution (51% below the industry standard) for the design and delivery of diverse chemical additives used in reservoir full fluid systems.This innovative technology finds applications across various areas such as well stimulation, completions, remediation, etc.
  - Led the design & fabrication of optimized extensional and shear micro-rheometers for dilute polymeric solutions to measure the elasticity of dilute fracturing fluids.
- **Process Engineer – Internship** — Newark, DE
  Delaware Research and Technology Center – Air Liquide — *May 2015 - Sep 2016*
  - Explored the environmental impact of foam fracking fluids compared to water-based fluids, demonstrating an impressive 80% reduction in environmental concerns in unconventional well treatments, and conducted CFD studies to analyze the rheology of energized N_2 and CO_2 foams, and their ability to carry proppants (e.g., sand particles) within fracture networks.

- **Graduate Research Assistant** Atlanta, GA
  Georgia Institute of Technology *Aug 2012 - May 2015*
  - Developed advanced theoretical models that account for the impact of microstructures on the responses of particulate media, focusing on the rheology of suspensions and emulsions as well as the conductivity of composites. Designed and implemented an experimental setup and 3D parallel numerical modeling techniques to accurately quantify buoyant transport and capillary fingering phenomena in porous media.

GRANTS AND CONTRACTS

- **PI: National Science Foundation, $300,000** Pending
  EAGER: Microbial-Mediated Hydrogen Loss in Underground Storage Using AI-Assisted Microfluidic Flow Cell
- **PI: Department of Energy, $1,100,000** Pending
  SBIR Phase II: Context-aware Neural-accelerated Exploration Pipeline for Volumetric Geo-Climate-Data
- **Co-PI: Department of Energy, $3,750,000** Pending
  Multidisciplinary Research and Workforce Development on PFAS Fate and Transport in Unsaturated Porous Media
- **Co-PI: Department of Transportation, $190,000** 2023 - 2025
  UTC: A Holistic Approach to Bridge Scour Design using Sediment Transport and SEAHive Elements
- **PI: American Chemical Society - PRF, $110,000** 2023 - 2025
  Probing Mesoscopic Structures in Petroleum Fluids Containing Magnetic Superquadric Particle
- **PI: Department of Energy, $200,000** 2023 - 2023
  SBIR Phase I: Context-aware Neural-accelerated Visualization Pipeline for Big Volumetric Data
- **PI: Run-to-R1 Texas State University, $214,000** 2023 - 2025
  Smart Polymeric Additives to Minimize Short-circuiting in Enhanced Geothermal Systems
- **PI: Department of Energy, $240,000** 2022 - 2023
  FECM: Infrastructure Assessment for Technology Innovation, Development and Training in Carbon Management
- **PI: Department of Energy, $150,000** 2022 - 2024
  BER: ESMs Latent Space Exploration for Uncertainty Quantification and Spatiotemporal Downscaling
- **PI: National Science Foundation, $50,000** 2022 - 2023
  AssetScope: Edge Intelligence for Continuous Monitoring in Commercial-scale Smart Infrastructures
- **Co-PI: Department of Agriculture, $240,000** 2022 - 2026
  Smart Farm for Precision Agriculture
- **Co-PI: Texas Department of Transportation, $465,000** 2022 - 2024
  Develop a Real-Time Decision Support Tool for Urban Roadway Safety Improvement
- **PI: MIRG Texas State University, $30,000** 2022 - 2023
  Big Data Compression, Reduction, and Intelligent Fusion for Technology-enhanced Infrastructures
- **PI: IRA Texas State University, $15,000** 2022 - 2023
  Fiber-Integrated Civil Infrastructures: Edge Intelligence to Harness Big Monitoring Data
- **Co-PI: Texas Department of Transportation, $297,000** 2021 - 2023
  Leveraging Artificial Intelligence (AI) Techniques to Detect, Forecast, and Manage Freeway Congestion
- **PI: Department of Energy, $150,000** 2021 - 2021
  SMART Competition Prize: A Smart Visualization Platform for Big Data with Seamless and Immersive Solution
- **Co-PI: Department of Energy, $1,200,000** 2021 - 2023
  SBIR Phase II: An End-to-End Solution for In-situ Stress Estimation Using Downhole Drilling Dynamics Data
- **PI: Department of Energy, $1,200,000** 2020 - 2022
  SBIR Phase II: Automated Data Collection and Transmission System for Subsurface CO2 Monitoring
- **Co-PI: MIT-Portugal Seed Project, $80,000** 2017 - 2018
  A parallel fully-resolved multiscale algorithm for flow simulation of particle-laden viscoelastic fluids

TEACHING

- **Texas State University: Instructor** 2021 - Present
  - **MSEC 7395:** Finite Element Method (Graduate Level).
  - **MSEC 7355:** Transport in Porous Media (Graduate Level).
  - **CE 5331:** Computational Mechanics in Geosystems (Graduate Level).
  - **ENGR 3380:** Fluid Mechanics (Undergraduate Level).
  - **CE 3330:** Soil Mechanics (Undergraduate Level).
  - **CE 3331:** Infrastructure Foundations (Undergraduate Level).
- **Georgia Institute of Technology: Teaching Assistant/Lab Instructor** 2012 - 2016
  - **EAS 4610:** Earth Modeling Systems using Finite Difference Method (Undergraduate Level).
  - **EAS 2600:** Intro to Earth Materials and Processes (Undergraduate Level).

PUBLICATIONS

- **Patents**
  4. Mousavi, S. M., Lee, B. J., **Faroughi, S. A.**. Passive control method to create a pulsation system for droplet breakup (submitted, 2023).
  3. **Faroughi, S. A.**. Data-driven marketplace to design, select and source complex fluid products and services (submitted, 2021).
  2. **Faroughi, S. A.**, Sullivan, P. Regmi, N. Composition of Highly stable slurries having long shelf-life over a broad range of storage temperature (submitted, 2020).
  1. **Faroughi, S. A.**, Sullivan, P. Regmi, N. Methods of manufacture and methods of use of highly stable slurries having long shelf-life over a broad range of storage temperature (submitted, 2020).

- **Books & Book Chapters**
  2. Fernandes, C., **Faroughi, S. A.**, Ferrás, L. L., & Afonso, A. M. (2022). Advanced polymer simulation and processing - Volume 1, Polymers.
  1. Fernandes, C., **Faroughi, S. A.**, Ferrás, L. L., & Afonso, A. M. (2022). Advanced polymer simulation and processing - Volume 2, Polymers.

- **Journal Papers** (*Undergraduate advisee; **Graduate advisee; ‡Postdoc advisee)

  Under Review

  41. **Faroughi, S. A.** & ‡Mousavi, S. M. (2023). Pore-scale Analysis of Wettability Heterogeneity Effects on Hydrogen Trapping Mechanisms in Underground Storage, (under review).
  40. **Sultanmohammadi, R. & **Faroughi, S. A.** (2023). Implicit Neural Representation to Compress and Visualize Multidimensional Earth System Data, (under review).
  39. ‡Mahjour, S. K., *Shakya, S., & **Faroughi, S. A.** (2023). General Circulation Model Reduction Under Climatic Uncertainty for Texas. (under review).
  38. **Pawar, N., **Sultanmohammadi, R., & **Faroughi, S. A.** (2023). Spatial Downscaling for Multiphase Flow in Porous Media Using Tensor Decomposition and Deep Learning, (under review).
  37. **Pawar, N., **Sultanmohammadi, R., S. K., & **Faroughi, S. A.** (2023). E3SM Climate Data Downscaling: A Comparison of Super-Resolution Deep Learning Models, (under review).
  36. Inturi V., ‡Mahjour, S. K., & **Faroughi, S. A.** (2023). Data Intelligence and Visualization in Distributed Fiber Optic Integrated Geo-infrastructure: Progress and Perspectives, (under review).
  35. ‡Mousavi, S. M. & **Faroughi, S. A.** (2023). Bubble Generation in Microgravity: A Study Using IsoAdvector and Modified Dynamic Contact Angle Schemes in T-Type Micro Junctions, (under review).
  34. ‡Mousavi, S. M. & **Faroughi, S. A.** (2023). Quantitative Comparison of Dam-break and Bubble Flows Based on CF-VOF and IR-VOF Schemes, (under review).

  In-Press & Published

  33. ‡Mahjour, S. K. & **Faroughi, S. A.** (2023). Selecting Representative Geological Realizations to Model Subsurface CO_2 Storage Under Uncertainty. International Journal of Greenhouse Gas Control, Volume 127, 103920.
  32. **Datta, P. & **Faroughi, S. A.** (2023). A multihead LSTM technique for prognostic prediction of soil moisture. Geoderma, 433, 116452.

31. ‡Mahjour, S. K. & **Faroughi, S. A.** (2023). Risks and Uncertainties in Carbon Capture, Transport, and Storage Projects: A Comprehensive Review. Gas Science and Engineering, 205117.
30. ‡Mahjour, S. K., Liguori, G., & **Faroughi, S. A.** (2023). Selection of Representative General Circulation Models Under Climatic Uncertainty for Western North America, Research Square, 2698287.
29. ‡Mousavi, S. M., Jarrahbashi, D., Lee, B. J., Karimi, N., & **Faroughi, S. A.** (2023). Impact of Hybrid Surfaces on the Droplet Breakup Dynamics in Microgravity Slug Flow: A Dynamic Contact Angle Analysis. Physics of Fluids, 35, 072003.
28. **Faroughi, S. A.**, & Huber, C. (2023). Parameterize the Viscosity of Crystal-rich Magmas using Rheological State Variables. Journal of Volcanology and Geothermal Research, 0377-0273, 107856.
27. ‡Fernandes, C., & **Faroughi, S. A.** (2023). Particle-level Simulation of Magnetorheological Fluids: A Fully Resolved Solver. International Journal of Multiphase Flow, 69, 104604.
26. Chun, B., ‡Mousavi, S. M., Lee, J., Lee, B. J., & **Faroughi, S. A.** (2023). On the effects of fractal geometry on reacting and nonreacting flows in a low-swirl burner: A numerical study with large-eddy simulation. Case Studies in Thermal Engineering, 49, 103385.
25. **Sultanmohammadi, R., & **Faroughi, S. A.** (2023). Heterogeneity Downscaling in Digital Micro-CT Images of Carbonate Rock Using Super-Resolution Deep Learning. Applied Computers & Geosciences, (In Press).
24. **Datta, P., & **Faroughi, S. A.** (2023). Angle of Repose for Superquadric Particles: Investigating the Influence of Shape Parameters, Computers & Geotechnics, (In Press).
23. ‡Mousavi, S. M., Sotoudeh, F., Chun, B., Lee, B. J., Karimi, N., & **Faroughi, S. A.** (2023). Anti-icing wing and aircraft applications of mixed-wettability surfaces: A comprehensive review. Cold Regions Science and Technology, (In Press).
22. ‡Mousavi, S. M. & **Faroughi, S. A.** (2023). Numerical Investigation of the Effects of Radiative Heat Loss on Combustion Instability Prediction, Engineering, (In Press).
21. **Faroughi, S. A.**, **Datta, P., ‡Mahjour, S. K., & Faroughi, S. (2022). Physics-informed Neural Networks with Periodic Activation Functions for Solute Transport in Heterogeneous Porous Media. arXiv preprint arXiv:2212.08965.
20. **Faroughi, S. A.**, **Pawar, N., ‡Fernandes, C., Das, S., Kalantari, N. K., & ‡Mahjour, S. K. (2022). Physics-Guided, Physics-Informed, and Physics-Encoded Neural Networks in Scientific Computing. arXiv preprint arXiv:2211.07377.
19. **Faroughi, S. A.**, & Del Giudice, F. (2022). Microfluidic Rheometry and Particle Settling: Characterizing the Effect of Polymer Solution Elasticity. Polymers, 14(4), 657.
18. **Faroughi, S. A.**, Roriz, A. I., & **Fernandes, C. (2022). A meta-model to predict the drag coefficient of a particle translating in viscoelastic fluids: a machine learning approach. Polymers, 14(3), 430.
17. ‡Fernandes, C., **Faroughi, S. A.**, Ribeiro, R., Isabel, A., & McKinley, G. H. (2022). Finite volume simulations of particle-laden viscoelastic fluid flows: Application to hydraulic fracture processes. Engineering with Computers, 1-27.
16. Boak J., Cohen, A. J.**Faroughi, S. A.**, Soroush, H., Richards, M. (2021), Geothermal Energy: A Sustainable Alternative to Well Abandonment, Canadian Society of Exploration Geophysicists - CSEG, 46, 01.
15. Cohen A. J., Soroush H., & **Faroughi, S. A.**. (2020). No Longer a Dream: AI-based Multimodal Data Integration for Subsurface Monitoring, Geo ExPro, 64.
14. **Faroughi, S. A.**, ‡Fernandes, C., Nóbrega, J. M., & McKinley, G. H. (2020). A closure model for the drag coefficient of a sphere translating in a viscoelastic fluid. Journal of Non-Newtonian Fluid Mechanics, 277, 104218.
13. ‡Fernandes, C., **Faroughi, S. A.**, Carneiro, O. S., Nóbrega, J. M., & McKinley, G. H. (2019). Fully-resolved simulations of particle-laden viscoelastic fluids using an immersed boundary method. Journal of Non-Newtonian Fluid Mechanics, 266, 80-94.
12. Bordbar, A., Faroughi, S., & **Faroughi, S. A.** (2018). A pseudo-TOF based streamline tracing for streamline simulation method in heterogeneous hydrocarbon reservoirs. American Journal of Engineering Research, 7(4), 23-31.
11. **Faroughi, S. A.**, Pruvot, A. J. C. J., & McAndrew, J. (2018). The rheological behavior of energized fluids and foams with application to hydraulic fracturing. Journal of Petroleum Science and Engineering, 163, 243-263.
10. **Faroughi, S. A.**, & Huber, C. (2017). A self-similar behavior for the relative viscosity of concentrated suspensions of rigid spheroids. Rheologica Acta, 56(1), 35-49.
9. Parmigiani, A., **Faroughi, S. A.**, Huber, C., Bachmann, O., & Su, Y. (2016). Bubble accumulation and its role in the evolution of magma reservoirs in the upper crust. Nature, 532(7600), 492-495.

8. **Faroughi, S. A.**, & Huber, C. (2016). A theoretical hydrodynamic modification on the soil texture analyses obtained from the hydrometer test. Géotechnique, 66(5), 378-385.
7. **Faroughi, S. A.**, & Huber, C. (2015). A generalized equation for rheology of emulsions and suspensions of deformable particles subjected to simple shear at low Reynolds number. Rheologica Acta, 54(2), 85-108.
6. **Faroughi, S. A.**, & Huber, C. (2015). Effective thermal conductivity of metal and non-metal particulate composites with interfacial thermal resistance at high volume fraction of nano to macro-sized spheres. Journal of Applied Physics, 117(5), 055104.
5. **Faroughi, S. A.**, & Huber, C. (2014). Crowding-based rheological model for suspensions of rigid bimodal-sized particles with interfering size ratios. Physical Review E, 90(5), 052303.
4. **Faroughi, S. A.**, & Huber, C. (2015). Unifying the relative hindered velocity in suspensions and emulsions of nondeformable particles. Geophysical Research Letters, 42(1), 53-59.
3. **Faroughi, S. A.**, & Huber, C. (2015). Response to "Comment on 'Effective thermal conductivity of metal and non-metal particulate composites with interfacial thermal resistance at high volume fraction of nano to macro-sized spheres'"[J. Appl. Phys. 117, 216101 (2015)]. Journal of Applied Physics, 117(21), 216102.
2. **Faroughi, S. A.**, Faroughi, S., & McAdams, J. (2013). A prompt sequential method for subsurface flow modeling using the modified multi-scale finite volume and streamline methods. Int. J. Num Analysis and Modeling, 4(2), 129-150.
1. **Faroughi, S. A.** & Manzari, M. T. (2012). The streamline method algorithm for solving incompressible one- and two-phase flow in 2D porous media on the structured mesh. Sharif Mechanical Engineering Journal, Volume 29, Issue 1, Page 125-134.

- **Conferences Proceedings & Abstracts**

33. ‡Mahjour, S. K., & **Faroughi, S. A.** (2023). Representative General Circulation Models: A Robust Selection Framework Under Climate Uncertainty. ARM/ASR Joint User Facility and PI Meeting, North Besthesda, MD, USA.
32. **Soltanmohammadi, R., ‡Mahjour, S. K., & **Faroughi, S. A.** (2023). Downscaling Digital Rock Micro-CT Image With Super-resolution Convolutional Neural Networks. SPE, Annual Technical Conference and Exposition, San Antonio, USA.
31. ‡Fernandes, C., & **Faroughi, S. A.** (2023). Simulation of Magnetorheological Fluids using an Open-source Fully-resolved Immersed Boundary Algorithm. XIXth International Congress on Rheology (ICR2023), Athens, Greece.
30. **Datta, P., **Pawar, N. M., & **Faroughi, S. A.** (2022). A Physics-informed Neural Network to Model the Flow of Dry Particles. AGU Fall Meeting, Chicago, USA.
29. **Pawar, N. M., & **Faroughi, S. A.** (2022). Complex Fluids Latent Space Exploration Towards Accelerated Predictive Modeling. 75th Annual Meeting of the APS Division of Fluid Dynamics, Indianapolis, USA.
28. ‡Mahjour, S. K., & **Faroughi, S. A.** (2022). Numerical Modeling of GreenDeld Carbon Storage Under Geological Uncertainty. AGU Fall Meeting, Chicago, USA.
27. **Pawar, N. M., ‡Mahjour, S. K., Kalantari, N. K., & **Faroughi, S. A.** (2022). Spatiotemporal Down-Scaling for Multiphase Flow in Porous Media using Implicit Hypernetwork Neural Representation. AGU Fall Meeting, Chicago, USA.
26. ‡Mahjour, S. K., & **Faroughi, S. A.** (2022). Uncertainty Quantification and Spatiotemporal Downscaling in Earth System Models. AGU Fall Meeting, Chicago, USA.
25. Boak J., Cohen, A. J.**Faroughi, S. A.**, Soroush, H., Richards, M. (2021), Geothermal Energy: A Sustainable Alternative to Well Abandonment, American Association of Petroleum Geologists (AAPG), Virtual.
24. ‡Fernandes, C., **Faroughi, S. A.**, Ribeiro, R., & McKinley, G. H. (2021). A CFD-DEM Eulerian-Lagrangian solver for particle-laden viscoelastic flows. Annual European Rheology Conference (AERC), Portugal.
23. ‡Fernandes, C., **Faroughi, S. A.**, Ribeiro, R.,& McKinley, G. H. (2021). A multi-scale approach for particle-laden viscoelastic flows using a discrete particle method. The 9th OpenFOAM Conference, Worldwide, Virtual.
22. Monteiro, L., ‡Fernandes, C., McKinley, G. H., & **Faroughi, S. A.** (2021). Digital-twin for particle-laden viscoelastic fluids: ML-Based models to predict the drag coefficient of random arrays of spheres. The 16th OpenFOAM Workshop (OFW16), Dublin, Ireland.
21. Araujo, R. A. I., **Faroughi, S. A.**, McKinley, G. H., & ‡Fernandes, C. (2021). ML driven models to predict the drag coefficient of a sphere translating in shear-thinning viscoelastic fluids. The 16th OpenFOAM Workshop (OFW16), 7- 11, Dublin, Ireland.

20. ‡Fernandes, C., **Faroughi, S. A.**, Nobrega, M. J., & McKinley, G. H. (2020). Exploratory - deep learning for particle-laden viscoelastic flow modelling. In MIT-Portugal 2020 Annual Conference.
19. ‡Fernandes C., **Faroughi, S. A.**, R. Ribeiro, J. Miguel Nóbrega, G.H. McKinley. (2021). CFD-DEM modeling oF Particle-laden Viscoelastic Flows in hydraulic Fracturing Operation, The 16th OpenFOAM Workshop (OFW16), Dublin, Ireland.
18. ‡Fernandes C., **Faroughi, S. A.**, O.S. Carneiro, J. Miguel Nóbrega, G.H. McKinley. (2020). Development of The Drag Coefficient of A Sphere Translating Through A Viscoelastic Fluid, 15th OpenFOAM Workshop Arlington, USA.
17. Fernandes C., **Faroughi, S. A.**, O.S. Carneiro, J. Miguel Nóbrega, G.H. McKinley. (2019). A fully-resolved immersed boundary numerical method to simulate particle-laden viscoelastic flows, 14th OpenFOAM Workshop Duisburg, Germany.
16. Fernandes C., **Faroughi, S. A.**, O.S. Carneiro, J. Miguel Nóbrega, G.H. McKinley. (2019). Development of a two-way coupled fully resolved immersed boundary method numerical code for particle laden viscoelastic flows, Congress on Numerical Methods in Engineering, Guimarães, Portugal.
15. **Faroughi, S. A.** and G. H. McKinley. (2017). Multi-particle transport in viscoelastic fluids: Particle level simulation, Society of Rheology 89th Annual Meeting, Denver, USA.
14. **Faroughi, S. A.** A. Robisson, and G. H. McKinley. (2017). Three-dimensional Eulerian-Lagrangian solver for suspensions of solid spherical particles with a viscoelastic matrix fluid, Society of Rheology 89th Annual Meeting, Denver, USA.
13. Huber C., **Faroughi, S. A.** and W. Degruyter. (2016) The rheology of crystal-rich magmas (Kuno Award Lecture), EGU Conference, Vienna.
12. **Faroughi, S. A.** and C. Huber. (2015). Hindrance Velocity Model for Phase Segregation in Suspensions of Poly-dispersed Randomly Oriented Spheroids, AGU Conference, San Francisco, USA.
11. **Faroughi, S. A.** and C. Huber. (2016). Theoretical developments to model microstructural effects on the rheology of complex fluids, Graduate Symposium, Georgia Institute of Technology, Atlanta, USA.
10. Parmigiani A., **Faroughi, S. A.**, C. Huber. (2015) Migration of buoyant non-wetting fluids in heterogeneous porous media, AGU Conference, San Francisco, USA.
9. **Faroughi, S. A.** and C. Huber. (2015). A viscosity model for concentrated suspensions of rigid, randomly oriented spheroids, Society of Rheology 87th Annual Meeting, Baltimore, USA.
8. Parmigiani, A., **Faroughi, S. A.**, C. Huber and O. Bachmann. (2015). From viscous fingering to bubbly flow: the fate of low Reynolds number, buoyancy driven non-wetting fluid transport at strong porosity transitions, Annual InterPore Conference, Italy.
7. **Faroughi, S. A.**, and C. Huber. (2014). A self-consistent rheological model for bubble and crystal-bearing magmas, AGU Conference, San Francisco, USA.
6. **Faroughi, S. A.**, and C. Huber. (2014). Rheology of magmatic systems; insight to underlying physics, Georgia Tech Graduate Symposium, Atlanta, USA.
5. Parmigiani, A., **Faroughi, S. A.** and C. Huber. (2014) Bubbles accumulation and their role on the eruptability of melt-rich silicic lenses in upper crustal magma reservoirs, AGU Conference, San Francisco, USA.
4. Saidi, M., H. Basirat Tabrizi, and **Faroughi, S. A.**. (2014). Minimum Spouting Velocity of Food Particles in a Gas-Solid Spouted Bed, American Institute of Chemical Engineering, AICHE Annual Meeting, Atlanta, USA.
3. **Faroughi, S. A.**, A. Parmigiani and C. Huber. (2013). Volatile dynamics in crystal-rich magma bodies, perspectives from laboratory experiments and theory, AGU Conference, San Francisco, USA.
2. **Faroughi, S. A.** and M. T. Manzari. (2011). Simulation of the contaminant transition in groundwater into surface water using the streamline method. 13th of marine industries conference, Kish Iland, Iran.
1. **Faroughi, S. A.** and H. Bahri. (2009). Numerical investigation on heat transfer and pressure drop for different sheet-shapes in surface heat converters. Mechanical Engineering Conference, Mashhad, Iran.

- **Invited Talks**
  4. **Faroughi S. A.**, TXST Mathematics Dep., Symposium (Deep Learning in Scientific Computing), Sep 2022.
  3. **Faroughi S. A.**, Qunata Services, R&D Seminar (Hydrogen Pipeline Integrity), May 2022.
  2. **Faroughi S. A.**, Kraton Corporation, R&D Seminar (Physics-informed Neural Networks), Mar 2022.
  1. **Faroughi S. A.**, AMD Inc., Visit Seminar (HPC and GPU-Enabled Computing Resources for CCS), Sep 2021.

SERVICES

- **Institutional & Departmental**
  - Hands-on Involvement with ABET Preparation and Documentation, December 2021 - Present
  - Serving in Advisory Committee of Graduate Students. December 2021 - Present
  - CE ITOC Representative, December 2021 - Present
  - Organization of the Department Colloquium, Spring 2022.
  - CE Water Resources Faculty Search Committee member, Fall 2022.
  - CE Senior Lecturers Faculty Search Committee member, Fall 2022.
  - CE Faculty Meeting Secretary, 2021 & 2022
  - Ingram School of Engineering's Representative for Outstanding Master's Thesis Award. 2022.
  - CE Transportation Faculty Search Committee member, Spring 2021
- **Professional & Community**
  - Guest Editor, Energies Journal, 2022.
  - Guest Editor, Polymers Journal, 2021 & 2022.
  - Reviewer, NSF proposals from Fluid Dynamics Divisions, 2022.
  - Reviewer, DOE proposals from Office of Science Programs, 2023.
  - Reviewer for top journals: Transport in Porous Media, Geophysical research Letters, Journal of Non-Newtonian Fluids, Water Resources Research, IEEE, Polymers, Energies, Energy & Fuels, JOR, Heat and Mass Transfer, Agriculture, JGR, EPSL, Advances in Water Research, Journal of Computational Sciences, Environmental Science and Technology, etc. (15-20 per year).
  - Tech. Committee Member, 5th ICGG Conference, China, 2015.

HONORS AND AWARDS

- Professional Engineering license, Texas Board of Engineers #148962, 2023.
- Article featured on POF website, American Institute of Physics, 2023.
- Excellence in Civil Engineering Education (ExCEEd) Certification, ASCE, 2022.
- Finalist & Winner, Geo Data Visualization Competition, DOE, 2020.
- Georgia Tech Create-X Startup Fund, 2017.
- MIT-Portugal Postdoc Fellowship Award, 2017.
- Schlumberger-MIT Postdoc Fellowship, 2016.
- Top Student of the month, School of Earth and Atmospheric Sciences, 2014.
- Article featured on PRE website-Kaleidoscope, American Physical Society, 2014.
- Awarded full scholarship in Georgia Institute of Technology for PhD program, 2012.
- Ranked First in M.Sc Theses Competition, Sharif Institute of Technology, 2011.
- Top 3 student of Mechanical Engineering Department at Sharif Uni. of Technology, 2011.
- Ranked 32 among 16000 participants in the National M.Sc. Examination, 2009.

PROFESSIONAL ASSOCIATION

- American Society of Mechanical Engineers (ASME) (2015-present).
- American Institute of Chemical Engineers (AIChE) (2014-present).
- Society of Rheology, SOR, (2015-present).
- American Physical Society, APS (2015-present).
- Society of Petroleum Eng., SPE (2015-present).
- American Geopgysical Union, AGU (2014-present).
- American Society of Civil Engineers, ASCE (2015-present).
- Society of Exploration Geophysicists, SEG (2014-present).
- HonorSociety.org at Georgia institute of Technology (2012-present).

ADVISING AND MENTORING

- **Postdoctoral Scholars & Graduate Students**
  - Md. Jashim Uddin (Postdoc, 2023-2025).
  - Mahmoud Mousavi (Postdoc, 2023-2025).
  - Kourosh Mahjour (Postdoc, 2021-2023).
  - Celio Fernandes (Postdoc, 2021-2022); Currently at University of Porto
  - Ramin Soltanmohammdi (PhD, 2022-2025).
  - Nikhil Pawar (PhD, 2021-2023); Received travel grant from APS Division of Fluid Dynamics
  - Jobayed Badhan (MSc, 2023-2025).
  - Sonia Akter (MSc, 2023-2025).
  - Pingki Datta (MSc, 2021-2023); Received PEOIP Scholarship; currently at Oregon State University
- **Undergraduate Students**
  - Sunistha Shakya, working on physics-informed neural networks, (2023). Received internship offer at UCLA
  - Ian Harmon, working on fiber optic AI-based event detection, (2023).
  - Cason Grumbles, working on optimizing the use of green energy systems, (2023).
  - Sofia Burgos, working on infrastructure carbon management, (2023).
  - Lane Totino, working on infrastructure carbon management, (2023).
  - Jackson McDonald, working on infrastructure carbon management, (2023).
  - Aimen Ahsan Hafeez, working on infrastructure carbon management, (2023).
  - Melanie Garza, working on infrastructure carbon management, (2023).
  - Grant Smith, working on lossy data compression, (2022).
  - Maverick Finn, working on data analysis, and data engineering, (2022).

SKILLS AND EXPERTISE

- **Management & Leadership**
  - Proven Problem-Solving and Critical Thinking Skills with Entrepreneurial Drive
  - Effective Leadership of Cross-functional Teams with Diverse Backgrounds
  - Strong Verbal and Written Communication Skills
  - Proficient in Agile Product Development and Project Management
  - Proficient in Enabling and Effective Task Distribution
  - Strategic Business Planning and Implementation with Long-term Vision
  - Flexibility and Thriving in Changing Environments
- **Computational Methods & Packages**
  - Finite Element Method: FreeFEM, COMSOL Multiphysics
  - Finite Volume Method: OpenFOAM, Fluent-ANSYS
  - Machine & Deep Learning Methods: TensorFlow, PyTorch
  - Physics-based Deep Learning: PiNN, PeNN, PgNN
  - Molecular Dynamics: OpenMD, LAMMPS
  - Discrete Element Method: LIGGGHTS, PFC
  - Lattice Boltzmann Methods: Palabos
  - Mesh Generation: snappyHexMesh, Gambit
  - Data Visualization: ParaView, GeoDeck, Techplot, Tableau
- **Programming Languages**
  - C, FORTRAN, Objective-C, C++
  - Python, Julia, Matlab
  - JavaScript, Node JS, React Native, Swift
  - Git, Github, Bitbucket, Cocoapods, Carthage

Diversity Statement

Salah A Faroughi, PhD, PE
Email: salah.faroughi@txstate.edu, Phone: 404-917-9780

As an educator and mentor, I place a strong emphasis on the transformative potential of cross-cultural exposure and the invaluable insights gleaned from diverse backgrounds. My approach involves attentive listening to my students, profound respect for their identities, and a conscientious effort to avoid projecting personal biases. My dedication to diversity, equity, and inclusion stands as an unshakable pillar of my professional philosophy. These principles are not merely theoretical constructs but are woven intricately into the fabric of my life's purpose.

My journey towards cultural competency has been shaped by a lifetime of experiences as a minority. From the moment I left my parents' home for college in 2005, I have continuously found myself in minority groups wherever I've lived. This exposure to a multitude of cultures, languages, and religions has provided me with a profound appreciation for the inherent value of diversity. Despite encountering instances of discrimination, I have steadfastly upheld the belief in the significance of embracing the richness found in the differences that shape human experiences. Throughout my life, I have actively immersed myself in new cultures, acquired languages, and proudly shared my own background in diverse settings.

While pursuing my PhD at Georgia Institute of Technology, I actively sought opportunities to engage with a diverse student body by applying for a graduate resident advisor position on campus. Over the span of two years (2013-2015), I fulfilled this role, immersing myself in the lives of students within the residential halls. Through these interactions, I had the privilege to learn from a wide spectrum of individuals, encompassing both those from the dominant culture and underrepresented groups. Their varied perspectives enriched my understanding across a myriad of subjects. This exposure to a global mosaic of students profoundly influenced my worldview and forged the bedrock of my values. My identity as a member of a minority group further equipped me to mentor and guide students confronting both academic and residential challenges stemming from their identities. In response, I orchestrated special and cultural events within Georgia Tech's Graduate Living Center, inviting students from the residential community to participate. These events not only facilitated an opportunity for students to gain insight into their peers' cultures and identities, but also served as a platform for them to proudly share their own heritage. The resounding success of these events was evident through the enthusiastic participation of hundreds of students on each occasion. These gatherings resonated as educational triumphs, characterized by a tapestry of diverse voices and perspectives, enhancing the cultural vibrancy of our community.

At Texas State University (TXST), I have established a dynamic and inclusive research team, guided by my deepening awareness and reverence for cross-cultural understanding. My primary objective revolves around expanding the presence of underrepresented students in STEM, while fostering a transformative shift in the discourse surrounding the persistent underrepresentation of minority groups in science and engineering. To ensure the cultivation of a diverse and expansive student body in my research team, I have taken proactive measures to advertise all research assistant positions extensively. This outreach strategy involves robust promotion through TXST's specialized student organizations that focus on underrepresented groups, such as the Society of Women in Engineering, the National Society of Black Engineering, and the Society for Advancing Chicanos/Hispanics and Native Americans in Science. Furthermore, I have engaged collaboratively with various community-based entities on campus, including First-Gen Proud and the Houston-Louis Stokes Alliance for Minority Participation. My partnership with the Student Advisory Council on Inclusive Excellence for Student Initiatives underscores my commitment to equitable access.

At TXST, I have also initiated the Carbon Transport and Storage Program (TxCTSP) with the purpose of empowering students hailing from underrepresented and structurally marginalized communities. This program is designed to equip these individuals, who represent the future workforce, with the necessary tools to tackle the challenges of the climate crisis and carbon management. Guided by my principles, I am committed in overcoming barriers that may impede the participation of historically underrepresented groups in climate and energy research activities. The selection process for TxST-CCS students is guided by a diversity priority

framework, giving precedence to (1) ethnic minorities, (2) women, (3) first-generation college students, and (4) other historically underrepresented groups. Candidates who align with these criteria are accorded consideration, along with an evaluation of their individual merit.

My journey at TXST is thus characterized by a resolute commitment to cultivating a research ecosystem that embraces and values diversity, aiming to drive transformative change within STEM and beyond. Through these initiatives, I strive to empower individuals from all backgrounds to contribute their unique perspectives, ultimately fostering innovation and progress.

My dedication to fostering a diverse and inclusive environment is at the heart of my identity as an educator, mentor, and advocate. I am committed to conscientiously reducing the influence of my own biases and preconceptions about concepts being "easy" or "hard" to grasp, "useful" or "useless" to pursue, "constructive" or "destructive" to endorse, and beyond. Drawing from my lived experiences and professional journey, my aim is to cultivate a space where individuals from all walks of life are not only welcomed and cherished but also empowered to bring their distinctive perspectives to enrich the collective fabric of knowledge and innovation.

Teaching Statement

Salah A Faroughi, PhD, PE
Email: salah.faroughi@txstate.edu, Phone: 404-917-9780

Teaching Philosophy:

1. Understanding the mechanisms governing student learning serves as the cornerstone of exemplary teaching knowing the fragility of their learning process: In the past six years in my career in academic and industrial settings, I have been deeply immersed in the area of constructive learning algorithms to train brain-inspired neural networks to solve complex physical problems. My experience showed the pivotal importance of careful analysis and labeling of training, validation, and testing datasets, as well as constraints in achieving successful supervised learning. The presence of redundant or vague features in these datasets or weak constraints could potentially results in a big rat hole leading to learning failure. This knowledge simply illuminates the intricate fragility of the learning process within human minds, and irrevocably changed my perspective on the necessary elements for teaching and training. This conclusion was further reinforced when I went through the prestigious ExCEEd Teaching Workshop by ASCE in 2022. This program consisted of intense faculty development opportunities to improve the teaching abilities and enhance the learning experience for students knowing the fragility of their learning process. I have come to acknowledge that a proficient educator must not only fathom the processes and strategies through which students construct knowledge but also harness this understanding to curate learning activities that resonate with their distinct talents, capabilities, and learning modalities. The potency of a teacher's impact is amplified when considering the interplay between students' individual interests, backgrounds, and experiences, as these factors collectively develop the ground for overpowering educational opportunities. Consequently, my pedagogical framework is anchored upon the following tenets:

- Content-Targeted Pedagogy: My lectures include an array of content-specific instructional strategies that serve as effective conduits for disseminating complex concepts with resonance and clarity.
- Interdisciplinary Enrichment: Driven by my background, I appreciate cross-disciplinary instruction that augments the breadth and depth of student learning, fostering a problem-solving perspective.
- Innovative Assessments: I employ new assessment techniques that not only measure instructional efficacy but also serve as tools for refining my guidance and gauging the extent of student attainment.
- Achievement-Centric Learning Environments: I am committed to create learning environments that nurture exceptional achievements for students, while embracing their rich diversity.
- Personal and Professional Growth Nexus: I am persistent in my commitment to both the personal and professional growth of each student under my purview.

2. Absorbing foundational scientific concepts is not always the main challenge faced by students, it is rather their direction applications: Based on my experiences as an instructor in academic settings, it has become evident that the crux of the matter for students doesn't lie solely in the absorption of foundational scientific concepts. Rather, the true challenge is the synthesis of these concepts in relation to real-world problems to be able to nail down different solution possibilities. As an engineer, this skillset is essential, prompting me to challenge, encourage, and support my students to gain this very top-notch skill. To this end, I would try the following approaches:

- Practical Conceptualization for Problem Solving: I initiate each module by unveiling a "big fundamental question" coupled with an "applied question" to inaugurate lectures. This dual-pronged approach stimulates students to traverse the bridge from abstract principles to practical quandaries, promoting a characteristic capacity to delineate requisite knowledge for multifaceted solutions. In each lecture, students are guided to first think and pinpoint the essential knowledge they need to acquire and understand. This equips them to solve problems using a range of approaches. The final chapter of all courses is designed to enhance students' problem-solving skills by tackling intricate problems. Here, students will be asked to simplify

problems by making assumptions, justify those assumptions, and solve the problem using the foundational concepts taught throughout the course. Additionally, they can adjust their assumptions as needed, especially when new developments arise. This method prepares them to confront complex problems after graduation, contributing to a world enriched with innovative engineers and exceptional scientists.

- Peer-Centric Assessment for Critical Thinking: I devised an interactive peer-based assessment model to provoke critical thinking competency in students, particularly in smaller classes (<25 students). This technique harnesses collective intelligence in cooperative learning, rooted in social interaction and is proven to be both highly effective and engaging. In this supervised assessment approach, students create homework to evaluate their peers, for which they require not only a solid grasp of foundational concepts, but also a great understanding to camouflage them in a problem. This approach also facilitates knowledge sharing, problem creation, peer assessment, and the development of strong communication skills among students. Moreover, it fosters collaborative teamwork, which has been shown to be highly effective socially, psychologically, and academically. I have implemented this method in 3- and upper-level undergraduate courses, and it has been very well received by my students.

3. Promote student success requires agile and adaptive teaching*:* The essence of teaching pivots around the edifice of student learning, a perspective fortified by ABET standards. My teaching commitment is underscored by an unwavering resolve to infuse researched learning concepts into my instructional environment. However, I remain attuned to the dynamic interplay between teaching innovations, student reactions, and institutional guidelines, thereby effectuating a harmonious balance between innovation and accommodation. In this ever-evolving pursuit of educational excellence, I stand poised to mold myself to be agile, casting light upon the boundless states of advanced student learning.

Teaching and Mentoring Experience:

1. Instructor at Texas State University

I joined Texas State University (TXST) in Fall 2021 as assistant professor, and since then I have been deeply engaged in instructing undergraduate and graduate courses, as well as mentoring and supervising postdoctoral fellows, graduate, and undergraduate students. The array of courses I've designed and taught thus far includes:

◦ MSEC 7395: Finite Element Method	(Graduate Level — 15 students)
◦ MSEC 7355: Transport in Porous Media	(Graduate Level — 20 students)
◦ CE 5331: Computational Mechanics in Geosystems	(Graduate Level — 15 students)
◦ ENGR 3380: Fluid Mechanics	(Undergraduate Level — 40 students)
◦ CE 3330: Soil Mechanics	(Undergraduate Level — 30 students)
◦ CE 3331: Infrastructure Foundations	(Undergraduate Level — 25 students)

In each of these courses, I applied my teaching philosophy as described earlier, but making adjustments according to the students' needs. For instance, in CE 5331, during the lesson on periodic boundary conditions, I kick off the class with a question: "How can we simulate the path of a particle through a 5 km pipe with the least computational effort?" I encourage students to ponder this issue and share potential ways to simplify the problem. To steer their thoughts, I present a follow-up question: "Do we need to create a mesh for the entire 5 km pipe, or could we simulate the full length using only a portion of the pipe?" Through this dialogue, students gradually approach the concept of cyclic boundary conditions. While this approach may consume a considerable portion of the lecture time, it ultimately renders the notion of cyclic (periodic) boundary conditions more comprehensible. Consequently, their grasp of the mathematical framework behind it becomes smoother, and they can readily discern its real-world application. Table 1, derived directly from students' course evaluations, offers a snapshot of my students' perspectives on my teaching approach:

Table 1. Sample students' feedback from course evaluations

Course	Comment
CE 3330	"Your lectures are phenomenal. The pace is perfect, the information is extremely pertinent to the homework, and examples are exactly what I need to see. I enjoy example heavy lectures, where I can see "how" a problem is worked so I love coming to lecture. Quite frankly you have been one of my best professors, especially when it comes to the Civil Engineering Department."
ENGR 3380	"I just wanted to thank you for such a great semester. I have enjoyed learning about fluid mechanics from you. While it is a very challenging class, I believe that you allowed us to succeed. You have been very understanding and helpful throughout this semester. I plan on reaching out to you to discuss my plan after my bachelor's degree is completed. I am very happy to say that I feel I have found another mentor to help me through this uncertain, yet hopeful time in my life."
CE 3331	"Honestly, I love your class, is well organized and structured. I like the way you explain the class as well as you engage with the students at the time of solving problems. I also like that you are fair with students. Also, that you take your time to evaluate students with the take home quizzes and follow up with the students that are not understanding the concepts."
CE 5331	"I wanted to take a moment to say thank you for presenting such an interesting and engaging class. It has truly been one of my favorites throughout my college career. I hope you have a great break and I hope to have a course with you in the future."

At TXST, mentoring early-stage scholar and student has been also the centerpiece of daily work. Thus far, I advised (am advising) 4 postdocs, 5 graduate students, and 8 undergraduate students. This diverse group of students hails from fields spanning Civil Engineering, Mechanical Engineering, Materials Science, and Computer Science. Recently, through a DOE-supported project, I established TxST-CCS program focusing on student training in subsurface clean energy initiatives. This program's overarching objectives are (i) to ensure that TXST has the requisite resources and capabilities needed to initiate and lead the early-stage R&D activities that are centered subsurface gas storage, and (ii) to ensure that TXST has the requisite resources and capabilities needed to support the education and training of minority students from underrepresented and structurally marginalized communities and prepare them, as the future workforce, to resolve the pressing climate crisis and green energy challenges. This program has started in Spring 2023, and since then has trained more than 6 graduate students and 15 undergraduate students. The TxST-CCS program provides research opportunities to undergraduate and graduate students, implements active learning and hands-on activities to enhance student knowledge in subsurface gas storage, offers scholarships to outstanding incoming and existing undergraduate and graduate students involved in carbon-management fields, and leverages a peer and near-pear mentoring structure to provide students with mentorship/leadership roles and run effective outreach activities to underserved students. Student success in the main goal of this program that I supervise. Within two years:

- Three undergraduate students in the program received internship from top companies
- Master student (Nikhil Pawar) received a prestigious travel grant from APS Division of Fluid Dynamics for his scholarly work under my supervision.
- Master student (Pingki Datta) received Philanthropic Educational Organization International Peace Scholarship for her scholarly work under my supervision and she received multiple PhD offer from top 20 engineering schools.
- The first postdoc (Celio Fernandez) received a permanent research position offer at University of Porto, the number one university in Portugal.

2. Mentoring Grad Students Massachusetts Institute of Technology (MIT)

During my postdoc period at MIT, I had the opportunity to mentor several grad students in our group (non-Newtonian fluid dynamics under the supervision of Prof. G. McKinley), and several master students from University of Minho whose advisor (Dr. M. Noberga) was on a sabbatical with our group at MIT. I worked closely with them to introduce them to advanced numerical simulations and data visualization methods. I also directed their research, especially the part that was related to the application of high-performance computing for particle-laden (complex) fluid flow simulation using OpenFOAM. It was a great opportunity to learn that mentors must tailor advice strategies to the goals and circumstances of individual mentees.

3. Teaching Assistant & Lab Instructor at Georgia Institute of Technology

During 2012 and 2016 at Georgia Tech, as a PhD candidate, I had the privilege to be the TA for the EAS 4610: Earth Modeling Systems: PDE and ODE Solutions using Finite Difference, and lab instructor for EAS 2600: Earth Processes Lab: Intro to Earth Materials and Processes. In summer 2014, I also had the opportunity to host and mentor several high school and undergrad summer students at our lab as part of a summer STEM enrichment and outreach program at Georgia Tech. I was managing them the entire summer to design and present experimental setups for several fundamental concepts in physics. Student, indeed, got very interested in my PhD experimental setup (water droplet settling in silicone oil), and worked overtime to help me immensely with image processing and data login. One of the high school students joined our department as undergrad in the following year.

Fundamental and Advanced Courses to Teach:

Your institution provides a prime platform for me to impart a diverse array of courses linked to my interdisciplinary background and research expertise. I welcome the chance to instruct required and fundamental courses tailored to the department's needs. Furthermore, I'm eager to develop and deliver the subsequent elective courses, fostering an extended dedication to learning across both undergraduate and graduate levels:

1. Undergraduate level - elective:

- Machine Learning for Earth System Modeling
  Python coding overview, TensorFlow overview, Regression, classification, and clustering methods, Recommendation systems, Regularizations, Association Analysis, Model accuracy handling
- Introduction to Numerical Analyses
  Concepts, Discretization methods, Integral solutions, Solution of ordinary differential equations, Linear algebra and solution of linear systems using direct and iterative methods

2. Graduate level - elective:

- Physics-informed Deep Learning in Geo-Energy Systems
  Deep learning intuition, Shallow neural network, Deep neural networks, Optimization algorithms, Hyperparameter tuning, Physics-inform and Physics-encoded loss functions, error minimization.
- Advanced Mechanics: Particulate Materials
  Phenomenological approach, Descriptive properties, Interparticle bonds and interactions, Constitutive models, Phase transitions, Colloidal dispersion, Self-assembly, Microstructural effects on mechanical and thermal behaviors
- Advanced Geofluids: Transport Phenomena
  Multiphase flow in porous media, Exact solutions for steady incompressible viscous flow, Similarity solutions for unsteady incompressible viscous flow
- Exascale and Multiscale Geosystems Modelling
  Steady and time-dependent PDEs, Non/Homogeneous PDEs, Different reference systems, Compositional modeling, Hands-on training/coding using open-source E3SM parallel code

These elective courses will be crafted with direct relevance to geo-energy systems and the design of advanced particulate and soft condensed matter, crucial in extensive industrial applications. These applications span disciplines like Civil, Mechanical, and Chemical Engineering, as well as Petroleum and Geotechnical Engineering, along with Geophysics.

Research Statement

Salah A Faroughi, PhD, PE
Email: salah.faroughi@txstate.edu, Phone: 404-917-9780

Research Interests:

The primary focus of my interdisciplinary research is centered around the "Energy-Environment" dual challenge. I investigate (i) the latent space in geo-climate data across different spatiotemporal scales in the context of exascale Earth systems (e.g., AI-augmented global and regional climate models, etc.), and (ii) the transport, thermophysics, and biogeochemistry of complex fluids and multiphase reacting flows in heterogeneous porous media in the context of geo-energy systems (e.g., subsurface hydrogen and carbon storage, geothermal, etc.). Central to my research are efforts to bridge knowledge gaps and incorporate uncertainties in addressing pressing challenges related to climate change and green energy adoption. To this end, I employ deep-learning and data-driven techniques firmly bounded by fundamental principles and physics, developed through cutting-edge experimental setups and high-fidelity computational models.

Research Thrusts:

My research group, the Geo-Intelligence Lab (GILab), focuses on three primary research thrusts collectively designed to acquire, explore, interpret, and visualize multidimensional datasets related to Earth systems and geo-energy systems, all while considering epistemic and aleatoric uncertainties in order to extract actionable insights aimed at fostering a sustainable future. Since 2020, my leadership and collaborative efforts in research have secured approximately **$5.0 million** in funding from private, state, and federal agencies. Results are disseminated in top journals like **Nature, GRL, PRE, POF, APS, JNNFM,** and many more.

Thrust 1. Earth system modeling to predict the climate-change-induced stressors, assess infrastructure and community vulnerabilities, and formulate adaptation strategies enhancing climate resiliency

This research thrust investigates climate dynamics using exascale Earth system modeling augmented with advanced deep learning techniques [1,2]. The main objective is to incorporate uncertainties to predict the emergence of climate extremes, assess climate-change risks, inform policies, and create adoption plans to enhance the resilience of strategic infrastructure and resources, e.g., see Fig. 1. Moreover, it explores advanced downscaling techniques [3] to accurately forecast the main climate features in complex, local terrains where mesoscale-forcing becomes important. This research initiative enjoys current funding from the US Department of Energy (DOE) and Agriculture (USDA); an additional proposal is currently undergoing review by DOE.

Sample Project. Incorporating Global Climate Epistemic Uncertainties into Regional Projections

The frequency and intensity of extreme events, such as droughts, floods, heat waves, and winter storms, have been on the rise due to the impacts of global warming on Earth's systems [4]. To prevent the recurrence of these catastrophes, the planning, construction, and maintenance of infrastructure must account for the impacts of changing patterns of extreme events [5].

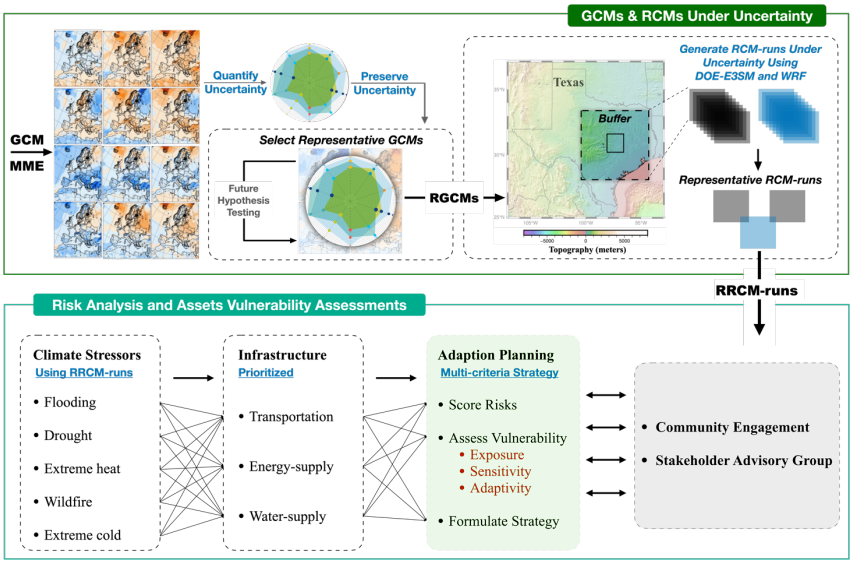

Figure 1. A schematic representation of our objectives and proposed research workflow to enhance climate resiliency in local region (e.g., Central Texas, an area surrounding Austin and roughly bordered by San Saba to Bryan and San Marcos to Hillsboro) by investigating the incorporation of global climate-change uncertainties into regional projections and vulnerability risk analysis.

Extreme events are usually hard to predict as the exact relationship of climate changes and extreme weather continues to evolve. Forecasting the nature and speed of climate-change is a challenging task, but it is required to assess, quantify, and make informed decisions about climate-change enhanced risks (e.g., drought, megafires, rising sea levels, eroding shorelines, loss of wetland, and deterioration of water quality). For this purpose, advanced numerical tools (e.g., DOE's E3SM [6]) have been widely used to develop a quantitative understanding of the multiscale dynamics of climates in response to different stimuli and/or perturbations [7]. However, there are still several challenges to be addressed. Climate models suffer from predictive limitations, introducing uncertainties in scenario testing and risk assessments. Fine-grid models are recommended but computationally costly, and model reduction methods sometimes fail to preserve uncertainty, hampering future projections. Most regions lack a comprehensive understanding of climate change vulnerabilities, especially in critical infrastructure and disadvantaged communities. Limited community involvement hinders the translation of climate analyses into actionable adaptation plans, making it difficult to ensure resilience in the near or far future [8-9].

This project aims to establish a multifaceted framework that integrates cutting-edge climate dynamic research and community engagement to enhance climate resiliency in specific regions. The objective is to investigate the projection of five extreme climate stressors over the next 30 years: flooding, drought, extreme heat, wildfires, and extreme cold [10]. The proposed framework, as shown in Fig. 1, will account for global and regional climate-change uncertainties in the projections that will be used to predict the likelihood of extreme events locally, conduct risk analysis, assess infrastructure and community vulnerabilities based on exposure, sensitivity, and adaptivity components, and formulate adaptation strategies in the region.

Thrust 2. Multiphase reacting flows in porous media with local heterogeneities, non-equilibrium phase partitioning, and complex solid-fluid interactions under geologic, biotic, and flow uncertainties.

This research thrust investigates transport phenomena in heterogenous porous media using real-rock microfluidics, cross-scale computational modeling and advanced deep learning techniques [11-14]. The central objective is to understand the effects of uncertain attributes on the fluid transport and trapping mechanisms under different biotic and abiotic conditions, e.g., see Fig. 2. In addition, it explores the possibility to translate the collective dynamical effects of these pore-scale attributes into Darcy-scale while preserving the uncertainty domain. This research initiative enjoys current funding from the Department of Energy (DOE); two additional proposals are currently undergoing review by the National Science Foundation (NSF).

Sample Project. Surrogate Model to Upscale Uncertain Pore-scale Attributes in Subsurface Energy/Gas Storage

Underground gas/energy storage that plays a pivotal role in accelerating the adoption of green energy sources, seasonal energy management, and combating climate change [15]. For example, subsurface hydrogen (H_2) storage in salt cavern can enable the efficient storage of excess hydrogen as a renewable energy source,

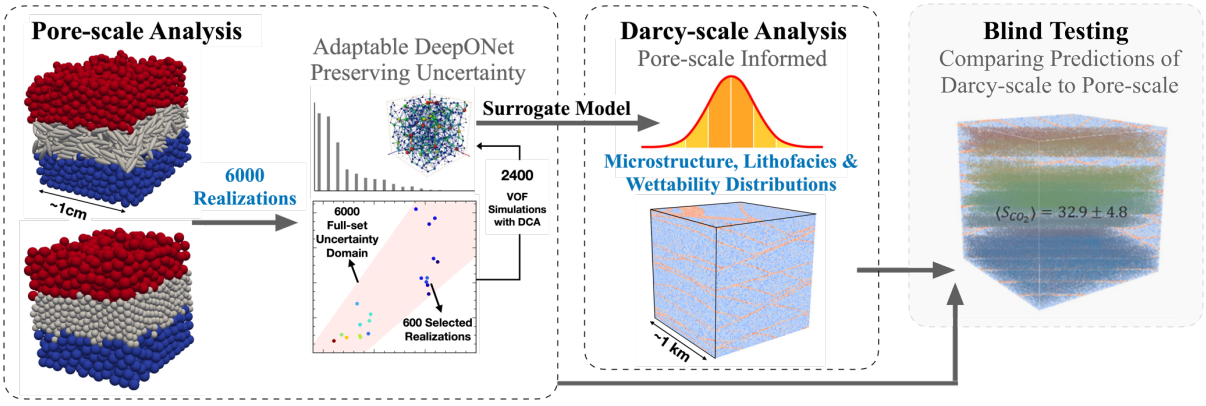

Figure 2. Proposed approach to investigate the impact of microstructural heterogeneities, intraformational barriers, and wettability on the carbon and hydrogen transport as well as their residual and solubility trapping across different spatiotemporal scales. Pore-scale simulations are conducted using volume-of-fluid (VOF) enhanced with a new dynamic contact angle (DCA) model to inform a deep neural operator (DeepONet).

transforming our energy landscape from conventional fuels to cleaner alternatives and bridging the gap between intermittent energy generation and constant energy demand [16]. Methane (CH_4) can be stored in depleted gas fields or aquifers to enable the accumulation of excess natural gas during periods of low demand (e.g., summer) and its subsequent release during periods of high demand (e.g., winter) [17]. Carbon dioxide (CO_2) can be also permanently stored in deep saline aquifers as a promising solution to reduce greenhouse gas emissions and partly mitigate climate change [18]. These storage solutions, once implemented safely and efficiently, can significantly contribute to our nation's economic growth and environmental sustainability [19].

However, there are still several grand challenges in understanding the gas flow and trapping mechanisms, including structural, residual, solubility, and mineral in underground storage systems. Most of these challenges stem from three main pore-scale attributes including (i) microstructural heterogeneities, (ii) intraformational barriers, and (iii) wettability that may alter significantly over time. For example, in H_2 storage, the presence of hydrogenotrophic microorganisms, such as methanogenic (conversion of H_2 to CH_4) or sulfate reducing bacteria (conversion of H_2 to H_2S) in subsurface formations can lead to the formation of biofilms causing local pore-clogging and wettability alteration [20, 21]. Similarly, in CO_2 storage, it is acknowledged that a large volume of CO_2 can be trapped locally beneath the intraformational barriers through the residual trapping mechanism induced by the high capillary pressure contrast between the barriers [22, 24]. Although a considerable body of literature exists on this subject, these knowledge gaps, severely impacting the efficacy of underground storage systems, have not been explored. It is hypothesized that the collective dynamical effects of these attributes at pore-scale can be translated into Darcy-scale using a surrogate statistical model. This project, as shown in Fig. 2, thus investigates the development of a surrogate model that estimates the properties of sedimentary facies in complex geologic formations based on uncertain microscopic attributes including microstructural heterogeneities, intraformational barriers, and wettability distributions.

Thrust 3. Exploration and visualization of multidimensional scientific datasets using deep-learning while honoring fundamental physicochemical principles, context awareness, and simplicity.

This research thrust investigates the implementation of deep learning-based algorithms, constrained by fundamental principles, to effectively model, interpret, and visualize structured and unstructured volumetric and imaging data in geosystems such as climate, geo-infrastructure, geofluids, geochemistry, geophysics, etc. [25-27]. The central objective is to implement algorithms that continuously gain intelligence and allow exploring terabytes of multi-modal data with no need for rigorous computing setup, e.g., see Fig. 3. This research initiative enjoys current funding from DOE, NSF, Texas DOT (TxDOT); a SBIR-phase II proposal is currently undergoing review by DOE.

Sample Project. Context-aware Neural-accelerated Visualization Pipeline for Big Geo-Climate Data

The emergence of multiteraflop machines with thousands of processors for scientific computing combined with advanced sensory-based experimentation has heralded an explosive growth of structured and unstructured data in geo-engineering fields [28-31]. Such scientific endeavors require powerful visualization

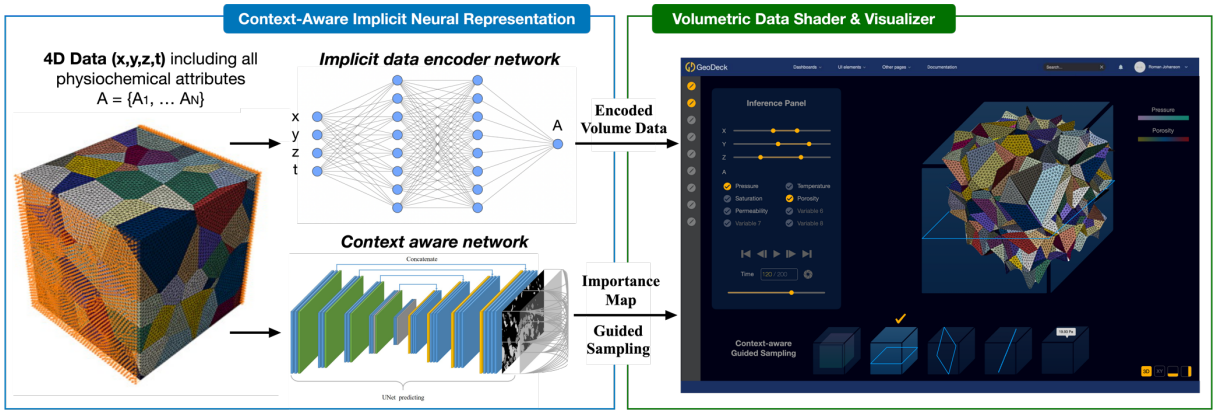

Figure 3. A schematic representation of the proposed context-aware neural-accelerated method to compress, visualize, and analyze terabytes of volumetric data (e.g., geo-climate data) interactively in real-time.

workflows as a fundamental step to understanding and interpreting big data [32]. An ideal data visualization workflow should provide scientists with a fast and intuitive tool to explore data interactively, identify interesting patterns, observe anomalies, and gain rapid insights into their unique discovery and decision-making processes [33]. Numerous research studies have concentrated on how to manage huge data volumes and efficiently show the practical and usable outcomes of data visualization and analysis [32], but there are still several grand challenges: (i) the size of the data that exceeds consumer compute/memory capabilities, (ii) the large dimensional space of the data that hinders the rapid exploration and insight hunting, and (iii) the state-of-the-art hardware acceleration that are optimized heavily for single-channel surface data visualization and not equally for multi-channel volumetric and imaging data.

The objectives of this project are to (i) relax the requirements of high-performance computing setup for visualizing big volumetric data (i.e., reduce the memory consumption by up to three orders of magnitude), and (ii) establish an intelligent, context-aware data rendering pipeline to explore complex scientific data across all scales interactively in real-time on consumer computers. It is hypothesized that terabytes of volumetric data can be stored, interpolated, and visualized interactively in real-time (i.e., 60 frame-per-second response) on consumer computers. This will be explored by transforming the data from a discrete form to a continuous form using context-aware implicit neural representations that reduce memory consumption by up to three orders of magnitude while keeping the rendering rate at 60 frame-per-second. The networks will be then converted into GPU program to construct a direct volumetric data rendering pipeline. To this end, three modules can construct as shown in Fig. 3.: Module 1: Neural representation of multi-channel volumetric and imaging data: Our observation, based on my DOE-SBIR award (DE-SC0023611), is that a big volumetric data with multiple variables can be fully represented, with a significant compression ratio up to 1000x, as an implicit function that takes in the coordinates as the input and outputs the attributes representing channels, i.e., $A = f(x, y, z, t)$. Armed with this proved observation, it is proposed to model the 2D/3D nanoscale imaging data f using a neural network f_θ with periodic activation function, where θ represents the network parameters. This network will be trained using the coordinates as the input and the attributes of channels as ground truth. In training process, the network encodes the data into its parameters θ, thereby reducing the memory usage by up to three orders of magnitude. The network can then be easily stored on the client machine and any slice of the multi-channel data can be generated in real-time by querying the appropriate input coordinates. Module 2: Life-time learning using few-shot technique and user inputs: To guide the locality of interest in the data or extract multi-channel simultaneous interpretation, it is proposed to furnish the neural representation function with life-long learning using two approaches: (1) few-shot training to continually adapt and improve its performance with new sets of data, and (2) user inputs to continually learn to find regions of interest (ROI) and adjust color maps, brightness, contrast, and thresholds, etc. As a result, over time, the network achieves high levels of precision and adaptability in nanoscale imaging applications; and Module 3: Neural-accelerated GPU shader: The network trained in Module 2 can be simply converted into a GPU program to construct a direct rendering pipeline. This technique resolves the rendering challenge on consumer computers, which are optimized for single-channel triangulated surface geometries and not multi-channel volumetric data. With this addition, our software can empower the users to sample (comb) through massive, multi-channel imaging datasets using points, rays, planar slices, spheres, and any arbitrary cut. Moreover, our software can leverage the identified ROIs for initial visualization or infer the encoded data in real-time on any arbitrary domain minimizing substantial human effort. In this project, the proof of concept is investigated using several annotated datasets with different characteristics on large-scale subsurface flow, polymeric materials, and climate system modeling generated by well-known physics-based computing engines (e.g., SimCCS, MFiX, GEOSX, E3SM [28-31]).

References:

[1] Mahjour, S. K., & Faroughi, S. A. (2022, December). Uncertainty Quantification and Spatiotemporal Downscaling in Earth System Models. In Fall Meeting 2022. AGU.

[2] Mahjour, S. K., Liguori, G., & Faroughi, S. A. (2023). Selection of Representative General Circulation Models Under Climatic Uncertainty for Western North America, Research Square, 2698287.

[3] Pawar, N., Sultanmohammadi, R., S. K., & Faroughi, S. A. (2023). E3SM Climate Data Downscaling: A Comparison of Super-Resolution Deep Learning Models, (under review: scientific report).

[4] Doss-Gollin, J., Farnham, D. J., Lall, U., & Modi, V. (2021). How unprecedented was the February 2021 Texas cold snap? Environmental Research Letters, 16(6), 064056.

[5] Busby, J. W., Baker, K., Bazilian, M. D., Gilbert, A. Q., Grubert, E., Rai, V., ... & Webber, M. E. (2021). Cascading risks: Understanding the 2021 winter blackout in Texas. Energy Research & Social Science, 77, 102106.

[6] E3SM (2022), Earth System Model Development using Energy Exascale Earth System Model, at https://e3sm.org

[7] Golaz, J. C., Van Roekel, L. P., Zheng, X., Roberts, A. F., Wolfe, J. D., Lin, W., ... & Bader, D. C. (2022). The DOE E3SM Model Version 2: overview of the physical model and initial model evaluation. Journal of Advances in Modeling Earth Systems, 14(12).

[8] Salathé, E. P., Leung, L. R., Qian, Y., & Zhang, Y. (2010). Regional climate model projections for the State of Washington. Climatic Change, 102, 51-75.

[9] Lu, Q., Zhong, P. A., Xu, B., Huang, X., Zhu, F., Wang, H., & Ma, Y. (2022). Multi-objective risk analysis for flood control operation of a complex reservoir system under multiple time-space correlated uncertainties. Journal of Hydrology, 606, 127419.

[10] McElroy, M. B., & Baker, D. J. (2013). Climate extremes: recent trends with implications for national security. Vt. J. Envtl. L., 15, 727.

[11] Mahjour, S. K., & Faroughi, S. A. (2023). Selecting representative geological realizations to model subsurface CO2 storage under uncertainty. International Journal of Greenhouse Gas Control, 127, 103920.

[12] Faroughi, S. A., Datta, P., Mahjour, S. K., & Faroughi, S. (2022). Physics-informed Neural Networks with Periodic Activation Functions for Solute Transport in Heterogeneous Porous Media. arXiv preprint arXiv:2212.08965.

[13] Mahjour, S. K., & Faroughi, S. (2022, December). Uncertainty Quantification and Spatiotemporal Downscaling in Earth System Models. In AGU Fall Meeting Abstracts (Vol. 2022, pp. A52F-01).

[14] Parmigiani, A., Faroughi, S., Huber, C., Bachmann, O., & Su, Y. (2016). Bubble accumulation and its role in the evolution of magma reservoirs in the upper crust. Nature, 532(7600), 492-495.

[15] Al-Shafi, M., Massarweh, O., Abushaikha, A. S., & Bicer, Y. (2023). A review on underground gas storage systems: Natural gas, hydrogen and carbon sequestration. Energy Reports, 9, 6251-6266.

[16] Salehmin, M. N. I., Me, M. F. H., Daud, W. R. W., Yasin, N. H. M., Bakar, M. H. A., Sulong, A. B., & Lim, S. S. (2023). Construction of microbial electrodialysis cells equipped with internal proton migration pathways: Enhancement of wastewater treatment, desalination, and hydrogen production. Science of The Total Environment, 855, 158527.

[17] Muhammed, N. S., Haq, B., & Al Shehri, D. (2023). Role of methane as a cushion gas for hydrogen storage in depleted gas reservoirs. International Journal of Hydrogen Energy.

[18] Malik, S., Makauskas, P., Karaliūtė, V., Pal, M., & Sharma, R. Assessing the Geological Storage Potential of Co2 In Baltic Basin: A Case Study of Lithuanian Hydrocarbon and Deep Saline Reservoirs. Available at SSRN 4493862.

[19] Qyyum, M. A., Dickson, R., Shah, S. F. A., Niaz, H., Khan, A., Liu, J. J., & Lee, M. (2021). Availability, versatility, and viability of feedstocks for hydrogen production: Product space perspective. Renewable and Sustainable Energy Reviews, 145, 110843.

[20] Li, M., Jian, Z., Hassanpouryouzband, A., & Zhang, L. (2022). Understanding hysteresis and gas trapping in dissociating hydrate-bearing sediments using pore network modeling and three-dimensional imaging. Energy & Fuels, 36(18), 10572-10582.

[21] Dopffel, N., Mayers, K., Kedir, A., Alagic, E., An-Stepec, B. A., Djurhuus, K., ... & Hoth, S. (2023). Microbial hydrogen consumption leads to a significant pH increase under high-saline-conditions–implications for hydrogen storage in salt caverns.

[22] Eigbe, P. A., Ajayi, O. O., Olakoyejo, O. T., Fadipe, O. L., Efe, S., & Adelaja, A. O. (2023). A general review of CO2 sequestration in underground geological formations and assessment of depleted hydrocarbon reservoirs in the Niger Delta. Applied Energy, 350, 121723.

[23] Ni, Hailun, et al. "Predicting CO2 residual trapping ability based on experimental petrophysical properties for different sandstone types." International Journal of Greenhouse Gas Control 86 (2019): 158-176.

[24] Daniel, R. F., & Kaldi, J. G. (2009). Evaluating seal capacity of cap rocks and intraformational barriers for CO2 containment.

[25] Pawar, N., Mahjour, S. K., Kalantari, N. K., & Faroughi, S. (2022, December). Spatiotemporal Down-Scaling for Multiphase Flow in Porous Media using Implicit Hypernetwork Neural Representation. In AGU Fall Meeting Abstracts (Vol. 2022, pp. H45M-1555).

[26] Faroughi, S. A., Roriz, A. I., & Fernandes, C. (2022). A meta-model to predict the drag coefficient of a particle translating in viscoelastic fluids: a machine learning approach. Polymers, 14(3), 430.

[27] Datta, P., & Faroughi, S. A. (2023). A multihead LSTM technique for prognostic prediction of soil moisture. Geoderma, 433, 116452.

[28] DOE-E3SM. (2022). Earth system model development using energy exascale earth seystem model, at https://e3sm.org

[29] DOE-GEOSX. (2022). Next-gen simulation for geologic carbon storage, at http://www.geosx.org

[30] DOE-MFiX. (2022). Open-source multiphase flow modeling for real-world applications, at https://mfix.netl.doe.gov/products/mfix/

[31] DOE-SimCCS. (2022). An open-source tool for optimizing CO2 capture, transport, and storage infrastructure, at https://simccs.org

[32] Khalid, Z. M., & Zeebaree, R. (2021). Big data analysis for data visualization: A review. In. J. of Sci. and Business, 5(2), 64.

[33] Midway, S. R. (2020). Principles of effective data visualization. Patterns, 1(9), 100141.

Professional References

Salah A Faroughi, PhD, PE
Email: salah.faroughi@txstate.edu, Phone: 404-917-9780

- Prof. Gareth McKinley
  Department of Mechanical Engineering
  Massachusetts Institute of Technology
  Phone: +1 617-258-0754
  Email: gareth@mit.edu

- Prof. Christian Huber
  Earth, Environmental, and Planetary Sciences
  Brown University
  Phone: +1 401-863-5876
  Email: christian_huber@brown.edu

- Prof. Chloe Arson
  Civil and Environmental Engineering
  Cornel University
  Phone: +1 607 255-3438
  Email: cfa36@cornell.edu

- Dr. Mahdi Roozbahani
  Department of Computer Science
  Georgia Institute of Technology
  Phone: +1 404 452 1094
  Email: mahdir@gatech.edu

- Dr. Kamal Shadi
  MetaScape LLC
  Phone: +1 404-952-7482
  Email: kamal.s@metascape.dev

LETTER

doi:10.1038/nature17401

Bubble accumulation and its role in the evolution of magma reservoirs in the upper crust

A. Parmigiani[1,2], S. Faroughi[2,3], C. Huber[2,3], O. Bachmann[1] & Y. Su[2]

Volcanic eruptions transfer huge amounts of gas to the atmosphere[1,2]. In particular, the sulfur released during large silicic explosive eruptions can induce global cooling[3]. A fundamental goal in volcanology, therefore, is to assess the potential for eruption of the large volumes of crystal-poor, silicic magma that are stored at shallow depths in the crust, and to obtain theoretical bounds for the amount of volatiles that can be released during these eruptions. It is puzzling that highly evolved, crystal-poor silicic magmas are more likely to generate volcanic rocks than plutonic rocks[4,5]. This observation suggests that such magmas are more prone to erupting than are their crystal-rich counterparts. Moreover, well studied examples of largely crystal-poor eruptions (for example, Katmai[6], Taupo[7] and Minoan[8]) often exhibit a release of sulfur that is 10 to 20 times higher than the amount of sulfur estimated to be stored in the melt. Here we argue that these two observations rest on how the magmatic volatile phase (MVP) behaves as it rises buoyantly in zoned magma reservoirs. By investigating the fluid dynamics that controls the transport of the MVP in crystal-rich and crystal-poor magmas, we show how the interplay between capillary stresses and the viscosity contrast between the MVP and the host melt results in a counterintuitive dynamics, whereby the MVP tends to migrate efficiently in crystal-rich parts of a magma reservoir and accumulate in crystal-poor regions. The accumulation of low-density bubbles of MVP in crystal-poor magmas has implications for the eruptive potential of such magmas[9,10], and is the likely source of the excess sulfur released during explosive eruptions.

Here, we use laboratory experiments and theoretical and numerical calculations to better understand the processes that control the dynamics of buoyant fluids in shallow magmatic systems. These fluids have a strong influence on the partitioning of volatile species and metals in magmas, as well as a deep impact on the scale and style of volcanic eruptions. Shallow magma reservoirs probably have stable, sharp transitions in crystallinity between crystal-rich and crystal-poor regions—an inference supported by geochemical, geological[11,12] and thermal[13] considerations. Crystal-poor caps form by progressive extraction of interstitial melts from mushy reservoirs[14,15]. It is also commonly assumed, particularly for evolved arc magmas, that these incrementally built reservoirs contain exsolved volatiles[1,2]. The MVP can be attributed to two sources: first, crystallization-driven exsolution ('second boiling') in the crystal mush; and second, periodic influx from degassing, underplating magma recharges.

In our model, we consider the buoyant migration of the MVP through an already formed mush–cap system (see Fig. 1 inset). In that context, the MVP is either produced directly by crystallization in the mush, or injected from below by periodic magma recharge. We argue for the existence of a process whereby the upward migration of the MVP is more efficient at high crystallinity, leading to an accumulation of MVP bubbles in shallower and less crystalline parts of the chamber. We do not include in our model the effect of concurrent crystallization of the mush, because crystallization in silicic mushes slows down significantly when the magma temperature approaches the solidus[16]. In fact, if any crystallization does occur, it will tend to enhance MVP extraction by increasing confinement in the mush (see below).

In the crystal-poor cap, the MVP forms a bubble suspension in which the relative velocity of bubbles with respect to the melt is controlled by, first, hydrodynamic interactions between the melt and the bubbles[17], and second, the effective buoyancy between the bubbles and melt. Coalescence is essentially precluded by the high melt viscosity and the low volume fraction, Ψ, of MVP (less than 10–20 vol%). Combining a theoretical model with laboratory experiments (see Extended Data Fig. 1 and Methods)[18], we find that bubble migration in viscous fluids slows down as the bubble volume fraction increases (solid line in Fig. 1). This effect is due to a reduction in buoyancy between a bubble and the suspension, and an increase in resistance to motion (drag from the enhanced return flow). These experiments also show that the development of bubble trains decreases the resistance of the bubbles to motion, but does not prevent this negative trend between bubble separation velocity and bubble volume fraction; the ascent of bubbles remains contingent on the downwelling of an equivalent volume of viscous melt.

In a crystal-rich environment, the solid volume fraction plays a key role in bubble migration. Viscous fingering (a heterogeneous displacement between two immiscible fluids) takes place when a non-wetting fluid (in our case, the MVP) is invading a porous medium filled with a more viscous wetting fluid[19] (here, the silicate melt). Confinement by crystals, and the viscosity contrast between the MVP and the melt, enables vertically elongated fingering channels to grow and remain stable in the mush, as long as the flux of MVP is maintained (Fig. 2a and Supplementary Video 1).

Once established, the connected MVP network provides low-resistance pathways for MVP migration—that is, the rate of energy dissipation in the melt is reduced[20,21]. We assume that the formation of these fingers does not deform the structure of the porous medium. The stress balance that controls fluid invasion involves a competition between viscous pressure drop, capillary stresses and friction between crystal grains[22]. Although the injection and migration of buoyant fluids can disturb the arrangement of a granular medium under low confining pressures[22,23] and lead to capillary fracturing, we argue that the deformation of the crystal mush is negligible at a confining pressure greater than 1.5–2 kbars. This is for several reasons. First, crystals are angular with rough surfaces, and can form interpenetrative frameworks that drastically increase rigidity and friction[24]. Second, under high normal stress, overcoming friction between crystals requires very large shear stresses at the pore scale. Third, in the mush, the pore pressure becomes significantly lower than the lithostatic pressure with depth; bubbles also need to overcome this pressure difference to deform the mush. Pore sizes of at most 0.1 μm should be needed for capillary forces to deform the mush[25]. Fingering, rather than brittle or plastic deformation, is therefore the main MVP transport regime in these crystal mushes.

[1]Institute of Geochemistry and Petrology, ETH Zurich, Zurich 8092, Switzerland. [2]School of Earth and Atmospheric Sciences, Georgia Institute of Technology, Georgia 30332, USA. [3]School of Civil and Environmental Engineering, Georgia Institute of Technology, Georgia 30332, USA.

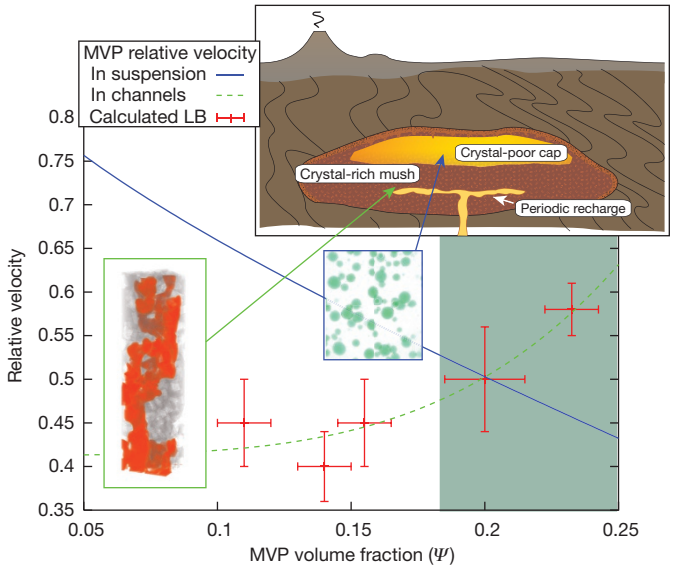

Figure 1 | Transport of a buoyant, non-wetting MVP in crystal-rich and crystal-poor magmas. Inset, representation of a crystal-rich mush zone underlying a crystal-poor cap. Main figure, the data show the relative velocity of bubbles in the cap (suspension; computed from equation (1); see Methods), and in the porous medium (crystallinity 50%; calculated by lattice Boltzmann (LB) simulations). The dashed line is a best-fit cubic power law for the relative velocity of the MVP in the porous medium. The error bars represent the range of steady-state velocities obtained when starting simulations with different initial conditions.

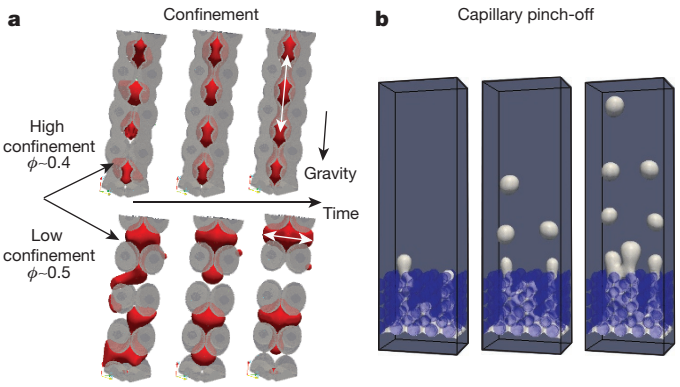

Figure 2 | Transport of a buoyant, non-wetting MVP in magmas with different crystal contents. a, The positive effect of crystal confinement on bubble coalescence and fingering formation. The MVP volume fraction is the same for both low-and high-confinement calculations. ϕ, porosity. **b**, Snapshots from a numerical simulation showing bubbles forming in a crystal-free environment as a result of the break-up of MVP fingers migrating through the underlying porous medium ('capillary pinch-off').

Assessing the processes that control the formation and efficiency of these MVP pathways in the porous medium requires a pore-scale approach (here, lattice Boltzmann simulations). Such an approach shows that crystal confinement promotes high-flux pathways for the MVP. Fingering becomes more stable as the MVP volume fraction, Ψ, increases (above ~10%) at a given crystal content (Fig. 1 and Extended Data Fig. 2), or as crystallinity increases at a given Ψ (Fig. 2a). During the waning stage of degassing events, a significant fraction of the MVP (up to 10–15 vol%) can remain trapped in the mush by capillary and viscous forces along past flow pathways, leading to a residual saturation of MVP (Extended Data Fig. 2g). The residual MVP primes the mush for a more efficient outgassing during subsequent magma recharge events (see Methods for more information on the effect of fingering instabilities on MVP transport).

In magma reservoirs, the dynamics of MVP migration in the crystal-poor cap and the mush must be coupled, because one provides the flow boundary conditions for the other. At the mush–cap transition, spatial variations in crystallinity destabilize MVP fingers and lead to capillary pinch-off (fingers breaking into a stream of bubbles[21]; Fig. 2b). To resolve the force balance that controls the MVP migration at the mush–cap transition, we resort to lattice Boltzmann pore-scale multiphase flow calculations over a physical domain that extends a few centimetres on either side of that interface.

The set-up for the coupled mush–cap pore-scale calculations is based on the assumption that most of the MVP that transfers to the cap exsolves below the mush–cap domain that we model. This assumption is valid whether we consider second boiling in the mush or recharge to be the source of the MVP. Therefore, we implement an MVP flux boundary condition at the inlet of the model domain (underneath the porous layer). After injection, the MVP accumulates at the inlet, and fingering emerges naturally through the porous layer (Fig. 2b). The model set-up is consistent with the notion that fingering of MVP extracted from deeper in the system controls the volatile flux to the cap.

Our modelling results show that gas bubbles accumulate in the crystal-poor cap and that the accumulation efficiency grows with increasing viscosity contrast between the fluids (Fig. 3). The numerical calculations are limited to a range of viscosity ratios, λ, of $1/20 \leq \lambda = \nu_{nw}/\nu_w \leq 1$, where ν_{nw} is the kinematic viscosity of the

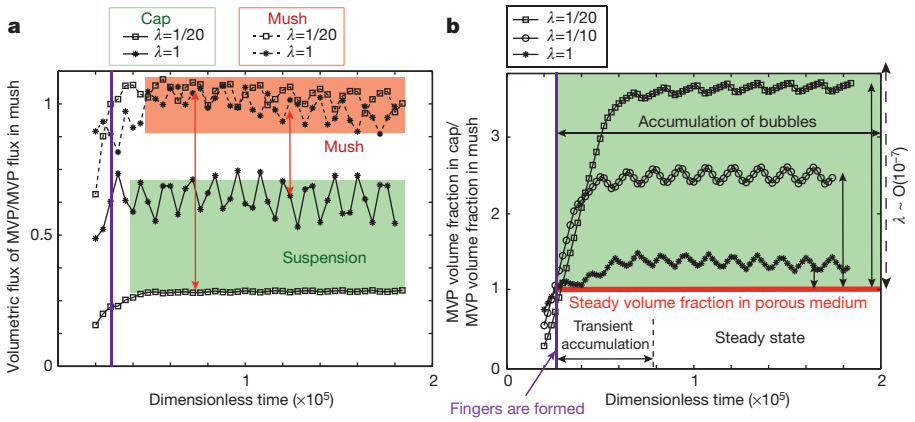

Figure 3 | MVP behaviour at the transition from crystal-rich to crystal-poor magma. a, **b**, Numerical calculations showing the change in transport regime of MVP from a confined medium (crystal-rich mush) to an unconfined horizon (crystal-poor cap; suspension). Panel **a** shows that the volumetric flux of MVP is greater in the mush than in the cap. Time is normalized according to $t' = t \times \nu_{nw}/R^2$, where R is the radius of the capillary tube, ν_{nw} is the kinematic viscosity of MVP, and λ is ν_{nw}/ν_w. Panel **b** shows a comparison of the volume fraction of MVP in the mush (red line) and in the cap (black symbols) for different viscosity ratios between melt and volatiles.

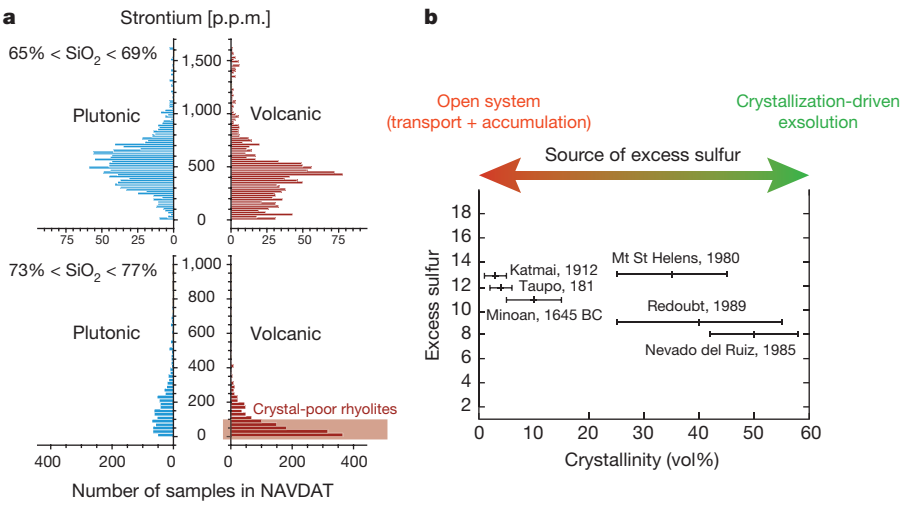

Figure 4 | Geological evidence for MVP accumulation in high-SiO_2, crystal-poor caps. a, Strontium content in whole-rock analyses of magmatic rocks from the NAVDAT database (http://www.navdat.org). While intermediate magmas (SiO_2 content between 65 wt% and 69 wt%) show a similar distribution of strontium in the plutonic and volcanic realms, the more silicic units (SiO_2 content between 73 wt% and 77 wt%) show a significantly larger proportion of low-strontium, highly evolved, erupted magmas (<100 p.p.m. strontium) than do plutonic samples. **b**, Excess sulfur produced by selected explosive eruptions (predominantly crystal-poor: Katmai[6], Taupo[7] and Minoan[8]; crystal-rich: Mount St Helens[30], Redoubt[31] and Nevado del Ruiz[32]), and their sources of sulfur in excess of the amount dissolved in the melt.

non-wetting phase (MVP), and ν_w is the kinematic viscosity of the wetting phase (the silicate melt). For such a range, the MVP flux is up to five times higher in the mush than in the crystal-poor region (Fig. 3a), and the difference correlates positively with viscosity contrast. In silicic magma, λ is typically around 10^{-7}. Our calculations therefore provide a lower bound for the accumulation efficiency of MVP in crystal-poor horizons in magmatic systems (see Methods).

The contrasting dynamics of MVP migration in crystal-rich and crystal-poor environments is a consequence of the different processes that control the rate of energy dissipation. Once MVP pathways are established in the crystal-rich mush, dissipation is minimal because the more viscous melt is mostly passive (MVP flux in the mush is independent of the viscosity ratio, as shown in Fig. 3a). In suspensions, the absence of solid confinement promotes capillary break-up, and the buoyant ascent of bubbles is limited by a volumetrically equivalent return flow of silicate melt, which increases the viscous drag on other bubbles. The transition from one regime to the other is responsible for bubble accumulation in crystal-poor environments.

We note that convection is likely to occur in the crystal-poor cap, especially when subjected to the injection of MVP from the mush below. Convective stirring will affect the motion of bubbles in several ways. For example, it will lead to bubble entrainment in the convective cells, and homogenize the spatial distribution of bubbles in the cap, disrupting plumes forming near the vents at the mush–cap boundary. Overall, we find that convection promotes bubble accumulation (see Methods).

The accumulation of bubbles in crystal-poor caps has implications for the evolution of shallow magma reservoirs. For instance, upper crustal plutons are dominated by granodiorite/tonalite magma bodies[11], but deficient in granite *sensu stricto* (that is, they are deficient in evolved compositions with low concentrations of compatible elements[4] such as strontium; Fig. 4a). In contrast, volcanic provinces can produce highly evolved (high-SiO_2, low-strontium), crystal-poor rhyolites that are volumetrically much more abundant than dacites (see, for example, the Yellowstone Province[26] and the Taupo Volcanic Zone[27]). Bubble accumulation adds gravitational potential energy to crystal-poor rhyolitic caps; this favours the eruption of such liquids, rather than their stalling into the crust and forming granitic bodies[5], and buffers the pressure drop during these eruptions[10], allowing near-complete evacuation of the eruptible pockets of magma and the formation of very large volcanic units (as in, for example, supervolcanic eruptions in Yellowstone[26], the Southern Rocky Mountain volcanic field[28] and the Taupo Volcanic Zone[27]).

Last, but not least, bubble accumulation affects the volatile budget released during eruptions and pluton/ore formation. Magma chambers evacuated during, for example, the Katmai[6], Taupo[7] and Minoan[8] eruptions are predominantly crystal-poor, and would not have undergone enough crystallization to yield their observed excess sulphur by second boiling. Hence, they require that sulfur-rich bubbles accumulate in the eruptible pods of magma (Fig. 4b). Crystal confinement can also have a significant role in the efficient devolatilization of magmas trapped in the crust and the release of metal-rich fluids that promotes the generation of the large porphyry copper systems associated with dying upper-crustal magma reservoirs[20,29].

Online Content Methods, along with any additional Extended Data display items and Source Data, are available in the online version of the paper; references unique to these sections appear only in the online paper.

Received 6 February 2015; accepted 26 January 2016.
Published online 13 April 2016.

1. Wallace, P. J. Volcanic SO_2 emissions and the abundance and distribution of exsolved gas in magma bodies. *J. Volcanol. Geotherm. Res.* **108,** 85–106 (2001).
2. Shinohara, H. Excess degassing from volcanoes and its role on eruptive and intrusive activity. *Rev. Geophys.* **46,** RG4005 (2008).
3. Self, S. The effects and consequences of very large explosive volcanic eruptions. *Phil. Trans. R. Soc. A* **364,** 2073–2097 (2006).
4. Halliday, A. N., Davidson, J. P., Hildreth, W. & Holden, P. Modeling the petrogenesis of high Rb/Sr silicic magmas. *Chem. Geol.* **92,** 107–114 (1991).
5. Hildreth, W. Quaternary magmatism in the Cascades: geological perspectives. *US Dept Interior/US Geol. Surv.* Prof. Pap. 1744 (2007).
6. Hildreth, W., Fierstein, J. Katmai volcanic cluster and the great eruption of 1912. *Geological Society of America Bulletin* **112,** 1594–1620 (2000).
7. Wilson, C. J. N., Rogan, A. M., Smith, I. E. M., Northey, D. J., Nairn, I. A., Houghton, B. F. Caldera volcanoes of the Taupo Volcanic Zone, New Zealand. *J. Geophys. Res. Solid Earth* **89,** 8463–8484 (1984).
8. Druitt, T. H., Costa, F., Deloule, E., Dungan, M. & Scaillet, B. Decadal to monthly timescales of magma transfer and reservoir growth at a caldera volcano. *Nature* **482,** 77–80 (2012).
9. Blake, S. Volatile oversaturation during the evolution of silicic magma chambers as eruption trigger. *J. Geophys. Res.* **89,** 8237–8244 (1984).
10. Huppert, H. E. & Woods, A. W. The role of volatiles in magma chamber dynamics. *Nature* **420,** 493–495 (2002).
11. Bachl, C. A., Miller, C. F., Miller, J. S. & Faulds, J. E. Construction of a pluton: evidence from an exposed cross-section of the Searchlight pluton, Eldorado Mountains, Nevada. *Geol. Soc. Am. Bull.* **113,** 1213–1228 (2001).
12. Heise, W., Caldwell, T. G., Bibby, H. M. & Bennie, S. L. Three-dimensional electrical resistivity image of magma beneath an active continental rift, Taupo Volcanic Zone, New Zealand. *Geophys. Res. Lett.* **37,** L10301 (2010).

13. Cooper, K. M. & Kent, A. J. R. Rapid remobilization of magmatic crystals kept in cold storage. *Nature* **506,** 480–483 (2014).
14. Bachmann, O. & Bergantz, G. W. On the origin of crystal-poor rhyolites: extracted from batholithic crystal mushes. *J. Petrol.* **45,** 1565–1582 (2004).
15. Hildreth, W. S. Volcanological perspectives on Long Valley, Mammoth Mountain, and Mono Craters: several contiguous but discrete systems. *J. Volcanol. Geotherm. Res.* **136,** 169–198 (2004).
16. Huber, C., Bachmann, O. & Manga, M. Homogenization processes in silicic magma chambers by stirring and mushification (latent heat buffering). *Earth Planet. Sci. Lett.* **283,** 38–47 (2009).
17. Faroughi, S. A. & Huber, C. A generalized equation for rheology of emulsions and suspensions of deformable particles subjected to simple shear at low Reynolds number. *Rheol. Acta* **54,** 85–108 (2015).
18. Faroughi, S. A. & Huber, C. Unifying the settling velocity in suspensions and emulsions of non-deformable particles. *Geophys. Res. Lett.* **42,** 53–59 (2015).
19. Lenormand, R., Touboul, E. & Zarcone, C. Numerical models and experiments on immiscible displacements in porous media. *J. Fluid Mech.* **189,** 165–187 (1988).
20. Huber, C., Bachmann, O., Vigneresse, J-L., Dufek, J. & Parmigiani, A. A physical model for metal extraction and transport in shallow magmatic systems. *Geochem. Geophys. Geosys*. **13,** Q08003 (2012).
21. Parmigiani, A., Huber, C., Chopard, B. & Bachmann, O. Pore-scale mass and reactant transport in multiphase porous media flows. *J. Fluid Mech.* **686,** 40–76 (2011).
22. Holtzman, R., Szulczewski, M. L. & Juanes, R. Capillary fracturing in granular media. *Phys. Rev. Lett.* **108,** 264504 (2012).
23. Oppenheimer, J., Rust, A. C., Cashman, K. V. & Sandnes, B. Gas migration regimes and outgassing in particle-rich suspensions. *Front. Phys.* **3,** 60 (2015).
24. Philpotts, A. R., Shi, J. & Brustman, C. Role of plagioclase crystal chains in the differentiation of partly crystallized basaltic magma. *Nature* **395,** 343–346 (1998).
25. Jain, A. K. & Juanes, R. Preferential mode of gas invasion in sediments: grain-scale mechanistic model of coupled multiphase fluid flow and sediment mechanics. *J. Geophys. Res.* **114,** B08101 (2009).
26. Christiansen, R. L. The quaternary and Pliocene Yellowstone plateau volcanic field of Wyoming, Idaho, and Montana. *U.S. Geol. Surv.* Prof. Pap. 729-G (2001).
27. Graham, I. J., Cole, J. W., Briggs, R. M., Gamble, J. A. & Smith, I. E. M. Petrology and petrogenesis of volcanic rocks from the Taupo Volcanic Zone: a review. *J. Volcanol. Geotherm. Res.* **68,** 59–87 (1995).
28. Lipman, P. W. & Bachmann, O. Ignimbrites to batholiths: integrating perspectives from geological, geophysical, and geochronological data. *Geosphere* **11,** 705–743 (2015).
29. Sillitoe, R. H. Porphyry copper systems. *Econ. Geol.* **105,** 3–41 (2010).
30. Devine, J. D., Sigurdsson, H., Davis, A. N. & Self, S. Estimates of sulfur and chlorine yield to the atmosphere from volcanic eruptions and potential climatic effects. *J. Geophys. Res.* **89,** 6309–6325 (1984).
31. Gerlach, T. M., Westrich, H. R., Casadevall, T. J. & Finnegan, D. L. Vapor saturation and accumulation in magmas of the 1989–1990 eruption of Redoubt Volcano, Alaska. *J. Volcanol. Geotherm. Res.* **62,** 317–337 (1994).
32. Sigurdsson, H., Carey, S., Palais, J. M. & Devine, J. Pre-eruption compositional gradients and mixing of andesite and dacite magma erupted from Nevado del Ruiz, Colombia in 1985. *J. Volcanol. Geotherm. Res.* **41,** 127–151 (1990).

Supplementary Information is available in the online version of the paper.

Acknowledgements Discussion of an early version of the paper with A. Burgisser, P. W. Lipman, O. Malaspinas, M. Lupi and W. Degruyter helped us to clarify some concepts. We also thank O. Malaspinas and the rest of the Palabos team, as well as M. L. Porter for discussing how to implement lattice Boltzmann algorithms. We thank J. Bourquin for help with redrafting several figures. A.P. and O.B. acknowledge support from the Swiss National Science Foundation (Ambizione grant no. 154854 to A.P., and project no. 200021-103441 to O.B.). S.F., C.H. and Y.S. acknowledge funding from a National Science Foundation CAREER grant (1454821; awarded to C.H.). This work was also supported by grants from the Swiss National Supercomputing Centre (CSCS) under projects s479 and s597, and the Euler Supercomputer from ETHZ.

Author Contributions C.H., O.B. and A.P. conceived the research. C.H. and, to a lesser extent, A.P. developed the physical model. A.P. performed the numerical modelling and analysed the results. S.F. developed the laboratory experiments and theoretical model for the transport of volatiles in crystal-poor magmas. Y.S. led the discussion on excess sulfur. C.H., O.B. and A.P. all wrote the manuscript.

Author Information Reprints and permissions information is available at www.nature.com/reprints. The authors declare no competing financial interests. Readers are welcome to comment on the online version of the paper. Correspondence and requests for materials should be addressed to A.P. (andrea.parmigiani@erdw.ethz.ch).

METHODS

Geological observations. *Magma differentiation.* Modelling of crystal fractionation in magmas predicts that the content of compatible trace elements such as strontium (highly enriched in plagioclase, the dominant mineral phase in the mid to upper continental crust) drops in the residual melt and should correlate with the SiO_2 content[4]. In geochemical datasets, such as the North American Volcanic and Intrusive Rock Database (NAVDAT; http://www.navdat.org), the distribution of strontium for a given SiO_2 range between volcanic and plutonic suites presents a striking conundrum. For dacitic/granodioritic compositions (intermediate SiO_2 content), the frequency of rock samples with similar strontium contents is nearly identical between volcanic and plutonic rocks; for high-SiO_2 magmas, there is a clear trend towards many more low-strontium compositions in volcanic units than in plutonic units. Clearly, geochemical datasets such as NAVDAT may carry sampling biases, but we argue that the number of samples considered (1,989 volcanic rock samples with 65–69% SiO_2; 2,355 volcanic rock samples with 73–77% SiO_2; 2,018 plutonic rock samples with 65–69% SiO_2; and 1,647 plutonic rock samples with 73–77% SiO_2; see Fig. 4a) and the prominence of the low-strontium mode in high-SiO_2 rhyolites imply that magmas depleted in strontium are more commonly represented in the eruptive than in the intrusive record. We assume that these low-strontium magmas are formed by interstitial/residual melt extraction from dacitic crystal-rich mushes, and segregate into liquid-dominated caps[15,16,33,34] that are consequently more prone to erupt than to stall in the crust.

Volatile budget of volcanic eruptions. Estimates of volatile mass balance in magmas stored in the crust are generally based on the volatile content dissolved in melt inclusions[35]. However, melt inclusion data are limited by several factors, including: (1) leakage of volatiles (loss through volume diffusion, cracks or cleavage surfaces); and (2) an inability to record volatiles trapped in hidden reservoirs (exsolved bubbles or sulfide phases). The excess sulfur paradox is a clear consequence of such limitations. Sulfur degassing from the melt during magma ascent in the conduit does not contribute to the excess sulfur because it is typically accounted for in the petrologic estimate from melt inclusions[2]. The processes that govern the unbalanced sulfur budget are the build-up of an abundant sulfur-rich MVP produced by crystallization-driven exsolution, the transport and accumulation of sulfur-rich MVP from deeper untapped portions of the magmatic system, and, in some cases, the breakdown of sulfides or anhydrite before an eruption[1,2,36,37]. In the context of the large excesses of sulfur released during the explosive eruption of crystal-poor rhyolitic caps, the contributions to the total sulfur mass budget from crystallization-driven exsolution and sulfide/anhydrite breakdown are bound to be tenuous, and call for an efficient migration and accumulation of MVP exsolved deeper down (by second boiling in the crystal-rich mushy roots of the magmatic system; see Fig. 4b).

MVP migration in the crystal-rich mush. At high crystallinity, buoyant bubbles are likely to deform along the direction perpendicular to gravity and, therefore, experience a significant hydrostatic pressure drop. Once this pressure drop is high enough to invade a pore throat, drainage is initiated and the blobs of MVP migrate vertically. The formation of anisotropic MVP clusters along the direction of gravity requires a confinement from the crystal phases to work against interfacial tension. Interfacial tension will tend to make bubbles spherical, whereas gravity will provoke the horizontal expansion of bubbles when their ascent is obstructed. Crystal confinement is therefore key to the development and stability of mobile MVP fingers in a crystal mush. In Extended Data Fig. 2, we show snapshots (Extended Data Fig. 2a–c show initial conditions and Extended Data Fig. 2d–f show the steady-state MVP distribution) for three numerical calculations conducted using a multiphase lattice Boltzmann model (that is, the interparticle potential Shan–Chen method[21,38–40]). We implemented this model using the open-source Palabos library (http://www.palabos.org) and ran the simulations on the supercomputer clusters at Georgia Tech, the Swiss Federal Institute of Technology Zurich (ETHZ) and CSCS-Switzerland (the lattice Boltzmann method and code validations are described in detail below). In these calculations, the pore volume fraction of MVP and the size of pore throats are identical but with different crystallinities (crystallinity ($1-\phi$) increases to the right). We see that increasing the spatial confinement (crystallinity) leads to enhanced coalescence and the formation of stable fingering. The run at highest crystallinity (Extended Data Fig. 2c, f) maximizes the vertical bubble pressure drop and is the only one that leads to the formation of a continuous fingering feature across the domain. In the other calculations, bubbles are mechanically trapped by capillary and viscous forces. A high MVP volume fraction and high crystallinity favour the formation and stability of viscous fingers, because they prevent the growth of Rayleigh–Plateau instabilities[41–43] that are responsible for the break-up of fingering.

In essence, fingering pathways, once established, require little displacement of the viscous melt in the porous medium and reduce therefore the rate of energy dissipation in the melt. This results in an increase of MVP discharge in the mush. In Extended Data Fig. 2g, we report the results of a set of calculations (78 in total) conducted with the same porous medium geometry (porosity 0.4) but a varying initial spatial distribution and volume fraction of MVP. The porous medium is made up of spherical pores, each connected to six cylindrical throats along each dimension (in three dimensions). Throat radii are randomly generated to introduce a random distribution of capillary entry pressure for the MVP invasion in neighbour pores. The calculations at a given MVP pore volume fraction are repeated with a different initial distribution of MVP in the pore space.

These calculations clearly show that the MVP discharge through the porous medium increases with the MVP pore volume fraction. At low MVP volume fraction (red region), MVP remains distributed as discrete bubbles trapped in the medium because of capillary and viscous forces. The discharge is negligible. At intermediate MVP pore volume fraction (green region), coalescence becomes important and makes the formation of percolating fingering pathways of MVP possible, which leads to a sharp increase in MVP discharge. However, in this region, the connectivity of fingering pathways depends on the initial distribution of MVP. In this regime, the runs that do not yield an efficient MVP discharge often display intermittent formation and destruction of fingering pathways, leading to successive periods of short-lived efficient transport and periods of capillary and viscous trapping of MVP bubbles. Above a certain pore volume fraction (blue region), the MVP always forms and sustains percolating fingering pathways and the MVP migration rate is fast.

Bubble suspension dynamics. The rising velocity of an isolated bubble through an infinite stagnant fluid can be described by the law derived by Hadamard and Rybczynski (reviewed in refs 44 and 45). However, when it comes to finding the velocity of a single bubble rising inside a cloud of bubbles, the dynamics becomes more complex because bubbles interact hydrodynamically with each other and with the ambient melt. For example, at low Reynolds number, the rising velocity of a trailing bubble aligned with another (lead) bubble along their direction of motion is greater than that of an individual bubble (the Smoluchowski effect; see ref. 46), while misaligned bubbles experience a greater viscous drag because of the melt return flow. Recently, Faroughi and Huber[18] characterized both local and non-local bubble interactions theoretically, and proposed a new hindrance function, $F(\Psi,\lambda)$, which represents the ratio of the migration velocity of a bubble in a suspension to that of the same bubble in a bubble-free melt. The relative velocity of bubbles in a suspension at low Reynolds number is controlled by the balance between buoyancy and viscous stresses. The presence of bubbles decreases the hydrostatic pressure by a factor $(1-\Psi)$, whereas the presence of a cloud of MVP bubbles dispersed in the melt affects the effective shear viscosity of the magma[17]. The general expression for the hindrance function is[18]:

$$F(\Psi,\lambda)=\frac{1-\Psi}{f_N^{c_d}f_I^{c_d}f^{\mu_f}}$$

where $f_N^{c_d}$ represents the drag caused by the return flow of melt, parameterized as:

$$f_N^{c_d}(\Psi,\lambda)=\left[1-\frac{\beta}{2}\left(\frac{\Psi}{\Psi_m}\right)^{\frac{1}{3}}\left(\frac{2+3\lambda}{1+\lambda}\right)+\frac{\beta^3}{2}\left(\frac{\Psi}{\Psi_m}\right)\frac{\lambda}{1+\lambda}\right]^{-1}$$

Ψ and Ψ_m are, respectively, the bubble volume fraction and the random close packing limit for spherical bubbles; $\beta=0.45$, being a geometrical proportionality constant determined experimentally[17]; $f_I^{c_d}$ captures Smoluchowski's effect:

$$f_I^{c_d}(\Psi,\lambda)=1-\left[\frac{1}{2}\left(\frac{2+3\lambda}{1+\lambda}\right)-\frac{1}{2}\right]\frac{\Psi}{\Psi_m}$$

and f^{μ_f} expresses the change in momentum diffusivity via:

$$f^{\mu_f}(\Psi,\lambda)=\frac{\mu_\Psi}{\mu_f}=\left(\frac{\Psi_m-\Psi}{\Psi_m(1-\Psi)}\right)^{-\left(\frac{\Psi_m}{1-\Psi_m}\right)\left(\frac{1+2.5\lambda}{1+\lambda}\right)}$$

Finally, under the assumption that bubbles are inviscid relative to the melt, we obtain the relative bubble velocity:

$$F(\Psi,\lambda\to 0)=\frac{U_{sus}}{U_t}=\left(\frac{1-\Psi}{1-\frac{\Psi}{2\Psi_m}}\right)\left[1-0.45\left(\frac{\Psi}{\Psi_m}\right)^{\frac{1}{3}}\right]\left(\frac{\Psi_m-\Psi}{\Psi_m(1-\Psi)}\right)^{\frac{\Psi_m}{1-\Psi_m}} \quad (1)$$

where U_{sus} and U_t are, respectively, the bubble velocity in the suspension and its Stokes ascent velocity. Equation (1) is plotted against experimental data over a wide range of particle volume fractions in Extended Data Fig. 1. We carried out experimental studies of bubble migration by using water injected at the top of a tank filled with silicon oil (Extended Data Fig. 3). The localized and fixed injection

points at the top of the tank (water is denser than silicon oils, so buoyancy is reversed compared with the typical situation in a magma reservoir) mimic the localized point sources that will transfer the MVP from the mush to the cap. The experimental set-up allows local bubble plumes to form, where hydrodynamic interactions introduce a smaller penalty to bubble buoyant migration. It is expected that bubble plumes ('vents') will form out of the mush in heterogeneous magma bodies; it was therefore necessary to validate equation (1) against this set of experimental data for our MVP cap suspension model (see Extended Data Fig. 1 inset). Note the significant decrease in MVP flux as the bubble fraction increases in a suspension; this contrasts strongly with the results shown in the section 'MVP migration in the crystal-rich mush', where the MVP flux increases significantly with increasing volume fraction in a porous mush.

Bubble residence time in crystal-poor caps. Crystal-poor caps are prone to convect, especially when buoyant bubbles are fluxed in from below. Convective motion will affect the migration of buoyant bubbles[47]. At low Reynolds numbers, the overall motion of bubbles can be decomposed as a vectorial sum between the imposed convective motion and the buoyant phase separation calculated above. The behaviour of bubbles is determined by the ratio of these two velocity components (sometimes parameterized as a Stokes number[47]). For small (millimetre-size) bubbles in a silicic magma, one can assume that bubbles remain highly coupled to the convective flow motion, except when the flow decelerates in boundary layers next to the edges of the reservoir. Thus, we adapt the model derived by Martin and Nokes[48] and also used by Dufek and Bachmann[34] for crystal suspensions to calculate the residence time of bubbles in the convecting cap.

The main differences between our calculations and those presented in refs 34 and 48 are: (1) in our calculations, the segregating phase comprises buoyant bubbles with free-slip conditions at the interface between bubbles and melt; and (2) we use the hindrance function derived above to correct for the presence of other bubbles, which can significantly affect the buoyant bubbles' ability to migrate in magmas. The model we obtain for the mass (here volume) conservation of bubbles in the cap therefore reads:

$$\frac{\partial}{\partial_t}\left(\frac{\Psi}{1-\Psi}\right) = -\frac{U_t}{H}\left(\frac{\Psi}{1-\Psi}\right)F(\Psi,\lambda) + \frac{q}{H} \tag{2}$$

where $F(\Psi,\lambda)$ is the hindrance function calculated from equation (1), H is the thickness of the crystal-poor layer, and q is the volumetric flux of MVP coming from the mush.

We first solve equation (2) with $q=0$, and retrieve a characteristic residence time for bubbles in a convecting magma. In Extended Data Fig. 4, we show the solution to this differential equation under magmatic conditions. We find that increasing the initial volume fraction of bubbles in a convecting magma has a positive impact on accumulation—that is, at a higher volume fraction, bubbles remain trapped in the convective motion longer because of the hindrance to phase separation. Moreover, the decay rate of the bubble fraction that remains suspended in the convecting magma no longer follows an exponential law[18,48], because of the nonlinear dependence of the MVP ascent velocity on the MVP volume fraction. We also calculate the residence time of bubbles with two arbitrary sizes over a wide range of dynamic shear viscosities of the melt, for dilute ($\Psi=0.01$) and high ($\Psi=0.3$) volume fractions (Extended Data Fig. 5a). We determine the residence time as the half-life of bubbles in the cap, $\Psi(t_{1/2})=0.5\Psi_0$ (see ref. 19).

Under steady-state conditions, equation (2) reduces to:

$$\left(\frac{\Psi}{1-\Psi}\right)F(\Psi,\lambda) = Q \tag{3}$$

where $Q = q/U_t$ is a dimensionless sourcing term. We solve this equation to find the volume fraction of bubbles that can accumulate in the convecting layer, Ψ_s. The equation is nonlinear because of the hindrance function, and can admit more than one root. The physically meaningful solution is plotted in Extended Data Fig. 5b, and shows that the accumulated MVP volume fraction increases monotonously with the influx of MVP from the mush. Interestingly, equation (3) does not admit a real solution for injection rates that are greater than 15% of the Stokes final velocity of a 2-mm-diameter bubble in an infinite pool of melt with a dynamic viscosity of 10^6 Pa s (Extended Data Fig. 5b). Because these injection rates are quite modest, we expect that accumulation of bubbles up to a few tens of per cent in crystal-poor layers in magma chambers is possible. At higher injection rates, accumulation is still possible and likely to occur. However, the lack of a steady solution to our simple convecting suspension model implies that the multiphase dynamics will probably depart from that of a convecting suspension. We hypothesize that, as the volume fraction of bubbles in the crystal-poor cap increases, more complex processes may arise and lead, for example, to massive Rayleigh–Taylor overturns[47].

Dynamic similarities with magma chamber dynamics. We explain the accumulation of MVP in crystal-poor horizons of magma reservoirs by the formation of continuous MVP fingers in crystal-rich environments[21,40] and their break-up at the crystallinity transition between crystal-rich and crystal-poor magmas. This break-up of MVP fingers results in a significant change in the viscous dissipation regime.

We investigate this scenario numerically using a rather simplified geometry. We model the complex geometry of the crystal mush at the pore scale as a capillary tube that opens in a crystal-free/solid-free environment (Extended Data Fig. 6a, b). This is a simple proxy for the more realistic mush–cap transition, but it captures its essential ingredients: the dynamics of two immiscible fluids through a change in spatial confinement, where the low viscosity fluid is non-wetting and buoyant. We justify this approximation with the finding[21] that the transport of immiscible fluids in a porous medium becomes mostly similar to an annular flow once the percolating pathway for the non-wetting fluid is reached. In our numerical calculations, a constant influx of MVP and a fixed pressure for the melt are set at the bottom boundary (inlet), while the top boundary (outlet) absorbs the outfluxing MVP and maintains a fixed pressure for the melt. The sides are periodic boundaries.

The competition between viscous, buoyancy, capillary and inertial forces controls both MVP transport and the breaking of continuous MVP fingering at the crystalline transition between crystal-rich and crystal-poor environments (bubble pinch-off frequency and volume[49–51]). Because this balance operates at the pore scale, we resort to pore-scale multiphase flow calculations to study the formation and destruction of fingering pathways in a heterogeneous medium. The force balance can be described with three dimensionless numbers, the Archimedes (Ar), Bond (Bo) and Reynolds (Re) numbers. Ar, Bo and Re represent, respectively, the ratio between buoyancy and viscous forces (equation (4)), the ratio between buoyancy and capillary forces (equation (5)) and the ratio between inertia and viscous forces (equation (6)):

$$\mathrm{Ar} = \frac{\rho_m \Delta\rho g D^3}{\mu_m^2} \tag{4}$$

$$\mathrm{Bo} = \frac{\Delta\rho g D^2}{\sigma} \tag{5}$$

$$\mathrm{Re} = \frac{\rho_m u_d D}{\mu_m} \tag{6}$$

where $\Delta\rho = \rho_{mvp} - \rho_m$ (ρ_{mvp} and ρ_m are the densities of MVP and melt), g is the acceleration due to gravity, μ_m the dynamic viscosity of the melt, D the bubble diameter and u_d the MVP average pore velocity. A rough estimate of these dimensionless numbers in shallow and highly evolved magmatic systems leads to $\mathrm{Ar} \ll 1$, $\mathrm{Re} \ll 1$ and $\mathrm{Bo} \approx 0.1$–1, we obtain a Bo of the order of approximately 0.1 and we force Re and Ar to be lower than unity. Therefore, our results can serve as good first-order estimates for MVP accumulation in crystal-poor environments. The numerical method described in the 'Lattice Boltzmann for two-phase fluid flows' section limits us to relatively small viscosity contrasts compared with those expected in magmatic systems. Once pathways of MVP are established in the mush, the melt plays a passive role and does not affect the ascent of the MVP. The same is not true for the suspension, where the viscosity of the melt controls the rate of energy dissipation; as such, we expect accumulation to become more efficient as the viscosity contrast between the wetting and the less viscous non-wetting fluid increases. We decided to use our numerical model to test whether bubbles are likely to accumulate under less optimal conditions, that is, when the viscosity contrast is $1/20 \leq \lambda \leq 1$. We found that bubbles accumulate in the crystal-poor region even when the two fluids share the same viscosity ($\lambda=1$), and that the accumulation potential increases as the viscosity contrast becomes more pronounced (Fig. 3).

Lattice Boltzmann for two-phase fluid flows. The lattice Boltzmann method (LBM) solves a discretized version of the continuum Boltzmann equation[52,53]. Based on statistical mechanics, the LBM focuses on the mechanical interaction of an ensemble average distribution of particles $f_i(\mathbf{x},t)$, and retrieves mass and momentum conservation (Navier–Stokes) equations from the statistical moment of the Boltzmann equation.

The LBM has been extended to multicomponent (MC) immiscible fluid flows. Among others, the MC Shan–Chen (SC) model[38,54] is often applied because of:

(1) its straightforward implementation; and (2) the numerical stability of the algorithm in complex geometries such as porous media. In this work, we use the SC model extended by ref. 39, which allows us to model immiscible fluids characterized by notable viscosity contrast. These improvements result from an explicit formulation of the forcing term acting on the particle distribution functions and the use of a multi-relaxation-time (MRT) collision procedure. Below, we describe the improved algorithm briefly; for more details, see refs 39 and 55.

Explicit forcing and MRT collision operator. The explicit evolution rule for the particle distribution function $f_i^{\alpha}(\mathbf{x},t)$ with a single-relaxation-time (SRT) collision operator, Ω_i^{α}, can be written as:

$$f_i^{\alpha}(\mathbf{x}+\mathbf{e}_i,t+1) - f_i^{\alpha}(\mathbf{x},t) = -\frac{1}{\tau_{\alpha}}\left(f_i^{\alpha}(\mathbf{x},t) - f_i^{\mathrm{eq},\alpha}(\mathbf{x},t)\right) + f_i^{F,\alpha}\left(1-\frac{1}{2\tau_{\alpha}}\right) \quad (7)$$

where τ_{α} is the relaxation time for fluid A and B (α = A,B) and relates to the fluids viscosity; $f_i^{\mathrm{eq},\alpha}$ is the equilibrium distribution function; and $f_i^{F\alpha}$ is the explicit forcing term[56].

The left-hand side of equation (7) is generally referred to as the streaming of f_i^{α} values from the lattice node $\mathbf{x}$ to one of its neighbours $\mathbf{x}+\mathbf{e}_i$; the right-hand side (the collision operator Ω_i^{α}) describes the exchange of momentum between the colliding f_i values. In equation (7), $\mathbf{e}_i$ are a set of velocity vectors connecting nearest neighbour nodes (the spatial discretization of the lattice). Here we use the D3Q19 lattice—a three-dimensional lattice in which each node is connected to 19 neighbours. Lattice velocities $\mathbf{e}_i$ and weights w_i for a D3Q19 lattice can be found in ref. 57. The equilibrium distribution function and the explicit forcing term in equation (7) read respectively:

$$f_i^{\mathrm{eq},\alpha}(\mathbf{x},t) = w_i\rho_{\alpha}\left(1+\frac{\mathbf{e}_i\bullet\mathbf{u}^{\mathrm{eq}}}{c_s^2}+\frac{(\mathbf{e}_i\bullet\mathbf{u}^{\mathrm{eq}})^2}{2c_s^4}+\frac{(\mathbf{u}^{\mathrm{eq}})^2}{2c_s^2}\right)$$

$$f_i^{F,\alpha}(\mathbf{x},t) = \frac{\mathbf{F}_{\alpha}\bullet(\mathbf{e}_i-\mathbf{u}^{\mathrm{eq}})}{\rho_{\alpha}c_s^2}f_i^{\mathrm{eq},\alpha}$$

Here, c_s is the lattice speed of sound and $\mathbf{u}^{\mathrm{eq}}$ is the fluid mixture velocity defined as:

$$\mathbf{u}^{\mathrm{eq}} = \frac{\sum_{\alpha}\rho_{\alpha}\mathbf{u}_{\alpha}\omega_{\alpha}}{\sum_{\alpha}\rho_{\alpha}\omega_{\alpha}}$$

where $\omega_{\alpha}=1/\tau_{\alpha}$ and the statistical moments ρ_{α} (density) and $\rho_{\alpha}\mathbf{u}_{\alpha}$ (momentum) are calculated respectively as:

$$\rho_{\alpha}=\sum_i f_i^{\alpha}; \qquad \rho_{\alpha}\mathbf{u}_{\alpha}=\sum_i f_i^{\alpha}\mathbf{e}_i+\frac{1}{2}\mathbf{F}_{\alpha}$$

The forcing vectors $\mathbf{F}_{\alpha}$ contain several contributions, notably cohesion (particle–particle), adhesion (particle–wall) and bulk (for example, gravity and buoyancy) forces. The cohesion forces, responsible for the physical separation between immiscible components, are calculated as:

$$\mathbf{F}_{\alpha}^{\mathrm{coh}}(\mathbf{x},t) = -\rho_{\alpha}(\mathbf{x},t)\mathrm{G}^{c}\sum_i w_i\rho_{\beta}(\mathbf{x}+\mathbf{e}_i)\mathbf{e}_i$$

where α and β are the two complementary phases and G^{c} is a free parameter that is used to tune the interfacial tension between the two fluids. The magnitude of the repulsive force applied by fluid B on fluid A at the node $\mathbf{x}$ (and vice versa) depends on the density gradient of fluid B (for example, $\nabla\rho_B=\sum_i w_i\rho_B(\mathbf{x}+\mathbf{e}_i)$). The evaluation of $\nabla\rho_{\alpha}$ is critical for the stability of the calculations. High-density gradients (thin fluid–fluid interfaces) require an extended neighbourhood to reach the required accuracy[58]. However, a better evaluation of density gradients comes at the price of an increase in computational time (especially in three dimensions). See refs 55, 59 for a detailed description of how to include adhesive and bulk forces. Here, in order to keep the numerical performance acceptable, we calculate the density gradients using the nearest neighbours only.

In order to improve the stability and accuracy of the SRT SC algorithm described above, we use an MRT collision operator, $\boldsymbol{\Omega}_{\alpha}^{\mathrm{MRT}}$. Then, the linear collision operator is re-cast into the space of velocity moments $\mathbf{m}=\mathbf{M}\times f=(\mathbf{m}_o,\mathbf{m}_1,\mathbf{m}_2\ldots\mathbf{m}_{17},\mathbf{m}_{18})$ (where $\mathbf{M}$ is the transformation matrix[57]); next, the relaxation parameter of each moment is adjusted individually to improve numerical stability. $\boldsymbol{\Omega}_{\alpha}^{\mathrm{MRT}}$ can be written as:

$$\boldsymbol{\Omega}_{\alpha}^{MRT} = -\mathbf{M}^{-1}\bullet\mathbf{S}^{\alpha}\times(\mathbf{m}^{\alpha}-\mathbf{m}^{\mathrm{eq},\alpha})+\frac{1}{2}\mathbf{M}^{-1}\bullet\mathbf{S}^{\alpha}\bullet\mathbf{m}^{F,\alpha}+\boldsymbol{f}^{F,\alpha}$$

In this equation, $\mathbf{S}^{\alpha}$ are diagonal matrices where the 19 diagonal components represent the relaxation parameter for each moments of f_i^{α}. As suggested in ref. 57, we use:

$$\mathbf{S}^{\alpha}=diag\begin{pmatrix}1,\ 1.19,\ 1.4,\ 1,\ 1.2,\ 1,\ 1.2,\ 1,\ 1.2,\ \frac{1}{\tau_{\alpha}},\ 1.4,\frac{1}{\tau_{\alpha}},\\ 1.4,\frac{1}{\tau_{\alpha}},\ \frac{1}{\tau_{\alpha}},\frac{1}{\tau_{\alpha}},1.98,\ 1.98,\ 1.98\end{pmatrix}$$

The 19 components of the vectors $\mathbf{m}^{\alpha}$, $\mathbf{m}^{\mathrm{eq},\alpha}$ and $\mathbf{me}^{F\alpha}$ can be calculated respectively as:

$$\mathbf{m}_i^{\alpha}=\sum_j\mathbf{M}_{ij}f_j^{\alpha}; \quad \mathbf{m}_i^{\mathrm{eq},\alpha}=\sum_j\mathbf{M}_{ij}f_j^{\mathrm{eq},\alpha}; \quad \mathbf{m}_i^{F,\alpha}=\sum_j\mathbf{M}_{ij}f_j^{F,\alpha}$$

The stability of the algorithm depends mainly on the choice of repulsion constant (G^{c}) and its correspondent value at solid wall nodes ($\mathrm{G}^{\mathrm{wall}}$, used to introduce wetting forces). Here we want to deal with a highly non-wetting MVP phase. The non-wetting behaviour of MVP affects its dynamics both in the porous medium (higher capillary entry pressures) and at the transition between crystal-rich and crystal-poor environments (pinch-off dynamics).

LB algorithm validation. In order to validate the MRT SC multicomponent algorithm that we use to model the capillary finger formation and the pinch-off dynamics (Figs. 2 and 3), we test our model with two benchmarks. The first test is an annular Poiseuille flow, where the non-wetting fluid A is located in the centre of the pipe such that $r < R_{\mathrm{in}}$, and the wetting fluid B is placed in the outer ring such that $R_{\mathrm{in}} \le r \le R_{\mathrm{out}}$ (where R is the radius of the pipe flow). Both fluids are accelerated by the same bulk force F^{b}. For the case of the two-phase Poiseuille profile problem, an analytical solution exists:

$$u(r) = \frac{F^{\mathrm{b}}}{2\nu_{\mathrm{A}}\rho_{\mathrm{A}}}(R_{\mathrm{in}}^2-r^2)+\frac{F^{\mathrm{b}}}{2\nu_{\mathrm{B}}\rho_{\mathrm{B}}}(R_{\mathrm{out}}^2-R_{\mathrm{in}}^2), 0\le|r|\le R_{\mathrm{in}} \quad (8)$$

$$u(r) = \frac{F^{\mathrm{b}}}{2\nu_{\mathrm{B}}\rho_{\mathrm{B}}}(R_{\mathrm{out}}^2-r^2), R_{\mathrm{in}}\le|r|\le R_{\mathrm{out}} \quad (9)$$

where ν_{α} is the kinematic viscosity of either fluid. In Extended Data Fig. 7a–c, we compare the analytical and numerical solutions for three different viscosity ratios (λ = 1/5, 1/10, or 1/20).

The second validation test is a three-dimensional calculation of the equilibrium shape of a drop of fluid A embedded in fluid B and in contact with a flat solid surface. The goal of this validation is to reproduce the correct equilibrium (static) contact angle between the fluids and solid phases for different wetting properties (Extended Data Fig. 7d–f).

33. Walker, B. J., Miller, C. F., Lowery, L. E., Wooden, J. L. & Miller, J. S. Geology and geochronology of the Spirit Mountain batholith, southern Nevada: implications for timescales and physical processes of batholith construction. *J. Volcanol. Geoth. Res.* **167,** 239–262 (2007).
34. Dufek, J. & Bachmann, O. Quantum magmatism: magmatic compositional gaps generated by melt-crystal dynamics. *Geology* **38,** 687–690 (2010).
35. Wallace, P. J. Volatiles in subduction zone magmas: concentration and fluxes based on melt inclusion and volcanic gas data. *J. Volcanol. Geotherm. Res.* **140,** 217–240 (2005).
36. Gerlach, T. M., Westrich, H. R. & Symonds, R. B. in *Fire and Mud: Eruptions and Lahars of Mt. Pinatubo, Philippine* 415–433 (Univ. Washington Press, 1996).
37. Costa, F., Scalliet, B. & Gourgaud, A. Massive atmospheric sulfur loading of the AD 1600 Huaynaputina eruption and implications for petrological sulfur estimates. *Geophys. Res. Lett.* **30,** 1068 (2003).
38. Shan, X. & Chen, H. Lattice Boltzmann model for simulation of flows with multiple phases and components. *Phys. Rev. E* **47,** 1815 (1993).
39. Porter, M. L., Coon, E. T., Kang, Q., Moulton, J. D. & Carey, J. W. Multicomponent interparticle-potential lattice Boltzmann model for fluids with large viscosity ratios. *Phys. Rev. E* **86,** 036701 (2012).
40. Huber, C., Parmigiani, A., Latt, J. & Dufek, J. Channelization of buoyant non-wetting fluids in saturated porous media. *Wat. Resour. Res.* **49,** 6371–6380 (2013).
41. Gauglitz, P. A., St. Laurent, C. M. & Radke, C. J. Experimental determination of gas-bubble break-up in constricted cylindrical capillary. *Ind. Eng. Chem. Res.* **27,** 1282–1291 (1988).
42. Guillot, P. & Colin, A. Stability of a jet in confined pressure-driven biphasic flows at low Reynolds number in various geometries. *Phys. Rev. E* **78,** 016307 (2008).
43. Beresnev, I. A., Li, W. & Vigil, R. D. Condition for break-up of non-wetting fluid in sinusoidally constricted capillary channels. *Transp. Porous Media* **80,** 581–604 (2009).

44. Clift, R., Grace, J. R. & Weber, M. E. *Bubbles, Drops, and Particles.* (Courier Dover Publications, 1975).
45. Batchelor, G. K. *An Introduction to Fluid Dynamics.* (Cambridge Univ. Press, 1967).
46. Sonshine, R. M., Cox, R. G. & Brenner, H. The Stokes translation of a particle of arbitrary shape along the axis of a circular cylinder. *Appl. Sci. Res.* **16,** 273–300 (1966).
47. Ruprecht, P., Bergantz, G.W. & Dufek, J. Modeling of gas-driven magmatic overturn: tracking of phenocryst dispersal and gathering during magma mixing. *Geochem. Geophys. Geosys.* **9,** Q07017 (2008).
48. Martin, D. & Nokes, R. Crystal settling in a vigorously convecting magma chamber. *Nature* **332,** 534–536 (1988).
49. Higuera, F. J. Injection and coalescence of bubbles in a very viscous liquid. *J. Fluid Mech.* **530,** 369–378 (2005).
50. Gerlach, D., Alleborn, N., Buwa, V. & Durst, F. Numerical simulation of periodic bubble formation at a submerged orifice with constant gas flow rate. *Chem. Eng. Sci.* **62,** 2109–2125 (2007).
51. Quan, S. & Hua, J. Numerical studies of bubble necking in viscous liquids. *Phys. Rev. E* **77,** 066303 (2008).
52. He, X. & Luo, L. S. A priori derivation of the lattice Boltzmann equation. *Phys. Rev. E* **55,** R6333–R6336 (1997).
53. Shan, X., Yuan, X. F. & Chen, H. Kinetic theory representation of hydrodynamics: a way beyond the Navier-Stokes equation. *J. Fluid Mech.* **550,** 413–441 (2006).
54. Shan, X. & Doolen, G. D. Multicomponent Lattice Boltzmann model with interparticle interaction. *J. Stat. Phys.* **81,** 379 (1995).
55. Coon, E. T., Porter, M. L. & Kang, Q. Taxila LBM: a parallel, modular lattice Boltzmann framework for simulating pore-scale flow in porous media. *Comput. Geosci.* **18,** 17–27 (2014).
56. He, X., Chen, S. & Doolen, G. D. A novel thermal model for the lattice Boltzmann method in incompressible limit. *J. Comput. Phys.* **146,** 282–300 (1998).
57. D'Humieres, D., Ginzburg, I., Krafzcyk, M., Lallemand, P. & Luo, L. S. Multiple-relaxation-time lattice Boltzmann models in three dimensions. *Phil. Trans. R. Soc. Lond. A* **360,** 437–451 (2002).
58. Sbragaglia, M. *et al.* Generalized lattice Boltzmann method with multirange pseudopotential. *Phys. Rev. E* **75,** 026702 (2007).
59. Huang, H., Thorne, D. T., Schaap, M. G. & Sukop, M. C. Proposed approximation for contact angles in the Shan-and-Chen type multicomponent multiphase lattice Boltzmann models. *Phys. Rev. E* **76,** 066701 (2007).

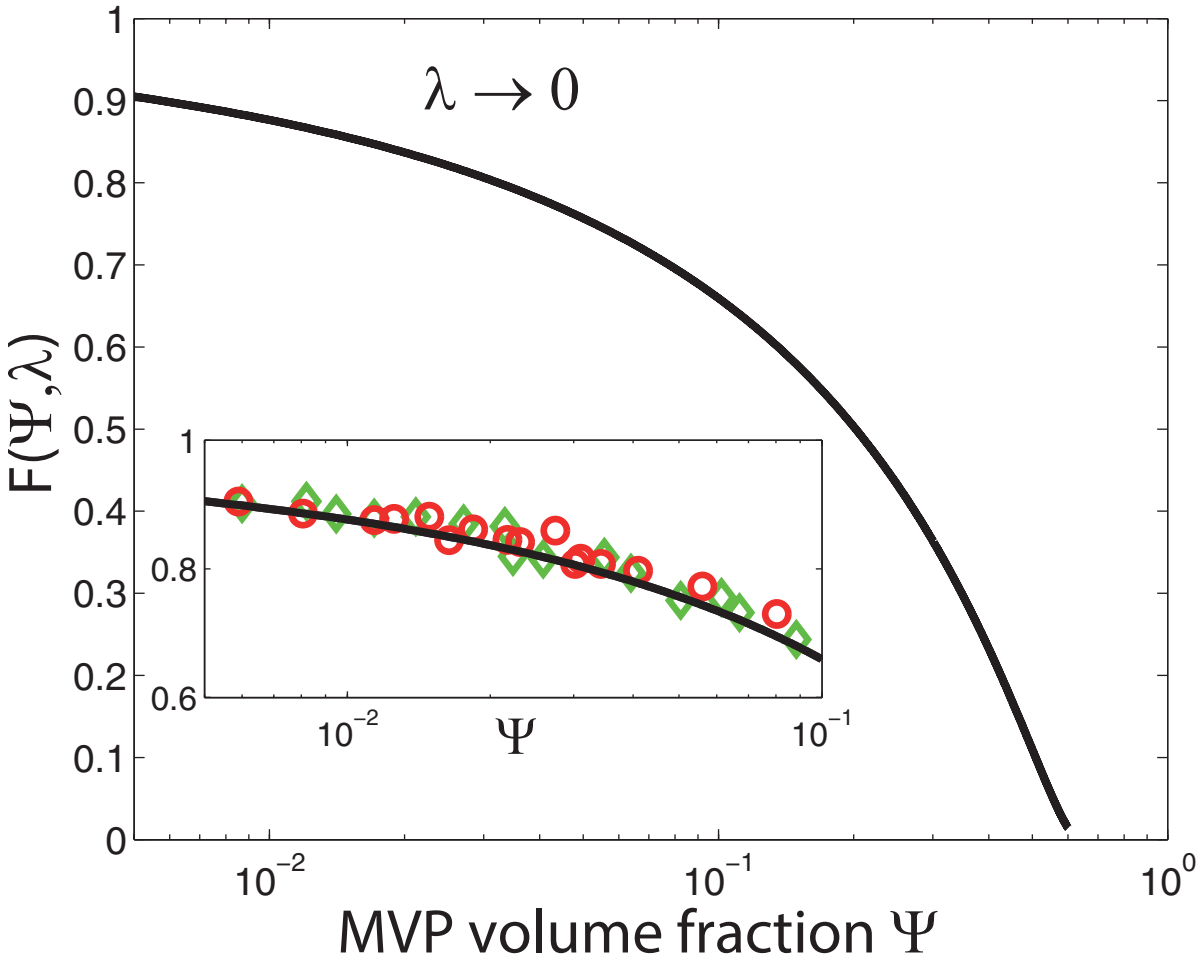

Extended Data Figure 1 | Hindrance function. The hindrance function, $F(\Psi,\lambda)$, defined by equation (1), for suspensions of MVP ($\lambda \to 0$) over a wide range of MVP volume fractions ($0 \leq \Psi \leq 0.6$). The inset shows the comparison of $F(\Psi,\lambda \to 0)$ with experimental data up to MVP volume fractions of 10%. Experimental data are taken from ref. 18, where the method of continuous injection is used, injecting the dispersed phase (water) into the highly viscous ambient phase (silicone oil, resulting in $\lambda = O(10^{-4})$).

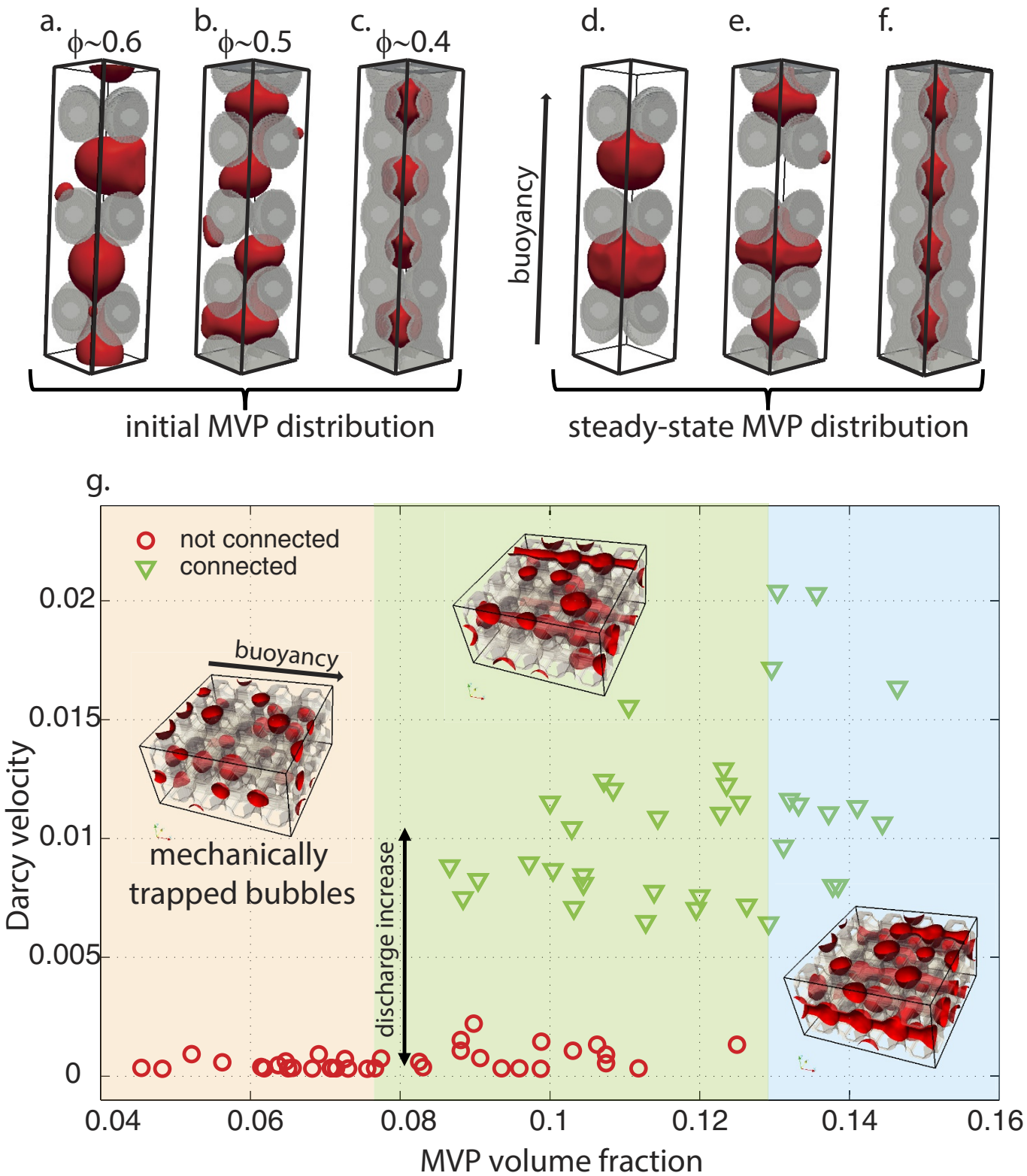

Extended Data Figure 2 | Confinement effect and MVP percolation. **a–f**, The results of three numerical calculations used to explain the effect of crystal confinement on fingering formation (see video in Supplementary Information). Porosity, ϕ, decreases from left to right. **a–c**, Three separate initial states, at different porosities; **d–f**, the corresponding steady states, at the corresponding porosities. At higher crystallinity ($1-\phi$), fingers can form and remain stable. **g**, Results of 78 calculations showing the correlation between the MVP volume fraction, Ψ, and the flux of MVP in the porous medium (the Darcy velocity, U_{Darcy}). At low Ψ, the low mobility of bubbles is such that U_{Darcy} is close to zero. Once continuous fingers are formed ('connected'; green and blue regions), the MVP flux experiences a strong increase because of the sudden and sharp decrease in the rate of viscous energy dissipation. Conversely, during a waning influx of MVP (moving from right to left in **g**), an MVP volume fraction of 10% or slightly more can remain trapped in the mush because of capillary and viscous trapping in the mush.

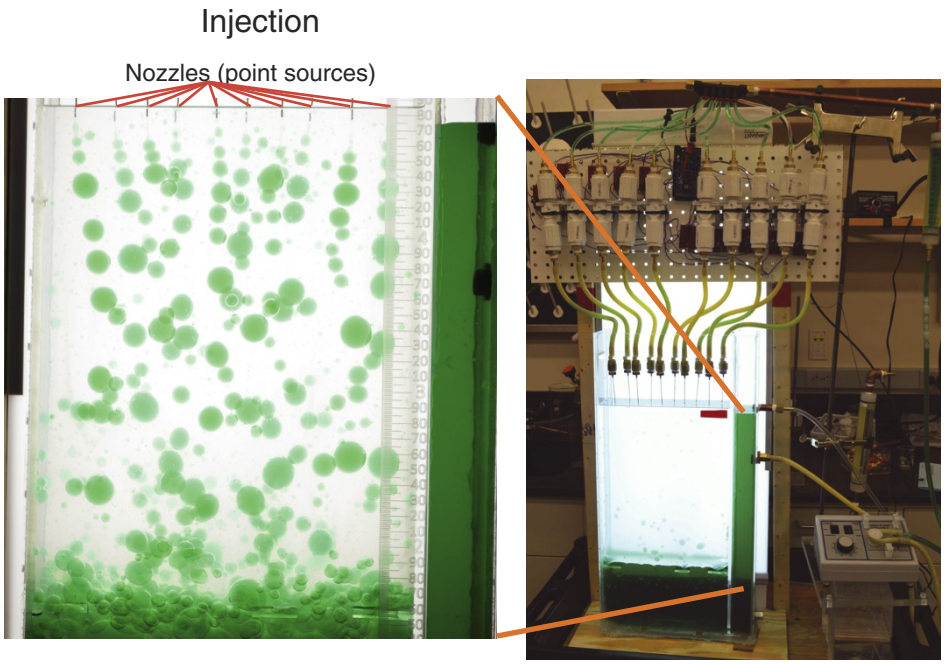

Extended Data Figure 3 | Experimental study of bubble separation in suspensions. Water droplets are released from localized nozzles at the top and sink into viscous silicon oil, forming bubble trains or plumes initially. The motion of water droplet is captured by a camera and used to test our bubble suspension migration model (equation (1)).

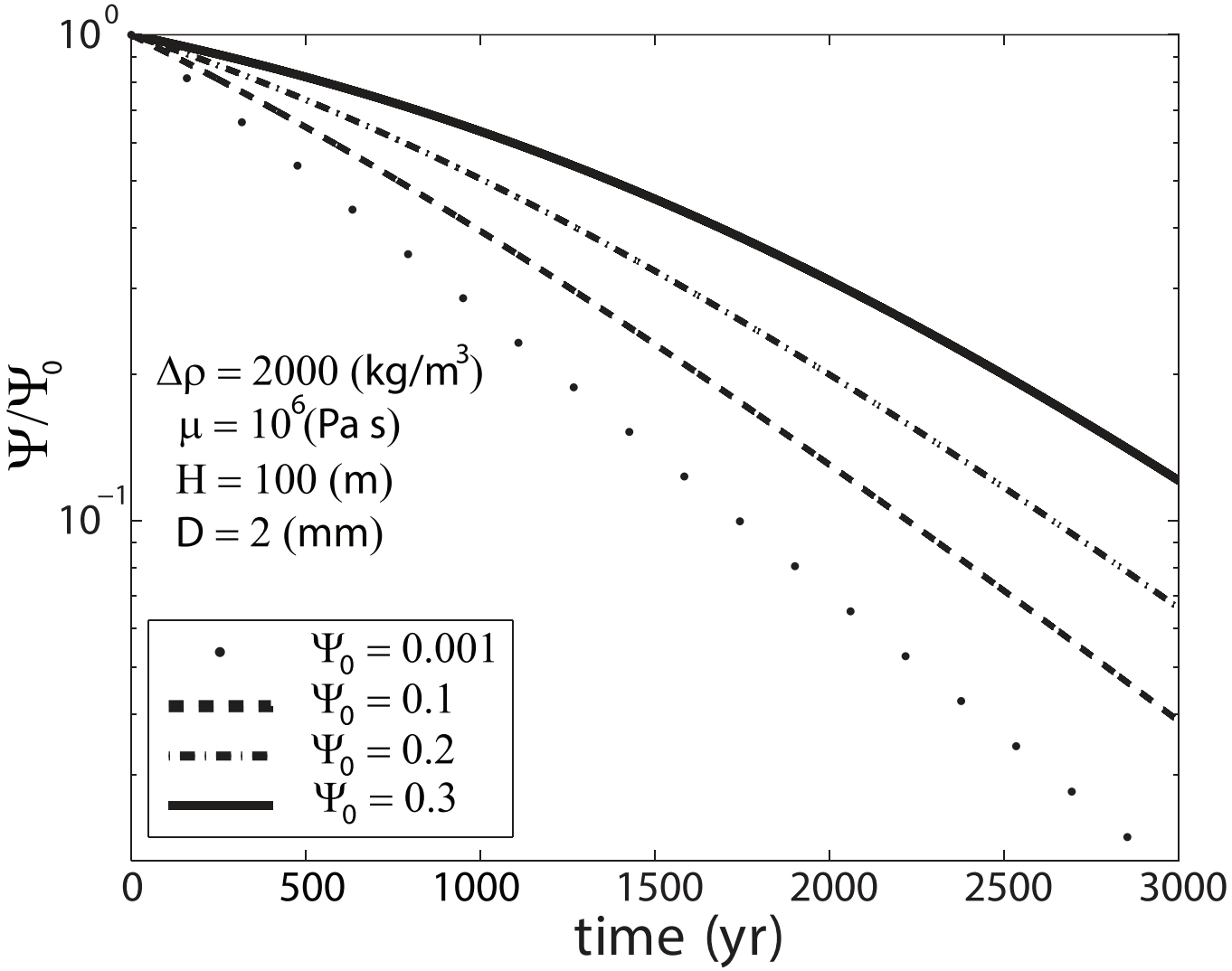

Extended Data Figure 4 | Residence time of bubbles in convecting crystal-poor magmas. For conditions and parameters consistent with exsolved volatile bubbles (2 mm diameter) in a viscous melt, the detrainment of bubbles over time depends on the initial bubble volume fraction, because of the hindered motion of bubbles in a suspension.

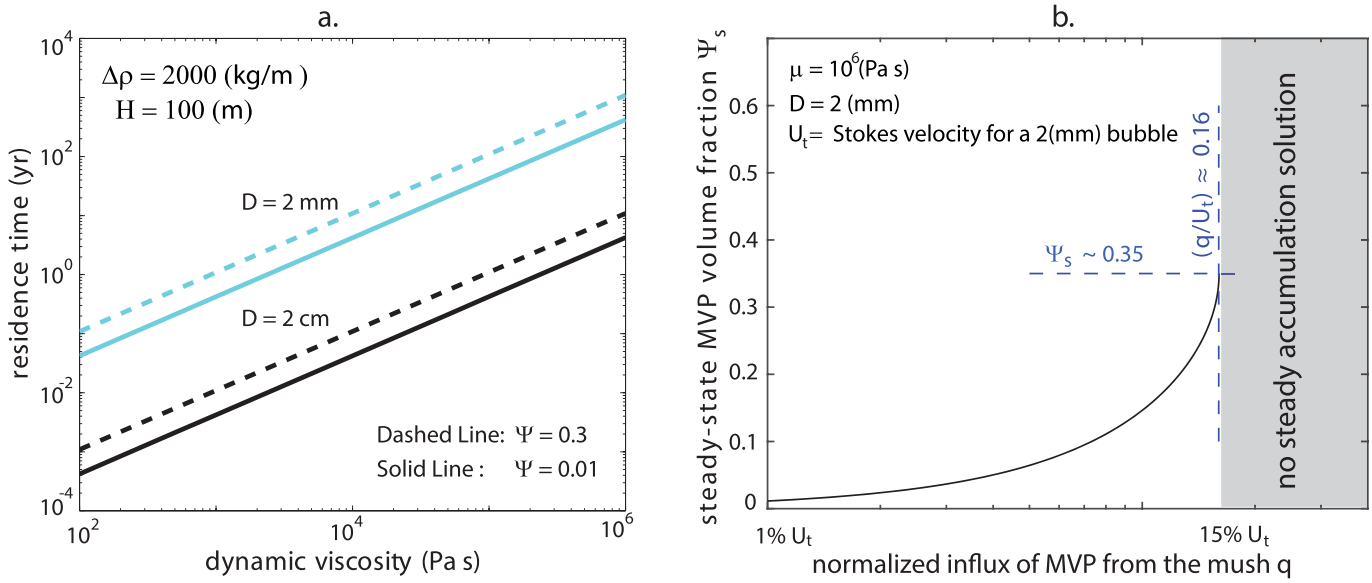

Extended Data Figure 5 | Bubble accumulation in convecting magma. a, **b**, Bubble residence time (**a**) and accumulation (**b**) in a convecting crystal-poor cap of thickness H (100 m). D refers to the average diameter of bubbles; $\Delta\rho$ is the density difference between MVP and the magma; q is the volumetric flux of MVP coming from the mush; and Ψ_s is the volume fraction of bubbles that can accumulate in the convecting layer.

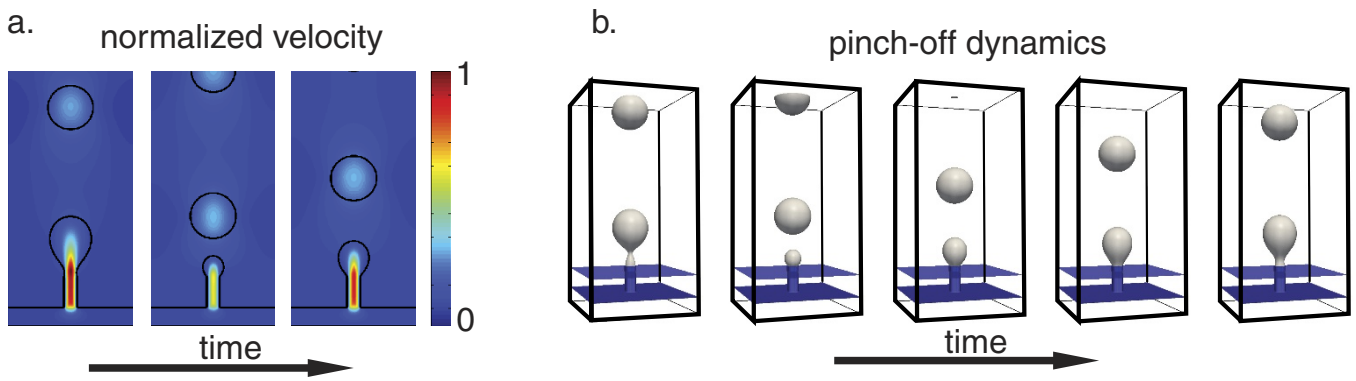

Extended Data Figure 6 | Pinch-off dynamics. a, **b**, Results of numerical calculations that show the transition in transport regime of MVP from a confined medium (crystal-rich mush; left) to an unconfined horizon (crystal-poor cap; right).

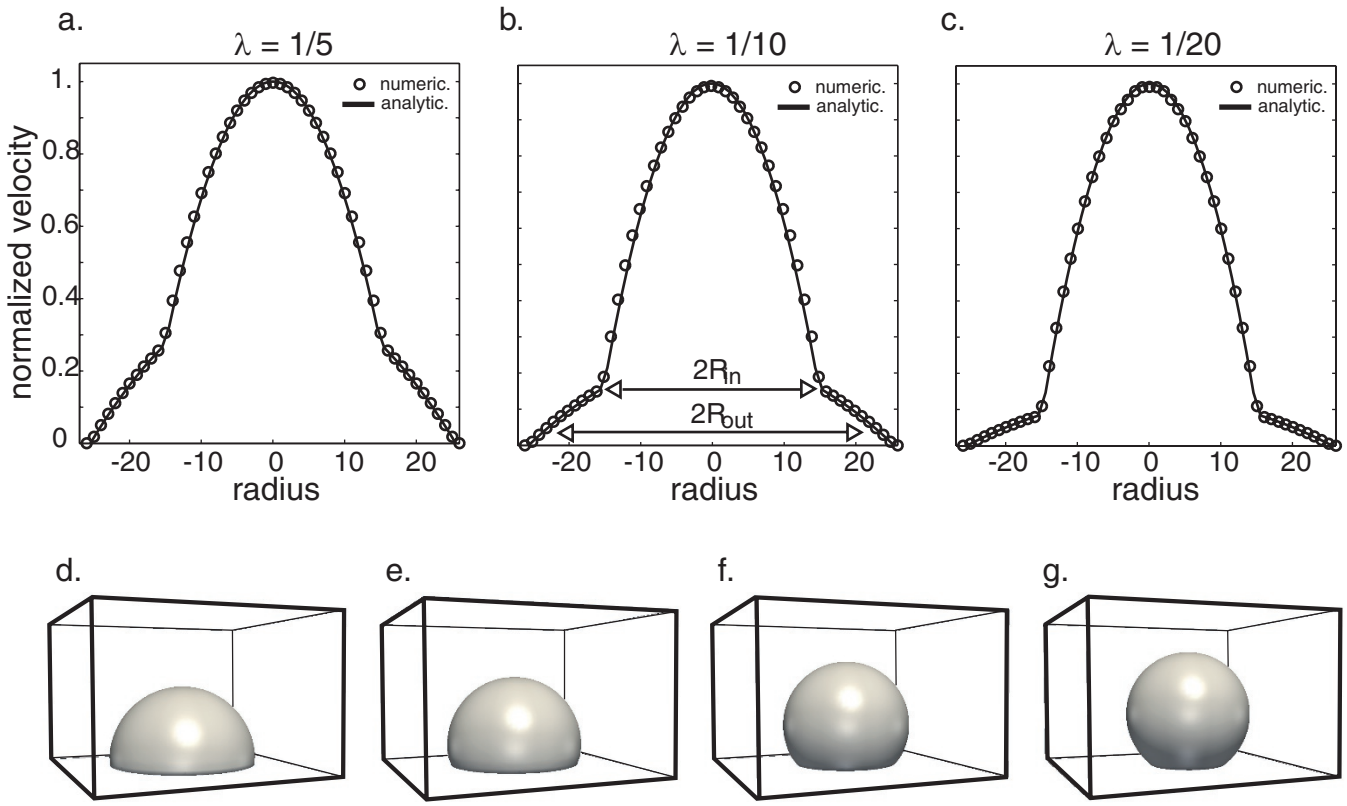

Extended Data Figure 7 | Validation of the lattice Boltzmann algorithm: cylindrical Poiseuille flow and static contact angles. a–c, Analytical (equations (8) and (9)) and numerical velocity (lattice Boltzmann algorithm) profiles for a three-dimensional, two-immiscible-phase, cylindrical pipe flow scenario at different viscosity ratios (λ=1/5, 1/10, or 1/20), showing normalized bubble velocity versus pipe radius. A bulk force, F_b, is applied to both fluids. R_{in} and R_{out} are the internal and external radius, respectively, for the annular flow. **d–g**, Different static contact angles obtained with our lattice Boltzmann algorithm. From left to right, we increase the non-wetting potential of the dispersed phase. The bubble contact angle accordingly increases from 90° to 150° (**d**, 90°; **e**, 110°; **f**, 130°; **g**, 150°). The calculations were done with an MRT collision operator (see Methods).

Geoderma 433 (2023) 116452

Contents lists available at ScienceDirect

Geoderma

journal homepage: www.elsevier.com/locate/geoderma

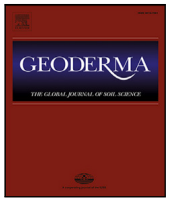

A multihead LSTM technique for prognostic prediction of soil moisture

Pingki Datta, Salah A. Faroughi *

Geo-Intelligence Laboratory, Ingram School of Engineering, Texas State University, San Marcos, TX, 78666, USA

ARTICLE INFO

Handling Editor: L.S. Morgan Cristine

Keywords:
Soil moisture forecasting
Prognostic prediction
Ensemble learning
Deep learning
Long Short-Term Memory (LSTM)
Multihead LSTM

ABSTRACT

Prognostic prediction of soil moisture is a critical step in various fields such as geotechnical engineering, agriculture, geology, hydrology, and climatology. For example, in agricultural applications, soil moisture prediction is needed one-day and one-week ahead of time to optimize crop planting quality and set irrigation schedule, respectively. In soil and environmental management applications, soil moisture prediction is usually needed one-month ahead of time. Therefore, a capability to accurately forecast soil moisture is of paramount importance. For this purpose, deep learning methods, especially the long short-term memory network (LSTM) method, have been used extensively. It is shown that such models can successfully forecast the soil moisture for a short time frame in future, but their accuracy sharply decreases for long time frames. To resolve this issue, in this study, we present a multihead LSTM model that learns a number of hypotheses and aggregates them for prognostic prediction tasks. The multihead LSTM model is comprised of four LSTM models that digest time series data of soil moisture aggregated at different scales as inputs. The outputs of these models, i.e., predicted soil moisture at a certain time in future, are then combined using a weighted averaging method to obtain the final prediction values. Different statistical measures, such as the root mean square error (RMSE), mean square error (MSE), mean absolute error (MAE), mean absolute percentage error (MAPE), and R-squared are employed to assess the performance of the multihead LSTM model predictions against the ground truth. The results show that the proposed multihead LSTM method is effective to forecast the soil moisture up to one-month in future with a R-squared value of 95.04%.

1. Introduction

Soil moisture or water content controls various phenomena in different fields such as agriculture, hydrology, soil use management, environmental management, and in earth work related construction. Its prediction ahead of time is critical for many applications as it helps in the comprehension of ecosystem and operation responses. For example, appropriate soil water content in the crop's root zone is critical for crop growth and yield quality (Yu et al., 2021). With the growing demand for agricultural water resources, assessing soil moisture ahead of time is needed to develop a realistic irrigation schedule leading to a better water resource utilization (Gao et al., 2022a; Adeyemi et al., 2018; Li et al., 2022; Filipović et al., 2022). The soil moisture forecasting is also crucial in hydrology as a major regulatory component in understanding groundwater status (Ahmed et al., 2021b). For construction projects, the initial estimations of soil water content may change, because construction time between site assessment, design, and construction phases vary significantly (Shitote et al., 2019). Forecasting soil moisture content over a certain time period for high-speed railways can also provide a useful reference for the safety of train operation, especially in colder climates (Chen et al., 2021).

Soil is a natural material whose properties may significantly vary spatially and temporally. Specifically, the soil water content can be affected by many pore-scale and macro-scale physicochemical phenomena. Different studies to date showed the feasibility to predict the soil moisture using data-driven models by accumulating and learning from past time series data (Elshorbagy and El-Baroudy, 2009; Zhang et al., 2019; Abioye et al., 2021). This has been conducted using Machine Learning (ML) and Deep Learning (DL) approaches that have become increasingly popular in recent years for decoding data characteristics and predicting future trends (Ge et al., 2019; Karandish and Šimunek, 2016; Adab et al., 2020). Several ML algorithms such as support vector machine (Taneja et al., 2021), random forest (Fathololoumi et al., 2021), Gaussian process regression (Wei et al., 2021), multivariate adaptive regression splines (Heddam, 2021), integrating boruta-random forest (Ahmed et al., 2021a), partial least squares regression (Zhang et al., 2021), have been used for this purpose. Hong et al. (2016) combined support vector machine and relevance vector machine to build a model for forecasting soil moisture about two-weeks ahead of time. Prasad et al. (2018) utilized an extreme learning machine model to forecast the soil moisture on monthly

* Corresponding author.
E-mail address: salah.faroughi@txstate.edu (P. Datta).

https://doi.org/10.1016/j.geoderma.2023.116452
Received 30 June 2022; Received in revised form 25 January 2023; Accepted 24 March 2023
Available online 1 April 2023

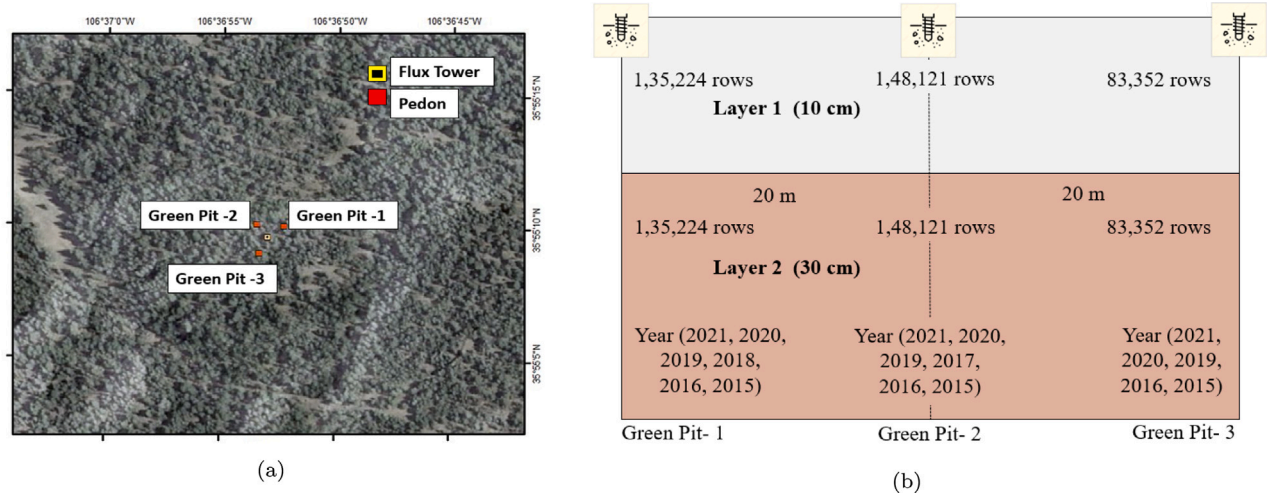

Fig. 1. Summary of the soil moisture data: Panel (a) shows the topographical view of the study area where a flux tower was set up at the center of the three pits (Chorover and Losleben, 2021), and the distance between pits was 20 m. Panel (b) shows the information regarding the VWC dataset that was collected for two shallow depth layers at 10 and 30 *cm*.

basis. Tunçay (2021) interpreted the field-scale variability of soil moisture one-month ahead of time for the achievement of optimal use of available water resources for crop production using ordinary kriging, regression kriging, and cokriging methods. In this research works, different soil features such as soil texture, bulk density, and land use for predicting soil moisture were applied. Yu et al. (2021) predicted soil moisture six-days ahead of time using different features such as temperature, precipitation, frost free period, and soil moisture.

Traditional machine learning models are limited in terms of learning time series data representing complex physical systems. This limitation necessitates more work in data pre-processing and feature extraction, and generally leads to models with poor generalization capabilities (Huang et al., 2010; Zaman and McKee, 2014; Ponkina et al., 2021). To resolve this issue, researchers adopted DL models such as multilayer perceptron (MLP) or feed forward artificial neural networks (ANN) (Han et al., 2021), and recurrent neural networks (RNN) (Adeyemi et al., 2018). Adeyemi et al. (2018) developed a dynamic soil moisture prediction model based on LSTM, a type of RNN, for irrigation scheduling decisions in agricultural fields. Filipović et al. (2022) also used LSTM to predict the volumetric soil moisture three-days ahead of time for optimal irrigation scheduling. Using the same method, Fang and Shen (2020) predicted soil moisture for one-day, two-days and three-days ahead of time with the accuracy of 0.89 based on R-squared value. Prakash et al. (2018) employed MLP, support vector regression, and RNN to predict soil moisture for one-day, two-days, and one-week ahead of time and reported the accuracy of 0.80 based on R-squared value. Yu et al. (2020) developed a model for soil moisture content at different depths in agricultural fields by integrating the temporal and spatial feature extraction advantages of ResNet (Muppidi et al., 2022) and BiLSTM (Heddam et al., 2022) models for the next one to six days. The accuracy of their model was 0.818–0.991 based on R-squared value. ElSaadani et al. (2021) developed a DL algorithm that combines the capabilities of convolutional neural network (CNN) and LSTM, dubbed as ConvoLSTM. They showed that ConvLSTM can predict soil temporal change after 1 day with a RMSE of 2.5% and R-squared of 0.9 for their study area. Recently, Gao et al. (2022a) examined deep bidirectional long short-term memory (Bid-LSTM) network and ANN for soil moisture prediction, and showed Bid-LSTM performed better for predicting soil moisture one-month ahead of time.

These studies all showed that the accuracy of soil moisture prediction sharply decreases with the extension of the prediction time. To overcome the problem, we propose a multihead LSTM model that simultaneously offers hourly, daily, weekly, and monthly soil moisture predictions with acceptable accuracy. This ensemble technique is comprised of four LSTM models that digest time series data of soil moisture aggregated at different time scales as inputs. The outputs of these models are then weighted to obtain the final predictions for soil moisture. The main objective of this research work is to accurately forecast soil moisture one-day, one-week, and one-month ahead of time, which can be respectively used for regulating agricultural planting parameters, making irrigation schedule, and using in hydrology and environmental management.

The paper is organized in the following manner: in Section 2, we present the characteristics of the raw datasets, report the data processing and analysis approaches to generate the training and testing datasets. In Section 3, the architecture of the multihead LSTM employed to predict the soil moisture is discussed, and the measures for evaluating the model performance are described. Next, in Section 4, we present the performance of individual LSTM models forecasting the soil moisture for the next-hour, next-day, next-week, and next-month. Then, we present the final outputs of the multihead LSTM model compared to the ground truth. Finally, in Section 5, we summarize the main conclusions of this work.

2. Data preparation

2.1. Study area

In this study, we employ a dataset collected by Chorover and Losleben (2021) from the south slopes of the San Antonio Mountain close to the Sulfur Spring (35.9195° N, −106.6145° E, 35.9192° S, −106.6148° W) as shown in Fig. 1(a). This site is classified as forest land and coniferous forest, and its vegetation is primarily a mixed conifer forest with a few small patches of grass. The total area of this site is 0.01 km^2, and the elevation is 2751–2753 m. The main attributes of this dataset are soil volumetric water content (VWC), temperature, electrical conductivity, and water potential at 10, 30, 60, and 135 *cm* depths. Data is measured continuously at 15-minute intervals and stored in Campbell CR1000 data loggers. Three pits, named as Green pit-1, Green pit-2, and Green pit-3, were used for continuous data collection. The horizontal distance between pits was 20 m, and the canopy height around the pit's footprint range from 10 to 31 m. We only employ the VWC data at 10 and 30 cm to train our model, because the datasets for 60 and 135 cm depth are not validated. The number of rows for VWC data points at 10 and 30 cm are summarized in Fig. 1(b). The annual average temperature, annual average precipitation, heating degree days, cooling degree days, average annual total snowfall are

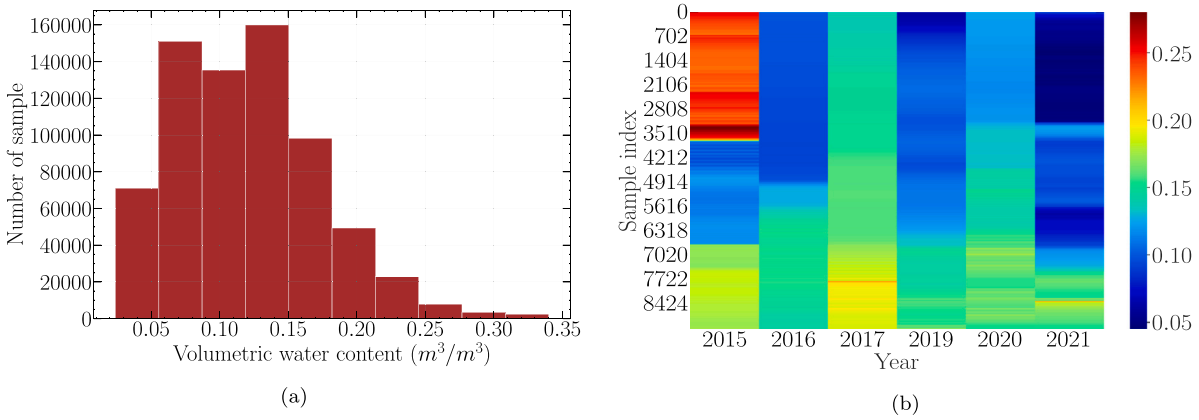

Fig. 2. Panel (a) shows the distribution of the raw data collected at 15-minute intervals between 2015 to 2021. The bar width shows the ranges of VWC, and the bar height shows the quantity of that range in the selected datasets. Most of the VWC data were within the range of 0.05 to 0.15 m^3/m^3. Panel (b) shows the yearly variation of VWC from 2015 to 2021. The VWC ranges were between 0.15 to 0.25 m^3/m^3 at 2015 that reduces to 0.05 to 0.10 m^3/m^3 at 2021.

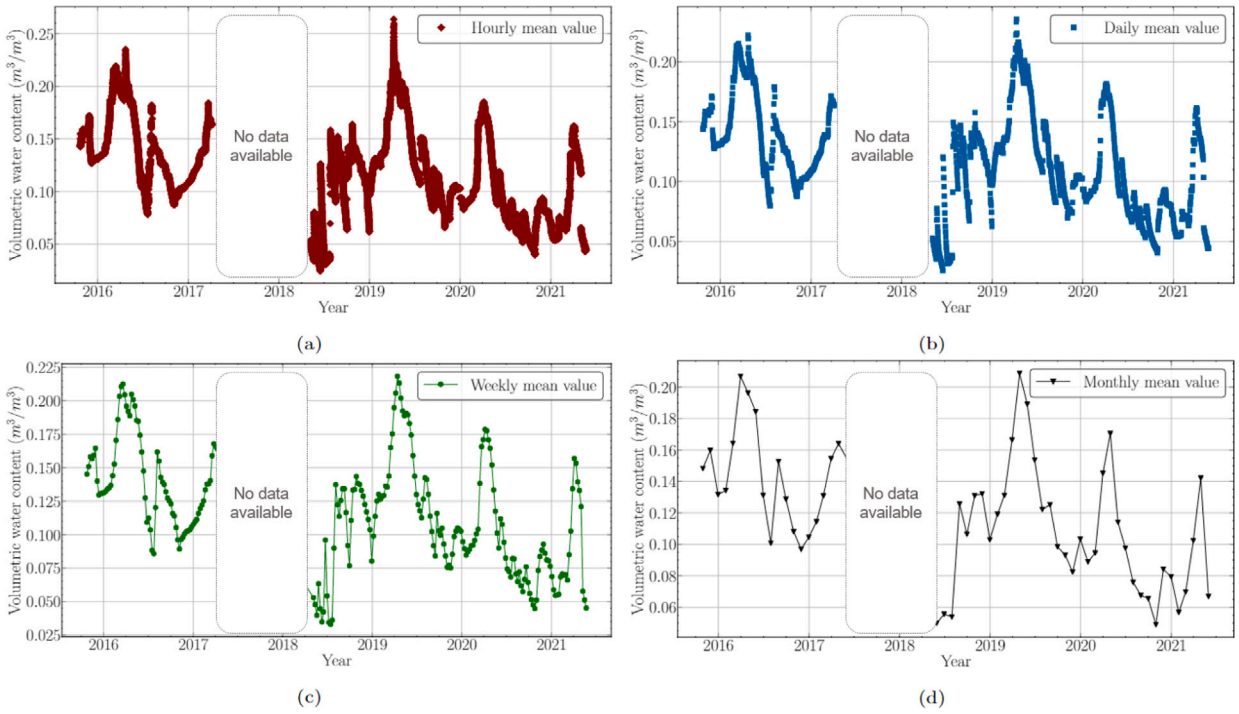

Fig. 3. Graphical representation of aggregated data from 15-minute intervals data; Panel (a) shows the hourly aggregated dataset. The density of this dataset is higher than all other aggregated datasets. Panel (b) shows the daily aggregated dataset, Panel (c) shows the weekly aggregated dataset, and Panel (d) shows the monthly aggregated dataset. The box labeled with "No data available" shows a lack of valid data points for the year of 2018.

37–66.5° F, 17.15 inch, 51.93° F, 57.8° F, and 29.9 inch with 0 inch average snow depth, respectively (Chorover and Losleben, 2021).

2.2. Data pre-processing

After observing all the 15-minute intervals for the VWC raw data from 2015 to 2021, we selected data ranging from 5% to 35% as shown in Fig. 2(a). The majority of the VWC data points were within the range of 0.05 to 0.15 m^3/m^3. Fig. 2(b) shows the yearly variation of VWC in this region between 2015–2021. This dramatic variation of soil moisture over years highlights the level of difficulty to develop a predictive data-driven model that can accurately forecast soil moisture for long time in future.

In this study, we used Green pit-2 and pit-3 data for training and validation purposes, and reserved Green pit-1 data for blind testing. We first aggregated the 15-minute interval dataset to form hourly, daily, weekly, and monthly datasets as plotted in Fig. 3. We obtained 33,654 rows of hourly aggregated data, 1,670 rows of daily aggregated data, 156 rows of weekly aggregated data, and 36 rows of monthly aggregated data as shown in Fig. 4. We aggregated the time series data by averaging based on resampling function (O'Connor et al., 2021; Harvey and Schwartz, 1998). The box labeled with "No data available" in Fig. 3 indicates the lack of valid data points for the year of 2018. Aggregated data were then used to generate the training, evaluation, and testing datasets. The training set comprised 80% of the Green pit-2 and pit-3 data, and the rest was used as validation set to evaluate the fit of the model while training. The data associated with Green pit-1 was used for blind testing (see Section 3.3 for detail on generating training and testing datasets).

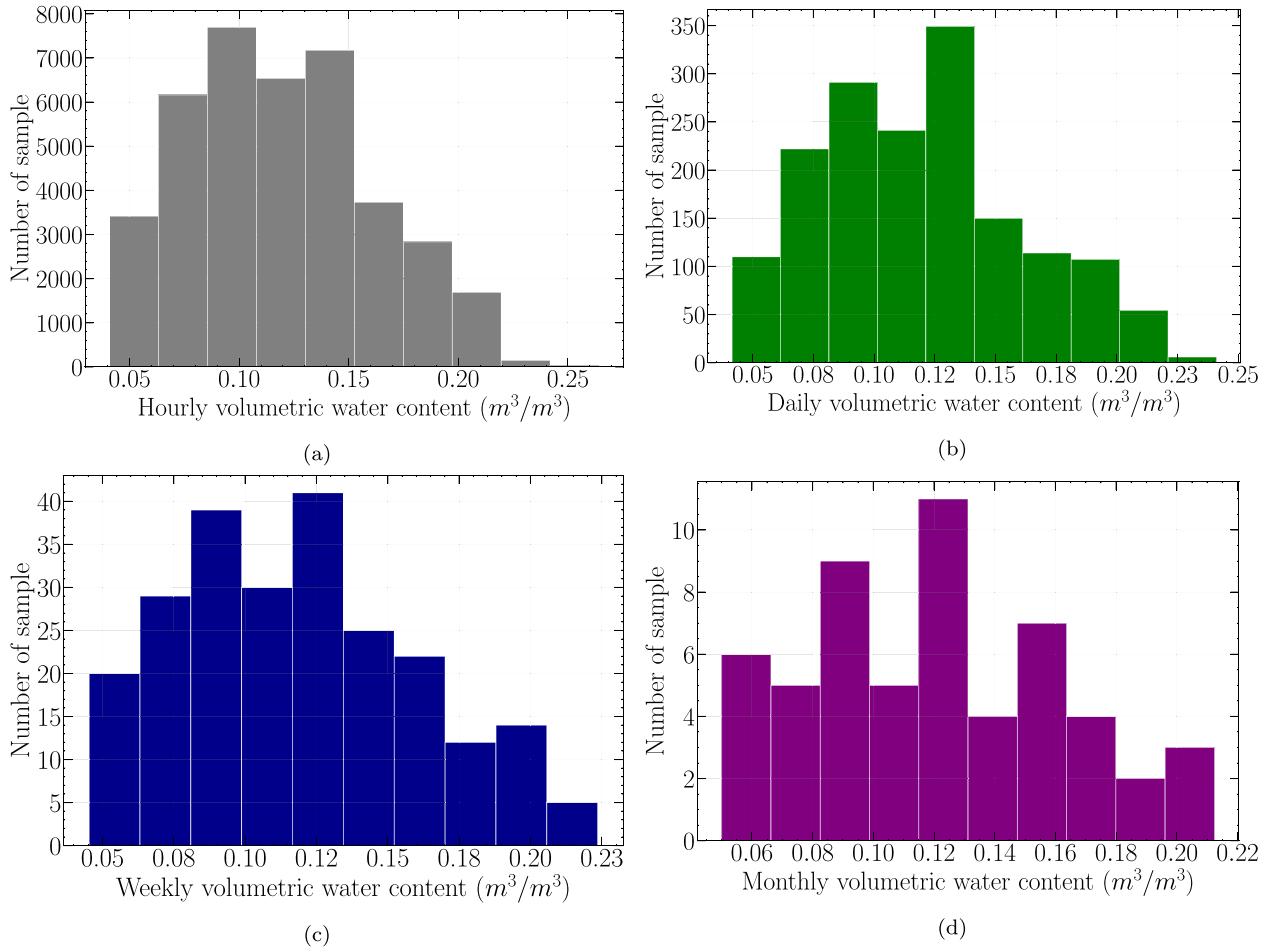

Fig. 4. Distribution of aggregated (a) hourly, (b) daily, (c) weekly, and (d) monthly VWC datasets. The bar width shows the ranges of VWC, and the bar height shows the quantity of that range in the selected datasets.

3. Methodology

3.1. LSTM model

Recurrent Neural Network (RNN) method is commonly used to model time series datasets (Lipton et al., 2015). However, due to gradient vanishing throughout successive back propagation rounds, RNN faces limitation in terms of learning long-term dependencies (Cho and Kim, 2022). By introducing cell interactions such as read, write, update, and forget into an RNN, one can alleviate the vanishing gradient problem (Hu et al., 2018). There are two well-known approaches to alleviate the RNN's vanishing gradient problem, namely Gated Recurrent Unit (GRU) and the LSTM architectures (Zia and Zahid, 2019; Dey and Salem, 2017; Golmohammadi et al., 2017). The former executes faster, but the latter is more accurate on a larger dataset as it is capable of learning long-term sequences. The LSTM architecture is made up of three layers: an input layer, hidden layers, and output layer (Zhao et al., 2016). The three gates of the memory cells are defined as forget gate (controls the information to be ignored from the previous state), input gate (controls the input from the previous state), and output gate (computes the output from the current memory cell) (Perera and Zimmermann, 2020). In Fig. 5, a schematic architecture of a single LSTM cell is shown, where x_t is the inputs, H_t is the next hidden state, H_{t-1} is the last hidden state, *tanh* is the hyperbolic tangent activation function, C_t is the next cell state, and σ is the logistic sigmoid function (Zhou et al., 2019). To maintain and update the state of memory cells, the LSTM model filters input through the gate structure (Qiu et al., 2020). Because of their gated design, LSTM cells are incredibly efficient and can learn extensive long-term correspondences (Pulver and Lyu, 2017).

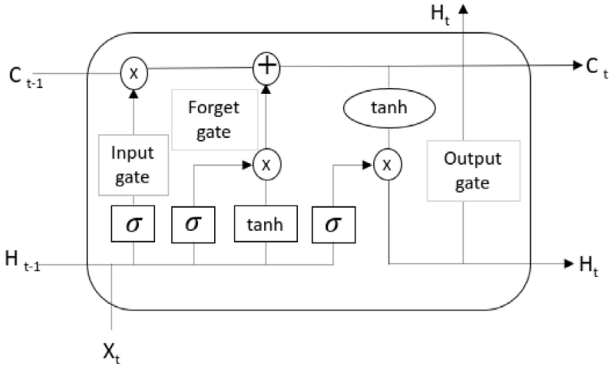

Fig. 5. A schematic diagram of a LSTM memory cell with hyperbolic tangent and logistic sigmoid activation functions (Zhou et al., 2019).

3.2. Multihead LSTM model

In this section, we construct a multihead LSTM model to predict the soil moisture ahead of time. Unlike typical single-head LSTM methods that learn a single hypothesis from training data, multihead LSTM leverage ensembling to learn a number of hypotheses and aggregate them for a certain prediction task. The architecture of the proposed multihead LSTM model is illustrated in Fig. 6. As shown, in this model, four LSTM networks named LSTM-1 through LSTM-4 are used that each digests a VWC time series data aggregated at different time intervals

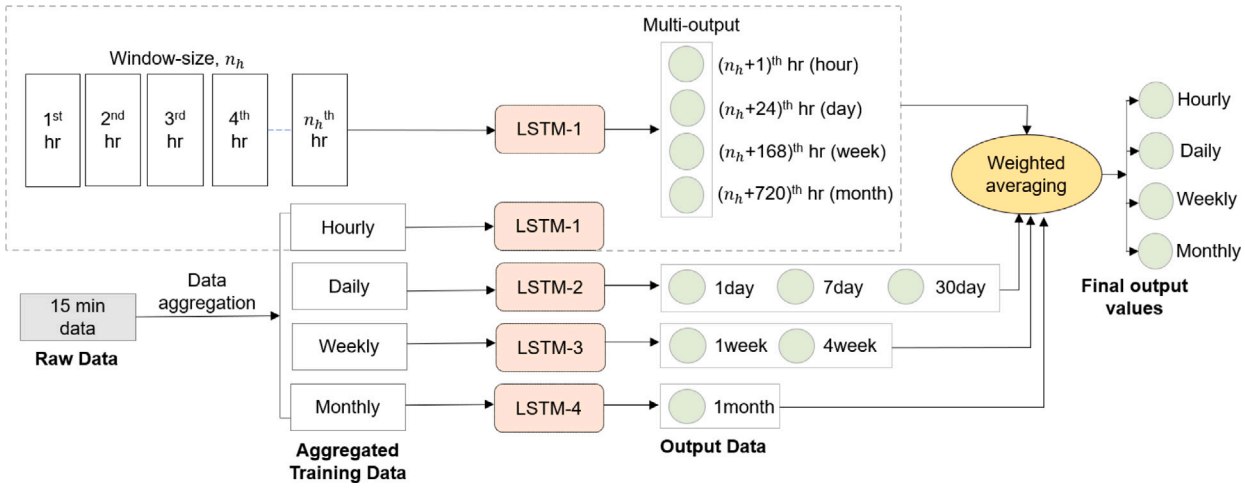

Fig. 6. A schematic architecture of the multihead LSTM model. For each individual LSTM model, multiple previous time steps, known as window-size, are used as inputs. Next, four outputs (hourly, daily, weekly, and monthly values) from LSTM-1, three outputs (daily, weekly, and monthly values) from LSTM-2, two outputs (weekly, and monthly values) from LSTM-3, and one output (monthly values) from LSTM-4 are obtained. The inputs and outputs are only shown for LSTM-1 with dotted box, and the same configuration is implemented for other LSTM networks. Once the predicted values by individual LSTM models are obtained, a weighted averaging approach is applied for obtaining the final prediction.

Table 1
Optimized hyperparameters for LSTM-1, LSTM-2, LSTM-3, and LSTM-4 models trained, validated, and tested on the training Green pit-2 and pit-3 datasets.

Model	Hyperparameter value
LSTM-1	activation = Rectified Linear (ReLU), neuron-input = 128, batch-size = 4096, learning-rate = 0.01, window-size = 7, optimizer = Adam, hidden layers = 10, epochs = 1800
LSTM-2	activation = Rectified Linear (ReLU), neuron-input = 64, batch-size = 1000, learning-rate = 0.05, window-size = 7, optimizer = Nadam, hidden layers = 25, epochs = 1800
LSTM-3	activation = Sigmoid, neuron-input = 180, batch-size=500, learning-rate = 0.001, window-size = 8, optimizer = Adam, hidden layers = 15, epoch = 4900
LSTM-4	activation = Sigmoid, neuron-input = 178, batch-size=10, learning-rate = 0.005, window-size = 4, optimizer = RMSprop, hidden layers = 12, epoch = 3500

formed in Section 2.2. The outputs of these networks are then combined using a weighted averaging technique to generate the final predicted hourly, daily, weekly, and monthly outputs.

According to Fig. 6, the hourly aggregated data is fed into LSTM-1 to forecast the next hour $(n_h + 1)$th, next day $(n_h + 24)$th, next week (n_h+168)th, and next month (n_h+720)th values, where n_h is the number of hourly input points known as the hourly window-size that needs to be tuned. LSTM-2 receives daily aggregated data as inputs to forecast the next day (n_d+1)th, next week (n_d+7)th, and next month (n_d+30)th values, where n_d is the number of daily input points known as the daily window-size that also needs to be tuned. LSTM-3 digests weekly aggregated data to forecast the next week $(n_w + 1)$th, and next month (n_w+4)th values, where n_w is the number of weekly input points known as the weekly window-size that is also a tuning parameter. Finally, the monthly aggregated data is fed into LSTM-4 to forecast the next month, $(n_m + 1)$th value, where n_m is the number of monthly input points known as the monthly window-size that also needs to be tuned. Once the forecast values by individual LSTM models are obtained, a weighted averaging approach (discussed in Section 3.3.2), is applied to combine the predictions. The multihead LSTM architecture leverages the fact that each LSTM model excels at forecasting the next time step with respect to the aggregated data. This increases the capability of ensemble model to learn patterns hidden within long-term sequences as well as enhances the model's confidence to forecast longer time into the future. The window-sizes discussed above are important parameters in the proposed multihead LSTM and must be tuned carefully to yield highest accuracy. The training data structure and the hyperparameter tuning (Anguita et al., 2012; Jung and Hu, 2015) for multihead LSTM is discussed in the following section.

3.3. Training data structure and hyperparameter tuning

The learning procedure and thus the training dataset generation in the multihead LSTM uses a window sliding process, where the data of previous known time step(s) (i.e., n_h, n_d, n_w, n_m) is used to extract pattern and forecast the data of next time steps(s). Window-size determines how many prior time steps are used to forecast the soil moisture value in the future. For example, if we assume $n_h = 7$ for LSTM-1, the training and testing data look like the sequences shown in Fig. 7(a). Here, one row of training/testing data is comprised of seven previous time steps as inputs and four subsequent time steps as outputs. Then, we iterate this process over the entire dataset by sliding one time steps to the right to create the next rows of training/testing dataset (Zeyer et al., 2016; Asci and Guvensan, 2019). The window-sizes for each LSTM network must be tuned through hyperparameter tuning process. To achieve highest accuracy and prevent overfitting, in addition to these window-sizes, other LSTM's important hyperparameters (e.g., activation function, neuron-input, batch-size, learning rate, optimizer, hidden units, epochs, etc., as reported in Table 1), must be tuned.

Overfitting can occur if the model is trained only on the training dataset (i.e., a model scores very well on the training set but performs poorly on the test set or blind dataset). A subset of data from the training set, referred to as the validation set, is usually kept aside for hyperparameter tuning. Hyperparameter tuning is based on experimental outcomes rather than theory. The simplest way to figure out what parameters are ideal is to try several various combinations and evaluate how each model performs. We employed the K-Fold cross-validation (K-Fold CV) technique to undertake hyperparameter tuning (Jung, 2018;

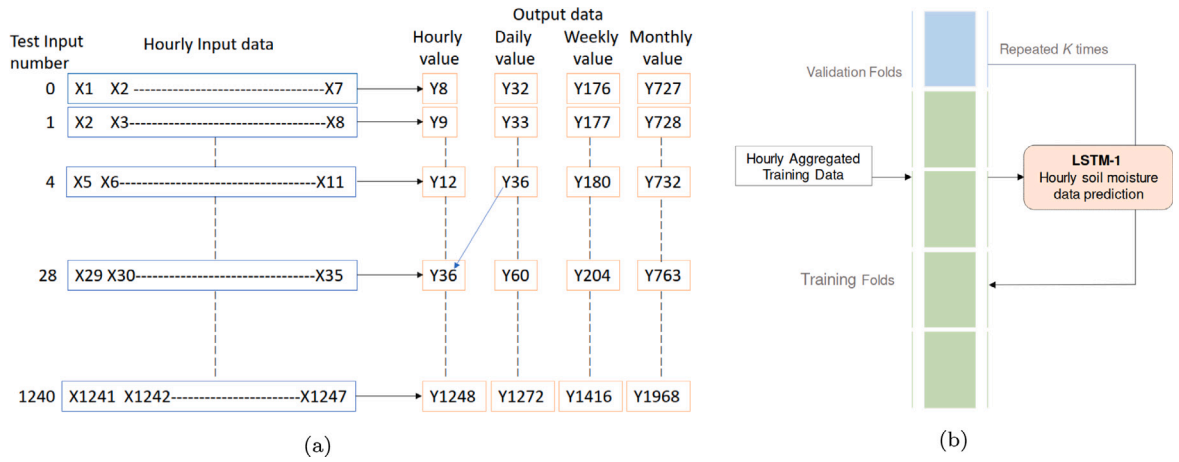

Fig. 7. Training data generation for LSTM-1; Panel (a) shows the generation of input data assuming the window-size, n_h, is 7. One row of the training data is comprised of previous seven time steps as inputs, and four subsequent time steps as outputs; Panel (b) shows the combination of K-Fold approach with the RandomSearchCV algorithm for hyperparameter tuning.

Rodriguez et al., 2009; Xiong et al., 2020). The training set is divided into K number of subsets, or folds, in the K-fold CV approach as schematically shown in Fig. 7(b). The LSTM models are then trained repeatedly K times, with training on $K-1$ of the folds and evaluation on the Kth fold (the validation set) each time. We average the performance on each of the folds at the end of training to reach at final validation metrics for the model. The trained models, each with its own set of hyperparameters, are compared against one another, and the one with the best accuracy metrics is chosen. We adopted 10-Fold CV in this study, which means that to analyze a new set of hyperparameters, we divide our training dataset into 10 folds and train and evaluate each model 10 times with selected hyperparameters. To optimize the computational cost of the hyperparameter tuning procedure, the K-Fold approach is combined with the RandomSearchCV algorithm (Memon et al., 2019). With a set number of rounds of random searches, this coupled strategy tries random possibilities within a specific range of values for each hyperparameter.

3.3.1. Statistical measures for model evaluation

The accuracy of the individual LSTM models as well as the multi-head LSTM model is evaluated using five common statistical measures, R-squared, MSE, RMSE, MAE, and MAPE. The R-squared coefficient defined as,

$$R\text{−squared} = 1 - \frac{\sum_{t=1}^{n}(y_t - y_i)^2}{\sum_{t=1}^{n}(y_t - \bar{y})^2}, \tag{1}$$

shows the fitness performance; hence, greater R-squared values with a maximum value of 1 are desirable. Where, y_i is the predicted value, y_t is the ground truth, and $\bar{y}$ represents the mean of the predicted values. The average squared distance between ground truth and predicted values is known as MSE or mean squared error (Chen et al., 2017) defined as,

$$MSE = \frac{1}{n}\sum_{t=1}^{n}(y_t - y_i)^2. \tag{2}$$

A higher MSE shows that the data points are widely spread around the central moment (mean), whereas a lower MSE indicates the reverse (Thompson, 1990), i.e., indicates a higher accuracy for the model's predictions. The root-mean-square error, or RMSE, defined as,

$$RMSE = \sqrt{\frac{1}{n}\sum_{t=1}^{n}(y_t - y_i)^2}, \tag{3}$$

is a measurement of the variations between ground truth and projected values by a model (Mayer and Butler, 1993). The Mean Absolute Error, MAE, defined as,

$$MAE = \frac{1}{n}\sum_{t=1}^{n}|(y_t - y_i)|, \tag{4}$$

assesses the average magnitude of mistakes in a set of forecasts without taking into account their direction (Liu et al., 2019). Lastly, the Mean Absolute Percentage Error, MAPE, is considered. The predicted values are closer to the ground truth when the MAPE value is lower. The mathematical expression for MAPE is defined as (Coleman and Swanson, 2007; Zeraatpisheh et al., 2019; Faroughi et al., 2022),

$$MAPE = \frac{100\%}{n}\sum_{t=1}^{n}\left|\frac{(y_t - y_i)}{y_t}\right|, \tag{5}$$

which is a type of scale-independent percentage error that can be also used to compare series on different scales.

3.3.2. Weighted averaging method

Weighting functions are used in engineering to indicate the relative influence of various parameters (Duan et al., 2007). Weighted averaging is a method that allows numerous models to contribute to a prediction in proportion to their goodness or anticipated performance (Choi and Lee, 2018). Results show that weighted averaging method improves over the individual model (Londhe and Atulkar, 2021). Here, we design a weighted averaging method to generate final predictions from all four LSTM models' outputs, where weights are assigned according to the goodness of the models calculated based on MAPE. The reason behind using MAPE is its scale-variance and easy interpretation (Zinszer et al., 2012). We employed the weighted averaging method described above for calculating all the daily, weekly, and monthly predictions as shown in Fig. 8. There was no need to apply weighted averaging to the hourly values due to having only LSTM-1 contributing to that.

In Fig. 8, W_{1D} and W_{2D} refer to the weights for daily outputs from LSTM-1 (Y_{1D}) and LSTM-2 (Y_{2D}), W_{1W}, W_{2W} and W_{3W} refer to the weights for weekly outputs from LSTM-1 (Y_{1W}), LSTM-2 (Y_{2W}) and LSTM-3 (Y_{3W}), and W_{1M}, W_{2M}, W_{3M} and W_{4M} refer to the weights for monthly outputs from LSTM-1 (Y_{1M}), LSTM-2 (Y_{2M}), LSTM-3 (Y_{3M}), and LSTM-4 (Y_{4M}). Also, Y_{1H} represents the hourly outputs from LSTM-1. We then represent the multihead LSTM's final hourly, daily, weekly, and monthly predicted value as Y_{1H}, Y_D, Y_W, and Y_M. We calculate the daily weight, W_{iD}, using,

$$W_{iD} = \frac{100 - MAPE_i}{(100 - MAPE_1) + (100 - MAPE_2)}, \tag{6}$$

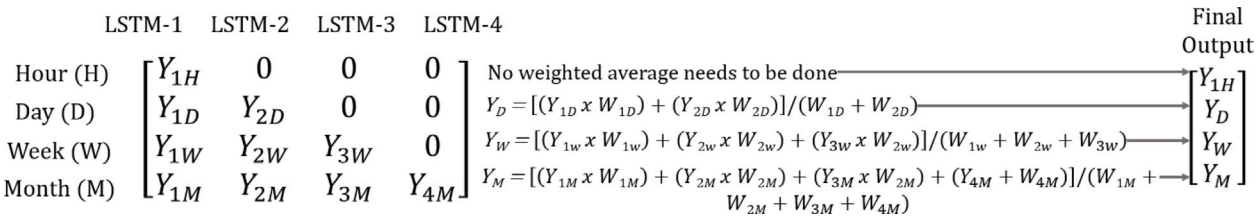

Fig. 8. Mathematical expression to calculate weighted averaging and obtain the multihead LSTM's final hourly, daily, weekly, and monthly predicted value. The weighted averaging method is performed for daily predicted values from LSTM-1 and LSTM-2, weekly predicted values from LSTM-1, LSTM-2, and LSTM-3, and monthly predicted values from LSTM-1, LSTM-2, LSTM-3, and LSTM-4.

where $i = 1, 2$ refers to the number of the LSTM model, and $MAPE_1$ and $MAPE_2$ refer to the value of MAPE, in percentage, obtained for LSTM-1 and LSTM-2. The weekly weight, W_{iW}, is calculated as,

$$W_{iW} = \frac{100 - MAPE_i}{(100 - MAPE_1) + (100 - MAPE_2) + (100 - MAPE_3)}, \quad (7)$$

where $i = 1, 2, 3$ refers to the number of LSTM model, and $MAPE_1$, $MAPE_2$, and $MAPE_3$ refer to the value of MAPE, in percentage, obtained for LSTM-1, LSTM-2, and LSTM-3. Lastly, the monthly weight, W_{iM}, is obtained as,

$$W_{iM} = \frac{100 - MAPE_i}{(100 - MAPE_1) + (100 - MAPE_2) + (100 - MAPE_3) + (100 - MAPE_4)}, \quad (8)$$

where $i = 1, 2, 3, 4$ refer to the number of LSTM model, and $MAPE_1$, $MAPE_2$, $MAPE_3$, and $MAPE_4$ refer to the value of MAPE, in percentage, obtained for LSTM-1, LSTM-2, LSTM-3, LSTM-4. We then compare the predicted values (Y_{1H}, Y_D, Y_W, and Y_M) by the multihead LSTM model with the ground truth.

4. Results and discussion

4.1. Individual model performance evaluation

In this section, we thoroughly evaluate all the LSTM models with their best architecture obtained from training phase using a blind dataset. As discussed in Section 2.2, the Green pit-1 was used to blind test the prediction performance of the individual LSTM models as well as the multihead LSTM model.

4.1.1. LSTM-1 model

The purpose of the LSTM-1 model is to digest hourly data and predict four outputs at different time scales such as the next hour, day, week, and month values. We employed a 10-fold CV technique in combination with the RandomSearchCV algorithm for hyperparameter tuning for LSTM-1 as described in Section 3.3. Table 1 reports the best set of hyperparameters (i.e., best architecture) obtained for LSTM-1 model. It is worth noting that only tuned hyperparameters are reported. We adopted the statistical measures for LSTM-1 given in Eqs. (1) to (4) to investigate the performance and accuracy of the LSTM-1 model. Hyperparameter tuning resulted in using 10 hidden layers along with other best parameters as reported in Table 1. We applied L1 regularization to avoid overfitting for the LSTM-1 model (Merity et al., 2017). The hyperparameter tuning framework suggested $n_h = 7$ as the best window-size as evidenced by R-squared values reported in Table 2. We presented Table 2 for LSTM-1 model as a representative, and applied the same process for other LSTM models. After training and validating on the Green pit-2 and pit-3 datasets, LSTM-1 was tested against blind dataset (i.e., Green pit-1). Note that LSTM-1 has four outputs each with their own statistical measures when tested on the entire test dataset (see Fig. 9), and Table 3 reports the averaged values for the statistical measures.

Fig. 9 shows the performance of the tuned LSTM-1 model that predicted the next hour values very similar to the ground truth and reasonably captured the trend as shown in Fig. 9(a). It happens owing to the well-documented capability of LSTM cells to predict the next time step. Though daily predicted values followed the same trend, the LSTM-1 prediction accuracy dropped slightly as shown in Fig. 9(b). The performance of LSTM-1 for weekly prediction reduced more than daily prediction, and the trend was not also captured well as shown in Fig. 9(c). There was even a bigger discrepancy between the monthly ground truth and predicted values and the trend as depicted in Fig. 9(d). The value of R-squared for hourly prediction is 0.9956, whereas the value of R-squared for monthly prediction is 0.7764 due to noticeable time-lag phenomena and increasing gaps between the ground truth and predictions. As expected, with increasing prediction horizon into the future, the accuracy of the LSTM-1 model tends to decrease. This proves that single head LSTM models (i.e., LSTM-1) do not accurately predict the long-term dependencies . Therefore, LSTM-1 does not have the ability to predict the daily, weekly, and monthly soil moisture values with a high accuracy. As a consequence, we proceed to our next model LSTM-2, using the daily aggregated data.

Table 2
Window-size tuning for LSTM-1. The R-squared values were recorded for hourly, daily, weekly, and monthly predictions. Tuning of LSTM-1 was started with the window-size of one, where a poor performance was observed and after that larger window-size was tried to obtain a maximum R-squared value.

Window size	1 h	1 day	1 week	1 month
5	0.9628	0.9781	0.6343	0.5200
7	**0.9956**	**0.9788**	**0.9611**	**0.7764**
8	0.8466	0.8656	0.7919	0.5377
10	0.9670	0.9726	0.7364	0.6544
12	0.7340	0.8477	0.8339	0.5646

Table 3
Comparison of the averaged statistical measures for the performance of the tuned LSTM models tested on the blind dataset (i.e., Green pit-1).

	LSTM-1	LSTM-2	LSTM-3	LSTM-4
R^2	0.9209	0.9401	0.8526	0.8257
RMSE	0.0217	0.0201	0.0261	0.0264
MAE	0.0165	0.0153	0.0180	0.0166
MSE	0.0005	0.0004	0.0006	0.0006
MAPE	0.1801	0.1799	0.1946	0.2230

4.1.2. LSTM-2 model

The purpose of LSTM-2 model is to digest daily aggregated data and predict three outputs at different time scales such as the next day, week, and month values. We applied a 10-fold CV technique in combination with the RandomSearchCV algorithm for LSTM-2 hyperparameter tuning as described in Section 3.3. Hyperparameter tuning resulted in using 25 hidden layers and $n_d = 7$ together with the other best hyperparameters as reported in Table 1 for LSTM-2. We documented the value of average statistical measures for the LSTM-2 model tested against the blind dataset in Table 3. We again leveraged L1 regularization to minimize the overfitting of the LSTM-2 model. Fig. 10 shows the performance of LSTM-2 model, where we observe some improvement compared to LSTM-1. LSTM-2 predicted the daily values very well and

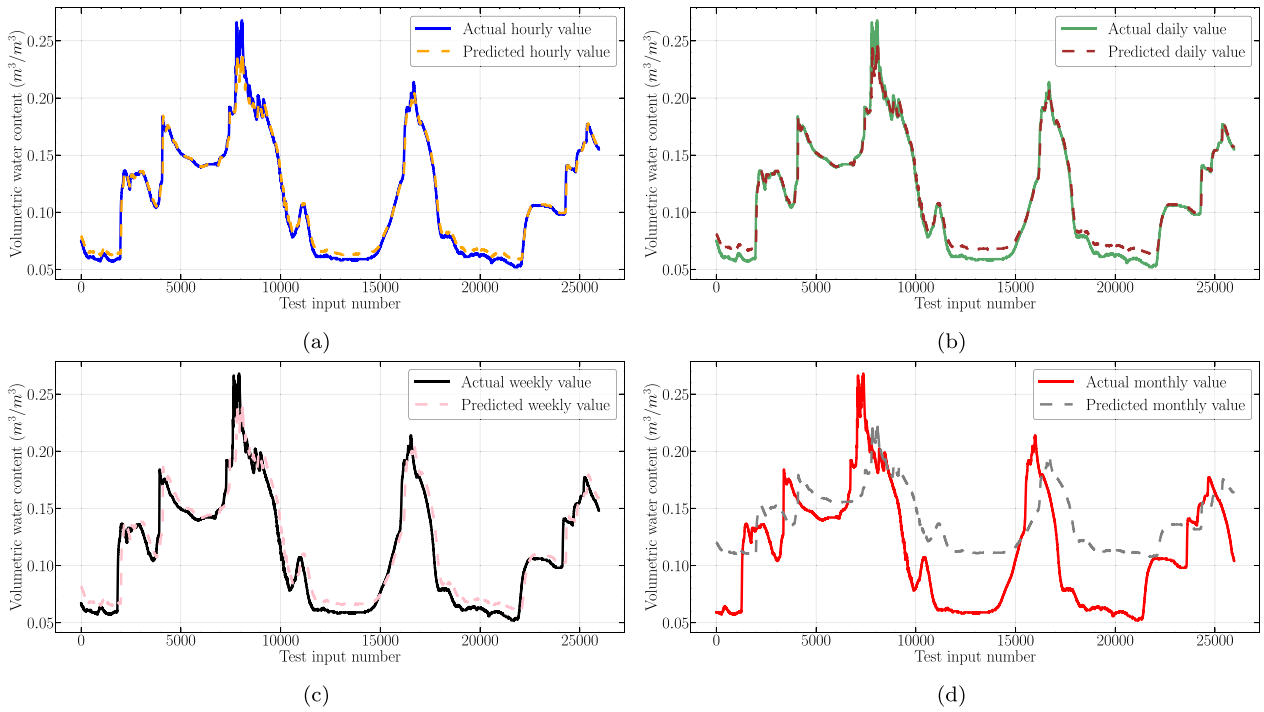

Fig. 9. Performance of the LSTM-1 model with hourly aggregated data as input values and (a) hourly, (b) daily, (c) weekly, and (d) monthly predicted values as outputs.

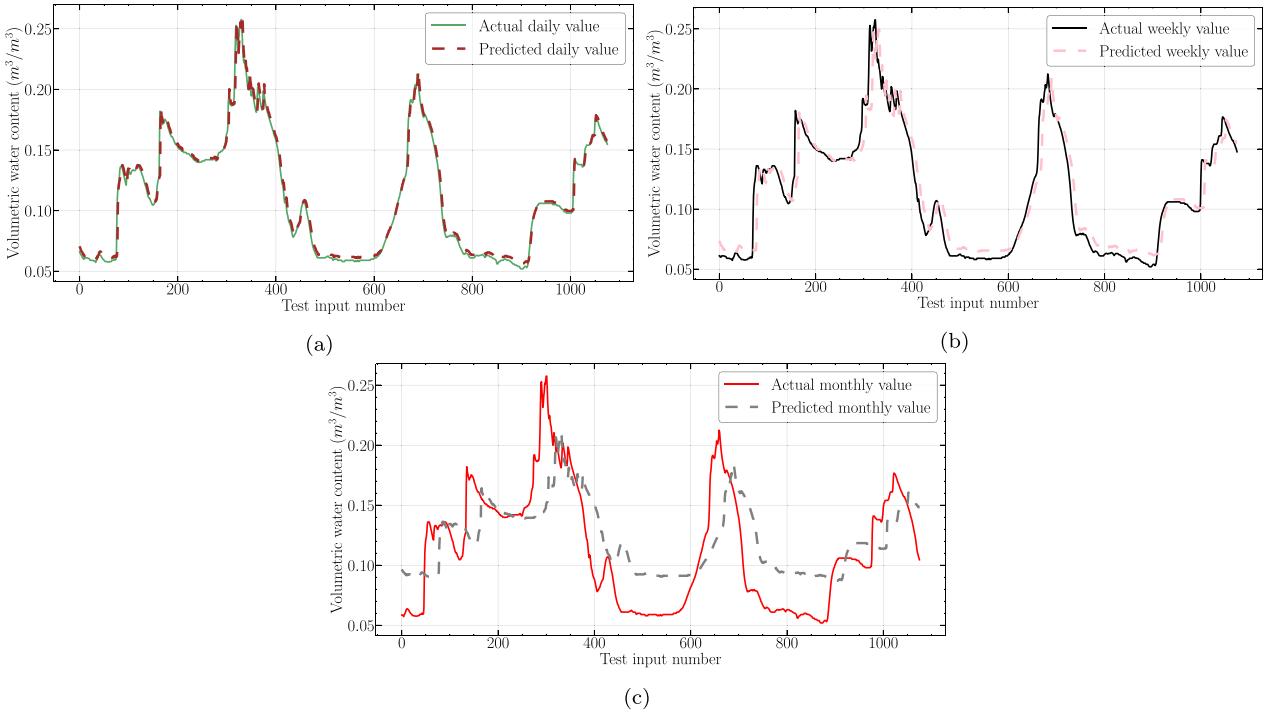

Fig. 10. Performance of the LSTM-2 model with daily aggregated data as input values and (a) daily, (b) weekly, and (c) monthly predicted values as outputs.

the trend was also captured accurately (i.e., compared to LSTM-1, the R-squared value increased from 0.9788 to 0.9989). This is because of the LSTM's dynamic nature, which allows it to create predictions based on model inputs preserved for a previous time period (Adeyemi et al., 2018). Still, there is some discrepancy between the ground truth and the predicted data for weekly values as shown in Fig. 10(b). We observed very less improvement in monthly predictions from LSTM-1 to LSTM-2 as shown in Fig. 10(c). The shifts observed in Fig. 10(b) and Fig. 10(c) provide evidence that the LSTM-2 model lacks the ability to accurately predict monthly and weekly values. The shift is attributed to the accumulation of uncertainty. It refers to the increase in the level of uncertainty in the predictions as the prediction horizon increases (Gao et al., 2022b). The R-squared value improved by 1.3% for monthly values from LSTM-1 to LSTM-2. Therefore, we proceed to our next model, LSTM-3, using the weekly aggregated data to obtain better predictions for weekly and monthly values.

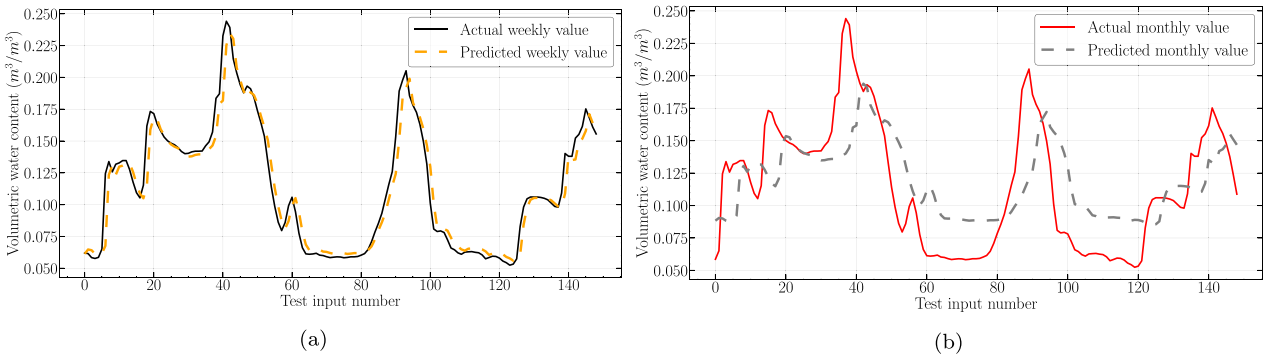

Fig. 11. Performance of the LSTM-3 model with weekly aggregated data as input values and (a) weekly and (b) monthly predicted values as outputs.

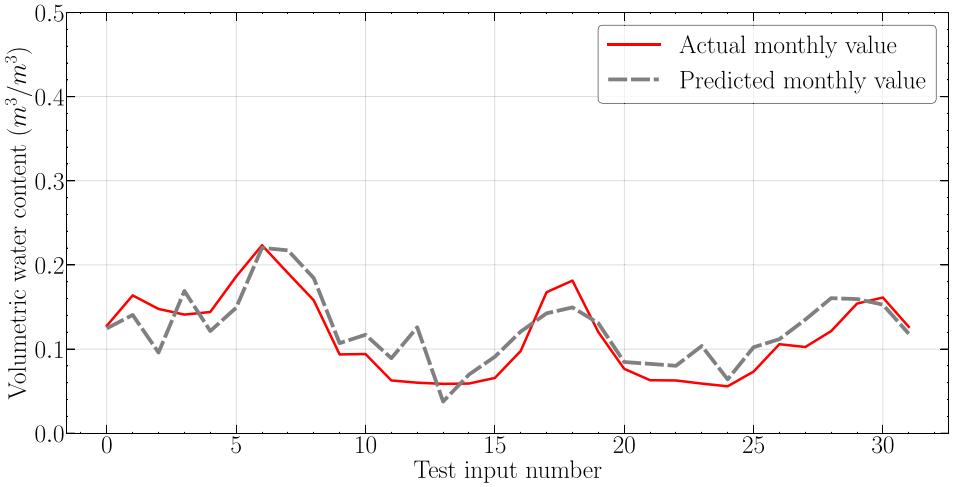

Fig. 12. Performance of the LSTM-4 model with monthly aggregated data as input and monthly predicted values as output.

4.1.3. LSTM-3 model

The purpose of the LSTM-3 model is to digest weekly data and predict two outputs such as the next week, and month values. We again employed the 10-fold CV technique in combination with the RandomSearchCV algorithm to conduct hyperparameter tuning for LSTM-3 as described in Section 3.3. Hyperparameter tuning for LSTM-3 resulted in using 15 hidden layers and $n_w = 8$ together with the other best hyperparameter for this model as reported in Table 1. Fig. 11 shows the performance of the LSTM-3 model, and Table 3 reports the average statistical measures for LSTM-3 tested against the blind dataset. We implemented dropout regularization to scale back overfitting by stochastically setting certain network connections to zero (Fang et al., 2018; Srivastava et al., 2014). LSTM-3 predicted the weekly values with higher accuracy compared to LSTM-1 and LSTM 2 (the R-squared value increased by 7.43% compared to LSTM-2), and the trend was also captured more accurately as shown in Fig. 11(a). The LSTM-3 model is thus more suitable and reliable for weekly prediction than LSTM-1 and LSTM-2. The monthly predictions by LSTM-3 were also improved compared to LSTM-1 and LSTM-2 as shown in Fig. 11(b). The gap between ground truth and monthly predicted value decreased and R-squared increased compared to LSTM-1 (by 8.18%) and LSTM-2 (by 5.69%). However, the accuracy of monthly predictions is still not within acceptable ranges for different practical applications. In consequence, we proceed to our next model, LSTM-4, using the monthly aggregated data to obtain a better prediction for monthly values.

4.1.4. LSTM-4 model

We developed LSTM-4 to digest monthly aggregated data and provide monthly prediction with a higher accuracy. We utilized a 6-fold CV approach in combination with the RandomSearchCV algorithm to tune the hyperparameters for LSTM-4 as described in Section 3.3. Hyperparameter tuning resulted in using 12 hidden layers and $n_m = 4$ along with other best parameters as reported in Table 1. We reported the average statistical measures for LSTM-4 in Table 3 tested against the blind dataset. We again adopted dropout regularization to minimize overfitting for the LSTM-4 model. Fig. 12 shows the performance of the LSTM-4 model. According to Fig. 12, the performance of the LSTM-4 model provides best result for monthly prediction. This indicates the improvement in the performance of monthly prediction based on statistical measures. Note that the number of data points in the monthly aggregated data is very limited and that is the reason behind the poor performance of the LSTM-4. Upon feeding more data, the accuracy of this model can be extremely improved, considering that LSTM models are extremely good in predicting the next time step (here for LSTM-4 the time step is a month), e.g., see hourly predictions by LSTM-1, daily prediction by LSTM-2, and weekly prediction by LSTM-3. As our next step, we combine all the LSTM models using weighted averaging to achieve predicted values with higher accuracy. We referred to this model as multihead LSTM model as described in Section 3.2.

We also analyzed the predicted values from the LSTM models and the ground truth using linear regression to further explain the models' forecasting performance. We determined the degree of correlation between the actual and predicted values for each LSTM model. Fig. 13 represents the correlation between the predicted and actual values of the testing data for LSTM-1, LSTM-2, LSTM-3, and LSTM-4. The more concentrated data points and the higher R-squared value indicate the more reliability of the model (Belagoune et al., 2021; Ghosh et al., 2019; Kaselimi et al., 2019). We obtained the best fit for LSTM-1 and

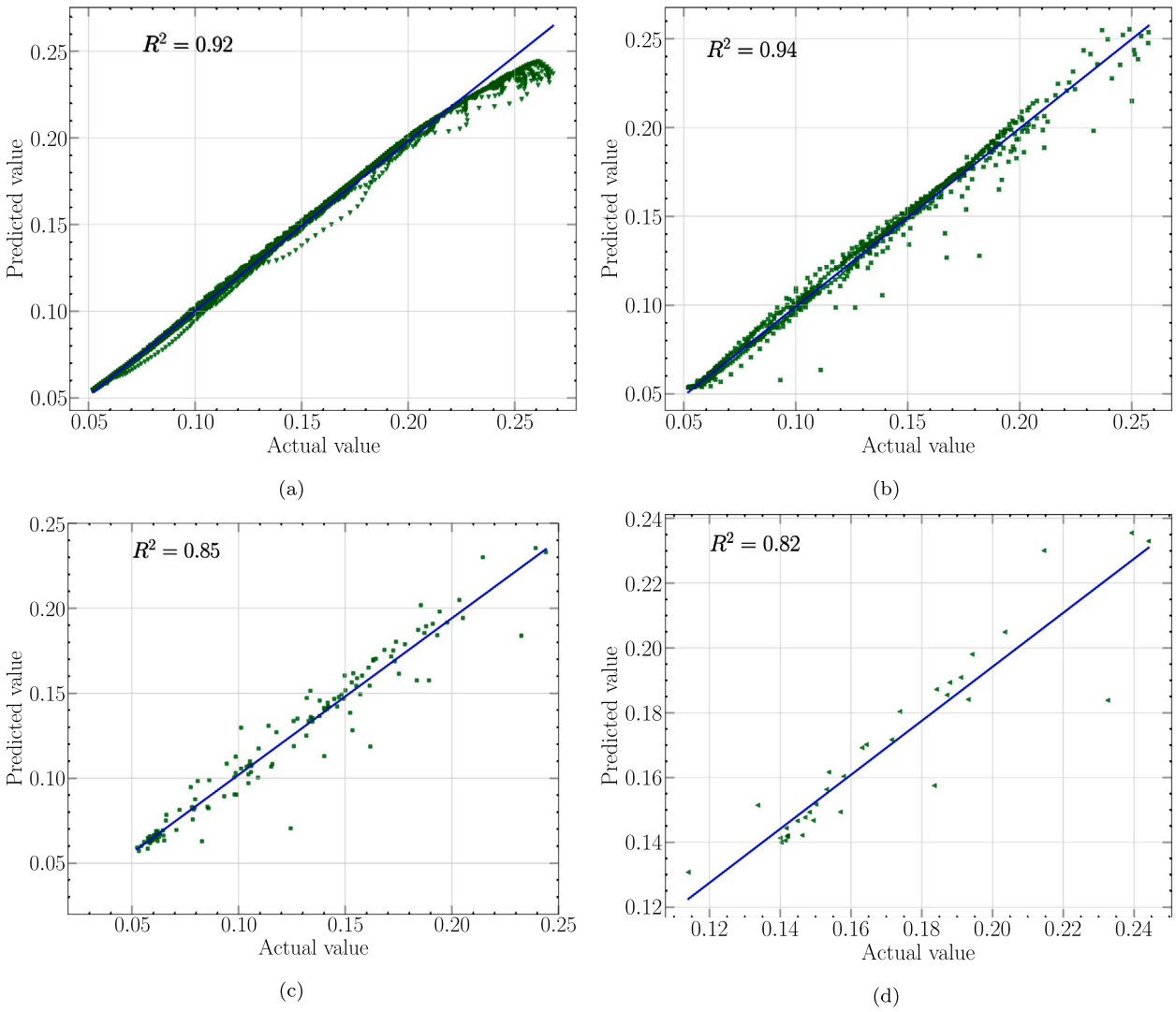

Fig. 13. Actual vs. predicted values plotted for (a) LSTM-1, (b) LSTM-2, (c) LSTM-3, and (d) LSTM-4 with associated R-squared values.

LSTM-2 with R-squared values of 0.92 and 0.94, respectively, as shown in Figs. 13(a) and 13(b). We observed a highly scattered data points with lowest R-squared for LSTM-4. We also observed a visual deviation of the data points from the regression line for LSTM-3 and LSTM-4. This deviation, i.e., the decline in the accuracy, is attributed to the lack of sufficient training data in the higher VWC range ($> 0.25\ m^3/m^3$). In general, LSTM-1 and LSTM-2 provide better performance than LSTM-3 and LSTM-4. LSTM-3 and LSTM-4 do not perform well because of inadequate amount of training data, but they can add significant value to the final predictions when assembled with other LSTM models, see Section 4.2.

4.2. Multihead LSTM performance evaluation

The multihead LSTM method attempts to build a number of hypotheses and aggregate them for the application of soil moisture prediction. We deployed multihead LSTM model to boost the prediction capabilities to at least one-month in advance of time with a greater accuracy. Fig. 14 shows the final outputs of the multihead LSTM model for one sample data sequence from the testing dataset. In Fig. 14(a), we first plotted the final outputs for this data sequence obtained from the individual LSTM models and then overlaid together. We clearly see that only the next time step is accurately predicted and the accuracy declines as longer time in future is inferred. If we select any random sample from the data, we will achieve similar result from individual LSTM models. In Fig. 14(b), we plotted the final outputs predicted using the multihead LSTM model. It digests the outputs of individual LSTM models and applies a weighted averaging method. Fig. 14(b) reports the mean value and standard deviation for the predicted values. The value of R-squared, RMSE, MAE, MSE, and MAPE are obtained as 95.04%, 0.2007, 0.0156, 0.00049, and 0.1794, respectively, for the multihead LSTM model. Based on the obtained statistical measures and those reported for individual LSTM models in Table 3, it can be concluded that the proposed multihead LSTM model performs better than all individual LSTM models to predict VWC up to one-month in advance.

5. Conclusion

In this work, we investigated the possibility to forecast soil moisture up to one-month ahead of time. We constructed a multihead LSTM model comprising four hypotheses and ensemble them for final prediction. A 15-minute intervals raw datasets for soil moisture at south slopes of the San Antonio Mountain close to the Sulfur Spring were aggregated to form hourly, daily, weekly, and monthly datasets. Four individual LSTM models were then trained and validated on aggregated Green pit-2 and Green pit-3 datasets, and best architecture (i.e., tuned hyperparameters) were obtained by employing the

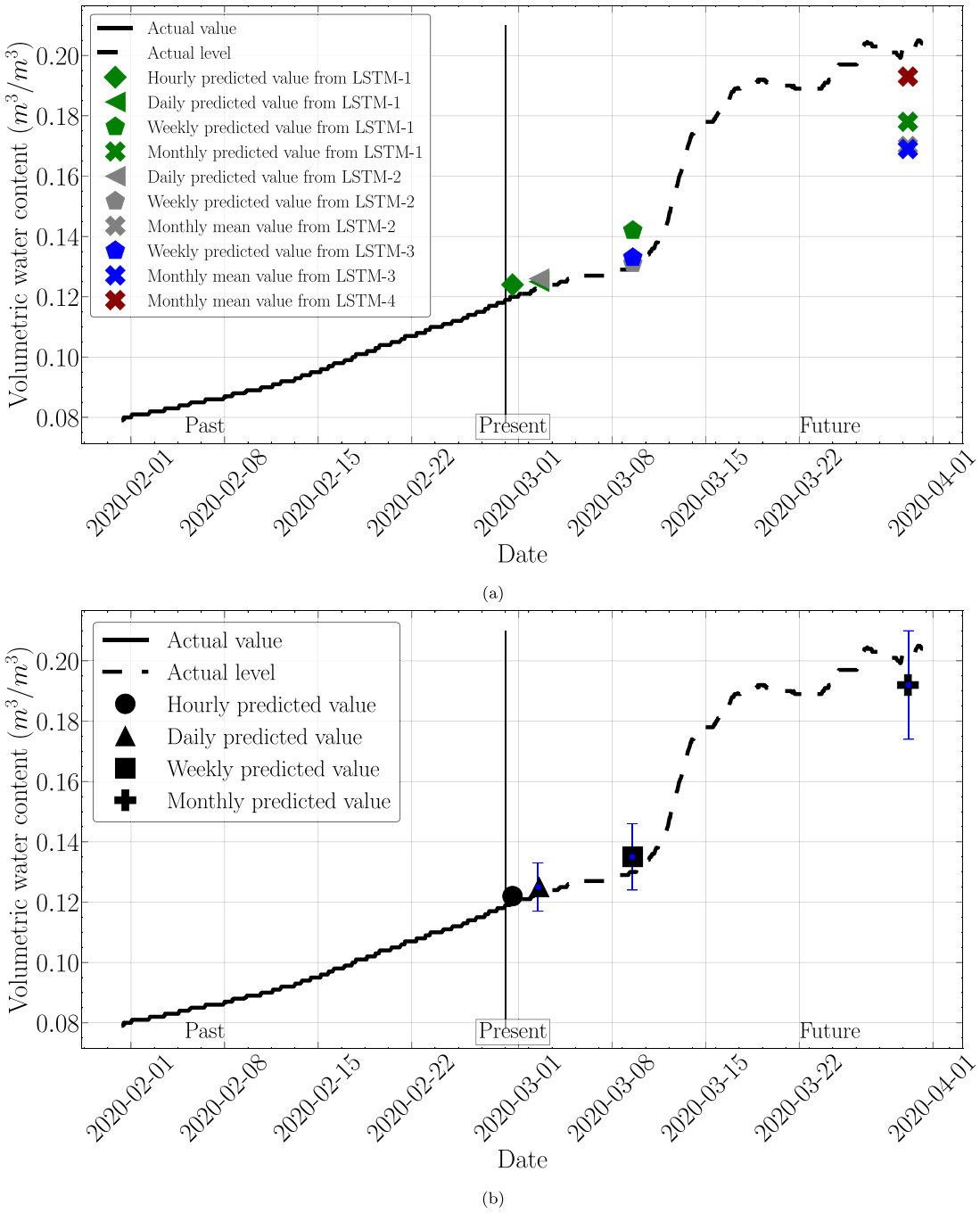

Fig. 14. A comparison between the individual LSTM models and multihead LSTM model to predict VWC up to one-month in advance: Panel (a) shows the performance of individual LSTM models. Panel (b) shows the performance of the multihead LSTM model for one sample data sequence from the blind test dataset.

cross-validation method in combination with the RandomSearchCV algorithm. The models were then tested blindly on Green pit-1 datasets. LSTM-1 and LSTM-2 models provided good accuracy for the hourly and daily predictions, but failed to predict weekly and monthly data accurately. LSTM-3 and LSTM-4 predicted the weekly and monthly values better compared to LSTM-1 and LSTM-2. Finally, the multihead LSTM model applied a weighted averaging technique to the outputs of individual LSTM models to boost the prediction accuracy. We observed that the multihead LSTM model performed better than all individual LSTM models achieving a R-squared value of 95.04% for predicting the soil moisture in the next hour, next day, next week, and next month. It is noteworthy that the individual and multihead LSTM models presented in this study only used the soil moisture data from the past to predict the future values of soil moisture. Therefore, the accuracy of the proposed model can be further increased if more physical attributes (e.g., temperature, humidity, pH, electrical conductivity, etc.) are also provided alongside the soil moisture as inputs; this can deemed as a future extension of this work.

Declaration of competing interest

The authors declare that they have no known competing financial interests or personal relationships that could have appeared to influence the work reported in this paper.

Data availability

Data will be made available on request.

Acknowledgments

S.A.F. would like to acknowledge supports by United States Department of Agriculture (USDA) (award no. 2022-77040-37653), and Texas State University Multidisciplinary Internal Research Grant (MIRG) (award no. 9000003028).

References

Abioye, Emmanuel Abiodun, Abidin, Mohammad Shukri Zainal, Mahmud, Mohd Saiful Azimi, Buyamin, Salinda, AbdRahman, Muhammad Khairie Idham, Otuoze, Abdulrahaman Okino, Ramli, Muhammad Shahrul Azwan, Ijike, Ona Denis, 2021. IoT-based monitoring and data-driven modelling of drip irrigation system for mustard leaf cultivation experiment. Inform. Process. Agric. 8 (2), 270–283.

Adab, Hamed, Morbidelli, Renato, Saltalippi, Carla, Moradian, Mahmoud, Ghalhari, Gholam Abbas Fallah, 2020. Machine learning to estimate surface soil moisture from remote sensing data. Water 12 (11), 3223.

Adeyemi, Olutobi, Grove, Ivan, Peets, Sven, Domun, Yuvraj, Norton, Tomas, 2018. Dynamic neural network modelling of soil moisture content for predictive irrigation scheduling. Sensors 18 (10), 3408.

Ahmed, AA Masrur, Deo, Ravinesh C, Ghahramani, Afshin, Raj, Nawin, Feng, Qi, Yin, Zhenliang, Yang, Linshan, 2021a. LSTM integrated with boruta-random forest optimiser for soil moisture estimation under RCP4. 5 and RCP8. 5 global warming scenarios. Stochastic Environ. Res. Risk Assess. 1–31.

Ahmed, AA, Deo, Ravinesh C, Raj, Nawin, Ghahramani, Afshin, Feng, Qi, Yin, Zhenliang, Yang, Linshan, 2021b. Deep learning forecasts of soil moisture: Convolutional neural network and gated recurrent unit models coupled with satellite-derived MODIS, observations and synoptic-scale climate index data. Remote Sens. 13 (4), 554a.

Anguita, Davide, Ghelardoni, Luca, Ghio, Alessandro, Oneto, Luca, Ridella, Sandro, 2012. The 'K'in K-fold cross validation. In: 20th European Symposium on Artificial Neural Networks, Computational Intelligence and Machine Learning. ESANN, i6doc. com publ, pp. 441–446.

Asci, Guven, Guvensan, M. Amac, 2019. A novel input set for lstm-based transport mode detection. In: 2019 IEEE International Conference on Pervasive Computing and Communications Workshops (PerCom Workshops). IEEE, pp. 107–112.

Belagoune, Soufiane, Bali, Noureddine, Bakdi, Azzeddine, Baadji, Bousaadia, Atif, Karim, 2021. Deep learning through LSTM classification and regression for transmission line fault detection, diagnosis and location in large-scale multi-machine power systems. Measurement 177, 109330.

Chen, LiLei, Chen, Jing, Wang, Chao, Dai, Yanhua, Guo, Rongyan, Huang, Qian, 2021. Modeling of moisture content of subgrade materials in high-speed railway using a deep learning method. Adv. Mater. Sci. Eng. 2021.

Chen, Zaifa, Liu, Yancheng, Liu, Siyuan, 2017. Mechanical state prediction based on LSTM neural netwok. In: 2017 36th Chinese Control Conference. CCC, IEEE, pp. 3876–3881.

Cho, Kyeungwoo, Kim, Yeonjoo, 2022. Improving streamflow prediction in the WRF-hydro model with LSTM networks. J. Hydrol. 605, 127297.

Choi, Jae Young, Lee, Bumshik, 2018. Combining LSTM network ensemble via adaptive weighting for improved time series forecasting. Math. Probl. Eng. 2018.

Chorover, J., Losleben, M., 2021. Soil moisture, soil temperature, electrical conductivity, water potential – Jemez Unburned Site – (2015–2021), HydroShare. URL http://www.hydroshare.org/resource/5602200fa76c477d86774553b70c71b9.

Coleman, Charles D., Swanson, David A., 2007. On MAPE-R as a measure of cross-sectional estimation and forecast accuracy. J. Econ. Soc. Meas. 32 (4), 219–233.

Dey, Rahul, Salem, Fathi M., 2017. Gate-variants of gated recurrent unit (GRU) neural networks. In: 2017 IEEE 60th International Midwest Symposium on Circuits and Systems. MWSCAS, IEEE, pp. 1597–1600.

Duan, Qingyun, Ajami, Newsha K, Gao, Xiaogang, Sorooshian, Soroosh, 2007. Multi-model ensemble hydrologic prediction using Bayesian model averaging. Adv. Water Resour. 30 (5), 1371–1386.

ElSaadani, Mohamed, Habib, Emad, Abdelhameed, Ahmed M, Bayoumi, Magdy, 2021. Assessment of a spatiotemporal deep learning approach for soil moisture prediction and filling the gaps in between soil moisture observations. Front. Artif. Intell. 4, 636234.

Elshorbagy, Amin, El-Baroudy, Ibrahim, 2009. Investigating the capabilities of evolutionary data-driven techniques using the challenging estimation of soil moisture content. J. Hydroinform. 11 (3–4), 237–251.

Fang, Kuai, Pan, Ming, Shen, Chaopeng, 2018. The value of SMAP for long-term soil moisture estimation with the help of deep learning. IEEE Trans. Geosci. Remote Sens. 57 (4), 2221–2233.

Fang, Kuai, Shen, Chaopeng, 2020. Near-real-time forecast of satellite-based soil moisture using long short-term memory with an adaptive data integration kernel. J. Hydrometeorol. 21 (3), 399–413.

Faroughi, Salah A., Roriz, Ana I., Fernandes, Célio, 2022. A meta-model to predict the drag coefficient of a particle translating in viscoelastic fluids: a machine learning approach. Polymers 14 (3), 430.

Fathololoumi, Solmaz, Vaezi, Ali Reza, Alavipanah, Seyed Kazem, Ghorbani, Ardavan, Saurette, Daniel, Biswas, Asim, 2021. Effect of multi-temporal satellite images on soil moisture prediction using a digital soil mapping approach. Geoderma 385, 114901.

Filipović, Nemanja, Brdar, Sanja, Mimić, Gordan, Marko, Oskar, Crnojević, Vladimir, 2022. Regional soil moisture prediction system based on Long Short-Term Memory network. Biosystems Engineering 213, 30–38.

Gao, Yuan, Miyata, Shohei, Akashi, Yasunori, 2022b. Multi-step solar irradiation prediction based on weather forecast and generative deep learning model. Renewable Energy 188, 637–650.

Gao, Peng, Qiu, Hongbin, Lan, Yubin, Wang, Weixing, Chen, Wadi, Han, Xiongzhe, Lu, Jianqiang, 2022a. Modeling for the prediction of soil moisture in litchi orchard with deep long short-term memory. Agriculture 12 (1), 25.

Ge, Xiangyu, Wang, Jingzhe, Ding, Jianli, Cao, Xiaoyi, Zhang, Zipeng, Liu, Jie, Li, Xiaohang, 2019. Combining UAV-based hyperspectral imagery and machine learning algorithms for soil moisture content monitoring. PeerJ 7, e6926.

Ghosh, Achyut, Bose, Soumik, Maji, Giridhar, Debnath, Narayan, Sen, Soumya, 2019. Stock price prediction using LSTM on Indian share market. In: Proceedings of 32nd International Conference on, vol. 63. pp. 101–110.

Golmohammadi, Meysam, Ziyabari, Saeedeh, Shah, Vinit, Von Weltin, Eva, Campbell, Christopher, Obeid, Iyad, Picone, Joseph, 2017. Gated recurrent networks for seizure detection. In: 2017 IEEE Signal Processing in Medicine and Biology Symposium. SPMB, IEEE, pp. 1–5.

Han, Heechan, Choi, Changhyun, Kim, Jongsung, Morrison, Ryan R, Jung, Jaewon, Kim, Hung Soo, 2021. Multiple-depth soil moisture estimates using artificial neural network and long short-term memory models. Water 13 (18), 2584.

Harvey, Christopher C., Schwartz, Steven J., 1998. Time series resampling methods. In: Paschmann, G., Daly, P.W. (Eds.), Analysis Methods for Multi-Spacecraft Data. p. 43.

Heddam, Salim, 2021. New formulation for predicting soil moisture content using only soil temperature as predictor: multivariate adaptive regression splines versus random forest, multilayer perceptron neural network, M5tree, and multiple linear regression. In: Water Engineering Modeling and Mathematic Tools. Elsevier, pp. 45–62.

Heddam, Salim, Kim, Sungwon, Elbeltagi, Ahmed, Kisi, Ozgur, 2022. Bidirectional long short-term memory-based empirical wavelet transform: a new hybrid artificial intelligence model for robust prediction of soil moisture content. In: Current Directions in Water Scarcity Research. 7, Elsevier, pp. 37–56.

Hong, Zhihao, Kalbarczyk, Z., Iyer, Ravishankar K., 2016. A data-driven approach to soil moisture collection and prediction. In: 2016 IEEE International Conference on Smart Computing. SMARTCOMP, IEEE, pp. 1–6.

Hu, Yuhuang, Huber, Adrian, Anumula, Jithendar, Liu, Shih-Chii, 2018. Overcoming the vanishing gradient problem in plain recurrent networks. arXiv preprint arXiv:1801.06105.

Huang, Caojun, Li, Lin, Ren, Souhua, Zhou, Zhisheng, 2010. Research of soil moisture content forecast model based on genetic algorithm BP neural network. In: International Conference on Computer and Computing Technologies in Agriculture. Springer, pp. 309–316.

Jung, Yoonsuh, 2018. Multiple predicting K-fold cross-validation for model selection. J. Nonparametr. Stat. 30 (1), 197–215.

Jung, Yoonsuh, Hu, Jianhua, 2015. AK-fold averaging cross-validation procedure. J. Nonparametr. Stat. 27 (2), 167–179.

Karandish, Fatemeh, Šimunek, Jiří, 2016. A comparison of numerical and machine-learning modeling of soil water content with limited input data. J. Hydrol. 543, 892–909.

Kaselimi, Maria, Doulamis, Nikolaos, Doulamis, Anastasios, Voulodimos, Athanasios, Protopapadakis, Eftychios, 2019. Bayesian-optimized bidirectional LSTM regression model for non-intrusive load monitoring. In: ICASSP 2019-2019 IEEE International Conference on Acoustics, Speech and Signal Processing. ICASSP, IEEE, pp. 2747–2751.

Li, Qingliang, Zhu, Yuheng, Shangguan, Wei, Wang, Xuezhi, Li, Lu, Yu, Fanhua, 2022. An attention-aware LSTM model for soil moisture and soil temperature prediction. Geoderma 409, 115651.

Lipton, Zachary Chase, Berkowitz, John, Elkan, Charles, 2015. A critical review of recurrent neural networks for sequence learning. CoRR abs/1506.00019 (2015). arXiv preprint arXiv:1506.00019.

Liu, Yao, Guan, Lin, Hou, Chen, Han, Hua, Liu, Zhangjie, Sun, Yao, Zheng, Minghui, 2019. Wind power short-term prediction based on LSTM and discrete wavelet transform. Appl. Sci. 9 (6), 1108.

Londhe, Aboli N., Atulkar, Mithilesh, 2021. Semantic segmentation of ECG waves using hybrid channel-mix convolutional and bidirectional LSTM. Biomed. Signal Process. Control 63, 102162.

Mayer, D.G., Butler, D.G., 1993. Statistical validation. Ecol. Model. 68 (1–2), 21–32.

Memon, Nimrabanu, Patel, Samir B., Patel, Dhruvesh P., 2019. Comparative analysis of artificial neural network and xgboost algorithm for polsar image classification. In: International Conference on Pattern Recognition and Machine Intelligence. Springer, pp. 452–460.

Merity, Stephen, Keskar, Nitish Shirish, Socher, Richard, 2017. Regularizing and optimizing LSTM language models. arXiv preprint arXiv:1708.02182.

Muppidi, Satish, PG, Om Prakash, et al., 2022. Dragonfly political optimizer algorithm-based rider deep long short-term memory for soil moisture and heat level prediction in IoT. Comput. J..

O'Connor, David, Lake, Evelyn MR, Scheinost, Dustin, Constable, R Todd, 2021. Resample aggregating improves the generalizability of connectome predictive modeling. Neuroimage 236, 118044.

Perera, Dilruk, Zimmermann, Roger, 2020. Lstm networks for online cross-network recommendations. arXiv preprint arXiv:2008.10849.

Ponkina, Elena, Illiger, Patrick, Krotova, Olga, Bondarovich, Andrey, 2021. Do ARMA models provide better gap filling in time series of soil temperature and soil moisture? The case of arable land in the Kulunda Steppe, Russia. Land 10 (6), 579.

Prakash, Shikha, Sharma, Animesh, Sahu, Sitanshu Shekhar, 2018. Soil moisture prediction using machine learning. In: 2018 Second International Conference on Inventive Communication and Computational Technologies. ICICCT, IEEE, pp. 1–6.

Prasad, Ramendra, Deo, Ravinesh C., Li, Yan, Maraseni, Tek, 2018. Soil moisture forecasting by a hybrid machine learning technique: ELM integrated with ensemble empirical mode decomposition. Geoderma 330, 136–161.

Pulver, Andrew, Lyu, Siwei, 2017. LSTM with working memory. In: 2017 International Joint Conference on Neural Networks. IJCNN, IEEE, pp. 845–851.

Qiu, Jiayu, Wang, Bin, Zhou, Changjun, 2020. Forecasting stock prices with long-short term memory neural network based on attention mechanism. PLoS One 15 (1), e0227222.

Rodriguez, Juan D., Perez, Aritz, Lozano, Jose A., 2009. Sensitivity analysis of k-fold cross validation in prediction error estimation. IEEE Trans. Pattern Anal. Mach. Intell. 32 (3), 569–575.

Shitote, Stanley, Ngug, Hannah Nyambara, Ambassah, Nathaniel, Okumu, Victoria, Thuo, John Kuria, 2019. Influence of variation in moisture content to soil bearing capacity in nairobi area and its environs.

Srivastava, Nitish, Hinton, Geoffrey, Krizhevsky, Alex, Sutskever, Ilya, Salakhutdinov, Ruslan, 2014. Dropout: a simple way to prevent neural networks from overfitting. J. Mach. Learn. Res. 15 (1), 1929–1958.

Taneja, Perry, Vasava, Hitesh Kumar, Daggupati, Prasad, Biswas, Asim, 2021. Multi-algorithm comparison to predict soil organic matter and soil moisture content from cell phone images. Geoderma 385, 114863.

Thompson, Patrick A., 1990. An MSE statistic for comparing forecast accuracy across series. Int. J. Forecast. 6 (2), 219–227.

Tunçay, Tülay, 2021. Comparison quality of interpolation methods to estimate spatial distribution of soil moisture content. Commun. Soil Sci. Plant Anal. 52 (4), 353–374.

Wei, Xin, Zhang, Lulu, Yang, Hao-Qing, Zhang, Limin, Yao, Yang-Ping, 2021. Machine learning for pore-water pressure time-series prediction: Application of recurrent neural networks. Geosci. Front. 12 (1), 453–467.

Xiong, Zheng, Cui, Yuxin, Liu, Zhonghao, Zhao, Yong, Hu, Ming, Hu, Jianjun, 2020. Evaluating explorative prediction power of machine learning algorithms for materials discovery using k-fold forward cross-validation. Comput. Mater. Sci. 171, 109203.

Yu, Jingxin, Tang, Song, Zhangzhong, Lili, Zheng, Wengang, Wang, Long, Wong, Alexander, Xu, Linlin, 2020. A deep learning approach for multi-depth soil water content prediction in summer maize growth period. IEEE Access 8, 199097–199110.

Yu, Jingxin, Zhang, Xin, Xu, Linlin, Dong, Jing, Zhangzhong, Lili, 2021. A hybrid CNN-GRU model for predicting soil moisture in maize root zone. Agricult. Water Manag. 245, 106649.

Zaman, Bushra, McKee, Mac, 2014. Spatio-temporal prediction of root zone soil moisture using multivariate relevance vector machines. Open J. Modern Hydrol. 4, 80.

Zeraatpisheh, Mojtaba, Ayoubi, Shamsollah, Jafari, Azam, Tajik, Samaneh, Finke, Peter, 2019. Digital mapping of soil properties using multiple machine learning in a semi-arid region, central Iran. Geoderma 338, 445–452.

Zeyer, Albert, Schlüter, Ralf, Ney, Hermann, 2016. Towards online-recognition with deep bidirectional LSTM acoustic models.. In: Interspeech. pp. 3424–3428.

Zhang, Qiuru, Shi, Liangsheng, Holzman, Mauro, Ye, Ming, Wang, Yakun, Carmona, Facundo, Zha, Yuanyuan, 2019. A dynamic data-driven method for dealing with model structural error in soil moisture data assimilation. Adv. Water Resour. 132, 103407.

Zhang, Fangfang, Wu, Shiwen, Liu, Jie, Wang, Changkun, Guo, Zhiying, Xu, Aiai, Pan, Kai, Pan, Xianzhang, 2021. Predicting soil moisture content over partially vegetation covered surfaces from hyperspectral data with deep learning. Soil Sci. Am. J. 85 (4), 989–1001.

Zhao, Rui, Wang, Jinjiang, Yan, Ruqiang, Mao, Kezhi, 2016. Machine health monitoring with LSTM networks. In: 2016 10th International Conference on Sensing Technology. ICST, IEEE, pp. 1–6.

Zhou, Siyu, Zhou, Lin, Mao, Mingxuan, Tai, Heng-Ming, Wan, Yihao, 2019. An optimized heterogeneous structure LSTM network for electricity price forecasting. IEEE Access 7, 108161–108173.

Zia, Tehseen, Zahid, Usman, 2019. Long short-term memory recurrent neural network architectures for Urdu acoustic modeling. Int. J. Speech Technol. 22 (1), 21–30.

Zinszer, Kate, Verma, Aman D, Charland, Katia, Brewer, Timothy F, Brownstein, John S, Sun, Zhuoyu, Buckeridge, David L, 2012. A scoping review of malaria forecasting: past work and future directions. BMJ Open 2 (6), e001992.

International Journal of Greenhouse Gas Control 127 (2023) 103920

Contents lists available at ScienceDirect

International Journal of Greenhouse Gas Control

journal homepage: www.elsevier.com/locate/ijggc

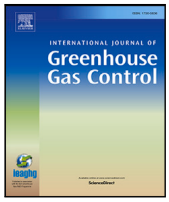

Selecting representative geological realizations to model subsurface CO_2 storage under uncertainty

Seyed Kourosh Mahjour, Salah A. Faroughi *

Geo-Intelligence Laboratory, Ingram School of Engineering, Texas State University, San Marcos, TX, 78666, USA

ARTICLE INFO

Keywords:
Representative geological realizations
Geological uncertainty
Unsupervised machine learning
Saline aquifer

ABSTRACT

Carbon capture and storage (CCS) is one of the quickest and most effective solutions for reducing carbon emissions. The majority of subsurface storage occurs in saline aquifers, for which geological information is lacking which in turn results in geological uncertainty. To evaluate uncertainty in CO_2 injection projections, the use of multiple geological realizations (GRs) has been practiced very commonly. In this approach, hundreds or thousands of high-resolution GRs is used that quickly becomes computationally expensive. This issue can be addressed with representative geological realizations (RGRs) that preserve the uncertainty domain of the ensemble GRs. In this study, we propose the use of unsupervised machine learning (UML) frameworks, including dissimilarity measurement, dimensionality reduction, clustering and sampling algorithms ta select a predetermined number of RGRs. We compare the simulation outputs of the RGR sets and the ensemble using the Kolmogorov–Smirnov (KS) test to select the best UML. The UML frameworks and their associated selection processes are evaluated using a saline aquifer with a single CO_2 injection well and 200 GRs with varying uncertain petrophysical characteristics. The best UML framework is selected to use only 5% of the GRs while maintaining the uncertainty domain of the ensemble GRs. In addition, the best UML framework is tested using a saline aquifer with three CO_2 injection wells and varied GRs. The results show that our proposed UML framework can be used to choose RGRs, capturing the whole uncertainty domain. Our approach leads to a significant reduction in the computational cost associated with scenario testing, decision-making, and development planning for CO_2 storage sites under geological uncertainty.

1. Introduction

Carbon capture and storage (CCS) is an innovative strategy for reducing human-caused CO_2 emissions (Tadjer and Bratvold, 2021). CCS involves capturing CO_2 from industrial sources, transporting it to a geological storage location, and injecting it in a deep formation, where it is stored indefinitely in the pore space of rocks (Wilkinson and Polson, 2019; Motie et al., 2018). Different types of geological CO_2 storage sites, including depleted oil and gas reservoirs and deep saline aquifers, have been regarded as suitable geologic sites for storing CO_2 to a depth of several thousand meters (Harp et al., 2017; Jin et al., 2017; Nilsen et al., 2015). During the development and management of CO_2 storage sites, geological realizations (GRs) are often used to estimate long-term CO_2 trapping, CO_2 plume migration, CO_2 leakage, etc. (Diao et al., 2020; Langhi et al., 2021; Shepherd et al., 2021; Faroughi et al., 2022). But the geological data used in building a model may be limited for each geological storage site, depending on the type of site and how much work has been done to characterize it. For instance, saline aquifers often lack the advantages of prior characterization efforts, such as depleted oil or gas reservoirs (Chen et al., 2020). Hence, the quality and quantity of geological data can lead to a high degree of uncertainty, which impacts the estimate of CO_2 storage capacities, the risk of CO_2 leakage, and the potential contamination of clean groundwater (Tadjer and Bratvold, 2021).

The evaluation and quantification of geological uncertainties are becoming more important in the decarbonization sectors (Jia et al., 2018; Sun and Durlofsky, 2019; Wilkinson and Polson, 2019). The geological structure of a storage site and the variability of its petrophysical characteristics are considered to be the main sources of geological uncertainty (Iraji et al., 2023). Standard approaches for quantifying geological uncertainty rely on the generation of many feasible GRs and the determination of the ensemble objective functions' statistical metrics (Tadjer and Bratvold, 2021). As a straightforward and rapid approach, Monte Carlo sampling is generally used to generate thousands of GRs and capture the uncertainty space (Bueno et al., 2011). Despite the benefits of probabilistic approaches in decision analysis and uncertainty quantification, it can be computationally expensive

* Corresponding author.
E-mail address: salah.faroughi@txstate.edu (S.A. Faroughi).

https://doi.org/10.1016/j.ijggc.2023.103920
Received 26 December 2022; Received in revised form 12 May 2023; Accepted 22 May 2023
Available online 9 June 2023

to process a large number of GRs using flow simulators (Mahjour et al., 2021a). Different methods for accelerating the process have been discussed in the literature. These techniques can be divided into two main categories: (i) data-driven simplifications (Douarche et al., 2014; Panjalizadeh et al., 2014) and (ii) physics-based simplifications (Wilson and Durlofsky, 2013; Aliyev and Durlofsky, 2017).

The most prevalent data-driven simplification is the use of data-fit proxy models. These are analytical functions that bypass the simulator during CO_2 injections and the post-injection period at the storage sites (Santos et al., 2020). This method is fast, enabling thousands of objective function determinations. Nevertheless, ignoring the physical laws governing multi-phase, multi-component fluid flow at the storage site makes it susceptible to erroneous evaluations, particularly for high-dimensional input-parameter spaces. Moreover, proxy models can contain non-negligible errors due to the assumptions and approximations used in their development (Trehan et al., 2017).

The physics-based category is the use of low-fidelity realizations, which simplify geological characteristics substantially (Schiozer et al., 2019). Examples include the application of up-scaled GRs. The main advantage of this strategy is its simplicity of implementation. Nevertheless, sub-grid heterogeneity impacts may be diminished. Another type of physics-based simplification is the use of reduced ensembles, in which a small number of realizations are selected from a large ensemble of GRs (Scheidt and Caers, 2009; Shirangi and Durlofsky, 2016; Mahjour et al., 2020a; Meira et al., 2020). There are several methods for generating reduced ensembles, which can be considered a wide category, including representative geological realizations (RGRs). In contrast to low-fidelity models, this method does not necessitate simplifications of the geological characteristics. Hence, critical heterogeneity and phenomena associated with CO_2 injection are accurately depicted if the fidelity of the model is maintained. However, the validity of solutions derived from RGRs, such as long-term CO_2 storage and CO_2 plume migration, is contingent on the assumption that the RGRs accurately reflect the total uncertainty domain (Preux, 2016). If the RGRs are not representative of the full range of possible geological scenarios, then the solutions derived from them may not accurately capture the variability and uncertainty of the subsurface systems. Inaccurate representations of the subsurface systems can lead to incorrect predictions of CO_2 storage and migration, which can have significant consequences for subsurface resource management and environmental impact assessments (Meira et al., 2016). For example, if an RGR fails to capture the possibility of an unexpected geological feature, such as the high-permeable or non-reservoir zones, then the simulations may not account for the impact of these features on CO_2 storage and migration. Therefore, it is important to carefully assess the representativeness of RGRs and ensure that they capture the full range of possible geological scenarios. This necessitates more research into the best use of existing RGR selection methods aimed at maximizing uncertainty representation. In general, there are two types of RGR selection methods: (i) rank-based (RB) methods, and (ii) unsupervised machine learning (UML) methods (Mahjour et al., 2022).

The RB method selects the RGRs representing 90%, 50%, and 10% of the static and/or dynamic characteristics of the CO_2 storage site (Scheidt and Caers, 2009). Typically, the dynamic reservoir characteristics are established through numerical modeling. Even though the dynamic reservoir characteristics correlate well with reservoir performance, a significant amount of time is needed to simulate the realizations and acquire the dynamic reservoir properties, particularly in cases of high uncertainty. The static reservoir characteristics, on the other hand, consider geological heterogeneity directly, eliminating the need for costly numerical simulations to derive the static features. Additionally, the dynamic reservoir properties are highly dependent on the CO_2 injection strategy (e.g., the number of wells and where they are placed). Therefore, if the injection strategy is altered throughout the development of the CO_2 storage site, the representativeness of the RGR will be affected (Mahjour et al., 2021b). Various studies have been conducted to select RGRs based on RB. Idrobo et al. (2000) and Faroughi et al. (2013) chose RGRs based on the ranking of the streamline time-of-flight (TOF) characteristic, which indicates the difference in flow response for each realization. McLennan and Deutsch (2005) ranked the realizations using the static characteristics of local connectivity in the steam-assisted gravity drainage (SAGD) reservoir. Chahooki et al. (2019) selected the RGRs by ranking the oil lithofacies volume (OLV) derived from rock physics. Thanh et al. (2020) ranked the entire ensemble based on the cumulative CO_2 injection. Although attempts have been made to enhance RB approaches, their use in RGR selection is still limited by certain factors. One of the fundamental shortcomings of current ranking methods is that they are very dependent on the applied measurement. If the measure has a poor correlation with the performance of reservoir production parameters, then the selected models will not fully reflect the whole set of realizations (Li et al., 2012).

Recently, UML has been widely used in different case studies to select RGRs (Shirangi and Durlofsky, 2016; Lee et al., 2017; Mahjour et al., 2020a; Haddadpour and Niri, 2021). UML seeks to find and analyze hidden structures in unlabeled data (Hinton and Sejnowski, 1999). Dimensionality reduction and clustering are two main UML examples. Dimensionality reduction consists of an algorithm that determines which attributes are most useful for discriminating between distinct data samples and eliminates the rest (Liu and Forouzanfar, 2018). In clustering, the algorithm automatically classifies data samples with similar characteristics into categories. Accordingly, the purpose of UML is to transform the realizations into a low-dimensional space and cluster those with similar static and/or dynamic characteristics (Liu and Forouzanfar, 2018). Lee et al. (2016) used the UML to choose similar realizations relying on the 3D facies models. Park et al. (2016) determined the similarity between realization pairs using UML and the norm of the difference in generalized travel time (GTT) from the water-cut response. Shirangi and Durlofsky (2016) used UML to assess various properties of the realizations to choose the RGRs. Pinheiro et al. (2018) selected the RGRs based on rock mass deformation models using UML. Several more studies have successfully used UML to choose RGRs. Scheidt and Caers (2009) showed that the UML technique for selecting the RGR set is superior to the RB method when it comes to maintaining uncertainty.

In this work, we look at different standard algorithms used in the UML frameworks to translate the realizations into a low-dimensional space and group them together based on a similar static property of the CO_2 geological site. These algorithms are widely adopted and well-established in the literature (Kang et al., 2019). Assuming those similar realizations within each cluster exhibit similar flow responses, it is unnecessary to simulate the entire set. Instead, a single RGR from each cluster is selected for processing by a flow simulator (Alzraiee and Garcia, 2012). Due to the use of different UML algorithms, this study can give a full evaluation of how to improve RGR selection for the development and management of CO_2 storage sites when geological uncertainties are present. To evaluate the efficacy of the UML frameworks in selecting the RGRs, we simulate multiple geological realizations from a 2D saline aquifer model with one CO_2 injection well (a base case). The distribution of simulation outputs from RGRs and the entire set is then determined in order to choose the best UML framework. Finally, we applied the best-performing UML framework to a test case that involved three CO_2 injection wells and different spatial petrophysical distributions (i.e., heterogeneities). This allowed us to evaluate the framework's performance under varying well numbers and geological conditions.

This paper is organized as follows: In Section 2, we describe the underlying physics behind CO_2 migration in porous media and its trapping mechanisms. In Section 3, we present a methodology for RGR selection using different UML algorithms, storage simulation considering different CO_2 trapping mechanisms, and uncertainty evaluation. In Section 4, the features of a 2D synthetic model to which the RGR selection method is applied are described. Section 5 presents the results and discussion, and finally, in Section 6, we present the main conclusions.

2. Underlying physics

The physical processes that govern the CO_2 plume migration and trapping mechanisms in geological storage sites are highly complicated due to CO_2 phase behavior and various types of sequestration techniques. Multi-phase/multi-component models are used to describe the flow of CO_2 in geological formations, e.g., deep saline aquifers (Nghiem et al., 2004). Based on the compositional Generalized Equation of State (Ranganathan et al., 2011), the mass balance equation for the components in the gaseous phase (g), aqueous phase (aq), and mineral phase (m) can be described as,

$$\begin{aligned}\frac{\partial \mathrm{N_{ig}}}{\partial \mathrm{t}} =& \nabla \cdot \left(\frac{\rho_{\mathrm{g}} k k_{\mathrm{rg}} m_{\mathrm{ig},g}}{\mu_g}\right)\left(\nabla \mathrm{p} + \nabla \mathrm{p_{cwg}} - \rho_g g \nabla z\right) + \\ & \nabla \cdot \left(\frac{\rho_{\mathrm{w}} k k_{rw} m_{\mathrm{ig},w}}{\mu_{\mathrm{w}}}\right)\left(\nabla \mathrm{p} + \nabla \mathrm{p_{cwg}} - \rho_{\mathrm{w}} g \nabla z\right) + \\ & \nabla \cdot \mathrm{J_{ig}} + \sigma_{\mathrm{ig},aq} + \mathrm{q},\end{aligned} \tag{1}$$

$$\frac{\partial \mathrm{N_{ia}}}{\partial \mathrm{t}} = \nabla \cdot \left(\frac{\rho_{\mathrm{w}} k k_{ru} m_{\mathrm{ia,w}}}{\mu_{\mathrm{iv}}}\right)\left(\nabla \mathrm{p} - \rho_{\mathrm{iv}} g \nabla z\right) + \nabla \cdot \mathrm{J_{ia}} + \sigma_{\mathrm{ia,aq}} + \sigma_{\mathrm{ia,mn}} + \mathrm{q}, \tag{2}$$

and

$$\frac{\partial \mathrm{N_{km}}}{\partial \mathrm{t}} = \sigma_{\mathrm{km,mn}}, \tag{3}$$

where J_{ja} is diffusion/dispersion of aqueous component, J_{ig} is diffusion/dispersion of gas component, N_{ia} is the number of moles of aqueous component i per grid volume, N_{ig} is the number of moles of gas component i per grid volume, $m_{ig,g}$ is the mole fractions of gas component i in gas phase, N_{km} is the number of moles of minerals per grid volume, $m_{ia,w}$ is mole fraction of aqueous component i in aqueous phase, $m_{ig,w}$ is the mole fractions of gas component i in aqueous phase, $\sigma_{\mathrm{ia,mn}}$ is reaction rate between aqueous and mineral component, $\sigma_{\mathrm{ia,aq}}$ is reaction rate between aqueous and aqueous component, $\sigma_{\mathrm{ig,aq}}$ is reaction rate between gaseous and aqueous component, q is well molar flow rate of gas component, $\sigma_{\mathrm{km,mn}}$ is mineral reaction rate, P is water pressure, P_{cwg} is capillary pressure between water and gas that is considered to be negligible in this study, g is gravity, k_{rg} is gas relative permeability, k_{rw} is water relative permeability, ρ_{g} is density of gas, k is permeability, ρ_{w} is density of water, z is depth and t is time step. The accumulation is represented by the terms on the left-hand side of Eq. (1), Eq. (2), and Eq. (3). The first and second terms on the right-hand side of Eq. (1) and Eq. (2), respectively, characterize convective and diffusive transport. q denotes the flow rates and, in this study, the CO_2 injection rate in Eq. (1) and Eq.(2).

The geological formation's physiochemical and hydrodynamic properties impose four CO_2 trapping mechanisms: (i) structural trapping, in which the injected CO_2 climbs beneath the cap rock preventing it from rising to the surface; (ii) residual trapping, in which the injected CO_2 becomes immobile due to capillary forces and relative permeability effects; (iii) solubility trapping, in which the injected CO_2 dissolves in the formation brine; and finally (iv) mineral trapping, in which the injected CO_2 interacts with the rock leading to the precipitation of solid carbonates, i.e., a type of permanent CO_2 storage (Kumar et al., 2020). Fig. 1 illustrates the contribution of various CO_2 trapping mechanisms at different phases of a typical CO_2 sequestration project's life cycle.

The main mechanism that prevents CO_2 from returning to the surface during injection is structural trapping. Mineral trapping, on the other hand, is the most secure method for storing CO_2 in the form of the carbonate, but it is the slowest CO_2 trapping mechanism (Kim et al., 2017). To evaluate the efficacy of a CO_2 injection method, it is also necessary to measure the amount of residual CO_2 trapping and solubility trapping. Residual gas Trapping Index (RTI), Solubility gas Trapping Index (STI), and Total trapping Efficiency Index (TEI) are the indices to provide a straightforward evaluation of a CO_2 injection process's efficacy (Nghiem et al., 2009). These indices are defined as,

$$RTI = \frac{m_{\mathrm{total}(rg)}}{m_{\mathrm{total}(i)}}, \tag{4}$$

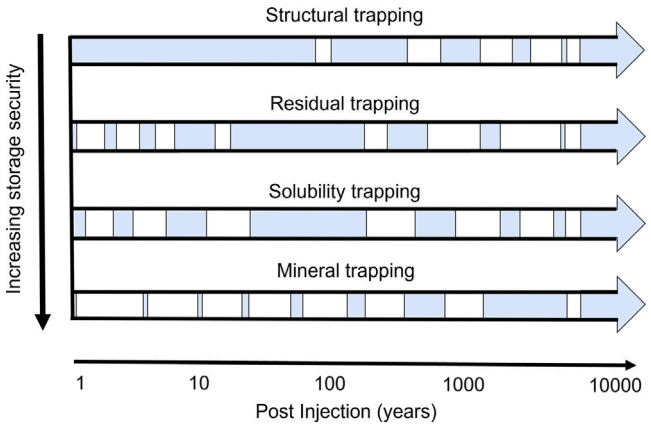

Fig. 1. Four mechanisms for CO_2 trapping: (i) structural trapping; (ii) residual trapping; (iii) solubility trapping; and (iv) mineral trapping. The main mechanism that prevents CO_2 from returning to the surface during injection is structural trapping. Mineral trapping, on the other hand, is the most secure method for storing CO_2 in the form of the carbonate, but it is the slowest CO_2 trapping mechanism. The blue color shows the relative contribution of each of these mechanisms to the overall CO2 storage over time (Hermanrud et al., 2009).

$$STI = \frac{m_{\mathrm{total}(sb)}}{m_{\mathrm{total}(i)}}, \tag{5}$$

and

$$TEI = RTI + STI, \tag{6}$$

where $m_{\mathrm{total}(rg)}$ is the total mass of CO_2 trapped as residual gas (kg), $m_{\mathrm{total}(i)}$ is the total mass of CO_2 injected (kg), and $m_{\mathrm{total}(sb)}$ is the total mass of CO_2 dissolved in the formation brine (kg). Fig. 1 illustrates the importance of various CO_2 trapping mechanisms at different phases of a typical CO_2 storage project's life cycle.

3. Methodology

The basis of the methodology is selecting RGRs to approximately indicate the characteristics (e.g., uncertainty domain) of the full ensemble. Fig. 2 shows our proposed workflow, which starts with the generation of multiple GRs under uncertainty. Different algorithms are then leveraged at each stage to select RGR sets. We validate the efficacy of each framework by processing the RGR sets and the entire ensemble with a numerical simulator and then comparing the distributions of the simulation outputs obtained from the RGR sets and the entire ensemble.

3.1. Generate multiple geological realizations (GRs)

To quantify geological uncertainty, multiple GRs must be generated. Several algorithms have been presented in the literature for this purpose. The most common are Derivative Tree (DT), Monte Carlo (MC), and Latin Hypercube (LH) methods (Mahjour et al., 2019). Although the selection of the optimal algorithm is dependent on the application being evaluated, two crucial factors must be addressed simultaneously (Beraldi and Bruni, 2014): (i) the number of GR should be adequate to cover the full uncertainty space, and (ii) the number of GR should be kept to a minimum to prevent incurring unnecessary computing costs. We adopted the LH method to generate realizations since it has a lower computational cost while considering many uncertain variables (Schiozer et al., 2017). Notably, this stage is independent of the RGR selection process and is not the subject of this study.

3.2. Unsupervised machine learning

This section focuses on selecting a small number of RGRs that represent the same uncertainty domain as the complete GRs. To this

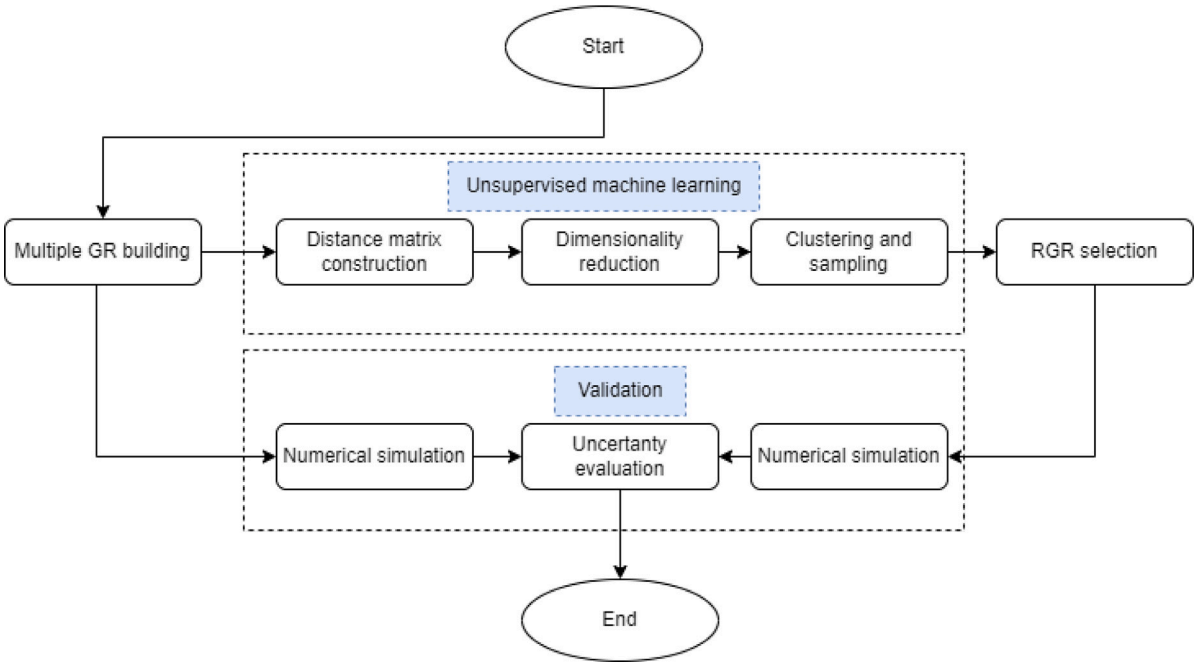

Fig. 2. Proposed workflow for selecting and validating the RGRs using different unsupervised machine learning frameworks. The workflow includes two main parts: (i) Selecting the RGRs using unsupervised machine learning frameworks and (ii) validating the efficacy of each algorithm by processing the RGR sets and the entire ensemble with a numerical simulator.

end, we employ UML consisting of three steps: (i) building a dissimilarity (distance) matrix, (ii) conducting dimensionality reduction, and (iii) performing clustering and sampling as elaborated in the following sections.

3.2.1. Dissimilarity matrix construction

The primary step of the UML process is constructing a matrix considering the distance indicators, δ, measured between each pair of realizations. The distance δ_{ij} indicates the degree of resemblance between realization i and realization j (Suzuki and Caers, 2006). To assess the distance indicators of pairwise realizations, it is necessary to define a specific reservoir characteristic and an appropriate distance measurement method (Scheidt and Caers, 2009). The selection of reservoir characteristics is crucial for the proper execution of UML. In terms of geological pattern distributions, many constructed geological realizations have certain distances resulting in similar flow responses. By separating these realizations, it can be feasible to generate simulation outputs based on a smaller subset of realizations with varying flow responses (Haddadpour and Niri, 2021). In this work, the reservoir quality index (RQI) is employed as a static reservoir characteristic to identify the distance between any two realizations. RQI has recently been widely applied in several reservoir subject areas, including permeability prediction, stratigraphy, and reservoir modeling (Mahjour et al., 2016; Shan et al., 2018; Oliveira et al., 2020; Yu, 2021; Belhouchet et al., 2021). Porosity and permeability, two petrophysical properties employed in the RQI equation, are also important for CO_2 storage and CO_2 plume migration (Soong et al., 2018; Xu et al., 2017). Mahjour et al. (2022) and Haddadpour and Niri (2021) analyzed RQI and found reasonable findings for realizations with similar flow behaviors. RQI is determined as,

$$RQI = 0.0314\sqrt{\frac{K}{\phi}}, \tag{7}$$

where K is the permeability in milli-darcy (mD) and ϕ is the porosity in fraction. The constant of 0.0314 is the permeability conversion factor from μm^2 to mD. Amaefule et al. (1993) deduced the RQI from the Kozeny–Carman equation, representing by,

$$K = 1014\frac{\phi^3}{(1-\phi)^2}\left(\frac{1}{F_s\tau^2 S_{gv}^2}\right), \tag{8}$$

where K represents the permeability in μm^2, F_s represents the shape factor, τ represents the tortuosity, and S_{gv} indicates the specific surface area per unit grain volume.

Each grid cell in the GRs has a location in space and a set of geological characteristics, including porosity and permeability. To build RQI maps, we calculate the RQI for every grid cell. The distance indicators between the RQI maps are then measured by different grid-based metrics. We apply five distance metrics, including Manhattan (Malkauthekar, 2013), Euclidean (Faisal et al., 2020), Wasserstein (Panaretos and Zemel, 2019), Chebyshev (Coghetto, 2016), and Hausdorff (Porter and Woods, 2012). We refer the reader to a review paper by Ontañón (2020) for further details on each distance measurement. This section concludes by constructing five $n \times n$ distance matrices based on different distance metrics and n RQI maps. The elements of the matrices are the pairwise model distance indicators, δ_{ij}. A valid distance matrix must satisfy the conditions of self-similarity, i.e., $\delta_{ii} = 0$ and symmetry, i.e., $\delta_{ij} = \delta_{ji}$ (Mahjour et al., 2020a).

3.2.2. Dimensionality reduction

A single GR with many grid cells produces a space with a high dimension, thereby increasing the computation complexity. The objective of dimensionality reduction is to eliminate superfluous dimensions and compress the data into a low-dimensional space in order to facilitate data processing (Zhang et al., 2018). The methods for dimensionality reduction use the distance metrics derived in the previous step. The metrics are applied in the transformation of high-dimensional realizations into a low-dimensional space (map), therefore keeping the essential characteristics of the original data (Mahjour et al., 2020b). Each point on the low-dimensional map corresponds to a specific RQI model, and the distance between points shows the similarity between models, i.e., the closer the points, the more similarity exists between the models (Mahjour et al., 2021a). The techniques for dimensionality reduction are either linear or nonlinear. Using a linear combination of the original data, the linear dimensionality reduction algorithms transform a high-dimensional space into a low-dimensional space (Sumithra and Surendran, 2015). They facilitate data visualization and classification. Nonlinear dimensionality reduction algorithms are frequently used to manage data with nonlinear interactions and intricate

structures (Orsenigo and Vercellis, 2013). Sorzano et al. (2014) found that nonlinear dimensionality reduction algorithms are highly efficient because they can adjust to the local data structure and handle non-linearity more efficiently. Hence, we leverage three nonlinear dimensionality reduction algorithms, including Multidimensional Scaling (MDS) (Cox and Cox, 2008), Isometric Map (IsoMap) (MacEachren and Davidson, 1987), and Kernel PCA (KPCA) (Schölkopf et al., 1997) to transform high-dimensional realizations into low-dimensional maps. We refer the reader to a review paper by Anowar et al. (2021) for further details on each algorithm.

3.2.3. Clustering and sampling

After the projection of data from a high-dimensional original space to a low-dimensional space, clustering methods are employed to classify models into multiple clusters (Mahjour et al., 2020a). Models that belong to the same cluster are similar to one another. Several clustering algorithms have been developed that can be classified into two major classes from a structural perspective: (i) partitional clustering, and (ii) hierarchical clustering (Jain and Dubes, 1988). In this work, similar models are clustered using deterministic K-means (DK-means) (Jothi et al., 2019) and Ward linkage-based clustering (WLC) (Sharma et al., 2019) as partitional clustering and hierarchical clustering, respectively. After the models are put into groups, one from each group is chosen to be the representative model. To achieve this, we employ centroid-based sampling to select the model closest to the cluster's center (Mahjour et al., 2020a). The Euclidean distance between a model and the cluster's center is measured to determine the model's proximity to the cluster's center. It is vital to highlight that choosing the optimal number of RGRs is a challenging task that requires careful consideration of various factors, including the UML framework used, the complexity of the geological realizations, the number and types of uncertain parameters, the desired level of accuracy, and the available computational resources (Mahjour et al., 2022). However, to ensure a fair comparison between different UML frameworks in this study, a constant number of RGRs is selected. The chosen sample size should be small enough to minimize computational costs while still capturing the full uncertainty space. While the selection of an optimal number of RGRs is essential for capturing the essential features of the uncertainty space and providing reliable estimates of model parameters, the primary focus of this study is to compare the effectiveness of different UML frameworks by selecting a fixed number of RGRs. In addition, the problems with the UML steps should be looked at together in order to come up with a new UML framework. Accordingly, we assess 30 possible UML frameworks based on various algorithms used for each UML step. Fig. 3 shows all of the frameworks investigated in this study. The code used to produce the data for unsupervised learning was developed in Python 3.8.1, employing the software's package-specific techniques.

3.3. Validation

The simulation outputs from the RGR sets and the entire ensemble are compared to comprehend the UML approaches' performance. Initially, we obtain each set's simulation outputs using a commercial flow simulator. Then, we evaluate the uncertainty domain of the sets, considering the cumulative distribution of simulation outputs.

3.3.1. Numerical simulation

During the flow simulation, the numerical model of the realizations is defined to determine the objective over time for evaluating the RGRs. The objectives should be aligned with the selection of the simulation's most significant outcomes. Based on the trapping mechanisms explained in Section 2, we solve the underlying physics behind CO_2 migration and determine three simulation outputs including (i) CO_2 structural trapping, (ii) CO_2 residual trapping, and (iii) CO_2 solubility trapping using CMG-GEM (Canada Modeling Group-Generalized Equation of State Model). During the simulation process for solubility trapping, chemical reactions between the gaseous and aqueous phases are considered (Maalim et al., 2021). Furthermore, We do not consider mineral trapping in this study because it mainly occurs after 1000 years (see Fig. 1) and our simulation period is 200 years.

3.3.2. Uncertainty evaluation

Once the simulation outputs are available, the uncertainty domain of the RGR set and the whole ensemble are measured and compared. The method of uncertainty measurement is crucial to evaluating the RGRs using the optimal UML framework. Analysis of the simulation outputs' statistical parameters is the conventional method for measuring the uncertainty space (Kaleris et al., 2001; Montanari and Brath, 2004). This measurement estimates the means, medians, variances, and range (maximum and minimum) of simulation outputs generated from the RGRs and the entire set. Currently, however, the distribution of simulation outputs has been expanded beyond statistical parameters in order to compare the uncertainty domain of the RGRs and the entire set (Khan et al., 2006). In this study, we evaluate the distribution of simulation outputs at the end-point of the simulation process for future decision-making processes under uncertainty (Schiozer et al., 2019). Accordingly, We compare the curves of the cumulative distribution function (CDF) that are made from the simulation results of the RGR set and the whole ensemble to check how close their uncertainty ranges are. The CDF of a random variable X is defined as,

$$F(x)_x = P(X \leq x), \text{ for all } x \in \mathbb{R} \tag{9}$$

where the right-hand side represents the probability that the random variable X takes on a value less than or equal to x (Xue et al., 2009). The CDF is defined for all $x \in \mathbb{R}$. We perform the Kolmogorov–Smirnov (KS) test (Ferreira et al., 2017) to measure the maximum vertical difference, $D_{\max}$, between the CDFs of two data sets, $F(x)_{RGR,m}$, and $G(x)_{full}$. The $D_{\max}$ value is defined as,

$$D_{\max} = \max_{\forall x} \left| F(x)_{RGR,m} - G(x)_{full,n} \right|, \tag{10}$$

where the number of realizations in the RGR set (m) and the number of realizations in the whole set (n) are already set based on the budget and simulation time. If $D_{\max}$ is lower than D_{critical}, defined as,

$$D_{\text{critical},0.5} = 1.36\sqrt{\frac{n+m}{nm}}, \tag{11}$$

at the 5% significance level (Ferreira et al., 2017), it can be concluded that the sets come from the same distribution and the RGRs are representative of the entire ensemble.

Although D_{critical} is an important criterion for determining the closeness of data distributions between two samples, it may not provide sufficient information about the correspondence between small RGR sets and large ensembles. Therefore, we used a significance level named D_{limit}, proposed by Ferreira et al. (2017), to aid in the selection of appropriate RGRs. D_{limit} is the maximum admissible distance between the CDF curves obtained from the subset and the full set for each specific case study. The user can choose the D_{limit} value based on an acceptable level required for the RGR selection process. In this study, the D_{limit} was set to 0.15, which was deemed acceptable based on visual inspection of the differences between the CDF curves. Thus, the RGR set was considered to have good representativeness of the full ensemble if Dmax, obtained from the RGR and GR samples, was lower than both D_{critical} and D_{limit}.

4. Model description

4.1. Geometric model

In this study, a saline aquifer model with a dimension of $(x, z, y) = (1000\text{ m}, 100\text{ m}, 10\text{ m})$ is used. The x and z directions are represented by 100 and 20 grid cells, and the y direction is represented by one grid cell, thus the numerical model is effectively a 2D vertical slice

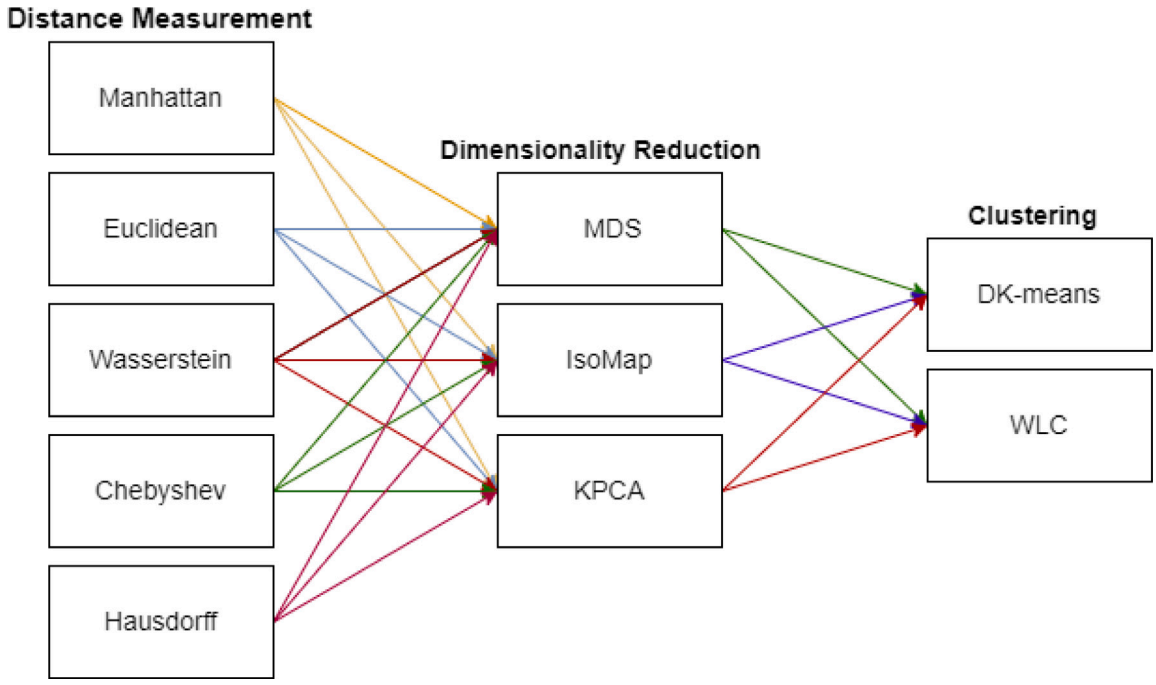

Fig. 3. Thirty UML frameworks based on various algorithms used for each UML step. General problems regarding the UML steps should be evaluated together to propose a new UML framework.

(with $\Delta x = 10$ m, $\Delta z = 5$ m, and $\Delta y = 10$ m created by CMG-GEM) as reported in Table 1. For the base case, one CO_2 injection well is used to investigate different UML frameworks for selecting the RGRs. The injection well perforation location is at the left bottom of the well. Table 1 also reports the model state parameters and aquifer's properties. To generate the petrophysical maps, synthetic well-log data is collected and prepared. We employ Gaussian geostatistical simulation (Chiles and Delfiner, 2009) to generate the porosity values based on the mean, 0.115, and standard deviation, 0.04, and the permeability values based on the mean, 85.06 mD, and standard deviation, 98.90, of the well-log data. The Kozeny–Carman equation (Amaefule et al., 1993) is used to establish the relationship between porosity and permeability. A spatial variogram model is used to characterize the spatial correlation of the porosity and permeability values. The range of the variogram is set to 320 meters in the horizontal direction and 33 meters in the vertical direction. These values are chosen to ensure that the simulation results adequately captured the spatial correlation between adjacent cells and to avoid over-fitting or under-fitting the data. We used CMG-Winprop to obtain aquifer fluid properties. The Peng–Robinson Equation of State (Stryjek and Vera, 1986) is used to estimate supercritical CO_2 properties. Henry's law (Li and Nghiem, 1986) is employed to model CO_2 solubility in brine. A simulation period of 200 years is considered adequate to appropriately simulate the CO_2 storage process.

The right side of the aquifer is considered to be infinite in this study. In modeling, this indicates that the boundary is positioned at a sufficient distance to ensure that it does not influence fluid flow. In reality, deep saline aquifers used for CO_2 sequestration can reach tens or hundreds of kilometers (Vilarrasa et al., 2010). The top and bottom of the aquifer are impervious, and while modeling the aquifer, a zero leakage coefficient is assumed.

4.2. Relative permeability model

The relative permeability of CO_2 and brine during the drainage process is calculated using Corey's model (Corey et al., 1977). Fig. 4 shows the relationship between the relative permeability of water (K_{rw}), the relative permeability of CO_2 (K_{rg}), and water saturation (S_w). The hysteresis effect on the relative permeability of CO_2 is modeled using the modified Land equation (Land, 1968), which has been integrated into CMG-GEM. The CMG-GEM calculates Land's coefficient to maintain internal consistency with the input values of critical gas saturation (S_{gcrit}), maximum gas saturation ($S_{\text{g,max}}$) and the maximum residual gas saturation ($S_{gr,\text{max}}$) (Liu et al., 2013). For the purposes of this paper, the S_{gcrit}, $S_{\text{g,max}}$ and the $S_{gr,\text{max}}$ are considered to be 0.2, 0.8, and 0.4, respectively.

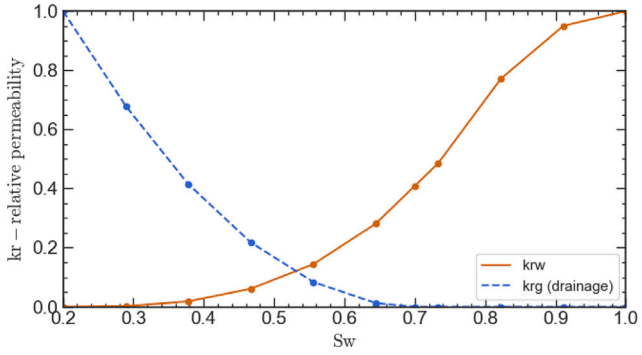

Fig. 4. The relationship between the relative permeability of the wetting fluid against CO_2 (non-wet), K_{rw}, and the relative permeability of CO_2, K_{rg}, versus water saturation, S_w. The numerical model developed by CMG.

5. Results and discussion

We generated $N = 200$ realizations using the LH method, considering different porosity and permeability model variations. The selected number of realizations ensures that the spatial distributions are sufficiently sampled. We then generated RQI models using porosity and permeability properties. The realizations were finally simulated using a commercial simulator, considering the trapping mechanisms to determine the simulation outputs, including (i) CO_2 structural trapping, (ii) CO_2 residual trapping, and (iii) CO_2 solubility trapping. Table 1 describes the inputs required for the simulation process. We calculated

Table 1
Grid and model parameters used to simulate CO_2 injection in a 2D saline aquifer.

Parameters	Value
Aquifer size (x,z,y)	1000 m × 100 m × 10 m
Number of grids	100 × 20 × 1
Grid size ($\Delta x, \Delta z, \Delta y$)	10 m × 5 m × 10 m
Porosity range	0.03–0.20
Permeability range	5–290 mD
Aquifer depth	1200 m
Reservoir temperature	25° C
Salinity (NaCl)	0.1%
Maximum injection rate	8000 m^3/day (under standard surface gas state)
Simulation period	200 years
CO_2 Injection period	1 year
Rock compressibility	5.5 × 10^{-7} kPa^{-1} (at reference pressure: 11800 kPa)
Water compressibility	4.5 × 10^{-7} kPa^{-1} (at reference pressure: 13100 kPa)
Surface gas rate (STG)	10000 m^3/day
Bottom hole pressure (BHP)	44500 kPa
Mass density of water at surface	1020 Kg/m^3

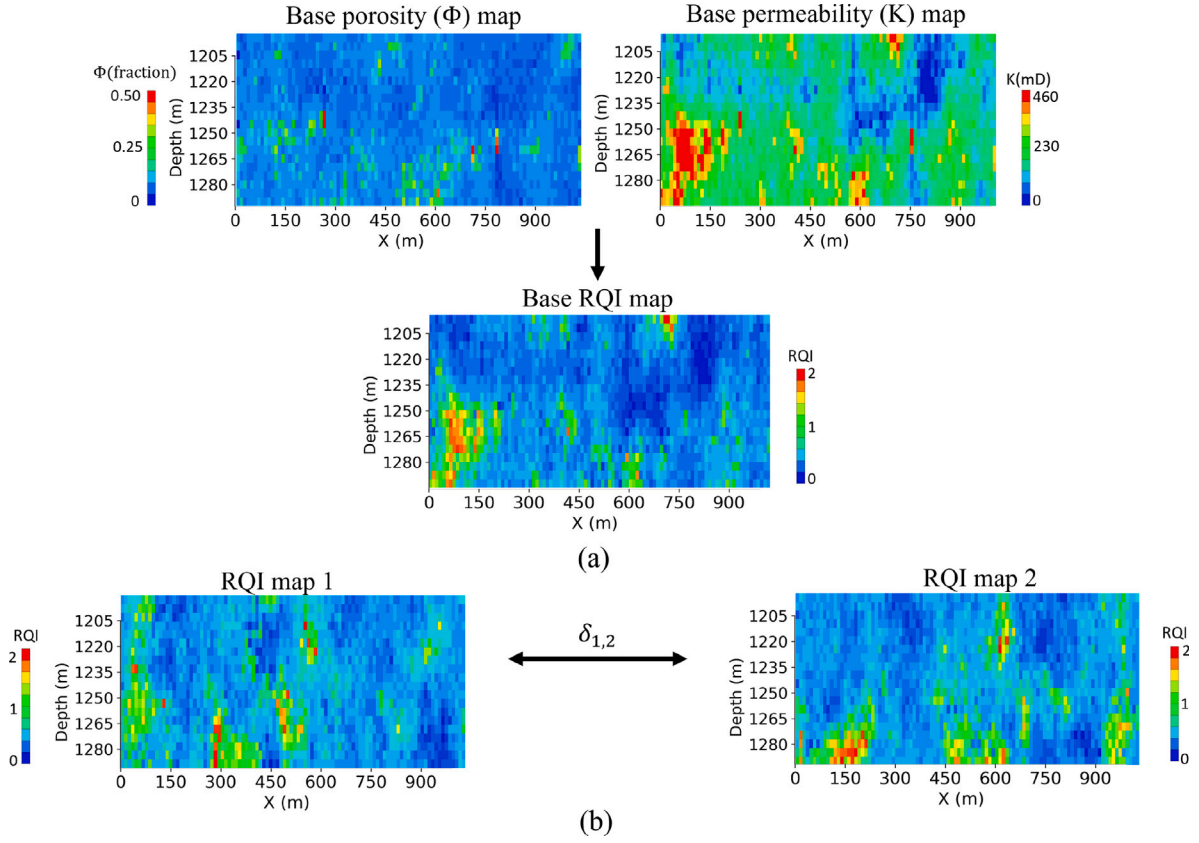

Fig. 5. (a) Calculating the RQI using porosity and permeability for each grid cell to construct the base RQI model, (b) Measuring the distance indicator $\delta_{1,2}$ between RQI map 1 and RQI map 2 as an example.

the RQI for each grid cell to construct the RQI map and measure the distances between the pairwise GRs. Fig. 5 depicts the building of the base RQI map using porosity and permeability maps and the distance measurement between two RQI maps. In this study, we selected 10 predetermined numbers of RGRs, which accounted for five percent of the entire set, to be chosen by each UML. This ensured that we could reasonably compare the efficiency of the UML frameworks. Next, we simulated the selected 10 RGRs along with the entire set of 200 GRs to determine their simulation outputs after a period of 200 years. Fig. 6 depicts the CO_2 saturation profiles considering the base case for the base GR in four-time steps, i.e., 1, 5, 50, and 200 years post-injection. However, the dimensions of the grid cells utilized in the plot are reported in The findings for 1 year and 5 years after injection indicating that CO_2 migrated from the lower portions of the storage site to the upper parts. CO_2 was built up in the top portion of the storage site in the 50 and 200 years after injection due to structural (cap-rock) trapping, while CO_2 accumulated in the lower and middle portions due to residual and solubility trapping. Due to the cessation of CO_2 injection and the setting of the leakage coefficient to zero, CO_2 trapping mechanisms changed little between 50 and 200 years of simulation. This maintained a constant CO_2 trapping rate.

Once the simulations are performed, the outputs of the simulations from the RGRs are used to make 90 CDF curves. The number of CDF curves is determined by 30 UML frameworks and three simulation outputs obtained from the RGRs (30 UML frameworks × 3 simulation outputs). The simulation outputs considered in this study are CO_2 structural trapping, CO_2 residual trapping, and CO_2 solubility trapping. After drawing the CDF curves of the RGRs for each simulation output,

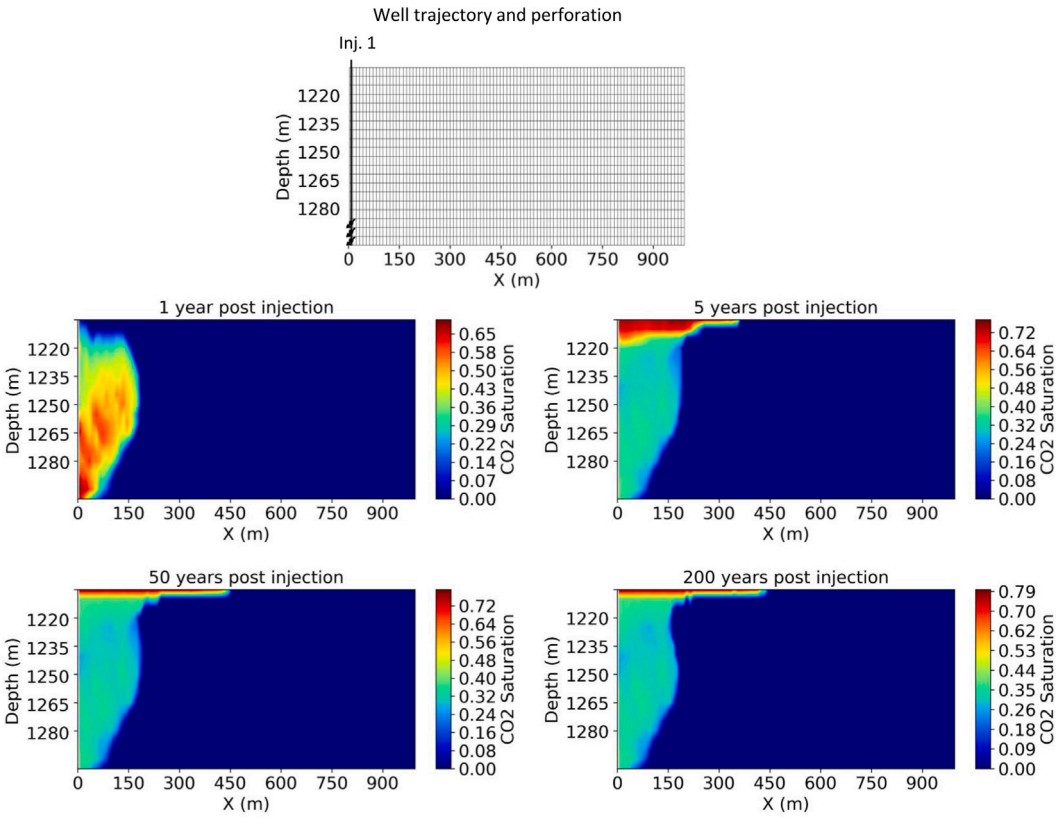

Fig. 6. CO_2 saturation profiles considering the base case for the base GR in four-time steps, 1, 5, 50, and 200 years post-injection. The injection well perforation location is at the bottom left. One year and 5 years after injection indicate that CO_2 migrated from the lower portions of the storage site to the upper portions. CO_2 was built up in the top portion of the storage site in the 50 and 200 years after injection due to structural (cap-rock) trapping, while CO_2 accumulated in the lower and middle portions due to residual and solubility trapping. Due to the cessation of CO_2 injection and the setting of the leakage coefficient to zero, CO_2 trapping mechanisms changed little between 50 and 200 years of simulation. This maintained a constant CO_2 trapping rate. In the top panel, grid cells are not to scale for better visualization, however, the dimension of the grid cells is $\Delta x = 10$ m, $\Delta z = 5$ m, and $\Delta y = 10$ m, as reported in Table 1.

we compared them to the CDF curves created from the corresponding simulation outputs for the entire set and calculated the D_{critical} for each framework. The D_{critical} is 0.28, determined according to Eq.((11)) and the D_{limit} is 0.15. We also calculated the D_{max} by comparing the CDF curves from the RGR sets to the corresponding CDF curves from the entire set. The average of D_{max} values is used to assess the quality of the UML frameworks.

5.1. Best UML framework

The best UML framework must have the lowest average D_{max}. Table 2 shows the five UML frameworks with the highest and lowest average D_{max} values. As reported, the combination of Euclidean/MDS/DK-means yielded the lowest average D_{max}, and thus, this combination is selected as the best UML framework for this case study. The Euclidean/MDS/DK-means UML framework has an average D_{max} value of 0.15, which is below the D_{critical} value of 0.28 and equal to the D_{limit} value of 0.15. The Euclidean distance metric was chosen due to its effectiveness in handling continuous data with normal distributions (Ontañón, 2020), while MDS was selected because it preserves pairwise distances between data points in low-dimensional spaces (Anowar et al., 2021), making it more suitable for capturing high-dimensional relationships among uncertain parameters in geological models. Finally, DK-means was selected as the clustering algorithm because it is a robust and efficient algorithm that is insensitive to outliers. The DK-means algorithm minimizes the within-cluster dispersion while incorporating a constraint on the distance between clusters, ensuring that the clusters are well-separated and distinct (Jothi et al., 2019). This is important for identifying suitable RGRs. Overall, the combination of these techniques was found to be the most effective in reducing uncertainty in the geological model and selecting the RGRs for further analysis.

Fig. 7 represents the 2D map of all realizations obtained by Euclidean/MDS/DK-means with 10 clusters. When the MDS algorithm was given a distance matrix with the Euclidean measurements between each pair of RGRs in a set, it put each RGR into a 2D map so that the distances between RGRs were kept as much as possible. In the 2D map, the RGRs are shown by black points. After projecting RGRs from a high-dimensional space to a 2D map, we used the DK-means to group the RGRs into several clusters. Then, using the centroid sampling method, we selected one RGR as a representative from each cluster. The visual inspection shows that the RGRs are evenly distributed over all models. The X-axis in the figure represents Dimension 1 (D1), while the Y-axis represents Dimension 2 (D2).

In Fig. 8, the CDF curves of the end-point simulation results from the RGRs and the whole set were compared. CDF curves demonstrate that the simulation outputs of RGRs selected from the Euclidean/MDS/DK-means framework came from the same distribution as the entire set for the base case. Furthermore, for the visual validation of the results, time series curves of the simulation outputs for RGR and the full sets are depicted in Fig. 9. It is evident from the figure that the RGRs properly captured the whole uncertainty domain.

5.2. Worst UML framework

In a separate assessment, as shown in Table 2, we examined the performance of the UML framework with the highest average Dmax, Hausdorff/KPCA/WLC combination. Unlike Euclidean distance, Hausdorff distance is not sensitive to the distribution of the data points and

Table 2
Five UML frameworks with the lowest and the highest average D_{max} values.

	Rank	Distance measurement	Dimensionality reduction	Clustering	Average Dmax
Five UML frameworks with the lowest average D_{max}	1	Euclidean	MDS	DK-means	0.15
	2	Chebyshev	KPCA	WLC	0.18
	3	Wasserstein	IsoMap	WLC	0.19
	4	Hausdorff	MDS	WLC	0.19
	5	Manhattan	KPCA	DK-means	0.20
Five UML frameworks with the highest average D_{max}	26	Hausdorff	MDS	DK-means	0.29
	27	Chebyshev	MDS	WLC	0.29
	28	Chebyshev	MDS	DK-means	0.30
	29	Hausdorff	IsoMap	WLC	0.30
	30	Hausdorff	KPCA	WLC	0.33

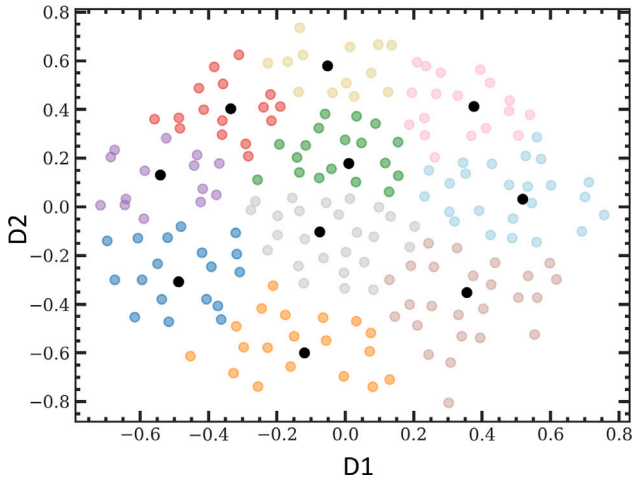

Fig. 7. A 2D map of 200 realizations generated by Euclidean/MDS/DK-means for the base case. The X-axis in the figure represents Dimension 1 (D1), while the Y-axis represents Dimension 2 (D2). 30 RGRs (black points) are selected using clustering and centroid-based sampling. The RGRs are evenly distributed over all models, showing the full uncertainly domain.

only considers the maximum distance between any two points in the sets (Ontañón, 2020). This can result in Hausdorff distance being less effective in capturing the underlying structure of the data. KPCA dimensionality reduction may not have been able to preserve the important features of the RGRs. KPCA works by transforming the original high-dimensional data into a lower-dimensional space by maximizing the variance of the data along the principal components. However, if the important features of the RGRs are not well captured by the first few principal components, KPCA may not be able to distinguish between the different RGRs effectively (Anowar et al., 2021). WLC is sensitive to outliers, which can lead to suboptimal clustering results (Sharma et al., 2019). Outliers can cause a significant increase in the variance within a cluster, which may result in merging the outlier with another cluster, even if they are not similar. In addition, WLC can lead to unbalanced clusters, where some clusters have significantly more data points than others. This can be a problem if the data are not evenly distributed or if the cluster sizes are important for the analysis. Taken as a whole, the constraints and deficiencies associated with Hausdorff/KPCA/WLC render this combination poor for identifying appropriate RGRs. Fig. 10 represents the 2D map of all the generated models with 10 clusters. However, the figure shows that the distribution of GRs across the 2D map is not well-distributed and symmetric. Fig. 11 compares the CDF curves of end-point simulation results from the RGRs and the whole set. The average D_{max} is 0.33 which is higher than $D_{critical}$ and D_{limit}. Hence, the simulation outputs of RGRs, selected using the Hausdorff/KPCA/WLC framework, do not match well with the distribution of the entire set.

In addition to evaluating the UML frameworks' simulation outputs, we also conducted a computational efficiency analysis to assess the strength of our method. We compared the elapsed time required to simulate the full ensemble with that of using 10 RGRs selected from Euclidean/MDS/DK-means for uncertainty quantification. The results showed that the elapsed time for the full ensemble was 230 min, while that for the 10 RGRs was only 11 min. This indicates that using RGRs can significantly reduce the time required for uncertainty quantification compared to the full ensemble approach. The difference in computational cost used for the full ensemble and the RGRs, however, can vary depending on several factors such as the complexity of geological realizations in each case study, the number of wells, and the computing power (Mahjour et al., 2021b).

5.3. Blind testing

We tested the Euclidean/MDS/DK-means framework as the best UML framework on a third case (test case) possessing three CO_2 injection wells and different porosity and permeability maps compared to the base case. We employed the LH method to generate a new set of $N = 200$ realizations while maintaining the same permeability and porosity ranges as the base case. It is important to note that the probabilistic nature of the LH method introduces stochasticity in the spatial distributions of porosity and permeability among the realizations. Hence, the spatial distributions of these parameters in the sets of realizations for the base case and the test case exhibit differences. The injection well perforation locations are at the bottom of each well, and we have a boundary of non-permeable vertical wells that prevent the fluid flow to the left side in our 2D model. This step is conducted to assess the performance of the best UML framework when applied to a blind case with totally different geological and dynamic features. The inputs and initial conditions required for the simulation process are the same as the inputs for the base case described in Table 1, and all wells are assumed to have the same injection rate. Fig. 12 shows the CO_2 saturation profiles considering the test case for the base GR in four-time steps: 1, 5, 50, and 200 years post-injection.

The time series simulation outputs for the test case considering the base GR are shown in Fig. 13. In the first year of simulation, there is a considerable rise in CO_2 structural trapping during CO_2 injection. With the cessation of CO_2 injection, the amount of injected CO_2 that climbed beneath the cap rock decreased gradually owing to CO_2 dissolving in the formation brine. Consequently, the amount of CO_2 trapped by the solubility trapping mechanism grew with time. Due to relative permeability effects, the CO_2 dissolution process also affected the immobile CO_2, resulting in a reduction in the amount of CO_2 held by the residual trapping mechanism over time.

Fig. 14 demonstrates that the 10 RGRs selected from Euclidean/MDS/DK-means framework provide the same CDF of simulation output as the full set. The average D_{max} value for the UML framework is 0.18, which is again smaller than the value of $D_{critical}$, 0.28. Fig. 15 shows a comparison between the simulation outputs of the RGRs and the entire set over time. It represents that the RGRs

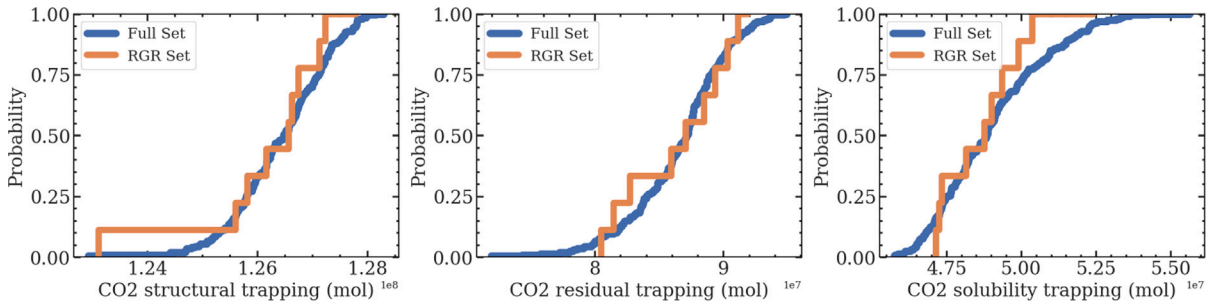

Fig. 8. The CDF curves were derived from the simulation outputs of the RGR set and the full set for the base case. RGR set was selected by the Euclidean/MDS/K-means framework. The D_{max} values for CO_2 structural trapping, CO_2 residual trapping, and CO_2 solubility trapping are 0.13, 0.14, and 0.18, respectively. The average D_{max} is 0.15, smaller than the D.

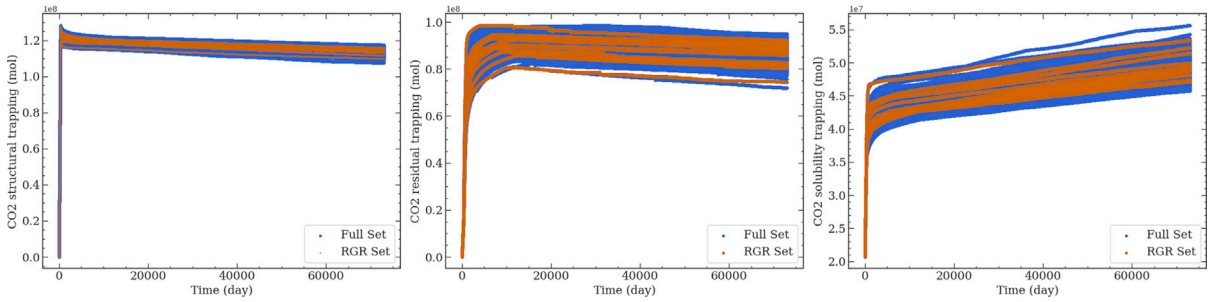

Fig. 9. Time series of CO_2 residual trapping (mol) curves for all 200 geological realizations (blue color) and 10 geological realizations (orange color) for the base case over 200 years. The RGRs properly captured the whole uncertainty domain.

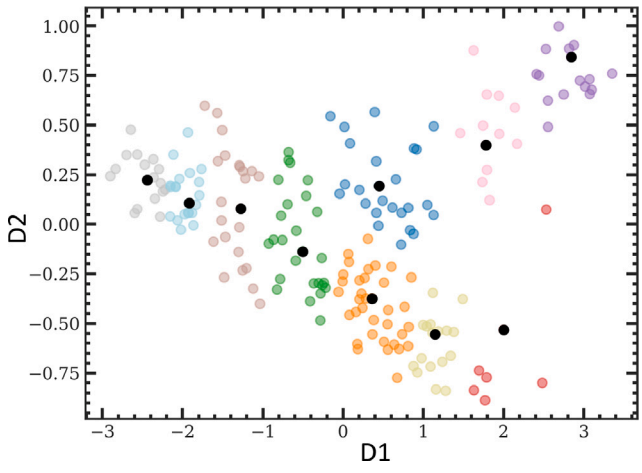

Fig. 10. A 2D map of 200 realizations generated by Hausdorff/KPCA/WLC for the base case. The X-axis in the figure represents Dimension 1 (D1), while the Y-axis represents Dimension 2 (D2). 30 RGRs (black points) are selected using clustering and centroid-based sampling. The distribution of GRs across the 2D map is not well-distributed and symmetric.

properly captured the whole uncertainty domain for the test case. Comparing the time series curves derived from the base case with the test case reveals that, in the test case, the RGRs better spanned the whole uncertainty space. This is because more grid cells were involved with CO_2 saturation in the test case with three wells than in the base case with one well. Since the distance indicators between the RQI maps were measured by different grid-based metrics, it stands to reason that if more grid cells were impacted by the simulation, we would obtain better results.

Our results show that the proposed UML framework for RGR selection based on static models, i.e., without running forward numerical simulations, can successfully select a smaller set that preserves the full uncertainty space of the full set of RGs. The selected RGRs can then be used for the purpose of fast scenario testing, decision-making, and development planning at CO_2 storage sites under geological uncertainties.

The consistency and validity of the procedure will be confirmed through future testing of UML frameworks using 3D real-case models with higher heterogeneity, including different facies, faults, and fractures. This can help to identify any weaknesses or limitations in the framework, which can then be addressed and improved upon. We also suggest more research and assessment of the approaches employed in this work to increase the efficacy and precision of the results, including (i) comparing the results and evaluating other algorithms for the GRs construction, (ii) evaluating the optimal number of RGRs for each UML framework, (iii) studying the spatial distribution and plume footprint of the CO_2 plume in both the full GR set and the RGR set, and (iv) examining the sensitivity of the results to different RGR numbers and evaluating the trade-off between computational efficiency and accuracy to determine the optimal number of RGRs required to achieve the desired level of uncertainty reduction and model performance.

6. Conclusions

This study investigated approaches for improving the selection of representative geological realizations (RGRs) to ensure that geological uncertainty is adequately represented throughout the development and management of CO_2 storage sites. We addressed the RGRs selection problem using unsupervised machine learning (UML). We evaluated and tested several UML algorithms, including (i) similarity distance measurement, (ii) dimensionality reduction, and (iii) clustering and sampling. The Kolmogorov–Smirnov (KS) test was employed to find the best UML framework by comparing and measuring the absolute

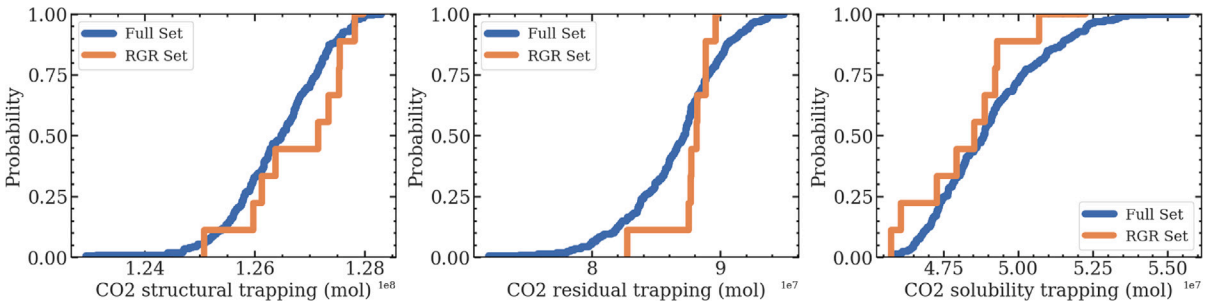

Fig. 11. The CDF curves were derived from the simulation outputs of the RGR set and the full set for the base case. RGR set was selected by the Hausdorff/KPCA/WLC framework. The D_{max} values for CO_2 structural trapping, CO_2 residual trapping, and CO_2 solubility trapping are 0.40, 0.41, and 0.20, respectively. The average D_{max} is 0.33 which is higher than $D_{critical}$ and D_{limit}. Hence, the simulation outputs of RGRs, selected using the Hausdorff/KPCA/WLC framework, do not match well with the distribution of the entire set.

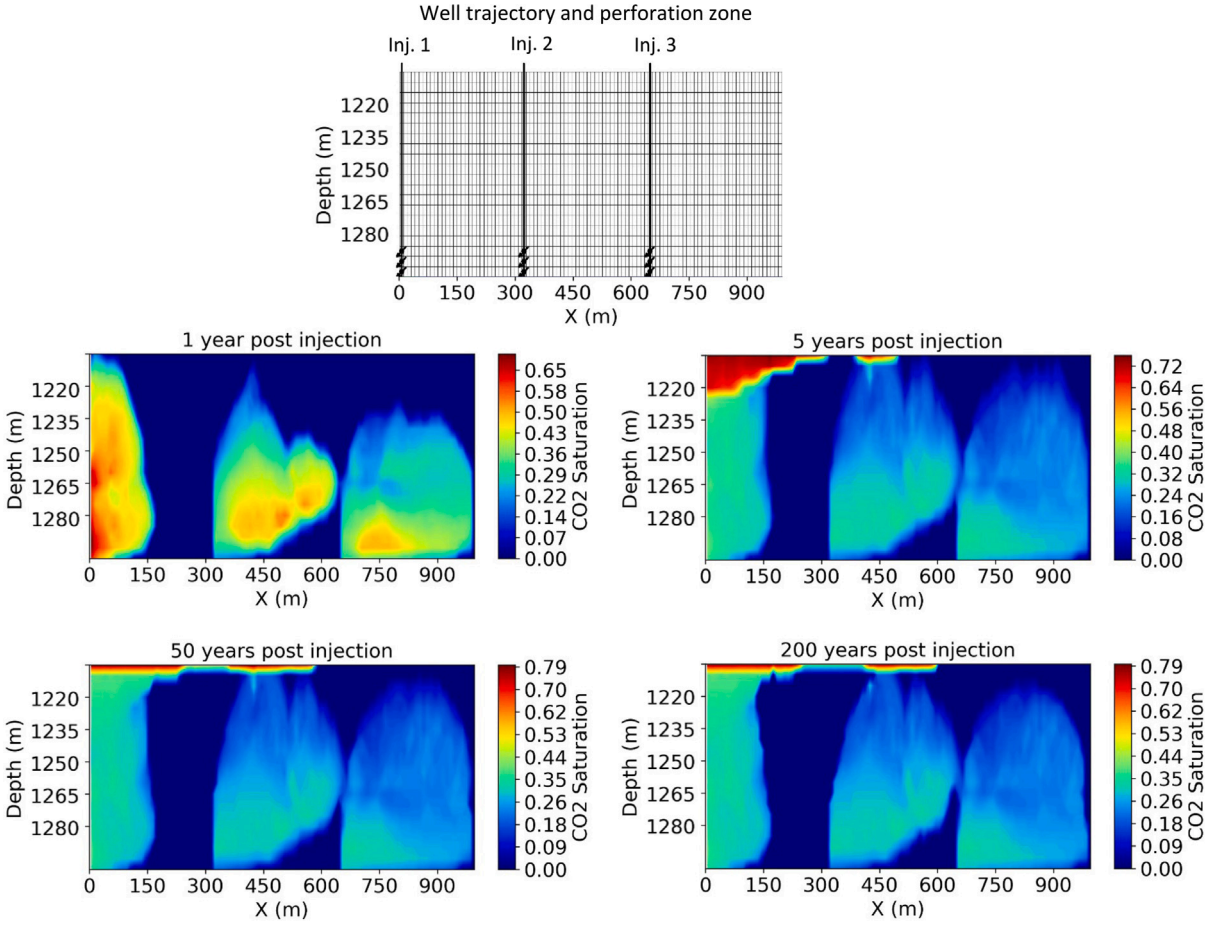

Fig. 12. CO_2 saturation profiles considering the test case for the base GR in four-time steps, 1, 5, 50, and 200 years post-injection. The injection well perforation locations are at the bottom of the three wells. One year and 5 years after injection indicate that CO_2 migrated from the lower portions of the storage site to the upper portions. CO_2 was built up in the top portion of the storage site in the 50 and 200 years after injection due to structural (cap-rock) trapping, while CO_2 accumulated in the lower and middle portions due to residual and solubility trapping. Due to the cessation of CO_2 injection and the setting of the leakage coefficient to zero, CO_2 trapping mechanisms changed little between 50 and 200 years of simulation. This maintained a constant CO_2 trapping rate. In the top panel, grid cells are not to scale for better visualization, however, the dimension of the grid cells is $\Delta x = 10$ m, $\Delta z = 5$ m, and $\Delta y = 10$ m, as reported in Table 1.

distance between the cumulative distribution functions (CDFs) of simulation outputs from the RGR sets to those of the entire GR ensemble using the Kolmogorov–Smirnov (KS) test. Our findings demonstrated that the combination of Euclidean distance measurement, multidimensional scaling, and deterministic K-means (the Euclidean/MDS/DK-means framework) is the most effective framework for selecting the RGRs while preserving the uncertainty domain. The application of the Euclidean/MDS/DK-means framework successfully retained the uncertainty domain of the full-set using only 5% of the GRs (10 out of 200). We also showed that the Euclidean/MDS/DK-means framework could be directly applied to varied CO_2 injection strategies with

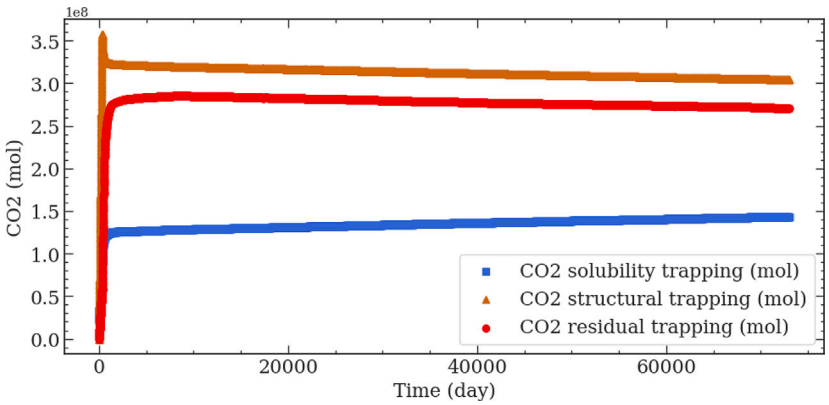

Fig. 13. The time series simulation outputs for the test case considering the base GR. First-year CO_2 injection increases structural CO_2 trapping. By ceasing CO_2 injection, the amount of CO_2 that rose beneath the cap rock reduced owing to dissolution in the formation of brine. Solubility trapping stored more CO_2 with time. Due to the relative permeability, CO_2 dissolution also affects immobile CO_2, reducing the amount of CO_2 stored by the residual trapping mechanism over time.

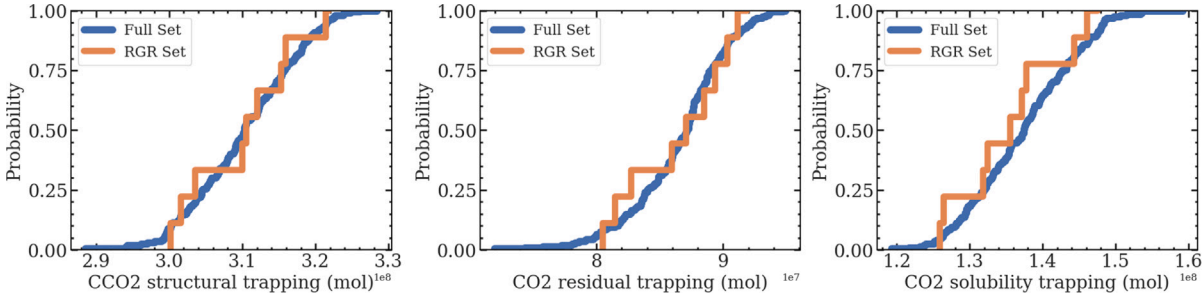

Fig. 14. The CDF curves derived from the simulation outputs of the RGR set and the full set for the test case. RGR set was selected by the Euclidean/MDS/DK-means framework. The D_{max} values for CO_2 structural trapping, CO_2 residual trapping, and CO_2 solubility trapping are 0.12, 0.15, and 0.17, respectively. The average D_{max} is 0.14, smaller than the D.

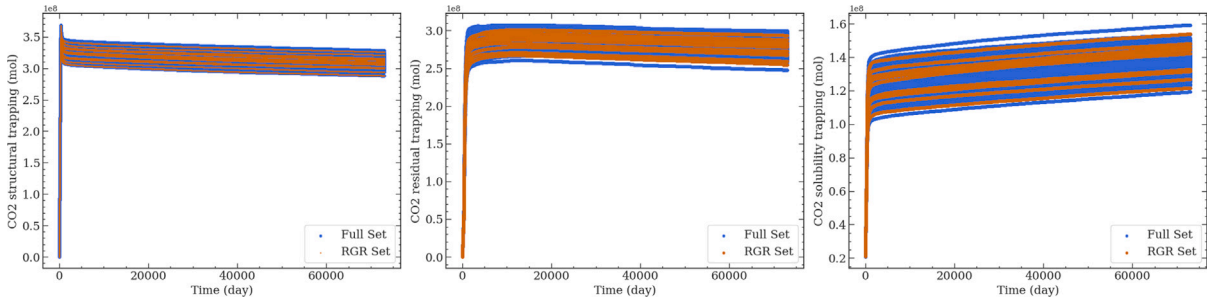

Fig. 15. Time series CO_2 trapped (mol) curves during 200 years for all 200 geological realizations (blue color) and 10 geological realizations (orange color) for the base case. The RGRs properly captured the whole uncertainty domain.

different numbers of wells and different spatial petrophysical distributions. The selected RGRs can be leveraged for rapid scenario testing, decision-making, and development planning for CO_2 storage sites with geological uncertainty.

Declaration of competing interest

The authors declare that they have no known competing financial interests or personal relationships that could have appeared to influence the work reported in this paper.

Data availability

Data will be made available on request.

Acknowledgments

S.A.F. would like to acknowledge support by the Department of Energy's Office of Fossil Energy and Carbon Management (DOE-FECM), USA (award no. DE-FE0032200), and Texas State University Multidisciplinary Internal Research Grant (MIRG), USA (award no. 9000003028).

References

Aliyev, Elnur, Durlofsky, Louis J., 2017. Multilevel field development optimization under uncertainty using a sequence of upscaled models. Math. Geosci. 49 (3), 307–339. http://dx.doi.org/10.1007/s11004-016-9643-0.

Alzraiee, Ayman, Garcia, Luis A., 2012. Using cluster analysis of hydraulic conductivity realizations to reduce computational time for Monte Carlo simulations. J. Irrig. Drain. Eng. 138 (5), 424–436. http://dx.doi.org/10.1061/(ASCE)IR.1943-4774.0000416.

Amaefule, Jude O., Altunbay, Mehmet, Tiab, Djebbar, Kersey, David G., Keelan, Dare K., 1993. Enhanced reservoir description: using core and log data to identify hydraulic

(flow) units and predict permeability in uncored intervals/wells. In: SPE Annual Technical Conference and Exhibition. OnePetro, http://dx.doi.org/10.2118/26436-MS.

Anowar, Farzana, Sadaoui, Samira, Selim, Bassant, 2021. Conceptual and empirical comparison of dimensionality reduction algorithms (pca, kpca, lda, mds, svd, lle, isomap, le, ica, t-sne). Comp. Sci. Rev. 40, 100378. http://dx.doi.org/10.1016/j.cosrev.2021.100378.

Belhouchet, H.E., Benzagouta, M.S., Dobbi, A., Alquraishi, A., Duplay, Joelle, 2021. A new empirical model for enhancing well log permeability prediction, using nonlinear regression method: Case study from Hassi-Berkine oil field reservoir–Algeria. J. King Saud Univ., Eng. Sci. 33 (2), 136–145. http://dx.doi.org/10.1016/j.jksues.2020.04.008.

Beraldi, Patrizia, Bruni, Maria Elena, 2014. A clustering approach for scenario tree reduction: an application to a stochastic programming portfolio optimization problem. Top 22 (3), 934–949. http://dx.doi.org/10.1007/s11750-013-0305-9.

Bueno, Juliana Finoto, Drummond, Rodrigo Duarte, Vidal, Alexandre Campane, Sancevero, Sérgio Sacani, 2011. Constraining uncertainty in volumetric estimation: A case study from Namorado Field, Brazil. J. Pet. Sci. Eng. 77 (2), 200–208. http://dx.doi.org/10.1016/j.petrol.2011.03.003.

Chahooki, Mostafa Zare, Javaherian, Abdolrahim, Saberi, Mohammad Reza, 2019. Realization ranking of seismic geostatistical inversion based on a Bayesian lithofacies classification-A case study from an offshore field. J. Appl. Geophys. 170, 103814. http://dx.doi.org/10.1016/j.jappgeo.2019.07.008.

Chen, Bailian, Harp, Dylan R., Lu, Zhiming, Pawar, Rajesh J., 2020. Reducing uncertainty in geologic CO2 sequestration risk assessment by assimilating monitoring data. Int. J. Greenhouse Gas Control 94, 102926. http://dx.doi.org/10.1016/j.ijggc.2019.102926.

Chiles, Jean-Paul, Delfiner, Pierre, 2009. Geostatistics: Modeling Spatial Uncertainty. vol. 497, John Wiley & Sons.

Coghetto, Roland, 2016. Chebyshev distance. doi:http://hdl.handle.net/11320/5497.

Corey, Arthur Thomas, et al., 1977. Mechanics of Heterogeneous Fluids in Porous Media. Water Resources Publications.

Cox, Michael A.A., Cox, Trevor F., 2008. Multidimensional scaling. In: Handbook of Data Visualization. Springer, pp. 315–347. http://dx.doi.org/10.1007/978-3-540-33037-0_14.

Diao, Yujie, Zhu, Guowei, Li, Xufeng, Bai, Bing, Li, Jun, Wang, Yongsheng, Zhao, Xinglei, Zhang, Bing, 2020. Characterizing CO2 plume migration in multi-layer reservoirs with strong heterogeneity and low permeability using time-lapse 2D VSP technology and numerical simulation. Int. J. Greenhouse Gas Control 92, 102880. http://dx.doi.org/10.1016/j.ijggc.2019.102880.

Douarche, Frédéric, Da Veiga, Sébastirn, Feraille, Mathieu, Enchéry, Guillaume, Touzani, Samir, Barsalou, R., 2014. Sensitivity analysis and optimization of surfactant-polymer flooding under uncertainties. Oil & Gas Sci. Technol.–Revue D'IFP Energies Nouvelles 69 (4), 603–617. http://dx.doi.org/10.2516/ogst/2013166.

Faisal, M., Zamzami, E.M., et al., 2020. Comparative analysis of inter-centroid K-means performance using euclidean distance, canberra distance and manhattan distance. In: J. Phys.: Conference Series. 1566, (1), IOP Publishing, 012112.

Faroughi, Salah A., Faroughi, Semko, McAdams, Julian, 2013. A prompt sequential method for subsurface flow modeling using the modified multi-scale finite volume and streamline methods. Int. J. Numer. Anal. Model. 4 (2), 129–150.

Faroughi, Salah A., Pawar, Nikhil, Fernandes, Celio, Das, Subasish, Kalantari, Nima K., Mahjour, Seyed Kourosh, 2022. Physics-guided, physics-informed, and physics-encoded neural networks in scientific computing. http://dx.doi.org/10.48550/arXiv.2211.07377, arXiv preprint arXiv:2211.07377.

Ferreira, Carla J., Davolio, Alessandra, Schiozer, Denis J., 2017. Evaluation of the discrete Latin hypercube with geostatistical realizations sampling for history matching under uncertainties for the norne benchmark case. In: OTC Brasil. OnePetro, http://dx.doi.org/10.4043/28073-MS.

Haddadpour, Hosein, Niri, Mohammad Emami, 2021. Uncertainty assessment in reservoir performance prediction using a two-stage clustering approach: Proof of concept and field application. J. Pet. Sci. Eng. 204, 108765. http://dx.doi.org/10.1016/j.petrol.2021.108765.

Harp, Dylan R., Stauffer, Philip H., O'Malley, Daniel, Jiao, Zunsheng, Egenolf, Evan P., Miller, Terry A., Martinez, Daniella, Hunter, Kelsey A., Middleton, Richard S., Bielicki, Jeffrey M., et al., 2017. Development of robust pressure management strategies for geologic CO2 sequestration. Int. J. Greenhouse Gas Control 64, 43–59. http://dx.doi.org/10.1016/j.ijggc.2017.06.012.

Hermanrud, Christian, Andresen, Terje, Eiken, Ola, Hansen, Hilde, Janbu, Aina, Lippard, Jon, Bolås, Hege Nordgård, Simmenes, Trine Helle, Teige, Gunn Mari Grimsmo, Østmo, Svend, 2009. Storage of CO2 in saline aquifers–Lessons learned from 10 years of injection into the Utsira Formation in the Sleipner area. Energy Procedia 1 (1), 1997–2004. http://dx.doi.org/10.1016/j.egypro.2009.01.260.

Hinton, Geoffrey, Sejnowski, Terrence J., 1999. Unsupervised Learning: Foundations of Neural Computation. MIT Press, http://dx.doi.org/10.7551/mitpress/7011.001.0001.

Idrobo, Eduardo A., Choudhary, Manoj K., Datta-Gupta, A., 2000. Swept volume calculations and ranking of geostatistical reservoir models using streamline simulation. In: SPE/AAPG Western Regional Meeting. OnePetro, http://dx.doi.org/10.2118/62557-MS.

Iraji, Shohreh, Soltanmohammadi, Ramin, Munoz, Eddy Ruidiaz, Basso, Mateus, Vidal, Alexandre Campane, 2023. Core scale investigation of fluid flow in the heterogeneous porous media based on X-ray computed tomography images: Upscaling and history matching approaches. Geoenergy Sci. Eng. 225, 211716. http://dx.doi.org/10.1016/j.geoen.2023.211716.

Jain, Anil K., Dubes, Richard C., 1988. Algorithms for Clustering Data. Prentice-Hall, Inc..

Jia, Wei, McPherson, Brian, Pan, Feng, Dai, Zhenxue, Xiao, Ting, 2018. Uncertainty quantification of CO2 storage using Bayesian model averaging and polynomial chaos expansion. Int. J. Greenhouse Gas Control 71, 104–115. http://dx.doi.org/10.1016/j.ijggc.2018.02.015.

Jin, Lu, Hawthorne, Steven, Sorensen, James, Pekot, Lawrence, Kurz, Bethany, Smith, Steven, Heebink, Loreal, Herdegen, Volker, Bosshart, Nicholas, Torres, José, et al., 2017. Advancing CO2 enhanced oil recovery and storage in unconventional oil play—experimental studies on Bakken shales. Appl. Energy 208, 171–183. http://dx.doi.org/10.1016/j.apenergy.2017.10.054.

Jothi, R., Mohanty, Sraban Kumar, Ojha, Aparajita, 2019. DK-means: a deterministic k-means clustering algorithm for gene expression analysis. Pattern Anal. Appl. 22 (2), 649–667. http://dx.doi.org/10.1007/s10044-017-0673-0.

Kaleris, V., Papanastasopoulos, D., Lagas, G., 2001. Case study on impact of atmospheric circulation changes on river basin hydrology: uncertainty aspects. J. Hydrol. 245 (1–4), 137–152. http://dx.doi.org/10.1016/S0022-1694(01)00356-0.

Kang, Byeongcheol, Kim, Sungil, Jung, Hyungsik, Choe, Jonggeun, Lee, Kyungbook, 2019. Efficient assessment of reservoir uncertainty using distance-based clustering: a review. Energies 12 (10), 1859. http://dx.doi.org/10.3390/en12101859.

Khan, Mohammad Sajjad, Coulibaly, Paulin, Dibike, Yonas, 2006. Uncertainty analysis of statistical downscaling methods. J. Hydrol. 319 (1–4), 357–382. http://dx.doi.org/10.1016/j.jhydrol.2005.06.035.

Kim, Youngmin, Jang, Hochang, Kim, Junggyun, Lee, Jeonghwan, 2017. Prediction of storage efficiency on CO2 sequestration in deep saline aquifers using artificial neural network. Appl. Energy 185, 916–928. http://dx.doi.org/10.1016/j.apenergy.2016.10.012.

Kumar, Sunil, Foroozesh, Jalal, Edlmann, Katriona, Rezk, Mohamed Gamal, Lim, Chun Yan, 2020. A comprehensive review of value-added CO2 sequestration in subsurface saline aquifers. J. Nat. Gas Sci. Eng. 81, 103437. http://dx.doi.org/10.1016/j.jngse.2020.103437.

Land, Carlon S., 1968. Calculation of imbibition relative permeability for two-and three-phase flow from rock properties. Soc. Petrol. Eng. J. 8 (02), 149–156. http://dx.doi.org/10.2118/1942-PA.

Langhi, Laurent, Strand, Julian, Ricard, Ludovic, 2021. Flow modelling to quantify structural control on CO2 migration and containment, CCS South West Hub, Australia. Petroleum Geosci. 27 (2), http://dx.doi.org/10.1144/petgeo2020-094.

Lee, Kyungbook, Jung, Seungpil, Choe, Jonggeun, 2016. Ensemble smoother with clustered covariance for 3D channelized reservoirs with geological uncertainty. J. Pet. Sci. Eng. 145, 423–435. http://dx.doi.org/10.1016/j.petrol.2016.05.029.

Lee, Kyungbook, Jung, Seungpil, Lee, Taehun, Choe, Jonggeun, 2017. Use of clustered covariance and selective measurement data in ensemble smoother for three-dimensional reservoir characterization. J. Energy Resour. Technol. 139 (2), http://dx.doi.org/10.1115/1.4034443.

Li, Shaohua, Deutsch, Clayton V., Si, Jinghua, 2012. Ranking geostatistical reservoir models with modified connected hydrocarbon volume. In: Ninth International Geostatistics Congress. pp. 11–15.

Li, Yau-Kun, Nghiem, Long X., 1986. Phase equilibria of oil, gas and water/brine mixtures from a cubic equation of state and Henry's law. Can. J. Chem. Eng. 64 (3), 486–496. http://dx.doi.org/10.1002/cjce.5450640319.

Liu, Faye, Ellett, Kevin, Xiao, Yitian, Rupp, John A., 2013. Assessing the feasibility of CO2 storage in the New Albany Shale (Devonian–Mississippian) with potential enhanced gas recovery using reservoir simulation. Int. J. Greenhouse Gas Control 17, 111–126. http://dx.doi.org/10.1016/j.ijggc.2013.04.018.

Liu, Zhe, Forouzanfar, Fahim, 2018. Ensemble clustering for efficient robust optimization of naturally fractured reservoirs. Comput. Geosci. 22 (1), 283–296. http://dx.doi.org/10.1007/s10596-017-9689-1.

Maalim, Abdiaziz Abdullahi, Mahmud, Hisham Ben, Seyyedi, Mojtaba, 2021. Assessing roles of geochemical reactions on CO2 plume, injectivity and residual trapping. Energy Geosci. 2 (4), 327–336. http://dx.doi.org/10.1016/j.engeos.2021.02.002.

MacEachren, Alan M., Davidson, John V., 1987. Sampling and isometric mapping of continuous geographic surfaces. The American Cartogr. 14 (4), 299–320. http://dx.doi.org/10.1559/152304087783875723.

Mahjour, Seyed Kourosh, Al-Askari, Mohammad Kamal Ghasem, Masihi, Mohsen, 2016. Identification of flow units using methods of Testerman statistical zonation, flow zone index, and cluster analysis in Tabnaak gas field. J. Petroleum Explor. Prod. Technol. 6 (4), 577–592. http://dx.doi.org/10.1007/s13202-015-0224-4.

Mahjour, Seyed Kourosh, Correia, Manuel Gomes, dos Santos, Antonio Alberto de Souza, Schiozer, Denis José, 2019. Developing a workflow to represent fractured carbonate reservoirs for simulation models under uncertainties based on flow unit concept. Oil & Gas Sci. Technol.–Revue D'IFP Energies Nouvelles 74, 15. http://dx.doi.org/10.2516/ogst/2018096.

Mahjour, Seyed Kourosh, Correia, Manuel Gomes, Santos, Antonio Alberto de Souza dos, Schiozer, Denis José, 2020a. Using an integrated multidimensional scaling and clustering method to reduce the number of scenarios based on flow-unit models under geological uncertainties. J. Energy Resour. Technol. 142 (6), http://dx.doi.org/10.1115/1.4045736.

Mahjour, S.K., Dos Santos, AA.D.S., Correia, M.G., Schiozer, D.J., 2020b. Two-stage scenario reduction process for an efficient robust optimization. In: ECMOR XVII. 2020, (1), European Association of Geoscientists & Engineers, pp. 1–25. http://dx.doi.org/10.3997/2214-4609.202035105.

Mahjour, Seyed Kourosh, Santos, Antonio Alberto Souza, Correia, Manuel Gomes, Schiozer, Denis José, 2021a. Scenario reduction methodologies under uncertainties for reservoir development purposes: distance-based clustering and metaheuristic algorithm. J. Petroleum Explor. Prod. Technol. 11 (7), 3079–3102. http://dx.doi.org/10.1007/s13202-021-01210-5.

Mahjour, Seyed Kourosh, Santos, Antonio Alberto Souza, Santos, Susana Margarida da Graca, Schiozer, Denis Jose, 2021b. Selection of representative scenarios using multiple simulation outputs for robust well placement optimization in greenfields. In: SPE Annual Technical Conference and Exhibition. OnePetro, http://dx.doi.org/10.2118/206300-MS.

Mahjour, Seyed Kourosh, da Silva, Luís Otávio Mendes, Meira, Luis Augusto Angelotti, Coelho, Guilherme Palermo, dos Santos, Antonio Alberto de Souza, Schiozer, Denis José, 2022. Evaluation of unsupervised machine learning frameworks to select representative geological realizations for uncertainty quantification. J. Pet. Sci. Eng. 209, 109822. http://dx.doi.org/10.1016/j.petrol.2021.109822.

Malkauthekar, M.D., 2013. Analysis of Euclidean distance and Manhattan distance measure in Face recognition. In: Third International Conference on Computational Intelligence and Information Technology (CIIT 2013). IET, pp. 503–507. http://dx.doi.org/10.1049/cp.2013.2636.

McLennan, Jason, Deutsch, Clayton Vernon, 2005. Ranking geostatistical realizations by measures of connectivity. In: SPE International Thermal Operations and Heavy Oil Symposium. OnePetro, http://dx.doi.org/10.2118/98168-MS.

Meira, Luis A.A., Coelho, Guilherme P., Santos, Antonio Alberto S., Schiozer, Denis J., 2016. Selection of representative models for decision analysis under uncertainty. Comput. Geosci. 88, 67–82. http://dx.doi.org/10.1016/j.cageo.2015.11.012.

Meira, Luis A.A., Coelho, Guilherme P., da Silva, Celmar G., Abreu, João LA, Santos, Antonio A.S., Schiozer, Denis J., 2020. Improving representativeness in a scenario reduction process to aid decision making in petroleum fields. J. Pet. Sci. Eng. 184, 106398. http://dx.doi.org/10.1016/j.petrol.2019.106398.

Montanari, Alberto, Brath, Armando, 2004. A stochastic approach for assessing the uncertainty of rainfall-runoff simulations. Water Resour. Res. 40 (1), http://dx.doi.org/10.1029/2003WR002540.

Motie, M., Bemani, A., Soltanmohammadi, R., 2018. On the estimation of phase behavior of CO2-based binary systems using ANFIS optimized by GA algorithm. In: Fifth CO2 Geological Storage Workshop. 2018, (1), EAGE Publications BV, pp. 1–5. http://dx.doi.org/10.3997/2214-4609.201803006.

Nghiem, Long, Sammon, Peter, Grabenstetter, Jim, Ohkuma, Hiroshi, 2004. Modeling CO2 storage in aquifers with a fully-coupled geochemical EOS compositional simulator. In: SPE/DOE Symposium on Improved Oil Recovery. OnePetro, http://dx.doi.org/10.2118/89474-MS.

Nghiem, Long X., Yang, Chaodong, Shrivastava, Vijay Kumar, Kohse, Bruce Frederick, Hassam, Mohamed Shamshudin, Chen, Dingjun, Card, Colin, 2009. Optimization of residual gas and solubility trapping for CO2 sequestration in saline aquifers. In: SPE Reservoir Simulation Symposium. OnePetro, http://dx.doi.org/10.2118/119080-MS.

Nilsen, Halvor Møll, Lie, Knut-Andreas, Andersen, Odd, 2015. Analysis of CO2 trapping capacities and long-term migration for geological formations in the Norwegian North Sea using MRST-co2lab. Comput. Geosci. 79, 15–26. http://dx.doi.org/10.1016/j.cageo.2015.03.001.

Oliveira, G.P., Santos, M.D., Roque, W.L., 2020. Constrained clustering approaches to identify hydraulic flow units in petroleum reservoirs. J. Pet. Sci. Eng. 186, 106732. http://dx.doi.org/10.1016/j.petrol.2019.106732.

Ontañón, Santiago, 2020. An overview of distance and similarity functions for structured data. Artif. Intell. Rev. 53 (7), 5309–5351. http://dx.doi.org/10.1007/s10462-020-09821-w.

Orsenigo, Carlotta, Vercellis, Carlo, 2013. Linear versus nonlinear dimensionality reduction for banks' credit rating prediction. Knowl.-Based Syst. 47, 14–22. http://dx.doi.org/10.1016/j.knosys.2013.03.001.

Panaretos, Victor M., Zemel, Yoav, 2019. Statistical aspects of Wasserstein distances. Annu. Rev. Stat. Appl. 6, 405–431. http://dx.doi.org/10.1146/annurev-statistics-030718-104938.

Panjalizadeh, Hamed, Alizadeh, Nasser, Mashhadi, Hadi, 2014. A workflow for risk analysis and optimization of steam flooding scenario using static and dynamic proxy models. J. Pet. Sci. Eng. 121, 78–86. http://dx.doi.org/10.1016/j.petrol.2014.06.010.

Park, Jihoon, Jin, Jeongwoo, Choe, Jonggeun, 2016. Uncertainty quantification using streamline based inversion and distance based clustering. J. Energy Resour. Technol. 138 (1), http://dx.doi.org/10.1115/1.4031446.

Pinheiro, Marisa, Emery, Xavier, Miranda, Tiago, Lamas, Luís, Espada, Margarida, 2018. Modelling geotechnical heterogeneities using geostatistical simulation and finite differences analysis. Minerals 8 (2), 52. http://dx.doi.org/10.3390/min8020052.

Porter, Jack R., Woods, R. Grant, 2012. Extensions and Absolutes of Hausdorff Spaces. Springer Science & Business Media.

Preux, Christophe, 2016. About the use of quality indicators to reduce information loss when performing upscaling. Oil & Gas Sci. Technol.–Revue D'IFP Energies Nouvelles 71 (1), 7. http://dx.doi.org/10.2516/ogst/2014023.

Ranganathan, Panneerselvam, van Hemert, Patrick, Rudolph, E. Susanne J., Zitha, Pacelli Z.J., 2011. Numerical modeling of CO2 mineralisation during storage in deep saline aquifers. Energy Procedia 4, 4538–4545. http://dx.doi.org/10.1016/j.egypro.2011.02.411.

Santos, Susana M.G., Santos, Antonio A.S., Schiozer, Denis J., 2020. Selecting representative models for ensemble-based production optimization in carbonate reservoirs with intelligent wells and WAG injection. In: ECMOR XVII. 2020, (1), European Association of Geoscientists & Engineers, pp. 1–28. http://dx.doi.org/10.3997/2214-4609.202035041.

Scheidt, Céline, Caers, Jef, 2009. Representing spatial uncertainty using distances and kernels. Math. Geosci. 41 (4), 397–419. http://dx.doi.org/10.1007/s11004-008-9186-0.

Schiozer, Denis José, Avansi, Guilherme Daniel, de Souza dos Santos, Antonio Alberto, 2017. Risk quantification combining geostatistical realizations and discretized Latin Hypercube. J. Braz. Soc. Mech. Sci. Eng. 39 (2), 575–587. http://dx.doi.org/10.1007/s40430-016-0576-9.

Schiozer, Denis José, dos Santos, Antonio Alberto de Souza, de Graça Santos, Susana Margarida, von Hohendorff Filho, João Carlos, 2019. Model-based decision analysis applied to petroleum field development and management. Oil & Gas Sci. Technol.–Revue D'IFP Energies Nouvelles 74, 46. http://dx.doi.org/10.2516/ogst/2019019.

Schölkopf, Bernhard, Smola, Alexander, Müller, Klaus-Robert, 1997. Kernel principal component analysis. In: International Conference on Artificial Neural Networks. Springer, pp. 583–588. http://dx.doi.org/10.1007/BFb0020217.

Shan, Liqun, Cao, Liyuan, Guo, Boyun, 2018. Identification of flow units using the joint of WT and LSSVM based on FZI in a heterogeneous carbonate reservoir. J. Pet. Sci. Eng. 161, 219–230. http://dx.doi.org/10.1016/j.petrol.2017.11.015.

Sharma, Shweta, Batra, Neha, et al., 2019. Comparative study of single linkage, complete linkage, and ward method of agglomerative clustering. In: 2019 International Conference on Machine Learning, Big Data, Cloud and Parallel Computing (COMITCon). IEEE, pp. 568–573. http://dx.doi.org/10.1109/COMITCon.2019.8862232.

Shepherd, Anita, Martin, Mike, Hastings, Astley, 2021. Uncertainty of modelled bioenergy with carbon capture and storage due to variability of input data. GCB Bioenergy 13 (4), 691–707. http://dx.doi.org/10.1111/gcbb.12803.

Shirangi, Mehrdad G., Durlofsky, Louis J., 2016. A general method to select representative models for decision making and optimization under uncertainty. Comput. Geosci. 96, 109–123. http://dx.doi.org/10.1016/j.cageo.2016.08.002.

Soong, Yee, Crandall, Dustin, Howard, Bret H., Haljasmaa, Igor, Dalton, Laura E., Zhang, Liwei, Lin, Ronghong, Dilmore, Robert M., Zhang, Wu, Shi, Fan, et al., 2018. Permeability and mineral composition evolution of primary seal and reservoir rocks in geologic carbon storage conditions. Environ. Eng. Sci. 35 (5), 391–400. http://dx.doi.org/10.1089/ees.2017.0197.

Sorzano, Carlos Oscar Sánchez, Vargas, Javier, Montano, A. Pascual, 2014. A survey of dimensionality reduction techniques. http://dx.doi.org/10.48550/arXiv.1403.2877, arXiv preprint arXiv:1403.2877.

Stryjek, R., Vera, J.H., 1986. PRSV: An improved Peng—Robinson equation of state for pure compounds and mixtures. Can. J. Chem. Eng. 64 (2), 323–333. http://dx.doi.org/10.1002/cjce.5450640224.

Sumithra, V., Surendran, Subu, 2015. A review of various linear and non linear dimensionality reduction techniques. Int. J. Comput. Sci. Inf. Technol. 6, 2354–2360.

Sun, Wenyue, Durlofsky, Louis J., 2019. Data-space approaches for uncertainty quantification of CO2 plume location in geological carbon storage. Adv. Water Resour. 123, 234–255. http://dx.doi.org/10.1016/j.advwatres.2018.10.028.

Suzuki, Satomi, Caers, Jef Karel, 2006. History matching with an uncertain geological scenario. In: SPE Annual Technical Conference and Exhibition. OnePetro, http://dx.doi.org/10.2118/102154-MS.

Tadjer, Amine, Bratvold, Reidar B., 2021. Managing uncertainty in geological CO2 storage using Bayesian evidential learning. Energies 14 (6), 1557. http://dx.doi.org/10.3390/en14061557.

Thanh, Hung Vo, Sugai, Yuichi, Nguele, Ronald, Sasaki, Kyuro, 2020. Robust optimization of CO2 sequestration through a water alternating gas process under geological uncertainties in Cuu Long Basin, Vietnam. J. Natural Gas Sci. Eng. 76, 103208. http://dx.doi.org/10.1016/j.jngse.2020.103208.

Trehan, Sumeet, Carlberg, Kevin T., Durlofsky, Louis J., 2017. Error modeling for surrogates of dynamical systems using machine learning. Internat. J. Numer. Methods Engrg. 112 (12), 1801–1827. http://dx.doi.org/10.1002/nme.5583.

Vilarrasa, Victor, Bolster, Diogo, Olivella, Sebastia, Carrera, Jesus, 2010. Coupled hydromechanical modeling of CO2 sequestration in deep saline aquifers. Int. J. Greenhouse Gas Control 4 (6), 910–919. http://dx.doi.org/10.1016/j.ijggc.2010.06.006.

Wilkinson, Mark, Polson, Debbie, 2019. Uncertainty in regional estimates of capacity for carbon capture and storage. Solid Earth 10 (5), 1707–1715. http://dx.doi.org/10.5194/se-10-1707-2019.

Wilson, Kurt C., Durlofsky, Louis J., 2013. Optimization of shale gas field development using direct search techniques and reduced-physics models. J. Pet. Sci. Eng. 108, 304–315. http://dx.doi.org/10.1016/j.petrol.2013.04.019.

Xu, Ruina, Li, Rong, Ma, Jin, He, Di, Jiang, Peixue, 2017. Effect of mineral dissolution/precipitation and CO2 exsolution on CO2 transport in geological carbon storage. Acc. Chem. Res. 50 (9), 2056–2066. http://dx.doi.org/10.1021/acs.accounts.6b00651.

Xue, Bin, Oldfield, Christopher J., Dunker, A. Keith, Uversky, Vladimir N., 2009. CDF it all: consensus prediction of intrinsically disordered proteins based on various cumulative distribution functions. FEBS Lett. 583 (9), 1469–1474. http://dx.doi.org/10.1016/j.febslet.2009.03.070.

Yu, Peng, 2021. Hydraulic unit classification of un-cored intervals/wells and its influence on the productivity performance. J. Pet. Sci. Eng. 197, 107980. http://dx.doi.org/10.1016/j.petrol.2020.107980.

Zhang, Dongmei, Shen, Ao, Jiang, Xinwei, Kang, Zhijiang, 2018. Efficient history matching with dimensionality reduction methods for reservoir simulations. Simulation 94 (8), 739–751. http://dx.doi.org/10.1177/0037549717742963.

ESM Data Downscaling: A Comparison of Super-Resolution Deep Learning Models

Nikhil Pawar[a], Ramin Soltanmohammadi[a], Seyed Kourosh Mahjour[a] and Salah A. Faroughi[a]

[a]Geo-Intelligence Laboratory, Ingram School of Engineering, Texas State University, San Marcos, Texas, 78666, USA

ARTICLE INFO

Keywords:

E3SM Data

Super-resolution CNN

Fast Super-resolution ESM-CNN

Efficient Sub-pixel CNN

Enhanced Deep Residual Networks

Super-resolution GAN

ABSTRACT

Generating climate change projections at finer spatial resolutions using climate models demand significant computational resources. To address this challenge, various deep learning-based techniques can be employed to produce higher-resolution climate change projections. This study evaluates and compares five deep learning-based super-resolution techniques including super-resolution convolutional neural networks, fast super-resolution convolutional neural networks ESM, efficient sub-pixel convolutional neural networks, enhanced deep residual networks (EDRN), and super-resolution generative adversarial networks (SRGAN). These techniques are applied to the Energy Exascale Earth System Model datasets, focusing on key surface variables: surface temperature, shortwave heat flux, and longwave heat flux. The models undergo training and validation using paired high-resolution (0.25°) and low-resolution (1°) data from the initial 9 years. Subsequently, blind testing is performed on the data for 10^{th} and 19^{th} years. Our findings show that EDRN surpasses all other algorithms in terms of peak-signal-to-noise ratio, structural similarity index, and mean squared error. EDRN demonstrated a noteworthy 33% reduction in mean squared error compared to BC interpolation for both 10^{th}-year and 19^{th}-year blind testing set. However, EDRN faces challenges in accurately capturing intricate details within climate change projections. On the other hand, SRGAN, being a generative model that relies on perceptual loss for learning, requires higher computational resources compared to EDRN, but showed a 25% improvement in the similarity of the perceptual image patch learned during both 10^{th} and 19^{th} years of blind testing compared to BC interpolation. Hence, SRGAN showed better accuracy in capturing boundaries, internal structure, and fine details in high-resolution climate change data compared to other techniques.

CRediT authorship contribution statement

Nikhil Pawar: Implementation of the models and preparation of the manuscript. **Ramin Soltanmohammadi:** Implementation of the models, Writing - Review & Editing. . **Seyed Kourosh Mahjour:** Data Preparation, Writing - Review & Editing.. **Salah A. Faroughi:** Conceptualization, Supervision, Funding acquisition, Writing - Review & Editing. All authors have read and agreed to the contributions of the manuscript.

1. Introduction

Understanding the changes in climate patterns and their impact on society is significantly important. Rising temperatures, increasing sea-level, and the escalating frequency of extreme weather events make many forms of our society vulnerable. These vulnerabilities extend to our health, urban infrastructure, natural resources, energy systems, and transportation systems (Nicholls and Cazenave, 2010; Trenberth, 2012; Vandal et al., 2017). Therefore, to conduct the risk assessment and adaptation planning for climatological issues, local and regional climate change future projections are of higher importance (Mahjour et al., 2023; Soltanmohammadi et al., 2024). Earth System Models (ESMs) represent physics-based numerical models that currently run on massive supercomputers. These models simulate Earth's past climate and project future scenarios, considering changes in atmospheric greenhouse gas emissions. However, the ESMs typically work at coarse horizontal resolutions, around 1° to 3°, which can lead to inaccuracies in representing crucial physical processes, such as extreme precipitation (Vandal et al., 2017; Schmidt, 2010; Passarella et al.,

ORCID(s): 0000-0002-4423-8884 (N. Pawar); 0000-0002-4423-8884 (R. Soltanmohammadi); 0000-0002-4423-8884 (S.K. Mahjour); 0000-0002-6543-1691 (S.A. Faroughi)

2022; Kharin et al., 2007). Recent progress has enabled global ESMs to operate at higher horizontal resolutions, approximately 0.25°, for extended durations. This development has demonstrated enhancements in simulating both regional average climate conditions and extreme events (Mahajan et al., 2015; Ahmadi et al., 2020), albeit at a high computational cost.

To address the computational challenge, downscaling techniques such as statistical downscaling and dynamical modeling, have been employed in the literature to generate high-resolution ESM climate change data. Dynamical downscaling aka regional climate models, necessitates the implementation of high-resolution (HR) regional dynamical models to extend large-scale boundary conditions acquired from a coarser global ESM to more detailed regional resolution. Similar to ESMs, regional climate models require substantial computational resources and exhibit limited transferability across different regions (Vandal et al., 2017). Therefore, to mitigate the computational cost constraints, statistical downscaling is employed. Statistical downscaling is a technique used to convert coarse-resolution climate data into high-resolution projections by incorporating observational data through the application of statistical methods (Passarella et al., 2022). This technique involves developing a statistical relationship between the observed climate data and the output of the climate model for the large-scale climate patterns resolved by global climate models. These relationships are then applied to the output generated by global climate models to transform climate model outputs into statistically refined products, which are often considered to be more appropriate for use as input to regional or local climate impact studies (Tabari et al., 2021). Statistical downscaling involves two categories for spatial downscaling: (i) regression models, and (ii) weather classification. Regression models includes automatic statistical downscaling (Hessami et al., 2008), Bayesian model averaging (Zhang and Yan, 2015), expanded downscaling (Bürger, 1996; Bürger and Chen, 2005), and bias-corrected spatial disaggregation (BCSD) (Thrasher et al., 2012). On the other hand, weather classification includes methods such as nearest neighbor estimates (Hidalgo et al., 2008) and hierarchical Bayesian inference models (Manor and Berkovic, 2015).

Recently, regression-based statistical downscaling has been extended to include machine learning techniques, such as neural networks (Fistikoglu and Okkan, 2011; Vu et al., 2016), quantile regression neural networks (Cannon, 2011), and support vector machines (Ghosh, 2010), for statistical downscaling. These techniques demonstrate superior performance when compared to conventional statistical downscaling methods. In addition to machine learning techniques, computer vision-based statistical downscaling techniques known as super-resolution (SR) emerge Vandal et al. (2017). These methods generalize patterns across images and show to learn local-scale patterns more efficiently than other statistical downscaling techniques. Vandal et al. (2017) introduced the stacked SR convolutional neural networks (SRCNN), DeepSD, which downscaled climate and ESM-based observational and topographical data across the continental United States. DeepSD outperforms BCSD, artificial neural networks, Lasso, and SVM in downscaling performance. Furthermore, Passarella et al. (2022) proposed a fast SRCNN ESM (FSRCNN-ESM) that surpasses DeepSD and FSRCNN models in downscaling features such as surface temperature, surface radiative fluxes, and precipitation in ESM data over North America. Noteworthy studies also leveraged a super-resolution generative adversarial networks (SRGAN) to enhance wind and solar data by a factor of 50 (Stengel et al., 2020). Advancements in this domain include physics-informed SRGAN, integrating climatologically important physical information such as pressure and topography into the network to achieve significant downscaling of temperature and precipitation data by a factor of 50 (Oyama et al., 2023). Accordingly, vanilla deep learning shows promise in downscaling ESM climate change data. However, there's a lack of systematic comparison of state-of-the-art SR techniques globally in the existing literature. In this study, we aim to fill this void by exploring five vanilla SR methods, namely, SRCNN (Dong et al., 2014), FSRCNN-ESM (Passarella et al., 2022), efficient sub-pixel convolutional neural networks (ESPCN) (Talab et al., 2019), enhanced deep residual networks (EDRN) (Lim et al., 2017) and SRGAN (Ledig et al., 2017). We conduct a systematic comparison of five vanilla deep learning-based SR techniques to assess their performance on an ESM climate change data named Energy Exascale Earth Systems Model (E3SM) (E3SM Project, 2018). Our focus is on key climate features such as surface temperature (TS), shortwave heat flux (FSNS), and longwave heat flux features (FLNS) over the entire world. Additionally, we employ sliced data from the 10^{th} and 19^{th} years for blind testing. To facilitate comprehensive model comparison, we employ evaluation metrics including absolute point error (APE) (Faroughi et al., 2022), peak-signal-to-noise ratio (PSNR) (Deng, 2018), structural similarity index (SSIM) (Dosselmann and Yang, 2011), learned perceptual image patch similarity (LPIPS) (Zhang et al., 2018), and mean squared error (MSE) (Motie et al., 2018).

The remaining sections of this work are structured as follows: Section 2 elaborates on the data acquisition and pre-processing. Section 3 discusses the SR CNN-based techniques employed in this paper. Section B discusses the evaluation metrics employed for comparing all the algorithms in the study. In Section 4, we investigate and analyze the results of individual algorithms, and compare the results of various algorithms. Finally, in Section 5, we summarize

the main conclusions of this work.

2. E3SM Simulation Data

For this study, we use the monthly output spanning the first 10^{th}-year and 19^{th}-year segments from the 1950-control simulation conducted using the global high-resolution (0.25°) configuration of the Energy Exascale Earth Systems Model (E3SM) (E3SM Project, 2018). The E3SM data undergo bilinear interpolation from their original non-orthogonal cubed-sphere grid to a regular $0.25° \times 0.25°$ longitude-latitude grid, resulting in the interpolated model data known as E3SM-HR. To generate corresponding low-resolution input images, the high-resolution data is further interpolated onto a $1° \times 1°$ grid using a bicubic (BC) method (Passarella et al., 2022). This interpolation process removes fine-scale details present in the original high-resolution data, creating low-resolution images. The objective of this study is to employ models based on super-resolution convolutional neural networks to regenerate high-resolution images from these coarsened data. In applying deep-learning techniques with gridded E3SM data, each grid point is treated as an image pixel. The global high-resolution data is organized into an image with dimensions of 720×1440 pixels, while the corresponding low-resolution image has dimensions of 180×360 pixels. The global data is then divided into 18 slices, and within each slice, the low-resolution images measure 60×60 pixels, while the high-resolution images measure 240×240 pixels. We select TS, FSNS, and FLNS to evaluate the SR models. As depicted in Fig. 1, the total number of datasets used for evaluation is calculated as follows: 10 (years) $\times$ 12 (months) $\times$ 5 (variables) $\times$ 18 (slices). In this study, all three variables are collectively incorporated by normalizing each of them and saving them as an RGB image. This normalization process ensures that the variables are brought to a standardized scale, enabling the use of a multi-channel network during training, thus enhancing the regeneration process. The total dataset is divided into training, validation, and blind testing sets. The training dataset consists of 80% of the total dataset for the first 9 years, while the remaining 20% is utilized for the validation set. For the purpose of blind testing, the two sets corresponding to the 10^{th}-year and 19^{th}-year features TS, FSNS, and FLNS are utilized.

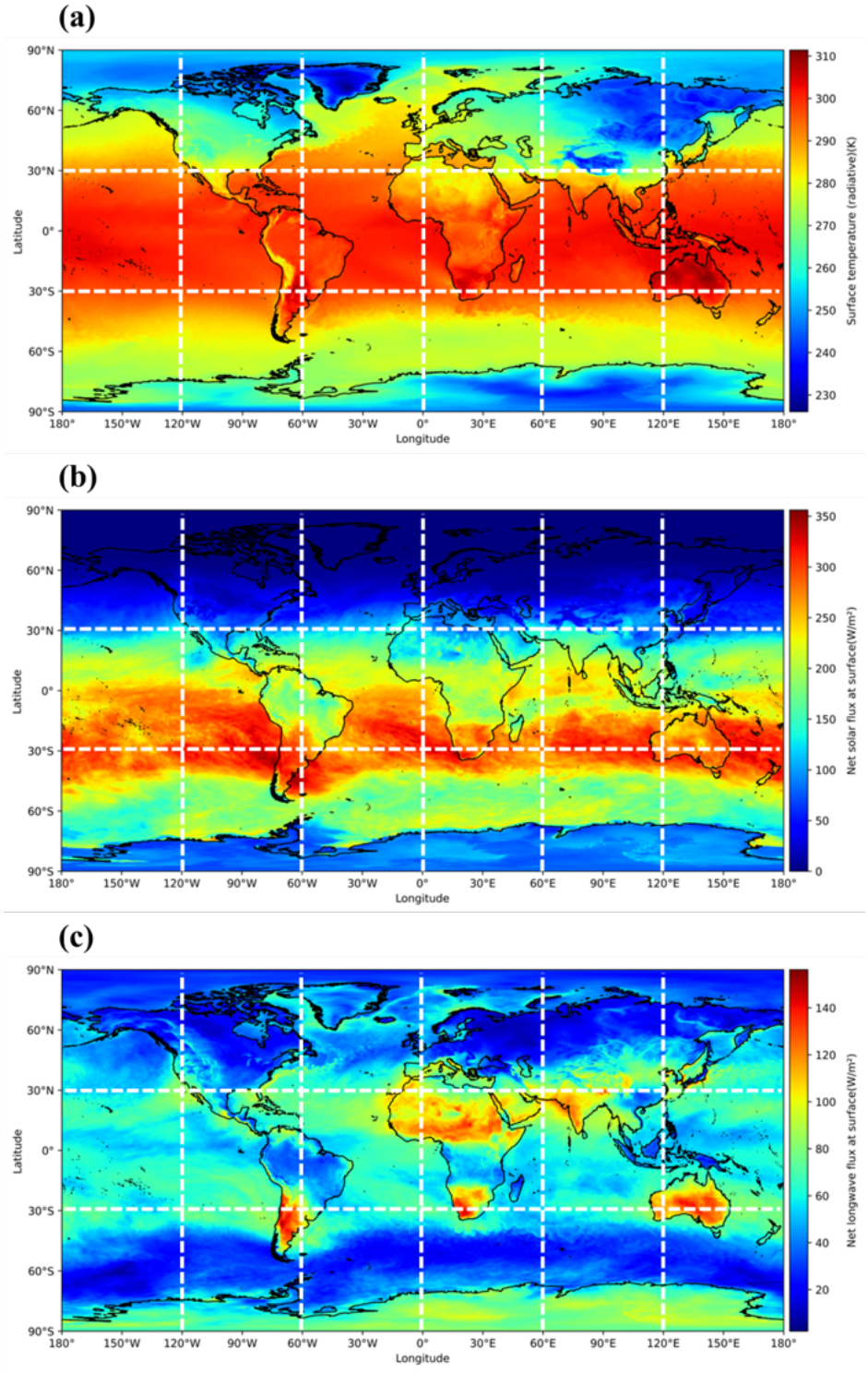

Figure 1: The schematic procedure of data production for super-resolution technique. Panel (a) displays surface temperature, Panel (b) shows net solar flux, and Panel (c) displays net longwave for the first month of year 1 obtained from the global high-resolution configuration of E3SM. It showcases the division of each month into 18 distinct sections, as visually represented. Each HR month comprises a matrix of dimensions 720 by 1440. Through the division into 18 segments, each individual section transforms into a 240 by 240 matrix, subsequently converted as a 240 by 240 image.

3. Methodologies

This section provides an overview of the five vanilla architectures used in our study: SRCNN, FSRCNN, ESPCN, EDRN, and SRGAN. The SRCNN model uses the BC interpolation as input and features a shallow architecture. In contrast, both the FSRCNN and the ESPCN techniques use the LR image as input for ESM climate data super-resolution. The EDRN model employs a deep architecture and incorporates skip connections to retain important features from earlier layers. The SRGAN architecture consists of a generator and a discriminator, where the generator generates a high-resolution image utilizing the low-resolution image. The algorithms and their architectural intricacies are detailed in Appendix A. Furthermore, the evaluation metrics used to assess the models' performance are succinctly described in Appendix B.

4. Computational Experiments

4.1. Training and Validation

The training process is conducted using an NVIDIA RTX A6000 GPU with 47.5 GB of dedicated GPU memory (vRAM). Additionally, the computer used for training is equipped with an Intel(R) Xeon(R) W7-3455 processor and boasts 512 GB of RAM capacity. Detailed information about the number of parameters and the time required for training each algorithm can be found in Table 1. The SRGAN model has the most trainable parameters (2,039,939) and the longest training time (970 hours). This is because the discriminator network in SRGAN compares two RGB images sized 240×240. The ESPCN model is the most computationally efficient, with a training time of 15.27 hours, despite having more trainable parameters than SRCNN and FSRCNN-ESM. This is due to the efficient training approach used in ESPCN, as discussed in (Shi et al., 2016).

Table 1
Comparison of the number of trainable parameters and training time in hours for the algorithms used in this study for 10,000 epochs.

Model	Number of parameters	Training Time (hours)
SRCNN	20,099	23.6
FSRCNN-ESM	31,032	26.38
EPSNN	74,128	15.27
EDRN	1,517,571	66.66
SRGAN	2,039,939	970

Table 2 presents the evaluation metrics for each algorithm on the training set. The results show a clear trend: PSNR increases from BC to EDRN, with SRGAN exhibiting the lowest PSNR values. In contrast, the SSIM values do not show a clear pattern across the dataset, although SRGAN has the lowest SSIM score. Furthermore, the MSE exhibits an inverse trend, decreasing from BC to EDRN, with SRGAN having a value slightly higher than BC but lower than the other methods. The lower PSNR and SSIM values for SRGAN have been reported in previous literature (Ledig et al., 2017). However, it is important to note that PSNR and SSIM are not perfect measures of super-resolution. While PSNR and SSIM may decrease, the visual quality of the generated images often improves, as they capture fine detail. Therefore, it is important to use additional metrics, such as LPIPS, to assess the performance of different algorithms. LPIPS measures perceptual similarity between images, and it is a more accurate measure of image resolution than PSNR and SSIM. In this regard, LPIPS decreases from 0.297 to 0.234 from BC to SRGAN, indicating that SRGAN generates more accurate HR images than the other models. Table 3 shows the evaluation metrics for each algorithm on the validation set. The results are similar to those for the training set, indicating that the models do not overfit the training dataset. Next, we will evaluate the performance of each algorithm on the blind testing dataset.

Table 2
Comparison of evaluation metrics for HR image of surface variables generated by different models and BC interpolation using the training set.

Mode	PSNR (dB)	SSIM	LPIPS	MSE
BC	22.29	0.77	0.297	0.018
SRCNN	22.75	0.79	0.289	0.016
FSRCNN-ESM	22.93	0.75	0.283	0.016
EPSNN	23.50	0.75	0.252	0.015
EDRN	**24.39**	**0.87**	0.241	**0.011**
SRGAN	21.68	0.58	**0.234**	0.017

Table 3
Comparison of evaluation metrics for HR image of surface variables generated by different models and BC interpolation using the validation set.

Mode	PSNR (dB)	SSIM	LPIPS	MSE
BC	22.25	0.77	0.296	0.018
SRCNN	22.78	0.79	0.288	0.016
FSRCNN-ESM	22.95	0.75	0.282	0.016
EPSNN	23.50	0.75	0.252	0.016
EDRN	**23.53**	**0.86**	0.250	**0.016**
SRGAN	21.64	0.57	**0.238**	0.017

4.2. SRCNN, FSRCNN and ESPCNN BlindTesting

SRCNN takes the BC interpolation image as input and generates an HR image using three convolutional layers. For blind testing, we consider a section for the features TS, FSNS, and FLNS for the second month in the tenth year of the blind testing dataset. The results show that the PSNR, SSIM, and LPIPS values for TS are 25.88, 0.83, and 0.230, respectively, while for FSNS, they are 24.70, 0.85, and 0.209. For FLNS, the corresponding values are 20.46, 0.78, and 0.278. This indicates that SRCNN can produce high-resolution images that closely resemble the ground truth HR. After the examination and comparison of three features with respect to their visual representation and evaluation metrics, it is obviuse that FLNS poses the greatest challenge for super-resolution. Therefore, we focus on a zoomed-in cross-section of the FLNS feature to assess the resolution of the generated high-resolution image, as depicted in panel (a) of Fig.2. The results show that SRCNN outperforms BC in terms of evaluation metrics. Furthermore, SRCNN is capable of reproducing the boundary of the zoomed-in cross-section; however, it struggles to recover the internal structure and fine details of the selected cross-section.

FSRCNN-ESM uses LR image as input, unlike SRCNN, which utilizes BC interpolated image. It is an improved extension of FSRCNN, where the model after the deconvolutional step utilizes an additional SRCNN-like convolutional layer to enhance accuracy. During blind testing, we focus on a specific section in the first month of the tenth year within the blind testing set, evaluating the features of TS, FSNS, and FLNS. For TS, the PSNR, SSIM, and LPIPS values are 25.54, 0.82, and 0.251, respectively. Correspondingly, for FSNS, they measure 25.64, 0.90, and 0.165. In the case of FLNS, the respective values are 20.77, 0.78, and 0.329. These results underscore FSRCNN's ability to produce HR images closely resembling the ground truth image. Similar to SRCNN, FSRCNN-ESM encounters the most substantial challenge when generating SR images with FLNS. Panel (b) of Fig. 2 provides a zoomed-in cross-section of FLNS to illustrate this. The outcomes indicate that FSRCNN-ESM surpasses BC interpolation in terms of evaluation metrics and is capable of generating edges for the zoomed-in FLNS cross-section.

ESPCN, similar to FSRCNN-ESM, uses an LR image as input but utilizes an efficient sub-pixel convolutional layer for super-resolution. We evaluated ESPCN on a blind testing dataset of TS, FSNS, and FLNS features from

the tenth month of the tenth year. The results show that ESPCN is capable of generating high-resolution images in climate change data, similar to FSRCNN-ESM. The PSNR, SSIM, and LPIPS values for TS are 26.00, 0.86, and 0.216, respectively, while for FSNS, they are 27.81, 0.92, and 0.115. As for FLNS, the corresponding values are 20.22, 0.75, and 0.287. Like SRCNN and FSRCNN-ESM, ESPCN presents the most significant challenge to generate FLSN. Hence the panel (c) of Fig. 2 shows a zoomed-in cross-section of the FLNS feature. It is evident that, compared to BC, the internal structure is slightly sharper, and the internal structure is somewhat clearer, leading to improvements in SSIM and PSNR but a reduction in LPIPS. However, due to its limited architectural depth, ESPCN cannot produce accurate internal structure and fine details in the climate change data, resulting in a blurriness similar to that seen in FSRCNN-ESM and SRCNN.

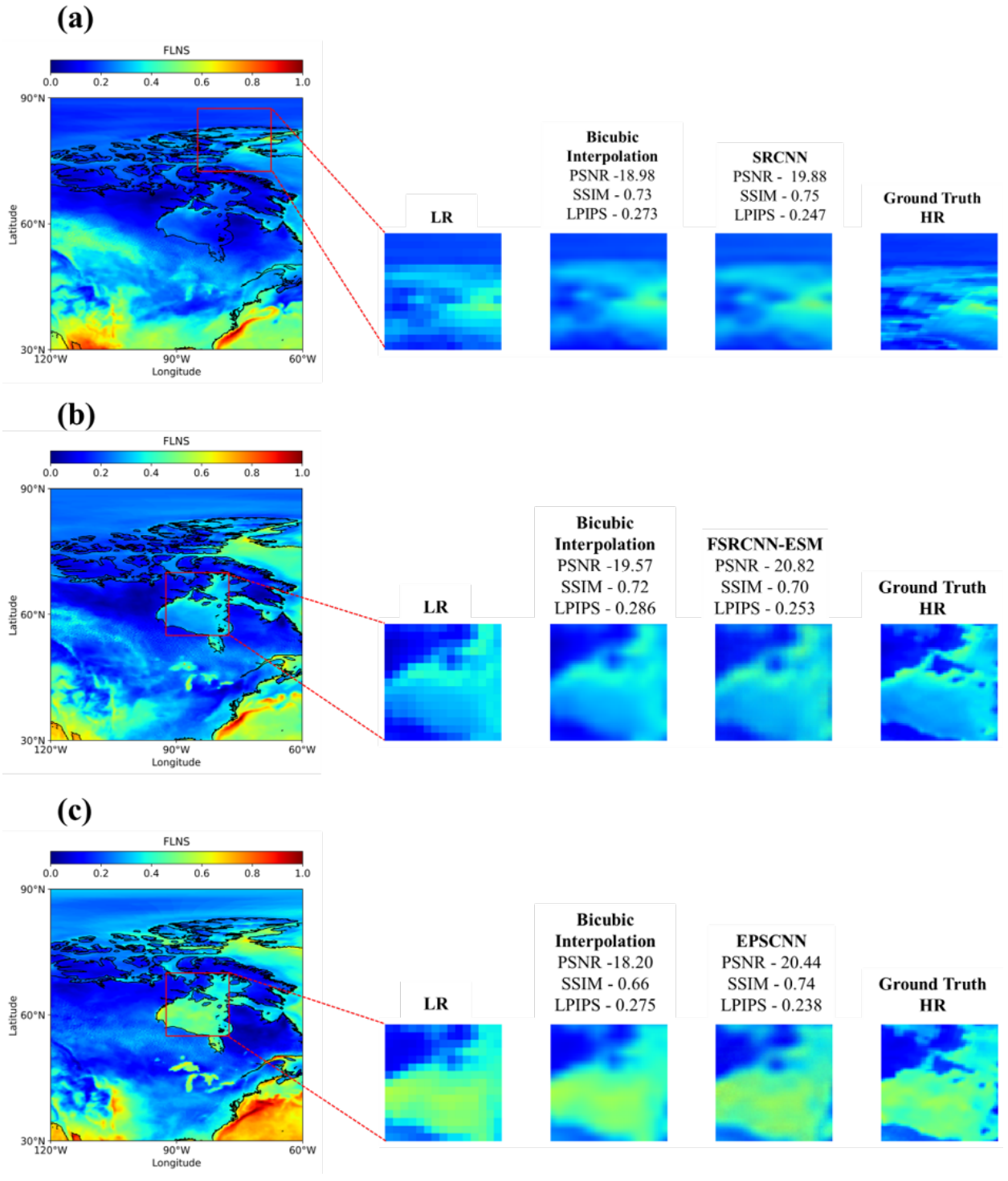

Figure 2: A comparison between generated HR, BC, and ground truth for the zoomed-in cross-section of net longwave flux. Panel (a) shows a comparison of LR, BC, SRCNN-generated, and ground truth images. Panel (b) compares LR, BC, FSRCNN-ESM-generated, and ground truth images. Panel (c) compares LR, BC, ESPCN-generated, and ground truth images.

4.3. EDRN BlindTesting

EDRN, an in-depth residual network designed for the SR task, is depicted in Figure 3 panel (a), showing LR, SR, ground truth images, and error images for TS, FSNS, and FLNS features during the 3rd month of the 10^{th}-year in the blind testing dataset. The PSNR, SSIM, and LPIPS values for TS are 27.30, 0.90, and 0.179, respectively, while for FSNS, they are 20.76, 0.85, and 0.231. As for FLNS, the corresponding values are 22.12, 0.85, and 0.238. The results show that the EDRN proficiently reconstructs HR images, preserving boundaries and closely resembling internal climate change data structure, all while maintaining a low APE. Despite its notable performance, EDRN faces a challenge in reconstructing FLNS, highlighted in Fig. 3 panel (b), showing a zoomed-in cross-section of the FLNS feature. Compared to BC interpolation, EDRN enhances PSNR, SSIM, and reduces LPIPS for the zoomed-in cross-section. However, it falls short of fully reconstructing fine climate change data details, though it excels in generating boundaries and internal structures due to its complex and deeper architecture compared to SRCNN, FSRCNN-ESM, and ESPCN.

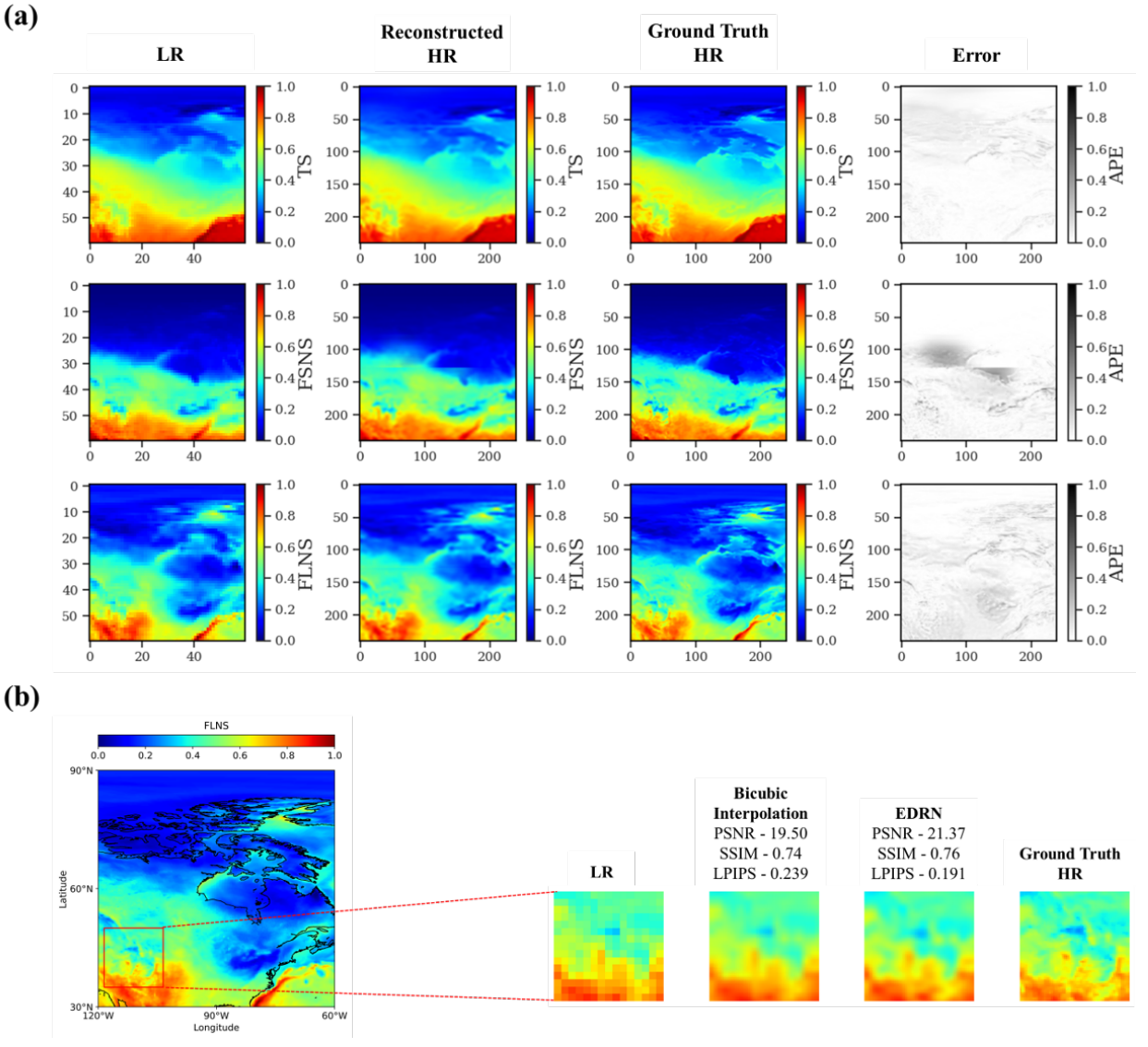

Figure 3: Comparison of the EDRN performances for generating high-resolution climate change projections. Panel (a) compares the generated HR surface variables from EDRN to the global HR configuration of the E3SM. The top row shows the TS, while the second and third rows show the FSNS and FLNS, respectively. For each row, the left column displays the LR surface variable, followed by the EDRN-generated HR surface variable, the ground truth HR surface variable from E3SM, and the APE between the generated and ground truth HR surface variables. Panel (b) compares the LR, BC, EDRN-generated, and ground truth images of a net longwave flux cross-section.

4.4. SRGAN BlindTesting

SRGAN, a more complex architecture than EDRN, comprising a generator and discriminator, is presented in Figure 4 panel (a). It shows LR, SR images generated using SRGAN, ground truth, and error images for TS, FSNS, and FLNS features during the 8th month of the 10^{th}-year in the blind testing dataset. The PSNR, SSIM, and LPIPS values for TS are 23.64, 0.77, and 0.214, respectively, while for FSNS, they are 25.87, 0.65, and 0.150. For FLNS, the corresponding values are 21.72, 0.64, and 0.219. Hence, SRGAN can capture boundaries and internal structures with minimal APE, as evident in the error images for TS, FSNS, and FLNS features. Moreover, panel (b) of Fig. 4 displays a zoomed-in cross-section of FLNS, indicating SRGAN's accuracy in capturing boundaries, internal structure, and intricate fine details, despite a low SSIM value. The application of LPIPS as an evaluation metric is justified, consid-

ering its capacity to assess perceptual image similarity, while PSNR and SSIM rely on MSE and structural similarity between the ground truth and generated HR images. Additionally, it's important to note that while the average PSNR value for SRGAN, as presented in Table 4, is lower than that for BC, there are instances, as shown in the panel (b) of Fig. 4, where there is a noticeable increase in PSNR.

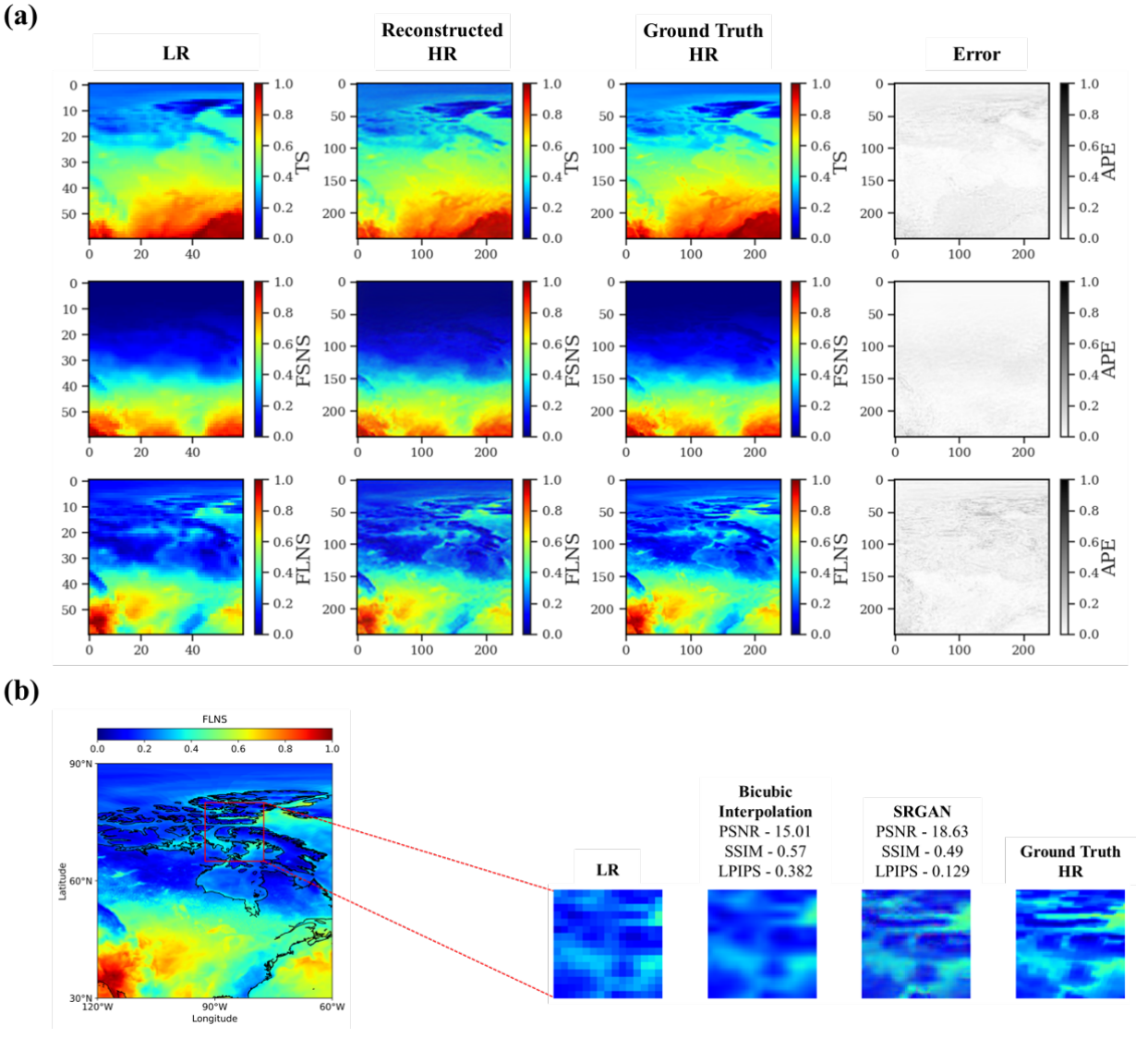

Figure 4: Comparison of the SRGAN performances for generating high-resolution climate change projections. Panel (a) compares the generated HR surface variables from SRGAN to the global HR configuration of the E3SM. The top row shows the TS, while the second and third rows show the FSNS and FLNS, respectively. For each row, the left column displays the LR surface variable, followed by the SRGAN-generated HR surface variable, the ground truth HR surface variable from E3SM, and the APE between the generated and ground truth HR surface variables. Panel (b) displays a comparison of the LR, BC, SRGAN-generated, and ground truth images of a net longwave flux cross-section.

4.5. Model Comparison

In the final analysis, we conduct a comparison of all five models to assess their effectiveness in generating high-resolution climate change projections. Figure 5 shows a comparison of the different algorithms for the FLNS feature in the 8th month of the 10^{th}-year in the blind testing dataset. Based on the evaluation metrics, PSNR and SSIM values increase from BC interpolation to EDRN, with SRGAN having the lowest SSIM and PSNR values just above BC

interpolation. However, SRGAN has the lowest LPIPS value, which indicates its superior performance in generating high-resolution images compared to other models. Furthermore, Fig. 6 shows the zoomed-in cross-section comparison of all the models for 2nd month in the 10^{th}-year blind testing dataset. A similar trend could be observed with the exception of FSRCNN-ESM performing better than ESPCN in terms of LPIPS and PSNR. This is because both the algorithms have very close values for evaluation metrics. Additionally, in terms of LPIPS, there is a significant drop from 0.291 for BC interpolation to 0.198 for SRGAN, which explains SRGAN's capability to generate both the boundary and fine details of the intricate structure.

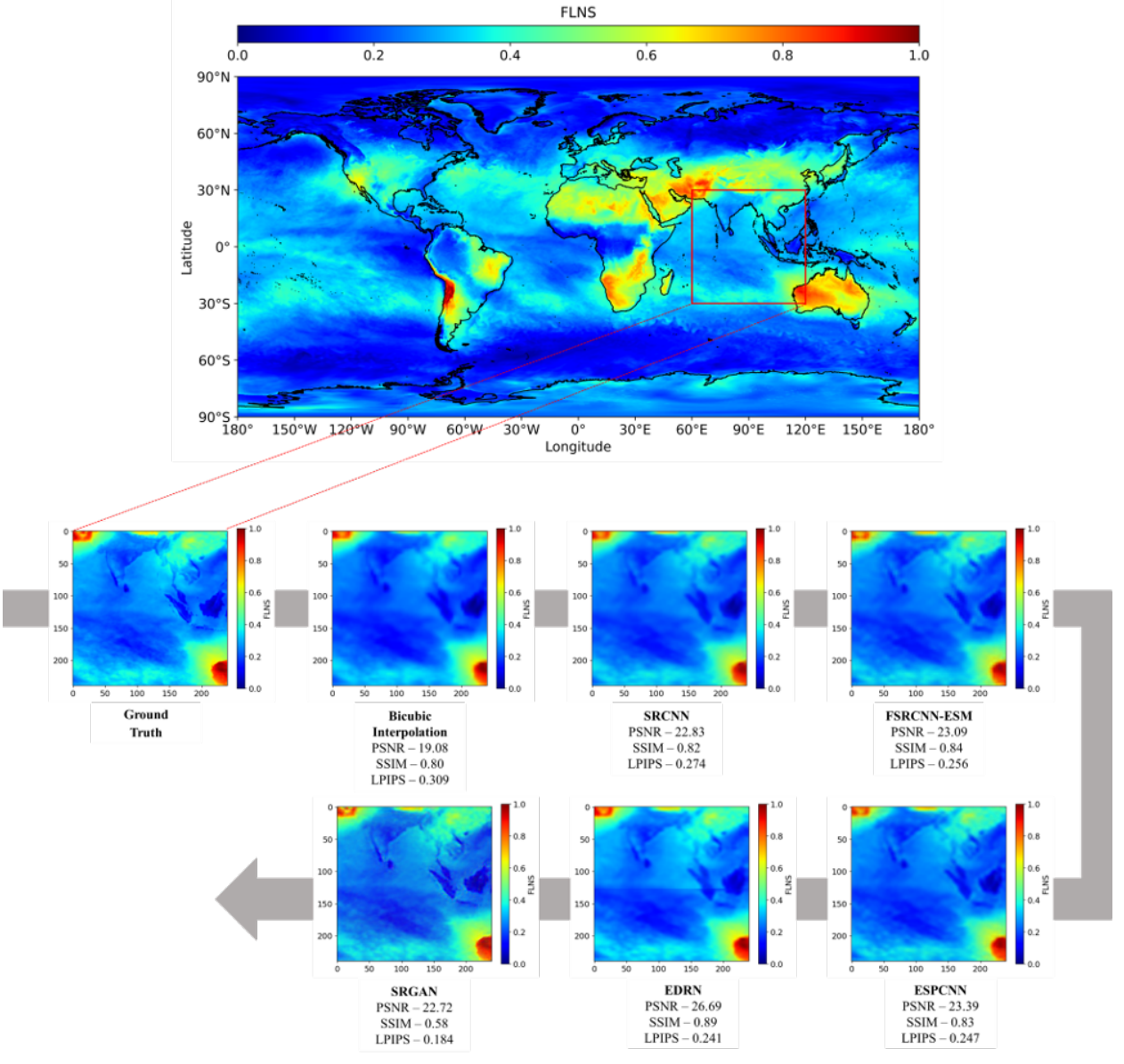

Figure 5: A comparison of various algorithms employed in this study for reconstructing HR images from LR images in the blind test reveals a consistent trend of decreasing LPIPS values from BC to SRGAN. This trend signifies that SRGAN achieves more accurate reconstruction compared to all other algorithms.

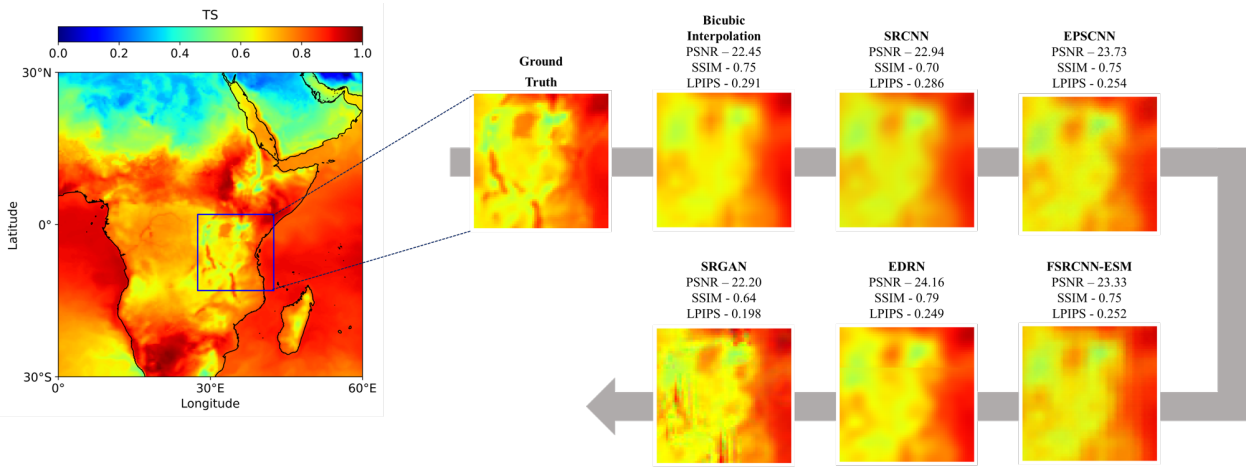

Figure 6: A comparison of various algorithms employed in this study to reconstruct HR cross-section of surface temperature. The trend indicates that SRGAN could reconstruct the perpetual features with higher accuracy compared to all other algorithms.

To understand the rationale behind the lower values of SSIM and PSNR, we present Fig. 6 which displays the MSE between the ground truth and the generated HR images using all algorithms employed in this investigation, along the diagonal axes. It is evident that the mean MSE for SRGAN slightly surpasses that of BC interpolation but remains lower than that of all the other algorithms. This is because SRGAN's loss function is based on perceptual similarity rather than statistical pixel-wise metrics, such as MSE. Hence, SRGAN generates HR images that are more perceptually realistic, even though they have lower PSNR, SSIM, and MSE values. Furthermore, to analyze the trend in the evaluation metrics, we plotted the values in the violin plot shown in Fig. 8. Panel (a) from the figure shows that the high-density distribution of PSNR for BC interpolation ranges from 15 to 35 dB. In contrast, the distribution for SRCNN is more compact and lies in the upper bound, with PSNR values ranging from 18 to 30 dB. This indicates that SRCNN results in a more concentrated PSNR distribution. Additionally, SRCNN exhibits a higher mean PSNR of 24.59 dB, compared to 24.13 dB for BC interpolation. Similarly, performance in terms of PSNR increases from FSRCNN-ESM to EDRN, with a high-density distribution of PSNR values for EDRN ranging from 18 dB to 36 dB and a mean PSNR value of 25.52. Notably, the mean PSNR value for EDRN is 25.52, indicating improved performance compared to all other algorithms. It should be noted that SRGAN has a high-density distribution for PSNR in the lower bound compared to other models, leading to the lowest mean PSNR value compared to all other algorithms.

In panel (b) of Fig. 8, SSIM shows a high-density distribution ranging from 0.69 to 0.98, with a mean value of 0.87 for BC interpolation. Applying SRCNN results in a more compact distribution, ranging from 0.73 to 0.93, with a reduced mean value of 0.83. For FSRCNN, the values range from 0.75 to 0.95, with a mean value of 0.87. For ESPCN, the values range from 0.75 to 0.97, with a mean value of 0.87. There is an improvement in the range for EDRN, i.e., from 0.82 to 0.99, accompanied by an enhancement in the mean, reaching 0.90. EDRN exhibits a compact and upper bound, high-density distribution for SSIM values, demonstrating superior performance compared to all other algorithms. Similar to PSNR, SSIM in the SRGAN has a high-density distribution in lower range values compared to other models further leading to the lowest mean SSIM value compared to all other algorithms. The Panel (c) of Fig. 8 shows the LPIPS value distribution for each algorithm. The results indicate a decreasing trend in the high-density distribution of data, becoming lower and more compact from BC interpolation to SRGAN. This trend is reflected in the mean values of LPIPS, which decrease from 0.258 to 0.193 from BC interpolation to SRGAN. This suggests that SRGAN outperforms all other algorithms. The LPIPS evaluation metric is more important compared to PSNR and SSIM, as it considers perceptual similarity compared to statistical image metrics. Panel (d) of Fig. 8 shows the inverse trend of PSNR, i.e., MSE decreases from BC to EDRN, with SRGAN having the lowest MSE.

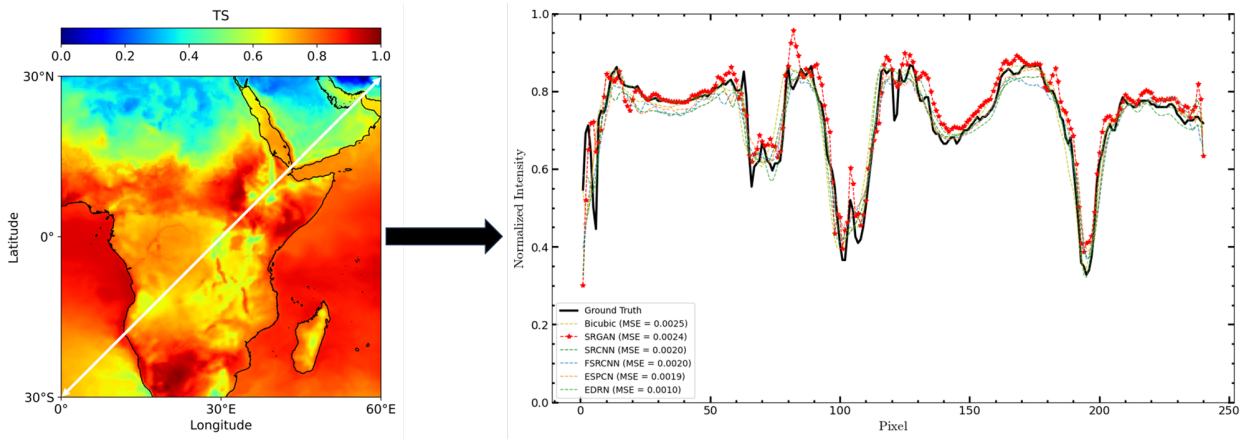

Figure 7: A comparison of the pixel values along diagonal axes indicated by the white arrow of all techniques used in this study, and the MSE between the technique and the ground truth data. Despite SRGAN achieving the lowest LPIPS score and producing images that closely resemble the ground truth, it exhibits the highest MSE. This discrepancy in MSE values explains why PSNR and SSIM metrics report lower scores for the SRGAN algorithm.

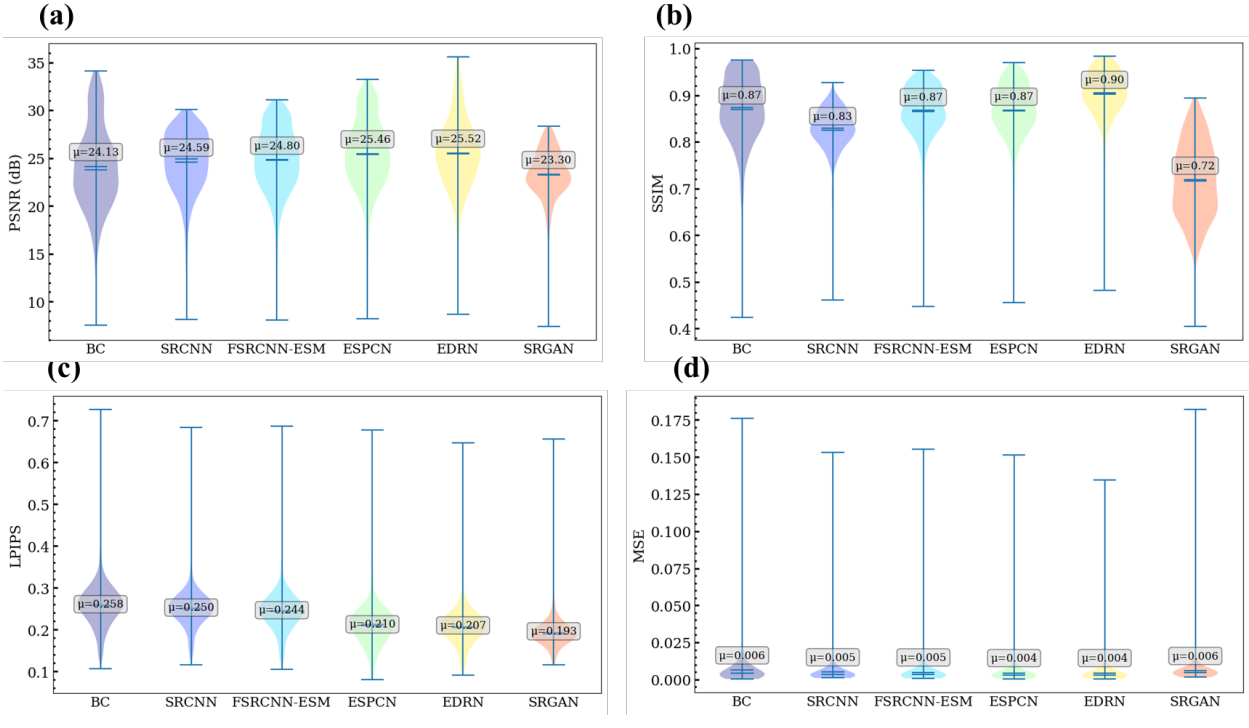

Figure 8: Violin plots for the evaluation metrics. Panels (a) to (d) depict the PSNR, SSIM, LPIPS, and MSE values, respectively, obtained from all five SR models, including BC interpolation.

Table 4
Comparison of evaluation metrics for HR image of surface variables generated by different models and BC interpolation using the blind testing set 10^{th}-year.

Mode	PSNR (dB)	SSIM	LPIPS	MSE
BC	24.13	0.87	0.258	0.006
SRCNN	24.59	0.83	0.250	0.005
FSRCNN-ESM	24.80	0.87	0.244	0.005
ESPCN	25.46	0.87	0.210	0.004
EDRN	**25.52**	**0.90**	0.207	**0.004**
SRGAN	23.30	0.72	**0.193**	0.006

Table 5
Comparison of evaluation metrics for HR image of surface variables generated by different models and BC interpolation using the blind testing set 19^{th}-year.

Mode	PSNR (dB)	SSIM	LPIPS	MSE
BC	24.17	0.87	0.257	0.006
SRCNN	24.69	0.82	0.248	0.005
FSRCNN-ESM	24.90	0.86	0.242	0.005
ESPCN	25.54	0.86	0.209	0.004
EDRN	**25.74**	**0.90**	0.206	**0.004**
SRGAN	23.30	0.71	**0.193**	0.006

Finally, when comparing Tables 2 (training), 3 (validation), and 4 (blind testing), we observe that the blind testing dataset yields better results for all evaluation metrics across all models, including BC interpolation, which is statistically based. To validate the results obtained from the blind test, we applied all the models to a random second blind test year, specifically the 19^{th}-year, as shown in Table 5. The results show a similar pattern to those of the blind testing dataset for the 10^{th}-year, thus confirming that the blind testing dataset consistently demonstrates superior performance compared to the training and evaluation datasets. This trend could be attributed to the lower number of data points in the blind testing set compared to training and evaluation datasets. Additionally, for the blind test, a similar trend could be observed in the training and evaluation datasets, where EDRN achieved the maximum PSNR and SSIM and the lowest MSE, while SRGAN attained the lowest LPIPS.

5. Conclusions

We investigated the application of super-resolution deep learning techniques for downscaling the Energy Exascale Earth Systems Model (E3SM) climate data. Our exploration includes five super-resolution methods: super-resolution convolutional neural networks (SRCCNN), fast super-resolution convolutional neural network ESM (FSRCNN-ESM), efficient sub-pixel convolutional neural networks (ESPCN), enhanced deep residual networks (EDRN), and super-resolution generative adversarial networks (SRGAN). The objective was to generate high-resolution climate change projections using the E3SM dataset. Through our evaluation and comparison of these techniques using various metrics, we observed distinct performance patterns for each model. Notably, SRGAN demonstrated superior perceptual similarity, outperforming others in learned perceptual image patch similarity, with a 25% improvement in SRGAN compared with BC for both 10^{th}-year and 19^{th}-year blind testing set. EDRN, on the other hand, showed remarkable performance in terms of peak signal-to-noise ratio (PSNR), structural similarity index, and mean squared error, generating high-resolution images with preserved boundaries and internal structure. A general trend was observed in the PSNR values, which increased in the following order: SRGAN, BC interpolation, SRCCNN, FSRCNN-ESM, ESPCN, and EDRN. The difference between EDRN and SRGAN in blind testing was 2.22 dB for 10^{th}-year and 2.44 dB for

19^{th}-year blind testing set. SRGAN showed lower traditional evaluation metrics, and higher perceptual resolution, highlighting the importance of considering perceptual similarity metrics in the evaluation. In terms of computational resources, the findings revealed that during training, SRGAN had the highest number of trainable parameters, totaling 2,039,939, is the longest training time (970 hours) compared to all other algorithms. Future work should focus on enhancing the accuracy of high-resolution climate change projections by incorporating additional physical information and optimizing algorithms. This could involve modifications such as adjusting activation functions and implementing few-shot learning to reduce computational costs. By leveraging these advancements, we can better address the complexities posed by climate change, ensuring more accurate and detailed representations for critical decision-making processes.

6. Acknowledgments

S.A.F. would like to acknowledge support from the Department of Energy's Biological and Environmental Research (BER) program. (award no. DE-SC0023044).

7. Availability Statement

The data and materials used in this study are available upon request.

A. Appendix:Methodology

A.1. SRCNN

The SRCNN architecture, as shown in Fig. 9 consists of three convolutional layers: patch extraction and representation, nonlinear mapping, and reconstruction (Dong et al., 2014). Prior to this, the LR image is upscaled to the desired size using BC interpolation, after which it is fed into these three convolutional layers. In the patch extraction step, patches are extracted from the low-resolution image and transformed into high-dimensional vectors, forming feature maps. Nonlinear mapping then converts these vectors into another set of high-dimensional vectors, representing high-resolution patches. Finally, the reconstruction layer combines these high-resolution patchwise representations to produce the final high-resolution image. The first convolutional layer has 64 filters and 9×9 kernel size, the second convolutional layer has 32 filters, a 1×1 kernel size, the final convolutional layer has 3 filters with a 5×5 kernel size, which constructs the HR image of the surface variable with a size of 240×240. The Adam optimizer is used as the optimization algorithm, while MSE is employed as the loss function for the model.

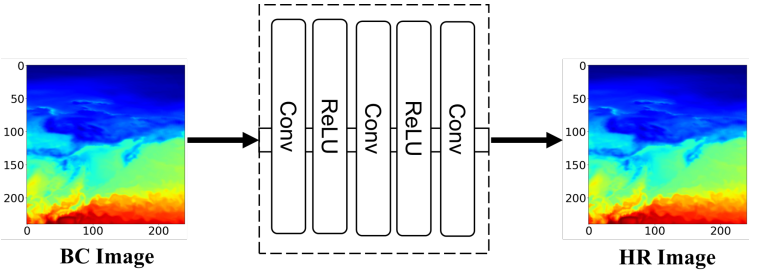

Figure 9: A schematic illustration of SRCNN architecture. The architecture takes a BC image of the surface variable as input, then generates an HR image of the surface variable.

A.2. FSRCNN-ESM

The FSRCNN-ESM (Passarella et al., 2022) consists of four conv blocks, one deconvolutional layer, and three convolutional layers, as shown in Fig. 10. The FSRCNN-ESM is an extension of FSRCNN (Passarella et al., 2022) designed to improve the accuracy of image reconstruction for ESM data. In the FSRCNN-ESM architecture, the first conv block consists of a convolutional layer with 64 filters, 5×5 kernel size, and the ReLU activation function. The second conv block has a convolutional layer with 32 filters, a 1×1 kernel size, and a ReLU activation function. The third and fourth Conv blocks each consist of a convolutional layer with 12 filters, 3×3kernel size. Following these,

there is a deconvolutional layer with 64 filters and 3×3 kernel size, and then another convolutional layer with 32 filters and 3 × 3 kernel size. Lastly, the final convolutional layer has 3 filters with a 3 × 3 kernel size, which constructs the HR image of the surface variable with a size of 240×240. The Adam optimizer is used as the optimization algorithm, while MSE is employed as the loss function for the model.

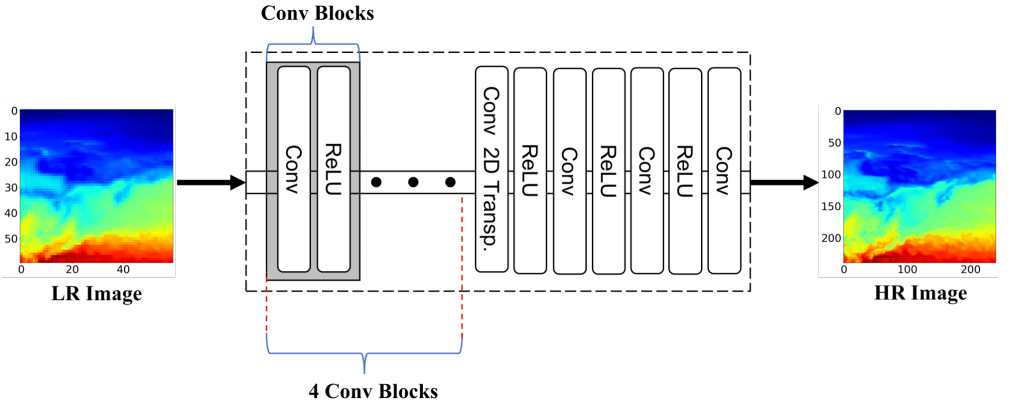

Figure 10: A schematic of FSRCNN-ESM architecture. The architecture takes a LR image of the surface variable as input, then generates an HR image of the surface variable.

A.3. ESPCN

ESPCN consists of four hidden convolutional layers, followed by a depth-to-space (sub-pixel) layer (Shi et al., 2016). The low-resolution (LR) image is used as the input. The information is then passed through the first convolutional layer with a kernel size of 5 × 5, which comprises 64 filters. The second layer is equipped with 64 filters and a 3 × 3 kernel size. This is followed by the third layer with 32 filters and 3 × 3 kernel size. The final layer has a kernel size of 3 × 3 and $r^2 \times c$ filters, where 'c' represents the number of channels in the HR image, and 'r' signifies the upscaling ratio. Throughout all four convolutional layers, the SAME padding, orthogonal kernel initializer, and ReLU activation function are employed. Subsequently, the information is forwarded to the sub-pixel layer, which generates an HR image with an upscaling ratio of 4. The optimization algorithm employed is the Adam optimizer, and the loss function for this model is the MSE.

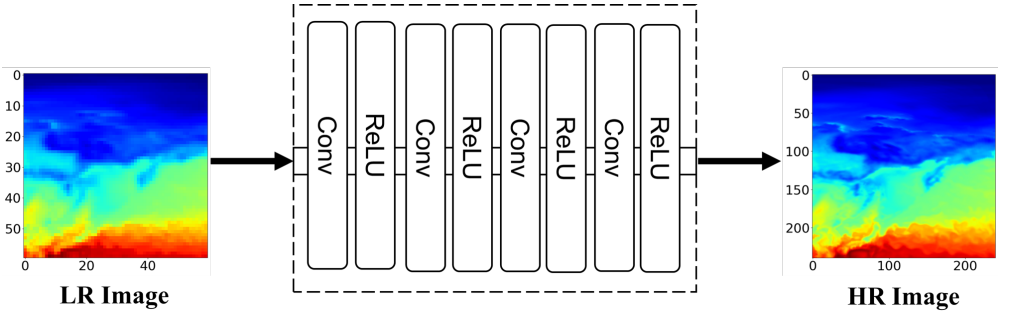

Figure 11: A schematic of the ESPCN architecture. The architecture takes an LR image of the surface variable as input and then generates an HR image of the surface variable.

A.4. EDRN

The EDRN architecture is an extension of the super-resolution residual networks (SRResNet), sharing the same architecture as SRResNet but with a notable difference in the residual block (Lim et al., 2017). The difference lies in the absence of a batch normalization layer after each convolutional layer in the residual block. The EDRN produces better SR images with enhanced PSNR and SSIM due to this update. The model we used, as shown in Fig. 12, takes

an LR image with an input size of 60×60 pixels. The first convolutional layer consists of a linear activation function, 64 filters, and a kernel size of 3×3. The padding for all Conv layers is set to "SAME." The architecture of the residual block is depicted in Fig. 15. The EDSR model contains 16 iterations of this residual block. Each Conv layer within the residual block has 64 filters and a kernel size of 3×3. The output of the residual block is then followed by a Conv layer with 64 filters and a 3×3-sized kernel. The output of this layer and the output of the first Conv layer are concatenated. The next block is an upsampling block consisting of four layers. The Conv layers in the upsampling block have 256 filters and a kernel size of 3x3. The depth-to-space (sub-pixel) layers, similar to the ESPCN model, are used with an upscale factor of 2. The loss function utilized for the model is mean absolute error, and the Adam optimizer is used.

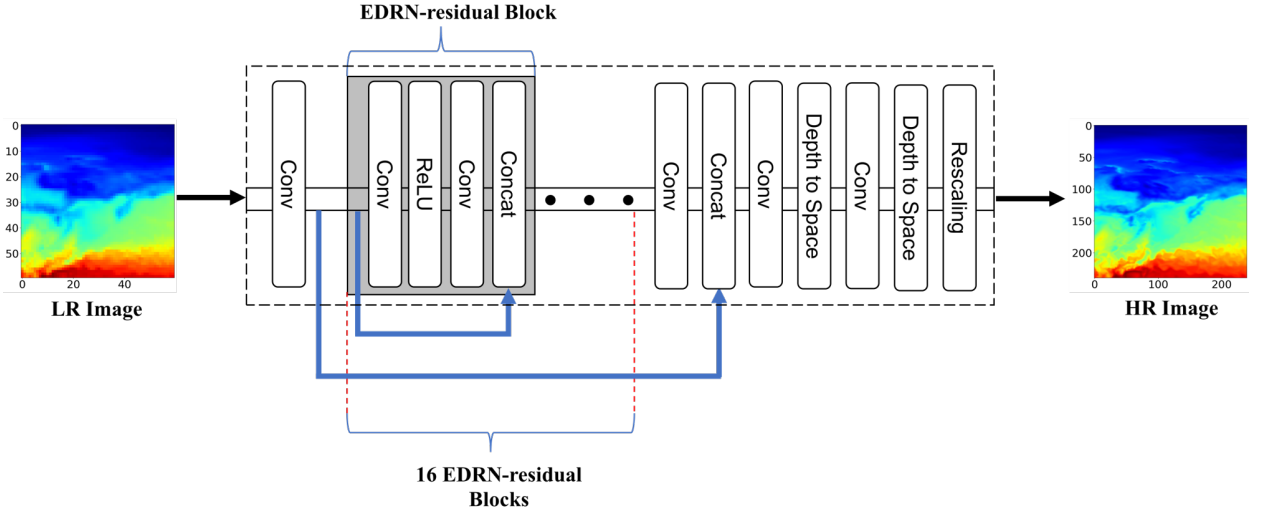

Figure 12: A schematic of EDRN architecture. The architecture takes an LR image of the surface variable as input and then generates an HR image of the surface variable.

A.5. SRGAN

The SRGAN architecture consists of a generator and a discriminator, as schematically shown in Fig. 13. This architecture is an extension of a generative adversarial networks designed for the super-resolution task. The generator takes an LR image of the surface variable with an input size of 60×60 pixels and generates an HR image of the surface variable with an output size of 240×240 pixels. On the other hand, the discriminator takes both the generated HR image and the ground truth image of the surface variable and tries to determine the similarity between them.

In SRGAN, the generator begins with a 60×60 LR input, which goes through a convolutional layer (Conv2D) with 64 filters, kernel size of 9×9, and SAME padding with PReLU (Ding et al., 2018) as an activation function. Following this initial layer, there are 16 residual blocks, each containing a Conv2D layer with 64 filters and a 3×3 kernel size, accompanied by batch normalization and a PReLU activation function. The information then proceeds through another Conv2D layer and batch normalization, maintaining the same configuration. In each residual block, the element-wise sum operation combines the input with the output of that block. The output of these 16 repeating residual blocks is then merged with the result of the first PReLU layer, followed by a Conv2D layer with 64 filters and 3×3 sized kernel, along with batch normalization. Subsequently, the resulting tensor is processed by the next two upscale blocks, each consisting of a Conv2D layer with 256 filters and a 3×3 kernel, followed by an upsampling layer and parametric activation function. Finally, we have the last Conv2D layer with 3 filters and a kernel size of 9×9 that generates an HR image of the size 240×240.

The discriminator in SRGAN evaluates the similarity between the generated HR image and the ground truth HR image to gauge their similarity. In this study, the discriminator is structured with a Conv2D layer with a kernel size of 3×3 64 filters, and a stride of 1. This is followed by an activation function, LReLU (Ding et al., 2018), with an alpha value set to 0.2. Subsequently, seven discriminator blocks are included in the architecture. Each discriminator block comprises a Conv2D layer, a batch normalization layer, and an activation function employing LReLU. While the kernel size remains fixed at 3×3, however, there are variations in the number of channels and stride. After the

seventh discriminator block, the output undergoes a flattening operation. The resulting data is then passed into a dense layer consisting of 1024 neurons and utilizing a LReLU activation function. The final layer is a single-unit dense layer employing a sigmoid activation function. The overall SRGAN loss is defined as (Ledig et al., 2017),

$$\mathcal{L} = \mathcal{L}_{cl} + 10^{-3}\,\mathcal{L}_{al}, \tag{1}$$

where $\mathcal{L}_{cl}$ and $\mathcal{L}_{al}$ represent the content and adversarial loss. The content loss is derived from the VGG-19 network (Ledig et al., 2017), and is computed as the MSE between the features of the generated HR profile and the features of the corresponding ground truth profile extracted from the network. The adversarial loss is derived from the discriminator network, which is calculated as binary cross-entropy between the predicted probability of the discriminator and the target label. For additional detail refer to Ledig et al. (2017); Li et al. (2021).

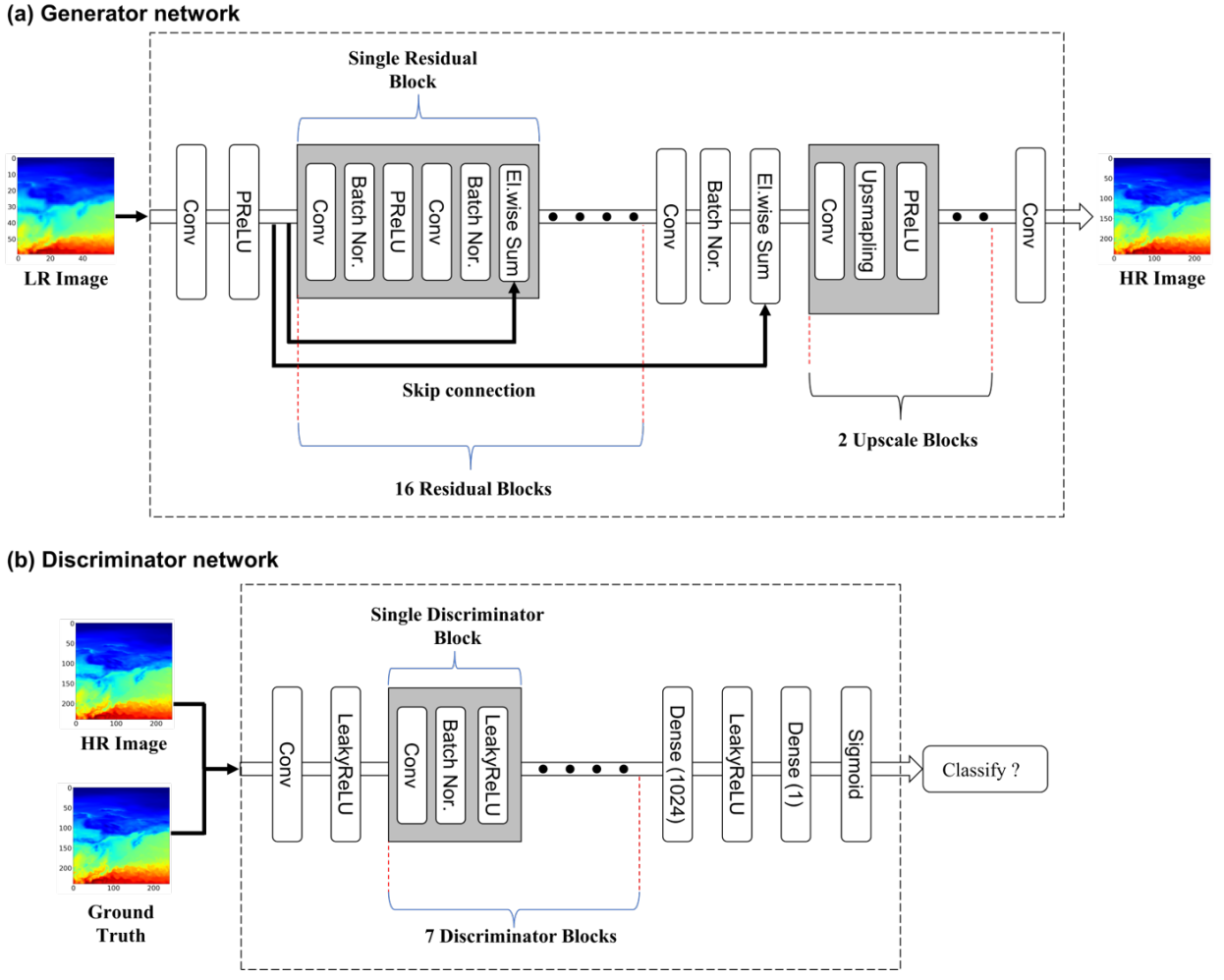

Figure 13: A schematic of the SRGAN architecture. Panel (a) depicts the architecture of the generator, which takes the LR image of the surface variable as input and generates the HR image of the surface variable. Panel (b) illustrates the discriminator architecture, which takes both the HR and the ground truth images of the surface variable and attempts to distinguish between them.

B. Appendix: Evaluation Metrics

To assess the effectiveness of our proposed framework, we employ a range of statistical metrics. We begin with the Absolute Point Error (APE), denoted as $E(x, y)$ (Faroughi et al., 2022), which is defined as follows:

$$\text{APE} = E(x, y) = |X_1 - X_2|, \tag{2}$$

The APE measures the point-wise difference between the reconstructed and ground truth profiles, where X_1 represents the reconstructed profile and X_2 is the ground truth profile.

Next, we utilize the Mean Squared Error (MSE) (Passarella et al., 2022), defined as:

$$\text{MSE} = \frac{1}{N}\sum_{i=1}^{N}(X_{1i} - X_{2i})^2, \tag{3}$$

Here, the MSE computes the average squared difference between corresponding data points in the reconstructed and ground truth profiles, where N is the total number of grids or pixels in an image.

Another metric in our evaluation toolbox is the Peak Signal-to-Noise Ratio (PSNR) (Deng, 2018), given by:

$$\text{PSNR} = 10 \cdot \log \frac{[max(X_1, X_2) - min(X_1, X_2)]^2}{MSE}, \tag{4}$$

PSNR measures the ratio between the maximum possible signal power and the power of noise that affects the fidelity of the representation. It is expressed in decibels (dB).

Additionally, we employ the Structural Similarity Index (SSIM) (Dosselmann and Yang, 2011), defined as:

$$\text{SSIM} = \frac{(2\mu_{x_1}\mu_{x_2} + c_1)(2\sigma_{x_1x_2} + c_2)}{(\mu_{x_1}^2 + \mu_{x_2}^2 + c_1)(\sigma_{x_1}^2 + \sigma_{x_2}^2 + c_2)}, \tag{5}$$

in the SSIM formula, μ_{x_1} and μ_{x_2} represent the mean values of the reconstructed and ground truth profiles, $\sigma_{x_1}^2$ and $\sigma_{x_2}^2$ are the variances, $\sigma_{x_1x_2}$ is the covariance, and c_1 and c_2 are small constants included for numerical stability. SSIM captures differences in structure, luminance, and contrast between profiles.

Finally, we incorporate the Learned Perceptual Image Patch Similarity (LPIPS) metric (Zhang et al., 2018), which is given by:

$$\text{LPIPS} = \frac{1}{M}\sum_{i=1}^{M}\left[\sum_{j=1}^{K} w_j \left|\phi_j(x_1)_i - \phi_j(x_2)_i\right|^p\right]^{\frac{1}{p}}, \tag{6}$$

here, ϕ_j represents feature maps from the j-th layer of a pre-trained deep neural network, w_j are the applied weights for each layer, M is the number of overlapping patches extracted from the profiles, K is the number of layers considered, and p is typically set to 2 for Euclidean distance. LPIPS leverages a deep neural network trained to mimic human perception of image similarity, allowing it to capture fine-grained perceptual differences between profiles by comparing their feature representations at multiple network layers. This enables a more comprehensive measure of profile similarity.

References

Ahmadi, S., Motie, M., Soltanmohammadi, R., 2020. Proposing a modified mechanism for determination of hydrocarbons dynamic viscosity, using artificial neural network. Petroleum Science and Technology 38, 699–705.

Bürger, G., 1996. Expanded downscaling for generating local weather scenarios. Climate Research 7, 111–128.

Bürger, G., Chen, Y., 2005. Regression-based downscaling of spatial variability for hydrologic applications. Journal of hydrology 311, 299–317.

Cannon, A.J., 2011. Quantile regression neural networks: Implementation in r and application to precipitation downscaling. Computers & geosciences 37, 1277–1284.

Deng, X., 2018. Enhancing image quality via style transfer for single image super-resolution. IEEE Signal Processing Letters 25, 571–575.

Ding, B., Qian, H., Zhou, J., 2018. Activation functions and their characteristics in deep neural networks, in: 2018 Chinese control and decision conference (CCDC), IEEE. pp. 1836–1841.

Dong, C., Loy, C.C., He, K., Tang, X., 2014. Learning a deep convolutional network for image super-resolution, in: European conference on computer vision, Springer. pp. 184–199. doi:https://doi.org/10.1007/978-3-319-10593-2_13.

Dosselmann, R., Yang, X.D., 2011. A comprehensive assessment of the structural similarity index. Signal, Image and Video Processing 5, 81–91. doi:https://doi.org/10.1007/s11760-009-0144-1.

E3SM Project, 2018. Energy exascale earth system model (e3sm). URL: https://doi.org/10.11578/E3SM/dc.20180418.36. [Computer Software].

Faroughi, S.A., Datta, P., Mahjour, S.K., Faroughi, S., 2022. Physics-informed neural networks with periodic activation functions for solute transport in heterogeneous porous media. arXiv preprint arXiv:2212.08965 .

Fistikoglu, O., Okkan, U., 2011. Statistical downscaling of monthly precipitation using ncep/ncar reanalysis data for tahtali river basin in turkey. Journal of Hydrologic Engineering 16, 157–164.

Ghosh, S., 2010. Svm-pgsl coupled approach for statistical downscaling to predict rainfall from gcm output. Journal of Geophysical Research: Atmospheres 115.

Hessami, M., Gachon, P., Ouarda, T.B., St-Hilaire, A., 2008. Automated regression-based statistical downscaling tool. Environmental modelling & software 23, 813–834.

Hidalgo, H.G., Dettinger, M.D., Cayan, D.R., 2008. Downscaling with constructed analogues: Daily precipitation and temperature fields over the united states. California Energy Commission PIER Final Project Report CEC-500-2007-123 .

Kharin, V.V., Zwiers, F.W., Zhang, X., Hegerl, G.C., 2007. Changes in temperature and precipitation extremes in the ipcc ensemble of global coupled model simulations. Journal of Climate 20, 1419–1444.

Ledig, C., Theis, L., Huszár, F., Caballero, J., Cunningham, A., Acosta, A., Aitken, A., Tejani, A., Totz, J., Wang, Z., et al., 2017. Photo-realistic single image super-resolution using a generative adversarial network, in: Proceedings of the IEEE conference on computer vision and pattern recognition, pp. 4681–4690.

Li, Y., Sixou, B., Peyrin, F., 2021. A review of the deep learning methods for medical images super resolution problems. Irbm 42, 120–133. doi:https://doi.org/10.1016/j.irbm.2020.08.004.

Lim, B., Son, S., Kim, H., Nah, S., Mu Lee, K., 2017. Enhanced deep residual networks for single image super-resolution, in: Proceedings of the IEEE conference on computer vision and pattern recognition workshops, pp. 136–144.

Mahajan, S., Evans, K.J., Branstetter, M., Anantharaj, V., Leifeld, J.K., 2015. Fidelity of precipitation extremes in high resolution global climate simulations. Procedia Computer Science 51, 2178–2187.

Mahjour, S.K., Liguori, G., Faroughi, S.A., 2023. Selection of representative general circulation models under climatic uncertainty for western north america .

Manor, A., Berkovic, S., 2015. Bayesian inference aided analog downscaling for near-surface winds in complex terrain. Atmospheric Research 164, 27–36.

Motie, M., Bemani, A., Soltanmohammadi, R., 2018. On the estimation of phase behavior of co2-based binary systems using anfis optimized by ga algorithm, in: Fifth CO2 Geological Storage Workshop, European Association of Geoscientists & Engineers. pp. 1–5.

Nicholls, R.J., Cazenave, A., 2010. Sea-level rise and its impact on coastal zones. science 328, 1517–1520.

Oyama, N., Ishizaki, N.N., Koide, S., Yoshida, H., 2023. Deep generative model super-resolves spatially correlated multiregional climate data. Scientific Reports 13, 5992.

Passarella, L.S., Mahajan, S., Pal, A., Norman, M.R., 2022. Reconstructing high resolution esm data through a novel fast super resolution convolutional neural network (fsrcnn). Geophysical Research Letters 49, e2021GL097571. doi:https://doi.org/10.1029/2021GL097571.

Schmidt, G., 2010. The real holes in climate science. Nature 463, 21.

Shi, W., Caballero, J., Huszár, F., Totz, J., Aitken, A.P., Bishop, R., Rueckert, D., Wang, Z., 2016. Real-time single image and video super-resolution using an efficient sub-pixel convolutional neural network, in: Proceedings of the IEEE conference on computer vision and pattern recognition, pp. 1874–1883.

Soltanmohammadi, R., Iraji, S., de Almeida, T.R., Basso, M., Munoz, E.R., Vidal, A.C., 2024. Investigation of pore geometry influence on fluid flow in heterogeneous porous media: A pore-scale study. Energy Geoscience 5, 100222.

Stengel, K., Glaws, A., Hettinger, D., King, R.N., 2020. Adversarial super-resolution of climatological wind and solar data. Proceedings of the National Academy of Sciences 117, 16805–16815.

Tabari, H., Paz, S.M., Buekenhout, D., Willems, P., 2021. Comparison of statistical downscaling methods for climate change impact analysis on precipitation-driven drought. Hydrology and Earth System Sciences 25, 3493–3517. doi:https://doi.org/10.5194/hess-25-3493-2021.

Talab, M.A., Awang, S., Najim, S.A.d.M., 2019. Super-low resolution face recognition using integrated efficient sub-pixel convolutional neural network (espcn) and convolutional neural network (cnn), in: 2019 IEEE international conference on automatic control and intelligent systems (I2CACIS), IEEE. pp. 331–335. doi:https://doi.org/10.1109/I2CACIS.2019.8825083.

Thrasher, B., Maurer, E.P., McKellar, C., Duffy, P.B., 2012. Bias correcting climate model simulated daily temperature extremes with quantile mapping. Hydrology and Earth System Sciences 16, 3309–3314.

Trenberth, K.E., 2012. Framing the way to relate climate extremes to climate change. Climatic change 115, 283–290.

Vandal, T., Kodra, E., Ganguly, S., Michaelis, A., Nemani, R., Ganguly, A.R., 2017. Deepsd: Generating high resolution climate change projections through single image super-resolution, in: Proceedings of the 23rd acm sigkdd international conference on knowledge discovery and data mining, pp. 1663–1672.

Vu, M.T., Aribarg, T., Supratid, S., Raghavan, S.V., Liong, S.Y., 2016. Statistical downscaling rainfall using artificial neural network: significantly wetter bangkok? Theoretical and applied climatology 126, 453–467.

Zhang, R., Isola, P., Efros, A.A., Shechtman, E., Wang, O., 2018. The unreasonable effectiveness of deep features as a perceptual metric, in: Proceedings of the IEEE conference on computer vision and pattern recognition, pp. 586–595.

Zhang, X., Yan, X., 2015. A new statistical precipitation downscaling method with bayesian model averaging: a case study in china. Climate Dynamics 45, 2541–2555.